EXPERIMENTAL INVESTIGATION OF THE RESPONSE OF FLAMES WITH DIFFERENT DEGREES OF PREMIXEDNESS TO ACOUSTIC OSCILLATIONS

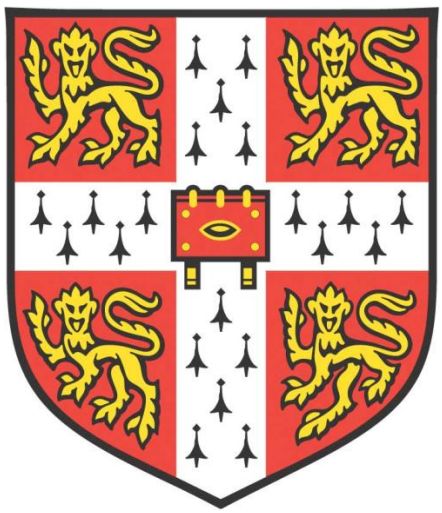

Anna Maria Kypraiou

Newnham College

Department of Engineering

University of Cambridge

This dissertation is submitted for the degree of Doctor of Philosophy

July 2017

I would like to dedicate this thesis to my family and friends…

ACKNOWLEDGEMENTS

First and foremost, I would like to thank my supervisor Prof. Epaminondas Mastorakos for his continuous help and support. His great technical expertise, invaluable advice and constructive guidance contributed to the successful completion of the present work. I am extremely grateful for giving me the opportunity to do this PhD. My time in Cambridge was a huge learning experience, not only academically, but also from a personal development perspective that I will always cherish.

I would like to thank my advisor Dr. Matthew Juniper for his invaluable suggestions and for the knowledge that I acquired through the constructive discussions we had. I am very grateful to Professor Ann Dowling, not only for the invaluable discussions and suggestions for my research project, but also for being a role model for me. In addition, I wish to thank Dr. Rama Balachandran for the insightful discussions and for sharing his expertise in the field of thermoacoustics.

Moreover, I cannot find words to express my gratitude to Dr. Nader Karimi, who conducted the experiments of the self-excited premixed flames presented in this work and also for his help and advice during my PhD. I want to express my gratitude to Dr. Patton Allison and Dr. Andrea Giusti for the constructive discussions and suggestions, it is always a pleasure to work with them. I also want to thank Dr. James Kariuki and Dr. Nicholas Worth for their precious assistance with the experimental techniques.

I am indebted to my colleagues from the Hopkinson Laboratory, namely Aleksandra Przydrozna, Alisha Kassam, Golnoush Ghiasi, Mustafa Khan, Robbie Stevens, Todd Davidson, Tafara Makuni, Edouard Machover, Elena Demosthenous, Joe Hobbs, Huangwei Zhang and all the others in the lab. Their help and kindness contributed to the productive working environment and to the very enjoyable time I spent in the laboratory.

I would like to express my gratitude to the gentlemen of the workshop, namely Michael Underwood, Roy Slater, Robert Leroy, Ken Griggs and John Harvey, who assisted in the assembly of several components of the apparatus. I also wish to thank Mr. Peter Benie for his help with the computing facilities, Mrs. Kate Graham and Mrs. Katia Babayan for their assistance.

I would like to greatly acknowledge the financial assistance of the EPSRC, Rolls Royce Plc and Onassis Foundation.

Finally, I would like to thank my family and friends whose unconditional support provided an invaluable help during this wonderful journey.

DECLARATION

This dissertation is the result of my own work and includes nothing which is the outcome of work done in collaboration except where specifically indicated in the text. No part of this dissertation has already been, or is being concurrently submitted for any other degree, diploma or qualification.

In accordance with the Department of Engineering guidelines, this thesis does not exceed 65,000 words, and it contains 150 figures.

Signed:_____

Date:_____

Anna Maria Kypraiou

Cambridge

ABSTRACT

This thesis describes an experimental investigation of the response of lean turbulent swirling flames with different degrees of premixedness (i.e. different mixture patterns) to acoustic forcing using the same burner configuration and varying only the fuel injection strategy. Special emphasis was placed on the amplitude dependence of their response. Also, the behaviour of self-excited fully premixed flames was examined. kHz OH* chemiluminescence was used to study qualitatively the heat release response of the flames, while kHz OH Planar Laser Induced Fluorescence (PLIF) was employed to understand the response of the flame structure and the behaviour of the various parts of the flame. The Proper Orthogonal Decomposition (POD) method was used to extract the dominant structures of the flame and their periodicity.

In the first part of the thesis, self-excited oscillations were induced by extending the length of the duct downstream of the bluff body. It was found that the longer the duct length and the higher the equivalence ratio, the stronger the self-excited oscillations were, with the effect of duct length being much stronger. The dominant frequencies of the system were found to increase with equivalence ratio and bulk velocity and decrease with duct length. For some conditions, three simultaneous periodic motions were observed, where the third motion oscillated at a frequency equal to the difference of the other two frequencies. A novel application of the POD method was proposed to estimate the convection velocity from the most dominant reaction zone structures detected by OH* chemiluminescence imaging. For a range of conditions, the convection velocity was found to be in the range of 1.4-1.7 bulk flow velocities at the inlet of the combustor.

In the second part, the response of fully premixed, non-premixed with radial fuel injection (NPR) and axial fuel injection (NPA) flames was investigated and compared. All systems exhibited a nonlinear response to acoustic forcing. The highest response was observed by the NPR flame, followed by the fully premixed and the non-premixed with axial fuel injection flame. The proximity of forced flames to blow-off was found to be critical in their heat release response, as close to blow-off the flame response was significantly lower than that farther from blow-off. In the NPR and NPA systems, it was shown that the acoustic forcing reduced the stability of the flame and the stability decreased with the increase in forcing amplitude. In the fully premixed system, the flame area modulations constituted an important mechanism of the system, while in the NPR system both flame area and equivalence ratio modulations were important mechanisms of the heat release modulations. The quantification of

the local response of the various parts of the flame at the forcing frequency showed that the ratio R_L (OH fluctuation at 160 Hz to the total variance of OH) was greater in the inner shear layer region than in the other parts in the case of NPR and NPA flames. In fully premixed flames, greater R_L values were observed in large regions on the downstream side of the flame than those in the ISL region close to the bluff body. The ratio of the convection velocity to the bulk velocity was estimated to be 0.54 for the NPR flame, while it was found to be unity for the respective fully premixed flame.

In the last part of the thesis, the response of ethanol spray flames to acoustic oscillations was investigated. The nonlinear response was very low, which was reduced closer to blow-off. The ratio R_L was the highest in the spray outer cone region, downstream of the annular air passage, while R_L values were very low in the inner cone region, downstream of the bluff body. Unlike NPR and fully premixed flames, in case of spray and NPA systems, it was found that forcing did not affect greatly the flame structure.

The understanding of the nonlinear response of flames with different degrees of premixedness in a configuration relevant to industrial systems contributes to the development of reliable flame response models and lean-burn devices, because the degree of premixedness affects greatly the flame response. Also, the understanding of the behaviour of forced spray flames is of great interest for industrial applications, contributing to the development of thermoacoustic models for liquid fuelled combustors. Finally, the estimation of the convection velocity is of importance in the modelling of self-excited flames and flame response models, since the convection velocity affects the flame response significantly.

CONTENTS

LIST OF TABLES

LIST OF FIGURES

LIST OF ABBREVIATIONS AND ACRONYMS

A	Forcing Amplitude
CRZ	Central Recirculation Zone
DNS	Direct Numerical Simulation
f	Forcing Frequency
FDF	Flame Describing Function
FFT	Fast Fourier Transform
FSD	Flame Surface Density
FTF	Flame Transfer Function
HVC	Helical Vortex Core
ICCD	Intensified Charge Coupled Device
ISL	Inner Shear Layer
L	Duct Length
LES	Large Eddy Simulation
L_{fl}	Flame Length
NFTF	Nonlinear Flame Transfer Function
NPA	Non-Premixed Flames with Axial Fuel Injection
NPR	Non-Premixed Flames with Radial Fuel Injection
OH PLIF	OH Planar Laser Induced Fluorescence
ORZ	Outer Recirculation Zone
P	Fully Premixed Flames
PDA	Phase Doppler Anemometry
PDF	Probability Density Function
PIV	Particle Image Velocimetry
PMT	Photomultiplier Tube
POD	Proper Orthogonal Decomposition
PSD	Power Spectral Density

PVC	Precessing Vortex Core
Q’	Heat Release Fluctuations
<Q>	Time-Averaged Heat Release
R_L	Ratio of OH Fluctuation at Forcing Frequency to the Total Variance of OH
RMS	Root Mean Square
S	Spray Flames
S_N	Swirl Number
SP	Self-excited Fully Premixed Flames
St	Strouhal Number
<u>	Time-averaged Velocity
U	Bulk Velocity
u’	Velocity Fluctuations
U_{air}	Air Velocity
U_B	Blow-off Velocity
U_f	Fuel Velocity
URANS	Unsteady Reynolds Averaged Navier Stokes
θ	Flame angle
φ	Equivalence Ratio

1 INTRODUCTION

1.1 Literature Background

This thesis describes an experimental investigation of self-excited fully premixed flames and an experimental study and comparison of the acoustic responses of lean turbulent swirling fully premixed, non-premixed and spray flames, using a configuration that is relevant to industrial systems. The understanding of the flame response is of great interest for gas turbine applications, contributing to the development of reliable flame response models and lean-burn devices.

Today, gas turbine engines are widely used for jet propulsion and electric power generation applications. A critical part of a gas turbine that has been the subject of significant research and development is the combustor, which must satisfy a wide range of requirements including: high combustion efficiency, wide flame stability limits, low pressure loss, outlet temperature distribution that is tailored to maximise the life of downstream components, low emissions of smoke and gaseous pollutant species, durability, maintainability and avoidance of combustion instabilities [1].

Traditionally, diffusion flames were used in the early combustors, where unmixed air and fuel enter the combustor chamber [2]. Mixing takes place simultaneously with combustion in the reaction zone. In non-premixed systems combustion occurs at air/fuel ratios close to stoichiometry at high temperatures. Although high combustion temperatures increase performance, the main concern is that they lead to the formation of high levels of NO_x emissions. Increasingly stringent requirements to reduce nitric oxide emissions led to the development of lean premixed combustors. In the premixed system, fuel and air are mixed upstream of the combustion chamber to ensure a fully premixed mixture at the chamber. While

lean premixed flames present the advantage of reduced fuel consumption and NO_x production (combustion occurs at lower temperatures), they are susceptible to combustion instabilities [3]. The increased susceptibility of the system to instabilities under lean operation is mainly attributed to the closer proximity to the lean blowout limit [4]. In addition, in premixed combustors limited secondary air is used, reducing the dampening effect present in earlier conventional diffusion flame burners [5]. Finally, non-premixed systems show more stability in operation than premixed systems, which present the potential risk of autoignition [2].

Flame stability at a wide range of operating conditions constitutes an important requirement of a combustor. In this study, flame stabilisation was achieved by using a bluff body and an axial swirler. When the swirl intensity exceeds a critical value, a central recirculation zone (RZ) is formed [6]. The length and width of the RZ is dependent on various parameters such as the Reynolds number, the shape of the bluff body, the enclosure geometry and the swirl intensity. A metric for evaluating the degree of swirl is the swirl number (S_N) derived by Beer and Chigier [7]. For an axial swirler with flat vanes of angle θ:

$$S_N = \frac{2}{3}.\frac{1-\left(\frac{D_{hub}}{D_{sw}}\right)^3}{1-\left(\frac{D_{hub}}{D_{sw}}\right)^2}.\tan\theta$$

Equation 1

Here, D_{hub} and D_{sw} are the swirler hub diameter and the swirler diameter respectively. Beer and Chigier [7] categorise flows based on the swirl number; for $S_N < 0.4$ the swirling flows are weak, while for $S_N > 0.4$ the swirling flows are strong and a central recirculation zone is formed.

A swirling flow with a bluff body constitutes a widely used geometry in commercial low NO_x combustors [1]. Based on the flow field schematic of a similar geometry, acquired using flow field measurements and simulations [8], the main features (Figure 1-1) are the following:

1. outer recirculation zone (ORZ) formed by the rapid expansion of the nozzle into the burner
2. inner recirculation zone (IRZ) formed downstream of the bluff body
3. high velocity annular jet

4. inner shear layer (ISL) and outer shear layer (OSL), which are important for flame stabilisation.

The recirculating flow in the ORZ transports hot combustion products to the base of the flame to mix with the fresh reactants. This constitutes a continuous source of ignition of the fresh reactants, resulting in a stable flame. The length and width of the ORZ depend on the Reynolds number, swirl number, and the enclosure geometry.

In turbulent swirling flows, apart from the aforementioned flow features [8], the formation of a three dimensional flow structure, defined as a precessing vortex core (PVC) has often been reported [9-11]. The PVC is a structure that forms when a central vortex core starts to precess around the axis of symmetry at a well-defined frequency. The development of a PVC is a function of swirl number, mode of premixing, equivalence ratio and combustor geometry and it strongly influences the flow and flame structure. Mixing and turbulence intensity are enhanced with the PVC formation, possibly resulting in increased combustion efficiency, however the PVC could be largely undesirable because of the possibility of resonant coupling with the acoustic modes of the combustor [10].

Combustion instabilities are excited by a feedback loop that couples heat release rate and pressure oscillations with the natural acoustic modes of the combustor [3, 12, 13]. These instabilities are encountered in combustion systems in applications of propulsion (rockets [14], ramjets [15] and afterburners [15-17]), power generation (land based gas turbines [18]) and other industrial uses (heating systems, furnaces [19] etc.). Thermoacoustic instabilities are an issue of major concern in gas turbines because they produce large amplitude pressure and heat release fluctuations, which result in oscillations in the mechanical and thermal loads to the engine components, flame blow-off and flashback [13]. Ultimately, these phenomena may lead to performance degradation and system failure [20]. Such instabilities may also result in incomplete combustion and hence, increased emissions, as well as elevated combustion noise. Therefore, in the past decades combustion research has included the study of thermoacoustic instabilities, however, the understanding of the underlying mechanisms of combustion instabilities in burner geometries that are relevant to industrial applications is still incomplete.

The generic feedback loop that is responsible for combustion instabilities [13] consists of the following steps (Figure 1-2a):

1. Flow and/or mixture fluctuations induce a perturbation in the heat release rate,
2. The heat release fluctuations generate acoustic (pressure and velocity) oscillations,

3. The acoustic oscillations induce flow and mixture fluctuations.

The interaction between heat release perturbations and acoustic oscillations is well understood. The conditions under which the heat release rate fluctuations add energy to the acoustic pressure field in the combustor are described by the Rayleigh criterion [21]. The heat addition process locally adds energy to the acoustic field when the heat release fluctuations and the pressure oscillations are in phase ($0^o < \theta_{p,q} < 90^o$). Conversely, the heat addition process removes energy from the acoustic field when the heat release and pressure oscillations are out of phase ($90^o < \theta_{p,q} < 180^o$). The transfer of energy from the combustion process to the acoustic field does not necessarily lead to an unstable combustor. Acoustic oscillations are excited only when the rate of energy added to the acoustic field by the combustion process is greater than the rate at which energy is removed by the acoustic field. Energy can be removed by viscosity, heat transfer and sound radiation. The mathematical expression of this statement is [13]:

$$\int_V \int_T p'(x,t)q'(x,t)dtdV \geq \int_V \int_T L_i(x,t)dtdV$$

Equation 2

where $p'(x,t)$ is the pressure oscillation of the combustor, $q'(x,t)$ is the heat release oscillation, V is the combustor volume, T is the period of oscillation, and $L_i(x,t)$ is the acoustic energy loss process. The integral on the left side of the Equation 2 is the integral form of the Rayleigh criterion, referred to as the Rayleigh integral, and the right side of the equation represents the damping processes.

In the next part of the instability feedback loop, the acoustic oscillations induce flow and mixture fluctuations. This depends on the geometry of the combustor and the fuel injection strategy. In fully premixed systems, acoustic oscillations generate only velocity fluctuations because the mixture is always and everywhere the same. However, in gas turbines fuel is injected and mixed a short distance upstream of the flame. If the fuel injection system is such that the fuel flow rate is constant and its location is far enough upstream to produce a uniform equivalence ratio across the mixing duct, a slowly time-varying velocity field will result also in a slowly-varying equivalence ratio associated with the constant fuel flow rate and the unsteady air flow rate [22, 23]. The term “imperfectly premixed” may be used to describe this situation. With fast velocity oscillations, and equivalent short wavelength equivalence ratio fluctuations, uniform mixing may be achieved by the time the mixture reaches the flame. If the fuel injection system additionally undergoes flow rate oscillations, or if its location is close enough to the

flame, this results in both temporal and spatial fluctuations of the equivalence ratio (equivalence ratio changing in space at the scale of the flame) [24-27].

The part of the feedback loop that involves the generation of heat release oscillations by velocity and/or equivalence ratio fluctuations, referred to as flame response, is not completely understood even though many studies have focused on the understanding of the mechanisms of flame response. The flame response studies can be categorised into two groups based on the nature of the inlet oscillations: self-excited and flame response studies. In a self-excited system, an unstable flame couples with the acoustics of the system. In order to determine the dominant frequency of the self-excited oscillations, pressure, velocity and/or chemiluminescence spectra are used [28]. In a forced system, acoustic oscillations at a chosen frequency and amplitude are generated externally, using a siren or loudspeakers. Self-excited studies are closer to the gas turbine applications than forced response studies, however in the former systems the isolation of the instability mechanisms is not possible. The aim of this work is to shed more light on this part of the feedback loop that is not fully understood. In particular, the behavior of fully premixed self-excited flames has been examined. Also, the response of turbulent flames with different degrees of premixedness (i.e. different mixture fraction patterns) to acoustic oscillations has been experimentally investigated, using the same burner configuration and varying only the fuel injection strategy.

Various mechanisms contribute to the occurrence of combustion instabilities in gas turbines, including (Figure 1-2b):

1. Fuel feed line-acoustic coupling [29]: In the case of unchoked fuel nozzles, the pressure drop across the fuel nozzle is modulated by pressure oscillations, resulting in modulated fuel injection rate and thus, in heat release fluctuations.
2. Oscillations in equivalence ratio [30]: Pressure oscillations modulate mixing, as well as fuel and/or air flow rates. Therefore, a time-varying reactants mixture is produced, which is convected downstream into the combustion chamber leading to a time-varying equivalence ratio and ultimately to heat release fluctuations.
3. Vortex shedding [31]: The formed vortical structures enhance the mixing of the system through the entrainment of hot products and reactants. In addition, vortical structures cause flame surface variation, resulting in heat release oscillations.
4. Periodic flame area variation [3]: Acoustic velocity-flame interactions cause an oscillatory flame area variation and subsequently, heat release fluctuations.

5. Periodic atomisation, vaporization and mixing [29]: The acoustic flow field-spray interaction produces modulations in the flame shape, evaporation rates, droplet size and mixing rate of the fuel vapor with the surrounding gases. These modulations could lead to oscillatory fuel supply and thus, time-varying equivalence ratio, producing heat release fluctuations.

In order to characterise the flame response, the flame transfer function (FTF) was introduced by Merk [32]. The FTF quantifies the relationship between overall heat release fluctuations and the imposed acoustic velocity oscillations and depends on the forcing frequency and amplitude:

$$FTF(f, u') = \frac{\frac{q'(f)}{\bar{q}}}{\frac{u'(f)}{\bar{u}}}$$

Equation 3

where $\bar{u}$ and $\bar{q}$ are the time averaged velocity and flame heat release, q' is the magnitude of the heat release rate oscillation and u' is the magnitude of the velocity oscillation, f is the forcing frequency and $u'/\bar{u}$ is the amplitude of the velocity oscillation, denoted as A (forcing amplitude). The FTF is a complex quantity: the FTF magnitude, often referred to as gain, quantifies the flame ability to amplify or damp the heat release rate response, while the FTF phase determines the delay between the velocity fluctuations travelling into the flame base and the respective heat release rate oscillations.

The flame response is categorised as linear and nonlinear based on the amplitude of the velocity fluctuations. In particular, for small amplitudes the flame response is characterised by the linear regime. In this case, $q'/\bar{q}$ scales linearly with $u'/\bar{u}$, with the flame transfer function gain being constant and independent of the velocity oscillations amplitude. The majority of the studies determining the FTF experimentally, study the flame response as a function of frequency. This contributes to the development of models for the frequency flame response in the linear regime. With the increase in forcing amplitude, the flame response is characterised by the nonlinear regime. In order to model the limit-cycle behaviours, experiments in the nonlinear regime should be conducted. The flame response nonlinearities, which may be caused by various flow and combustion processes, lead to the saturation of the heat release rate, thus the flame transfer function gain is dependent on the velocity oscillations amplitude. The role of the nonlinear flame response to the overall dynamics of the system is of

paramount importance, however the influence of the combustor geometry, fuel injection strategy and disturbance parameters (e.g. forcing amplitude, experimental conditions) on the combustion process nonlinearities, as well as the mechanisms responsible for these nonlinearities are not fully understood. This study aims to shed more light on the understanding of the nonlinear response of flames with different degrees of premixedness to acoustic forcing, using the same burner geometry and varying only the fuel injection strategy. For this purpose, the nonlinear flame transfer function (NFTF) of the different flames was measured for different forcing amplitudes.

Apart from combustion instabilities, lean blowout constitutes a major challenge for both land-based gas turbines and aircraft engines. In the case of the former, it requires costly shutdown and restarting procedures, whereas in the latter it constitutes a safety hazard [33]. Lean blow out refers to partial or global flame quenching and occurs when the equivalence ratio is reduced below a certain threshold. As the equivalence ratio approaches the lean flammability limits, the resistance of the burner to external disturbances or small deviations from the equilibrium points is greatly weakened [34]. Thus, the flame can be quenched by a small external disturbance in the inlet turbulence, fuel composition, fuel flow rate, and/or air flow rate. Near lean blow out, combustion dynamics can possibly exhibit low frequency fluctuations, or partial/global quenching may occur without significant oscillations [35, 36]. In the present work, the response of forced flames to acoustic oscillations was investigated using experimental conditions closer and farther from the blow-off condition.

1.1.1 Self-Excited Flame Studies

Despite the significant research effort in the field of thermoacoustic instabilities, the reliable prediction of frequencies and amplitudes of thermoacoustic oscillations remains a challenge. This is mainly attributed to the complex interactions among flow field, heat release and acoustic modes of the combustor. Also, a small modification of the burner geometry or a change in the operating conditions can change greatly the stability of the system, i.e. presence or not of precessing vortex cores or transition from attached to detached flames [37-39]. High-speed OH* chemiluminescence and OH PLIF measurements simultaneously with acoustic pressure measurements, as well as phase-averages of these quantities have been applied for the investigation of combustion instabilities [40-44].

Instabilities can be broadly classified into three groups according to their frequency [45]. Low-frequency instabilities occur between 30-50 Hz and are usually related to incipient blow out (referred to as ‘bulk’ mode of oscillations). Intermediate-frequencies, between 50-

1000 Hz, usually correspond to the longitudinal acoustic modes of the combustor and can relate to the coupling between fuel-air ratio and the acoustic oscillations. High frequency instabilities (frequencies above 1000 Hz) are often associated with tangential acoustic modes. Experimental efforts have identified a number of the parameters that affect the frequency of oscillations, that include equivalence ratio and air flow rate [46], total flow rate [47], forcing amplitude [48], flame speed [49], coupling between heat input and unsteady flow [50] and the geometry of the burner [43, 51, 52] to name a few.

A large number of studies have examined the mechanisms that control self-excited thermoacoustic instabilities in different burner configurations, similar to the ones used in gas turbines. In these systems, the swirling flow may result in the formation of unsteady three-dimensional vortex structures, such as helical vortex cores [10, 53] that precess around the combustor and may possibly influence mixing and combustion or may cause flame roll-up and local extinction [54]. The examination and understanding of the role of these structures, as well as the flow-flame interactions in a system undergoing thermoacoustic instabilities is very important. Previous experimental and numerical studies have investigated three-dimensional vortex structures and suggested that their behaviour can be modulated by combustion [10, 53]. Combustion can either increase or decrease the strength of the structures [10, 55]. In addition, heat release influences the frequency and shape of the structures depending on various parameters, such as thermal power, equivalence ratio, swirl number and method of fuel injection [10]. Premixed or partially premixed combustion can produce large PVC, similar in structure to that found isothermally: this is attributed to the radial location of the flame front at the swirl burner exit. Provided the flame is prevented from flashing back to the inlets values of Strouhal number for the PVC were excited by ~2 compared to the isothermal condition at equivalence ratios around 0.7. Confinement caused this parameter to drop by a factor of three for very weak combustion. Except at exceptionally weak equivalence ratios, it was found that 100% axial fuel injection suppresses the PVC amplitude by more than an order of magnitude, although its residual presence can still be detected in many systems. Finally, it was concluded that coupling between the acoustics and flame/flow dynamics occurs through a number of mechanisms including wobble/precession of the flow and flame coupled with variations in the size and shape of the CRZ arising from changes in swirl number throughout the limit cycle [10].

The interaction of acoustic oscillations with the flow structure, governing the flame dynamics was also examined by previous studies [11, 41, 56]. An experimental study by Steinberg et al. [41] on a self-excited swirling flame in a model gas turbine combustor, at which fuel and air were not fully mixed before entering the combustion chamber, revealed several

simultaneous periodic motions of the flow field: the reactants entering the combustor oscillated at a dominant frequency, which was defined as thermoacoustic frequency by the authors, a helical precessing vortex core (PVC) moved around the combustor at a frequency different from the thermoacoustic frequency, whereas an axial contraction and extension of the PVC at the thermoacoustic frequency was reported. Chemiluminescence measurements demonstrated that the global heat release rate oscillated at the thermoacoustic frequency, while the heat release centroid exhibited a movement around the burner at the difference between the thermoacoustic and PVC frequencies. Thus, the PVC interacted with the flame periodically during the thermoacoustic cycle. Based on the various shapes of the flame and the PVC interaction, an oscillation of the flame surface area was observed at different phase angles of the thermoacoustic cycle, which affected significantly the thermoacoustics of the burner. Finally, from the narrow-band frequency range of the PVC fluctuation, it was deduced that the helical mode frequency was almost constant and thus, insensitive to the flow rate fluctuations at higher frequencies.

A nonlinear coupling between the instability and the PVC under unstable combustion was also reported by other studies [43, 57, 58]. Self-excited and forced experiments on a premixed swirling flame [58] suggested that the heat release and pressure fluctuations were modulated with the thermoacoustic frequency, however the flow velocity signal exhibited peaks at the thermoacoustic frequency, the PVC and often at a frequency that corresponded to their difference. Also, at high forcing amplitudes the PVC disappeared, whereas at intermediate forcing amplitudes the velocity and the heat release signals revealed peaks at the PVC, forcing frequency and their difference.

A practical way to alter the combustor stability and control the self-excited frequencies of a combustor is by varying the length of the duct downstream of the flame. In this work, self-excited instabilities were induced in a fully-premixed methane flame by extending the length of the combustion chamber downstream of the bluff body. The duct length variation changes the relationship between pressure and heat release rate and between pressure and velocity, subsequently influencing the driving and damping responses of the burner [59]. Using such an experimental design, Kim and Santavicca [52] verified their prediction based on a theoretical thermoacoustic model that the lower eigenfrequencies would be observed in the longer duct. A similar observation was made by Noiray et al. a few years earlier, who used a piston to vary the duct length in a premixed combustor. Huang et al. [60], using their numerical model, observed a different response of the flame to low and high frequency oscillations, with the first having a more potent effect on the fluctuations of the total flame surface area and heat release.

The effect of the length of the downstream tube has also been examined by Durox et al. [43]. The effect of swirling angle in a self-excited premixed methane flame was primarily investigated. In the case of the short duct (L_{duct}=200 mm), for all the blade angles tested, no combustion oscillations were noticed, whereas for the longer duct (L_{duct}=300 mm) strong thermoacoustic oscillations were found, regardless of the swirling angle. These thermoacoustic oscillations are capable of producing a flatter flame zone [61]. Significant differences were also found in the corresponding power spectral densities with the peak corresponding to the PVC being at a higher frequency for the 300 mm duct length case. Depending on the swirl angle, the same spectrum also exhibited two additional peaks not found in the spectrum for the 200 mm condition: one corresponding to the thermoacoustic instability, and one to the difference of the two peaks.

In another study on self-excited premixed flames, where the duct length was varied, CH* chemiluminescence images showed evidence of flame-vortex interactions [62]. The combined effects of flame-vortex interactions on self-excited combustion instabilities were examined using a lean premixed gas turbine combustor, where the fuel injector location and the duct length were varied independently [63]. A lower and a higher frequency instability regimes were reported at 220 Hz and 350 Hz respectively. With the increase in equivalence ratio, instabilities shifted from the lower to the higher regime, while the instability strength was influenced greatly by the fuel injection location. In flames at which the equivalence ratio varied in space and/or in time, the flame-vortex interactions and the equivalence ratio fluctuations resulted in driving combustion instabilities.

As mentioned above, the burner geometry and the operating conditions affect greatly the stability of the system and the flame kinematics. In this work, the effect of the duct length and of the experimental conditions on the dominant frequencies of the system is investigated in order to provide useful insight into the mechanisms of thermoacoustic instabilities that are not fully understood. Also, the combination of this information with the estimation of the global heat release fluctuations and flame transfer functions based on the most dominant frequencies would contribute to an in depth understanding of the system. The results of this study would be useful for the comparison with data acquired from forced excitation studies or for the validation of computational models. This is very important since in the literature flame transfer functions are estimated experimentally mainly based on forced flames.

The effect of the mode of premixing on combustion instabilities was investigated using the Turbomeca burner [64]. A flame at which the fuel was injected into the air flow within the swirler shortly upstream of the combustion chamber, thus a certain degree of unmixedness was

present in the combustion chamber, was compared with a fully premixed flame using chemiluminescence imaging, stereoscopic particle image velocimetry (PIV) and single-shot laser Raman scattering. It was deduced that the mode of premixing did not affect the flame behaviour significantly, however differences were reported in the flame anchoring -the fully premixed flame showed a steadier flame anchoring-, the flow field in the inner recirculation zone and the CO concentrations.

A detailed experimental study by Meier et al. (see configuration in Table 1-1, I) [65] of a stable flame and a self-excited methane flame with temporal and spatial equivalence ratio variations, using the Turbomeca gas turbine model combustor, included OH* chemiluminescence, laser Doppler velocimetry, OH PLIF measurements and the detection of simultaneous mixture fraction, temperature and major species concentration measurements using laser Raman scattering. Phase-averaged measurements revealed a large variation of all measured quantities during the oscillation cycle. From this, a sequence of events contributed to the understanding of the feedback loop of the flame, which was a fluctuating fuel supply in combination with a convective time delay. The pulsating flame showed great differences compared to the stable flame in terms of flame shape, flow field, mixing and reaction progress. A geometrically identical burner was used by Brisebois et al. [44], studying the behaviour of a self-excited fully premixed swirling flame, which was affected by a helical vortex core (HVC) that rotated around the burner (Table 1-1, J). In addition, Meier et al. (see configuration in Table 1-1, K) [66] investigated a self-excited swirling methane diffusion flame in a gas turbine model combustor using the aforementioned experimental methods. The thermal expansion of the reacting gases affected significantly the flow field, inducing a periodic motion of the inner and outer recirculation zones. In fact, the biggest phase-averaged variations were observed in the inner and outer recirculation zones and in particular, a pronounced axial and radial movement was exhibited by the IRZ and ORZ respectively.

1.1.2 Forced Flame Response Studies

In this section, previous response studies focused on forced fully premixed, non-premixed and spray flames are presented.

1.1.2.1 Response of Fully Premixed Flames

A large number of experimental [40, 67-70], theoretical [71-73] and computational [74] studies have been conducted in order to understand the forced flame response to inlet disturbance oscillations and its underlying mechanisms.

The majority of the earlier flame response studies focused on the response of laminar premixed flames to acoustic oscillations [71, 75-81]. It has been found that the flame response is greatly influenced by the flame structure, forcing frequency and amplitude and that multiple mechanisms could affect the flame response. This fundamental understanding motivated the examination of the flame response of turbulent flames in more complex burner configurations.

A study on the response of turbulent flames investigated the effect of imposed mass flow oscillations on the flow field and the behavior of axial jet and swirling flames [70]. It was shown that the interaction of ring vortex structures with the flame plays a key role in controlling the combustion instabilities. Two dimensionless parameters were used to characterise the formation of the aforementioned structures: the forcing level (normalised mass flow rate RMS fluctuation at the exit of the combustor) and Strouhal number ($St = fL/U$, with f being the forcing frequency, L a characteristic length scale and U the fluid velocity). In addition, a different response was exhibited by the jet and swirling flames, which was explained by the fact that in swirling flames the air entrainment is greater than that in jet flames, leading to a local variation in equivalence ratio. In this study, the effect of the swirler on the flame response was investigated in the fully premixed configuration.

An experimental research on swirling turbulent premixed flames revealed that the flame-vortex interaction was stronger in the case of V-shaped flames than that of M flames. The flame dynamics were found to depend on Strouhal number, flame length and flame angle, suggesting that flame shape and location influence greatly the global flame response [69]. Also, it was shown that the overall heat release rate oscillation was controlled by the non-dimensional ratio of half the convective wavelength to the flame length ($0.5\lambda_{conv}/L_{fl}$) [82]. It was reported that the increase in swirl number increased turbulence intensity and flame angle, but decreased flame length leading to reduced flame transfer function gain due to the increased flame stiffness (reduced flame sensitivity to imposed disturbances). Finally, it was deduced that the structure of the stable flame affects significantly the flame dynamics of the self-excited and forced conditions.

The response of a forced flame to acoustic oscillations was studied by means of experimental and analytical tools by Borghesi et al. [83]. It was found that the response of the flow field to acoustic fluctuations influenced greatly the flame dynamics. It was concluded that combustion instabilities in gas turbines may depend on how swirling flows respond to acoustic forcing, and especially in the parts where flow recirculation occurs.

Whereas large relative pressure fluctuations ($P'/Pmean$~20-50%) are observed in rockets, in lean premixed gas turbine combustors the pressure amplitudes are on the order of 1-5% of the mean pressure [84, 85]. It was shown that acoustic processes remain in the linear regime even under limit cycle operation, while instability amplitude saturation is caused by nonlinearities between flow and heat release fluctuations [67, 85-87]. Dowling proposed a linear acoustics/non-linear heat release fluctuations computational model to predict the limit cycle behavior in a laminar premixed flame. For small amplitude fluctuations, a linear relationship between heat release and velocity oscillation was assumed, whereas when the unsteady flow velocity took values greater than the mean the heat release saturated [86].

Balachandran et al. (see configuration in Table 1-1, A) investigated experimentally the nonlinear response of a bluff body stabilised turbulent premixed ethylene flame to acoustic oscillations [40]. Three different methods for measuring heat release were tested and compared: global OH* and CH* chemiluminescence, flame surface density (FSD) based on OH PLIF and local heat release rate (RX) from simultaneous OH and CH_2O PLIF measurements. The results of these methods were very similar, implying that the flame surface density can be used as an estimate of the heat release even in large forcing amplitudes. Also, the use of chemiluminescence as a marker for heat release rate in turbulent flames was validated. The heat release fluctuations increased initially linearly with inlet velocity amplitude, while a nonlinear heat release response was observed for velocity amplitudes greater than 15% of the bulk velocity, depending on the forcing frequency and equivalence ratio. The present work extends the study of Balachandran et al. [40], investigating and comparing the response of fully premixed flames with that of non-premixed and spray flames to acoustic oscillations for various air velocities, global equivalence ratios and forcing amplitudes. For this purpose, the flame kinematics and the nonlinear flame transfer functions were compared closer and farther from the blow-off condition.

In most cases, the nonlinearities are linked with a great variation in the flame shape, modulating the phase between heat release and pressure. In particular, the phase changes with the forcing amplitude, for example because the flame length reduces as the flame gets more wrinkled, reducing the convection time from the injector to the point of maximum heat release. In the study of Balachandran et al. [40] the nonlinearity was associated with shear layer roll up into vortices. Imaging demonstrated that the vortices generated flame area when the flame wrapped around them, but also destruction of flame area was observed downstream of the vortex, resulting in heat release saturation. It was suggested that the flame response was mainly associated with the flame surface area variation, which was found to be in agreement with the

results of the numerical study by Armitage et al. [74] using a flame surface density based model for the same configuration and conditions. Another source of nonlinearity occurred at high amplitudes and at some equivalence ratios, where leakage of energy at higher harmonics was reported, even though a small content of harmonic frequency was observed in the inlet velocity oscillation [40]. It was suggested that flame sheet kinematics play an important role in the saturation mechanism of the response of premixed flames to acoustic oscillations. In addition to the vortex induced saturation, flame shape and flame position variations have been reported to affect significantly the flame response, constituting an important saturation mechanism. At large forcing amplitudes, not only variations of the mean shape of the flame were found, but also there was a change in the flame shape during the acoustic cycle [88]. At high forcing amplitudes, apart from vortex-roll up, flame lift-off, which occurred during the phase of the cycle of peak instantaneous axial velocity, was also found by Bellows et al. [89, 90] and Terhaar et al. [91] to be an important mechanism of the flame transfer function saturation. These nonlinearities were attributed to a decrease in flame area.

Many studies have focused on the development of methods for the determination of the flame transfer function as a function of forcing frequency and amplitude in laminar and turbulent flames based on experiments [16, 40, 67, 70, 81, 87, 92, 93], theoretical models [3, 72, 77, 86, 94-97] and numerical simulations [74, 98-101]. As far as the experimental studies are concerned, loudspeakers or a siren are used to impose oscillations in the inlet, and the flame response is estimated using OH* or CH* chemiluminescence, which have been reported to correlate linearly with the heat release rate in premixed systems [102, 103]. A few experimental flame response studies [104-106] estimated flame transfer functions by measuring the transfer functions of acoustic waves across the flame with the use of the multi-microphone method. For fully premixed flames, the flame transfer function results based on the multi-microphone method showed a good agreement with the results acquired from chemiluminescence measurements. However, the main advantage of the multi-microphone method was reported to be in flames with time- and/or space-varying equivalence ratio, where the chemiluminescence measurements might be unreliable. Finally, it should be noted that this method requires an estimate of the post-flame temperatures, which could be expensive and complicating.

The OH* response of a swirling premixed flame to high amplitude acoustic oscillations was studied experimentally, by means of an amplitude dependent flame transfer function and phase-averaged OH* chemiluminescence images [93]. It was suggested that for low frequencies (up to 235 Hz), partial extinction constituted the dominant mechanism of flame transfer function

saturation, while for frequencies greater than 270 Hz a vortex propagating into the outer recirculation zone was observed.

The gain of the transfer function was reported to be influenced greatly by the forcing frequency and equivalence ratio. Previous analytical [72, 107] and experimental studies [40, 68] suggested that for a constant equivalence ratio the gain of the transfer function decreases with the increase in forcing frequency. For a fixed forcing frequency, the transfer function increases with the increase in equivalence ratio, suggesting that the flame dynamics are dependent on the flame structure. In fact, based on the work by Marble and Candel [108], additional analytical and experimental studies reported that flame structure [68], flame angle [72] and flame length [69, 107], affect greatly the flame transfer function.

Most of the experimental studies on the flame response have been limited only to the estimation of the global flame transfer function without any additional quantitative or qualitative examination of the flame response locally. However, this additional information about the local flame response is of paramount importance. Thus, in the present work, apart from the estimation of the global flame transfer function, the flame kinematics were investigated by developing a novel method for quantifying the local response at the various parts of the flame at the forcing frequency. Previously, the local flame response was determined based on the amplitude of the flame sheet oscillation during the cycle by Shanbhogue et al. [109], who investigated the response of a premixed natural gas bluff body stabilised flame to small acoustic oscillations (less than 3% of the mean velocity). The flame response was found to be different in the near and far field, dominated by linear and nonlinear kinematic processes respectively. In the near-field, the flame response increased with the downstream distance until becoming maximum, while in the far-field the flame response decreased with the downstream distance. An estimation of local flame transfer functions, between velocity and local heat release at every point in the combustor, is possible with LES, giving useful insight into the maximum and minimum response zones.

Finally, computational methods have been used to study the response of the bluff body stabilised premixed flame that has been investigated experimentally by Balachandran et al. [40]. Armitage et al. [74] estimated the FDF for this flame using URANS (Unsteady Reynolds-Averaged Navier Stokes). The shape of the response was captured qualitatively, but the heat release fluctuations amplitude presented an offset. URANS was also used by Ruan et al. [101] to study the same condition, implementing a more advanced combustion model. The computed FDF showed a reasonable agreement with the measured FDF for various forcing frequencies and amplitudes, however the FDF was found to be underpredicted at high forcing amplitudes.

Large eddy simulations (LES) via the open source Code_Saturne were performed by Han and Morgans [100], capturing the flame dynamics qualitatively and the heat release rate quantitatively with reasonable accuracy. They reported that the agreement of the FDF with the experimental data was better than that obtained previously for this case using numerical simulations.

1.1.2.2 Response of Non-Premixed Flames

Apart from the response of fully premixed flames to acoustic oscillations, which has been studied extensively in the literature, the response of systems with various degrees of premixedness to acoustic oscillations and to additional temporal and/or spatial equivalence ratio fluctuations has been investigated less extensively in different burner configurations. The equivalence ratio or mixture fraction fluctuations constitute an important mechanism of nonlinear response, because they affect the nonlinear dependence of the heat release rate on the equivalence ratio [68]. Given that the majority of experimental studies in the literature have been conducted in different combustor configurations and that the geometry affects the flame kinematics significantly, a direct comparison of the response of flames with different levels of premixedness is not easy. However, understanding the response of a flame with different degrees of premixedness using the same geometry is very important, as it can contribute to the development of reliable flame response models and lean-burn devices. Thus, the main goal of the present study is to investigate the effect of the degree of premixedness on the flame response using the same burner configuration and changing only the fuel injection strategy. This section describes some of the main literature investigations on the response of systems with a certain degree of premixing, along with a comparison with the fully premixed flame response based on the same geometry, where it was available. Table 1-1 presents the combustor configurations used. For these configurations T_{conv}/T_{turb} (see definition in Section 5.1), Strouhal number, St (defined as fd/U) and fL_{fl}/U, where f the forcing frequency, U the bulk velocity, d the characteristic length of the combustor and, L_{fl} the flame length were estimated and presented in Table 1-2 for the configurations of Table 1-1 at which the data was available.

Balachandran et al. [22] (see configuration in Table 1-1, B) conducted an experimental investigation of the response of imperfectly premixed bluff body stabilised ethylene flames to acoustic oscillations, resulting in time-varying equivalence ratio. Flame transfer functions were estimated using global heat release rates based on OH* and CH* chemiluminescence and velocity fluctuations using the two-microphone technique. The response of the imperfectly premixed flames was found to have contributions through two mechanisms: flame area variations and equivalence ratio fluctuations, depending on the degree to which the flame was

compact acoustically and convectively. In particular, a non-dimensional frequency, fL_{fl}/U, was defined by normalising the frequency of forcing with the convection time, which was calculated by dividing the length of the flame, L_{fl}, with the bulk velocity, U. It has been found that this parameter influences greatly the flame response to fluctuations. It was reported that when the flame length was comparable or greater than the wavelength of forced oscillations ($fL_{fl}/U \geq 1$), i.e. at high forcing frequencies, the flame vortex-interactions constituted the dominant mechanism of heat release modulation and the magnitude of flame transfer functions of fully premixed and imperfectly premixed flames was similar. When the flame was compact ($fL_{fl}/U << 1$), i.e. at low forcing frequencies, the temporal variation of equivalence ratio was the dominant mechanism and the response of the imperfectly premixed flames was greater than that of fully premixed flames.

Kim and coworkers conducted experimental investigations of the amplitude dependent forced response of hydrogen enriched natural gas fully premixed flames and flames with a certain degree of premixedness with a time-varying velocity and equivalence ratio, while the mixture ratio inhomogeneities were assumed to be a function of x-direction only, assuming a uniform fuel distribution in the radial direction [27] (see configuration in Table 1-1 C). The convection times of equivalence ratio inhomogeneities varied, since the fuel injection location was modulated between 152 mm and 304 mm. The velocity and equivalence ratio fluctuations were measured using the two-microphone technique and infrared absorption technique respectively, while the flame transfer function was estimated by global CH* chemiluminescence measurements. It was found that the generation and convection of velocity and equivalence ratio oscillations depend on the experimental conditions and on the system configuration. Important aspects of the geometry of the system are the location and impedance of the fuel injection and the design of the fuel injector. Unlike the fully premixed flame, unsteady local extinction, as a result of flame stretching, was observed in the downstream part of the imperfectly premixed flame and specifically, when the flame angle was increasing. This was found to be an important mechanism of nonlinear response. Also, periodic flashback was reported to be a possible saturation mechanism. The phase difference between velocity and equivalence ratio $\Delta\varphi_{u'-\varphi'}$ at the burner was reported to be very important, because in the case of the imperfectly premixed flame it determined the linear and nonlinear response [27]. ($\Delta\varphi_{u'-\varphi'}$) is determined by the mixed acoustic-convective mode in the mixing section and therefore, it is a function of forcing frequency, fuel injection location and impedance and mean nozzle velocity.

The estimation of the mixing characteristics and thus, the quantitative measurement of the spatio-temporal evolution of equivalence ratio fluctuations in a flame is not trivial. A relevant study investigated the response of three systems: a fully premixed flame with fuel forcing, a fully premixed flame with acoustic forcing and an acoustically forced flame with a certain level of premixedness [110] (see configuration in Table 1-1, D). Flame transfer functions, which link the flame describing function to the acoustic flame transfer matrix, showed that the imperfectly premixed flame demonstrated the greatest response. In addition, global and spatially resolved transfer functions for equivalence ratio oscillations were estimated based on the ratio of the CH* and CO^*_2 chemiluminescence. The global mixing transfer function of the oscillating fuel supply, based on calibration measurements of steady state operating conditions with various equivalence ratios and overall mass flow rates, and using a solenoid valve in the fuel supply line, revealed a low pass character in the gain and a decreasing phase. A good agreement was reported between this measured transfer function and that calculated from a model based on a convection-diffusion equation. The spatially resolved mixing transfer function, which was calculated using radial slices of the chemiluminescence measurements, showed that most of the streamwise mixing was due to the shear layers inside the chamber and not due to the mixing section of the burner. Later, the same burner configuration was employed for the investigation of the nonlinear flame response, based on the multi-microphone method, of fully premixed and flames with a certain degree of premixedness. The level of premixedness was modulated gradually by changing the fuel split between two injection positions, while the fuel mass flow was kept constant [105]. For a forcing frequency of 166 Hz, the imperfectly premixed flame exhibited a greater response than that of the fully premixed flame, in spite of the destructive interaction because of the large gain of the equivalence ratio oscillations. The contribution of the equivalence ratio fluctuations was found to saturate fast resulting in a lower response of the imperfectly premixed flame than that of the fully premixed flame at high forcing amplitudes. A previous LES study based on the aforementioned industrial gas turbine combustor [111] reported that at the same instant different regions of the flame damped the acoustic oscillations, whereas other parts fed them. Significant differences in time delays were revealed even for parts of the flame located next to each other.

Chaudhuri and Cetegen [112] studied the response of bluff body stabilised conical turbulent premixed flames for three different types of mixture stratification (spatial mixture gradients): uniform, inner and outer enrichment (see configuration in Table 1-1, E). The flame transfer function was estimated from CH* chemiluminescence and velocity measurements using a photomultiplier tube and a hot film probe respectively. The level of the flame response

of the flame was reported to depend greatly on the spatial equivalence ratio gradients. The highest response was exhibited by the outer enrichment case, followed by the uniform and inner enrichment cases. The highest response of the outer enrichment case was attributed to the enhanced interaction between the fuel rich jet boundary and the vortical structures formed in that region, as a result of forcing. The lowest response of the inner enrichment condition was explained by its robust inner core.

Kim and Hochgreb [113] (see configuration in Table 1-1, F) estimated the response of stratified (equivalence ratio gradients in the radial direction) lean premixed flames to acoustic oscillations, based on CH* chemiluminescence measurements and assumed that the temporal equivalence ratio oscillations in the combustion chamber were negligible. It was found that a small modulation in the equivalence ratio distribution functions in the injector at a constant input power affected greatly the unforced flame geometry, influencing the flame sheet kinematics of the flames in the linear and nonlinear regime. In the nonlinear regime, leakage of energy at the higher harmonics was also observed. In addition, for a given total power and equivalence ratio, the flame response, based on OH* chemiluminescence measurements, depended greatly on the equivalence ratio split, forcing frequency and forcing amplitude, with significant nonlinearities with respect to forcing amplitude and stratification ratio (the stratification ratio was defined as the ratio of equivalence ratios of the inner to the outer streams) [24]. Inner enriched flames exhibited the highest response compared to premixed and outer enriched flames, which showed a similar response. Han et al. [24] estimated spatially resolved transfer functions of forced stratified flames from high speed chemiluminescence images, using the aforementioned geometry. It was suggested that the location and magnitude of the fluctuations along the flame branches were affected by the stratification ratio.

Measurements of flame transfer functions, estimated from the multi-microphone method, were conducted for fully premixed flames and flames with various levels of fuel-air mixing (time- and space-varying equivalence ratio), modulating the length of the mixing tube (see configuration in Table 1-1, G) [114]. The amplitude was found to be the greatest for the shortest mixing tube and decreased with increasing mixing tube length. Also, the effect of equivalence ratio oscillations on the heat release rate was examined by estimating the flame transfer function for equivalence ratio fluctuations. This was achieved by subtracting the measured flame transfer function of the fully premixed from that of the flame with a certain degree of fuel-air mixing, assuming that the shape and position of the studied flames were similar. In another study employing the same configuration, flame transfer functions of a fully premixed flame and a flame with a certain degree of fuel-air mixing were analysed based on

OH* chemiluminescence and multi-microphone measurements. Global OH* chemiluminescence, as well as planar line-of-sight chemiluminescence and density fluctuation data acquired with an intensified camera and a vibrometer respectively were compared (see configuration in Table 1-1, H) [115]. For the fully premixed system the results of these techniques were consistent. However, in the case of equivalence ratio fluctuations OH* chemiluminescence did not constitute a good indicator for heat release, as the flame transfer function amplitude was found to be overpredicted because of the sensitivity of OH* on the local fuel-air mixture.

The assumption that the measured chemiluminescence is proportional to the heat release rate is valid only in case of fully premixed systems and in the weakly turbulent and wrinkled flamelet region and in the absence of strong acoustic oscillations [116]. The quantification of chemiluminescence intensity radiated from flames that are not fully premixed is not trivial, because chemiluminescence intensity is sensitive to fuel flow rate and equivalence ratio [103, 117-119]. Balachandran et al. [22, 40] suggested that OH* or CH* chemiluminescence can be used as an indicator of heat release fluctuations in the case of a fully premixed and an imperfectly premixed flame [23]. As mentioned previously, the comparison of OH*, CH* chemiluminescence measurements and FSD, based on OH PLIF measurements, showed a good quantitative agreement. In the case of flames with time- and/or space-varying equivalence ratio the OH* chemiluminescence measurements should be interpreted very carefully, because the above assumption is ambiguous without simultaneous measurements of fuel/air ratio. Even though quantitative measurements of the mixing and reaction progress inside the combustor are very useful in order to identify the underlying mechanisms of the system, only a small number of studies in the literature provide this type of information due to the high cost and complexity. The quantification of the OH* chemiluminescence measurements is beyond the scope of the present work, and thus the magnitude of the chemiluminescence intensity data should be interpreted with caution, however the trend of the variation is expected to be qualitatively correct [27].

As mentioned previously in this section and in Section 1.1.2.1, local extinction constitutes an important mechanism of nonlinear response in forced fully premixed flames [93] and in flames with a time- and/or space-varying equivalence ratio [27]. In particular, in configurations that are much closer to real engines, limited literature exists on the investigation of the effect of acoustic oscillations in conditions close to the lean blow out limits, thus the flame response close to blow-off is examined in the present work. The focus is usually on premixed flames only [120-122]. In one of these studies [121], the blow-off of bluff-body

stabilised premixed flames under harmonic forcing of the upstream mixture velocity was investigated. The results suggest that the presence of velocity fluctuations has a strong impact on the flame behaviour, and both the blow-off mechanism and stability limits of forced flames can be different from the one observed in unforced flames. These investigations have been further extended to include upstream spatial mixture gradients [112, 123]. Results show that the behaviour of the flame and the blow-off limits are strongly affected by the spatial variation of the equivalence ratio upstream of the reacting region. Since many practical systems operate in conditions where fuel and air are not fully premixed before entering the combustion zone, it is of great interest to further extend the study of the response of flames with spatial variation of the equivalence ratio to configurations much closer to practical devices. In the case of imperfect premixing, the time-varying velocity field may introduce time-varying and spatially-varying equivalence ratio distributions, or in the case of fully non-premixed systems, time-varying heat release rate due to the time-varying mixing rates. Hence, the study of the forced response of systems characterised by different levels of premixing could also allow us to explore the impact of different mechanisms on the flame stability. In this work, the effect of air fluctuations on the behaviour of swirling flames at conditions close to the lean blow out limits has been investigated conducting experiments based on two configurations with different fuel injection strategies.

1.1.2.3 Response of Spray Flames

The experimental studies that focus on the response of forced spray flames to acoustic oscillations are relatively limited in the literature [33, 124, 125], even though they are very important for industrial applications. These systems are very complex, involving complicating physical and chemical processes, such as fuel atomisation, evaporation, droplets/flame/acoustics interactions etc. The complexity of spray flames was reported in a study of a three-dimensional swirling flame using Direct Numerical Simulation (DNS), in which it was found that fully premixed, imperfectly premixed and diffusion reaction zones might coexist [126]. Apart from the driving mechanisms of premixed flames that might also be present in a spray system at which rapid evaporation and mixing take place, physical processes related to liquid atomisation and droplet evolution could also interact with the acoustic field leading to local equivalence ratio oscillations and thus, heat release fluctuations. The estimation of flame transfer functions based on forced spray flames is very important, since it would contribute to the development of thermoacoustic models of liquid fueled combustors. However, flame transfer functions with liquid fuel flow modulations have been investigated only in a few laboratory scale experiments. In the present work, the response of ethanol spray flames to

acoustic oscillations was investigated for various experimental conditions closer and farther from blow-off. The flame kinematics, the global flame transfer function and the local response of the various parts of the spray flames results were compared with the respective results of the other systems studied.

Yi and Santavicca [33] examined the response of a 1-Decene or Jet-A flame to small amplitude fuel modulations (less than 2% of the mean fuel). The fuel was injected into the swirling air at 0.02 m upstream of the dump plane, using a single-point microlaminated fuel nozzle. Combustion occurred mainly in the premixed mode, as the evaporation time was smaller than the convection time. The flame transfer function was defined as the Laplace transform of the overall CH* chemiluminescence divided by the Laplace transform either of pressure measurements 0.29 m upstream the fuel nozzle or of fuel pressure immediately upstream of the fuel nozzle. The derived FTFs were not sensitive to fuel modulation amplitude, implying that the FTFs were linear and that heat release fluctuations were caused mainly by instantaneous fuel flow rate modulations instead of droplet size and distribution. Also, it was found that the FTF gain increased with the equivalence ratio and flame temperature nonlinearly, but the mechanisms explaining this response were not examined.

An experimental study of the response of spray flames to acoustic oscillations was conducted with a multi-jet steam assisted liquid fuel injector [124]. Flame transfer functions were estimated as the ratio of OH* or CH* chemiluminescence intensity fluctuations and the velocity fluctuations level from laser Doppler velocimetry measurements at the burner exit. The gain and phase of the transfer functions of the spray flames presented some similarities with those of premixed flames for experimental conditions at which there was no soot production.

The types of atomisers that are mainly used in the literature allow the modulated, by the acoustic forcing, airflow to pass through them. This creates a time-varying droplet size distribution that is transported further downstream towards the flame as a wave. As a result, an equivalence ratio wave appears that interacts with the flame to produce periodic heat release oscillations [127]. The FTFs are greatly affected by droplet size. Yu et al. [128] reported that droplet size determines the minimum fuel modulations required to attenuate combustion instability. The heating and evaporation time was found to be smaller for smaller droplets. This is consistent with the finding that the dynamic evaporation process might have a great influence in combustion instability [129]. Concerning the interaction between the acoustic field and the evaporation process, a theoretical study by Hsiao et al. [130] suggested the use of a response function in order to quantify the dynamic behavior of droplet vaporisation.

In this work, a pressure atomiser was used, and since the pressure oscillations caused by the acoustic forcing were negligible compared with the pressure drop at the atomiser, the acoustic forcing was assumed to have no direct influence on the droplet size distribution. Droplet size can be measured by PDA and combined Mie scattering and OH PLIF, however this is out of the scope of the present work.

Numerical models have been developed to analyse the flame response to forcing and investigate the underlying mechanisms of the flame response [33, 131]. To achieve an accurate prediction of the flame response and fully characterise the system's dynamics, the validation of computational studies with experiments, covering a wide range of experimental conditions across the operating envelop of the system, is imperative. Most studies on forced spray flames investigate experimental conditions that are far from blow-off, however the influence of forcing on the flame dynamics closer to blow-off is important. A recent experimental work on swirl stabilised unforced kerosene spray flames approaching lean blow out conditions used the Proper Orthogonal Decomposition method for the extraction of the dominant flame structures. The analysis revealed a rotation mode, associated with the motion of the swirl, and an axial oscillation mode [132].

1.1.3 Proper Orthogonal Decomposition

High speed OH* chemiluminescence and OH PLIF are used successfully in capturing the flame kinematics in turbulent flames, however a large amount of data is generated. The traditional methods for the analysis of such data are based on averaged information (mean and RMS quantities), resulting in the loss of significant amount of information. The Proper Orthogonal Decomposition (POD) method is a well-established statistical method that is increasingly used for the analysis of fast (i.e. kHz) combustion diagnostics, Large Eddy Simulations (LES) and Direct Numerical Simulations (DNS) data that allows to reduce large datasets down to their most prominent spatial features (referred to as POD Modes) of the system, aiming at extracting information that cannot be captured through the classical ensemble-averaging techniques. The POD method has been used in a wide range of applications, including turbulent fluid mechanics [133] and combustion systems [134]. In the present work, the POD method was applied to the OH* chemiluminescence and OH PLIF data of the self-excited and forced flames to extract the dominant flame structures and their periodicity. This information provides useful insight into the understanding of the mechanisms of the nonlinear flame response of the various systems.

POD has been used in the analysis of LES [135, 136] and DNS data [137, 138]. In particular, the POD code that was used in the present study was initially developed by Ayache and Mastorakos [136], who conducted a numerical investigation of the model flame TECFLAM, a non-premixed, swirling natural gas (>96% CH_4) flame. The POD analysis of an inert and a reactive case yielded two different sets of results. For the inert case, the axial velocity and mixture fraction fluctuations study revealed the presence of two pairs of diametrically opposed vortices. One pair was associated with an increase and the other pair with a decrease in axial velocity. In the reactive case, only one pair of counter-rotating vortices was observed. This work also underlined the striking resemblance of certain pairs of consecutive modes (e.g. 2-3, 5-6) that had similar morphologies, energy content and spectral densities.

Additionally, OH* chemiluminescence images were analysed with the POD method in the study of blow-off dynamics of stratified premixed flames [139] and in the understanding of vortex shedding and its contribution to blow-off and flame stability [140].

Also, the POD method was used in the study of self-excited and forced flames. The results of a POD analysis of phase-averaged Flame Surface Density (FSD) data [141] suggested that the POD method can be applied successfully in unstable combustion to investigate the dominant global and local heat release rate fluctuation information, which is of paramount importance in understanding the mechanisms of thermoacoustic instability.

Often in swirling flames the first two POD modes correspond to the precessing vortex core as the most dominant structure [142]. A POD analysis of the OH* chemiluminescence data, acquired from a forced premixed flame, showed that the first two POD Modes (Mode 0 corresponded to the average chemiluminescence) represented the PVC structure, which caused a transversal heat release modulation without producing acoustic fluctuations, while the third POD Mode revealed a strong response to the forcing frequency associated with a change in the flame angle [143].

Flow-flame interactions were investigated with the application of POD on PIV and OH PLIF data in self-excited premixed and imperfectly premixed flames. Stöhr et al. [11], Boxx et al. [144] and Steinberg et al. [47] found that the precessing vortex core was captured by the two most energetic POD Modes, demonstrating that the dominant frequency of the power spectrum corresponded to the rotation frequency of the PVC, while the third POD Mode represented the global thermoacoustic oscillation [144]. In another study by Steinberg et al. [41] the PSD of both Modes 1 and 2 exhibited two strong peaks, one corresponding to the precession of the vortex core around the burner and the second was at the difference between the PVC and

the thermoacoustic frequency. The PSD of the third POD Mode revealed a peak at the thermoacoustic frequency.

The analysis of PIV data using POD, based on bluff body stabilised turbulent premixed and stratified flames, showed coexisting toroidal and helical structures [145]. The dominant structures depended greatly on the mixture stratification in the flow field. Also, the dominant modes of the reactive and non-reactive flows were different because the unstable modes were modulated by gas expansion and high temperatures.

Finally, the spectral Proper Orthogonal Decomposition (sPOD) method was developed recently with the aim to separate modes based on their spectral contents, with the spectrum showing a well-defined peak [146]. sPOD was applied to particle image velocimetry (PIV) data and OH* chemiluminescence data in order to study the interaction of self-excited and forced oscillations. Two different PVC structures were observed, which were affected in a different manner by forcing, as well as a low frequency mode which influenced greatly the global heat release response.

1.1.4 Convection Velocity

As described previously, thermoacoustic oscillations may be induced when pressure oscillations and the flame response to the ensuing flow or mixture strength oscillations become coupled. The speed at which these perturbations propagate downstream is referred to as the convection velocity, which is of importance in the modelling of self-excited flames and in the Nonlinear Flame Transfer Function (NFTF) analysis, since the convection velocity affects the flame response significantly [79, 147]. Previous experimental studies investigating the convection velocity were limited mainly to simple laminar premixed flame configurations and for forced, rather than self-excited, flames. Karimi et al. [81] reported a good correlation between the measured convection speed (from the flame surface of the forced laminar flame) and the overall time delay of the Flame Transfer Function (from PMT measurements). Birbaud et al. [148] suggested that the convection speed depends on the forcing frequency and amplitude, while Baillot et al. [94] revealed that the convection velocity is a function of forcing frequency, but not of spatial location. Apart from these experiments, the convection velocity has also been examined through theoretical studies [79, 147]. Birbaud et al. [80] and Preetham et al. [79] reported that the convection velocity can be altered by the experimental configuration used. The ratio of the convection velocity and the mean velocity was found to be between 0.6 and 1.7 [81], while it was 1.13 and 1.02 at 35 Hz and 70 Hz respectively on a conical Bunsen flame [94]. This ratio was estimated to be 0.5 at 150 Hz in an axisymmetric wedge flame [43].

The ratio of the mean velocity to the convection velocity was found to be in the range 1-1.8 for Strouhal numbers St=0.4-2.6 [147].

Given that the majority of the previous experimental studies were conducted using simple configurations, the investigation of convection velocity based on more complex burner geometries is of great scientific interest. In this study, the Proper Orthogonal Decomposition (POD) method is applied to OH* chemiluminescence data, acquired from three flames: a) a self-excited turbulent premixed recirculating flame with swirl, b) a forced turbulent swirling fully premixed flame and c) a forced turbulent swirling non-premixed flame with radial fuel injection, i.e. configurations relevant to industrial systems, to estimate the convection velocity of the most dominant structures of each system.

1.2 Motivation and Scope

Combustion instabilities constitute a major challenge for the development of modern gas turbines, not only because they are associated with the generation of unsteady combustion, but also because they lead to considerable system degradation. In the search for the optimization of efficiency and longevity of gas turbines, several different operation modes have been employed to date. Lean flames present the advantage of reduced fuel consumption and NO_x production, but they are prone to unsteady heat release rates, because of their vulnerability to thermoacoustic instabilities [3]. The accurate prediction of the flame response is difficult, because the heat release fluctuation is affected by many parameters. Flame-vortex interactions, equivalence ratio and velocity oscillations and flame area fluctuations have been suggested to be some of the most important driving mechanisms of instabilities [149]. Many experimental studies have focused on the understanding of the mechanisms of flame response. The flame response studies can be categorised into two groups based on the nature of the inlet oscillations: self-excited and flame response studies. Apart from the use of advanced diagnostic techniques and the conventional analysis of high-speed OH* chemiluminescence and OH PLIF imaging, the Proper Orthogonal Decomposition (POD) method has been proven to be a useful tool for the extraction of the dominant structures and their periodicity, providing useful insight into the dominant mechanisms of the flame response [143].

As far as the self-excited flame studies are concerned, the stability of the system and the flame kinematics were found to be influenced significantly by the burner geometry and the operating conditions. Varying the length of the combustion chamber downstream of the flame constitutes a practical way to alter combustion stability and control the self-excited frequencies of a combustor. The investigation of the effect of the duct length and experimental conditions

on the dominant frequencies of the system provides useful insight into the mechanisms of thermoacoustic instabilities [59]. The combination of this information with the estimation of the global heat release fluctuations and flame transfer functions based on the most dominant frequencies contributes to an in depth understanding of the system. In the literature, flame transfer functions are estimated experimentally mainly based on forced flames, thus these results can be useful for the comparison with data acquired from forced excitation studies or for the validation of computational models.

Concerning forced response studies, most of the experimental investigations have focused mainly on the response of fully premixed in space and in time systems to acoustic oscillations, while less attention was given to the response of systems with various degrees of premixedness to acoustic oscillations and to additional temporal and/or spatial equivalence ratio fluctuations. The role of the nonlinear flame response to the overall flame kinematics of the system is of paramount importance, however the influence of the combustor geometry, fuel injection strategy and disturbance parameters (e.g. forcing amplitude, experimental conditions) on the combustion process nonlinearities, as well as the mechanisms responsible for these nonlinearities are not fully understood. Additionally, in the existing literature the majority of the flame response studies have been conducted in different combustor geometries, which makes the direct comparison of the response of flames with different levels of premixedness very difficult, since the geometry affects the flame response significantly. Studying the effect of the degree of premixedness on the flame response using the same burner configuration is very important, as it can contribute to the development of reliable flame response models and lean-burn devices.

The majority of the studies, determining the flame transfer functions experimentally, study the flame response as a function of frequency. There is therefore a need for detailed experiments to understand the amplitude dependence of flame transfer functions, which can then improve the prediction capabilities [96]. Also, most of the experimental studies estimate the global flame transfer functions, without conducting any additional qualitative or quantitative investigations of the flame response locally. Various parts of the flame may exhibit a different response to the imposed oscillations, thus the examination of the local response to the imposed oscillation is of great interest.

The study of the response of forced spray flames is less popular in the literature than that of forced gaseous fully premixed and non-premixed flames, even though they are very important for industrial applications. These systems are very complex, involving complicating physical and chemical processes, such as fuel atomisation, evaporation,

droplets/flame/acoustics interactions. Although flame transfer functions of forced spray flames are of great scientific interest, contributing to the development of thermoacoustic models of liquid fueled combustors, their estimation is presented only in a few laboratory scale experimental studies.

Local extinction constitutes an important mechanism of nonlinear response in fully premixed flames [93] and in flames with time and/or space varying equivalence ratio [27]. However, in configurations that are much closer to real engines, limited literature exists on the examination of the influence of acoustic oscillations in conditions close to lean blow out limits. The existing studies are mainly focused in fully premixed configurations. There is thus, a need for the investigation of flame kinematics and flame response measurements in the case of forced non-premixed flames when the blow-off condition is approached.

Finally, the estimation of the convection velocity is of significant importance in modelling of self-excited flames and in the Nonlinear Flame Transfer Function (NFTF) analysis, since the convection velocity affects greatly the flame response. Most of the existing convection velocity studies were mostly limited to forced rather than to self-excited flames. Given that the majority of the previous experimental studies investigating the convection velocity were conducted mainly to simple laminar premixed flame configurations, the estimation of the convection velocity based on more complex burner geometries is of great scientific interest.

1.3 Specific Objectives

The main objectives of this thesis are the following:

1. To study the behavior of self-excited fully premixed methane flames. The specific objectives are:
    a. to study the flame kinematics;
    b. to estimate global heat release fluctuations and flame transfer functions based on the most pronounced frequencies of the system;
    c. to evaluate the effect of duct length, equivalence ratio and bulk velocity on the dominant frequencies of the system;
    d. to extract the dominant flame structures and their periodicity using the Proper Orthogonal Decomposition (POD) method.

2. To investigate and compare the response of three methane flames with different degrees of premixedness (i.e. different mixture fraction patterns) to acoustic oscillations using

the same burner configuration. In particular, only the fuel injection strategy was varied for the study of a fully premixed flame, a non-premixed flame with radial fuel injection and a non-premixed flame with axial fuel injection.

3. To examine the response of ethanol spray flames to acoustic oscillations using the aforementioned burner geometry.

The specific objectives of the forced response investigation of the three flames with the different degrees of premixedness and of the spray flames to acoustic oscillations are:

   a. To study the flame kinematics and understand the global heat release response as well as the behavior of the local flame structure;
   b. To evaluate the effect of air velocity, global equivalence ratio and forcing amplitude on the flame response;
   c. To estimate and compare the amplitude dependence of the nonlinear flame transfer functions;
   d. To investigate the response of forced flames when blow-off condition is approached;
   e. To characterise the dominant flame structures and their periodicity using the Proper Orthogonal Decomposition (POD) method.

4. To estimate the convection velocity of the most dominant flame structures using the POD method.

1.4 Outline of the Thesis

This dissertation describes the experimental investigation of the response of flames with varying degrees of premixedness (fully premixed, non-premixed with radial and non-premixed with axial fuel injection) to acoustic oscillations and the response of spray flames to acoustic oscillations using the same burner configuration. The main objective is to compare and understand the amplitude dependence of the flame response. Experiments have provided data on the acoustic response of the aforementioned flames at various conditions, which could be useful for the CFD validation. Chapter 2 describes the experimental apparatus and the various experimental methods used in this work. Also, the methodology employed for the post-processing analysis of the experimental data is described in the same chapter. Chapter 3 presents

the results from the study of self-excited fully premixed flames. Chapter 4 describes the results from the study of the response of fully premixed flames to acoustic oscillations. The results of the response of non-premixed flames with radial fuel injection to acoustic oscillations (time-varying velocity field, and time- and space-varying equivalence ratio) are analysed in Chapter 5. Additionally, the comparison of the response of forced fully premixed and non-premixed flames with radial fuel injection is discussed in Chapter 5. In Chapter 6, the response of non-premixed flames with axial fuel injection to acoustic oscillations is discussed. Chapter 7, presents the response of spray flames to acoustic forcing. Also, the comparison of the response of forced spray and non-premixed flames with axial fuel injection is analysed in Chapter 7. Chapter 8 summarises the conclusions reached in all the above chapters.

1.5 Figures of Chapter 1

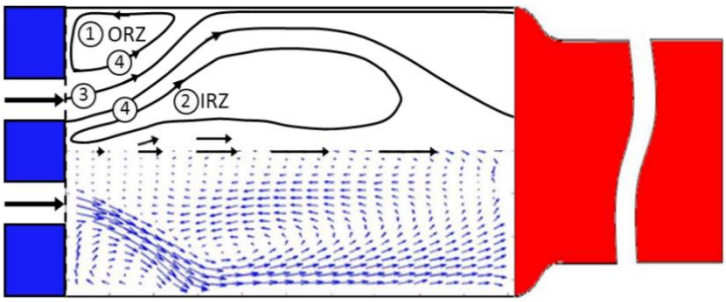

Figure 1-1: Time-averaged fluid mechanic features for a swirling flow with a bluff body [8].

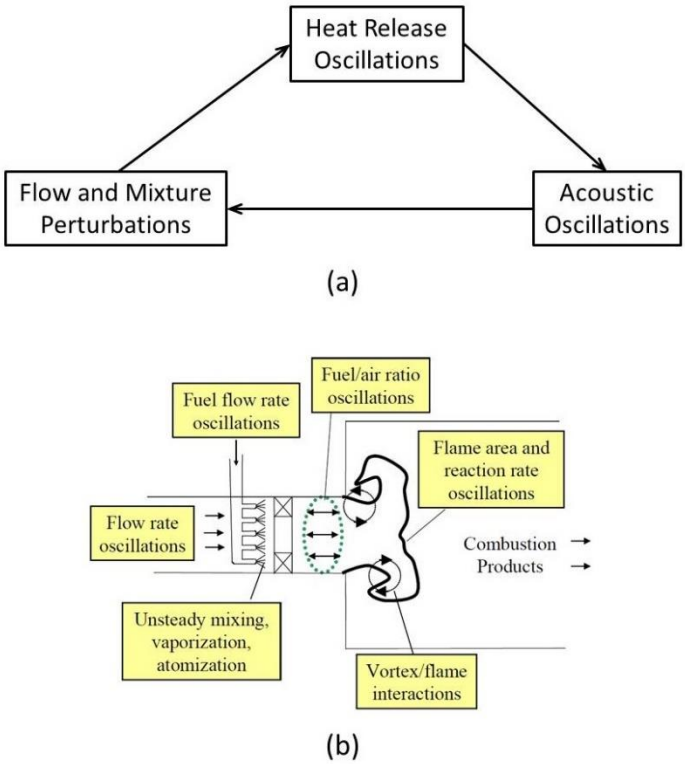

Figure 1-2: Feedback loop for combustion instabilities (a) and mechanisms of combustion instabilities (b) (From [13]).

1.6 Tables of Chapter 1

*A) Balachandran Fully Premixed Flames [40]	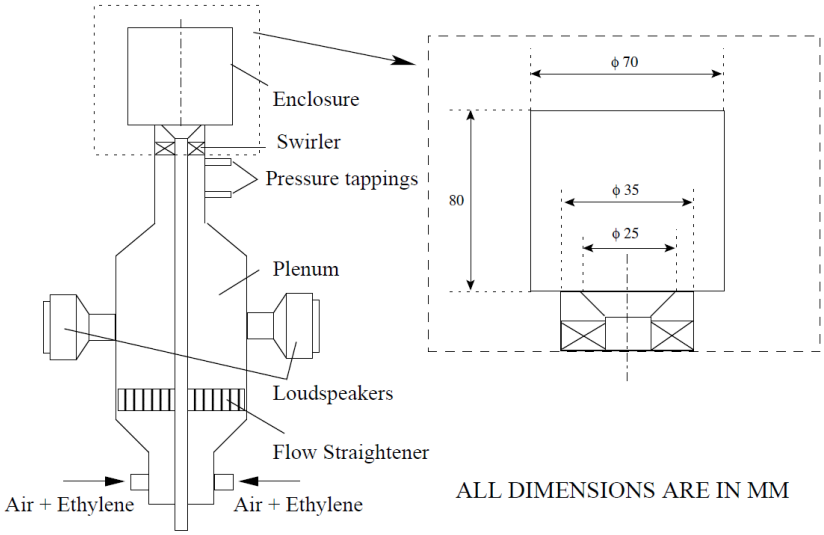
*B) Balachandran Imperfectly Premixed Flames [22]	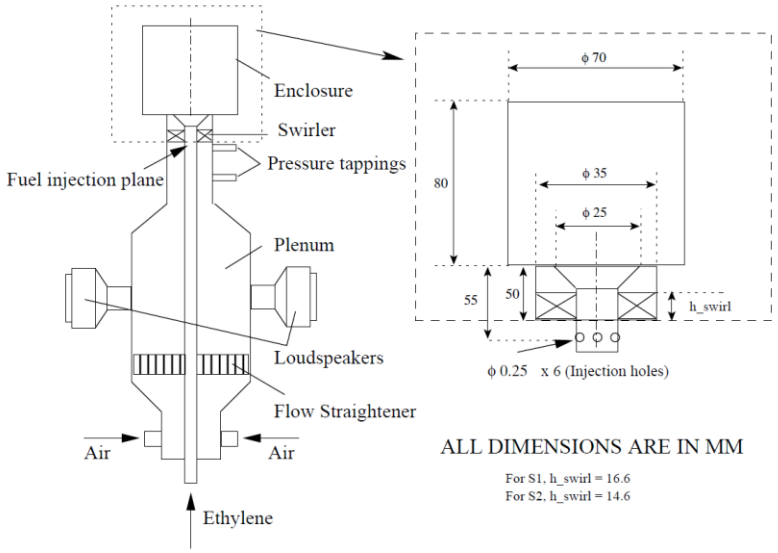
*C) Santavicca Premixed-Partially Premixed Flames [27]	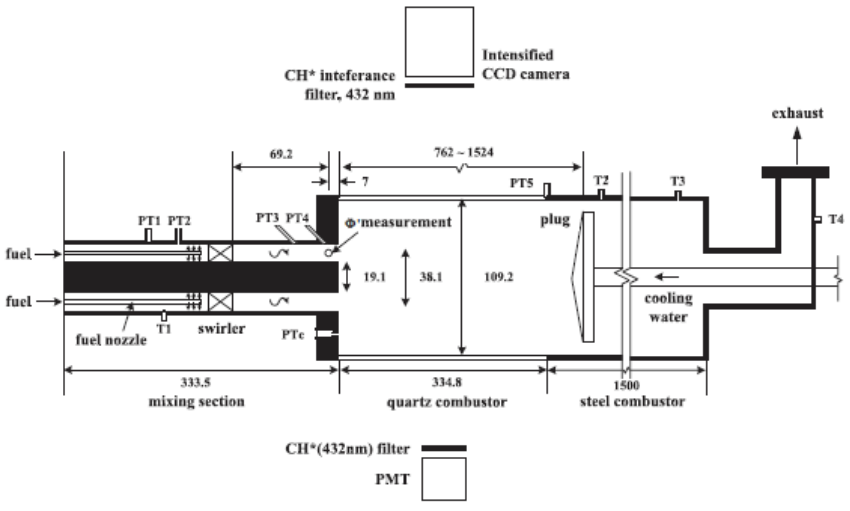

Table 1-1 continued

D) Paschereit Premixed and Partially Premixed Flames [105, 110]	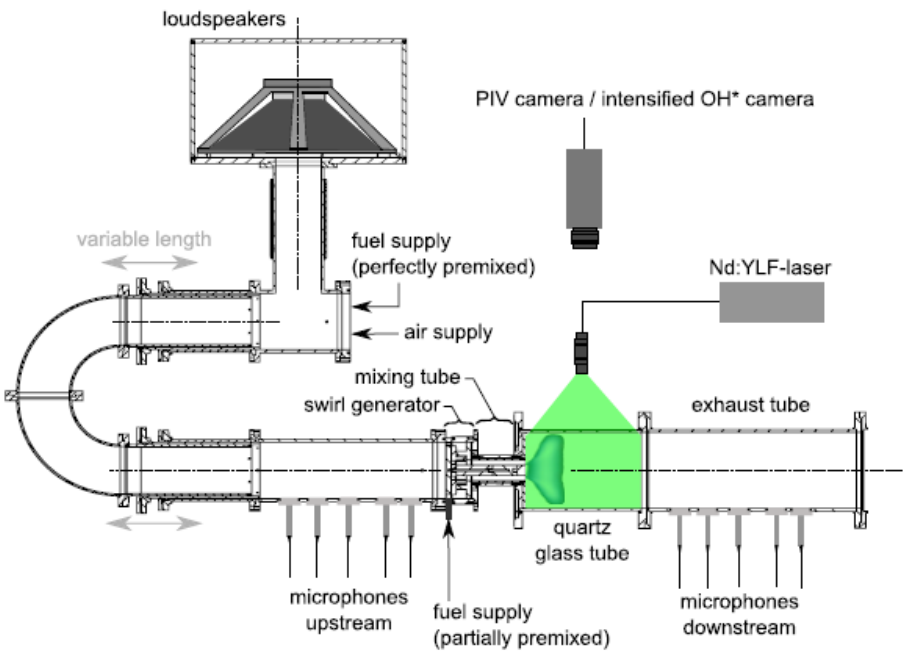
E) Chaudhuri and Cetegen Stratified Flames [112]	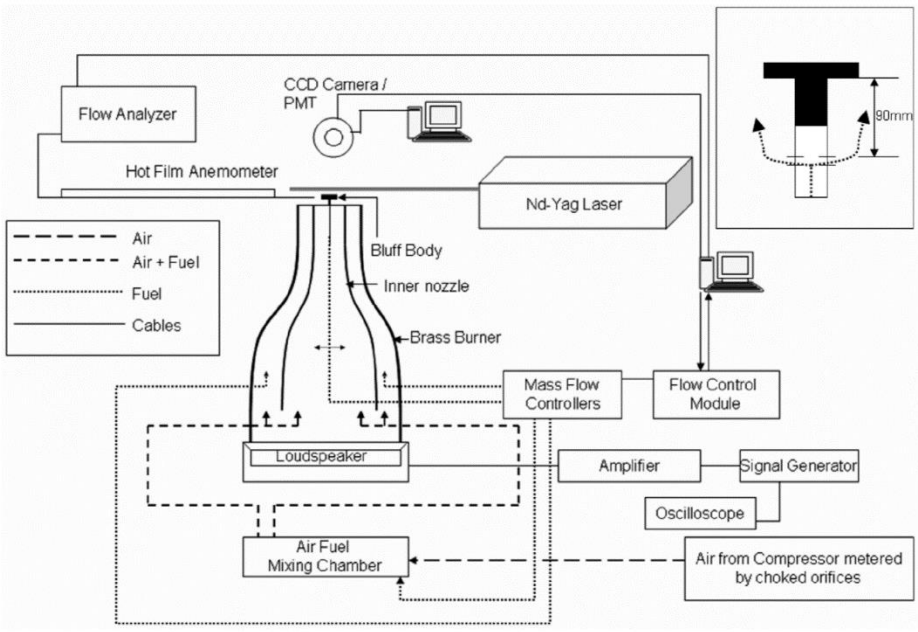

Table 1-1 continued

*F) Hochgreb Stratified Premixed Flames [24, 113]	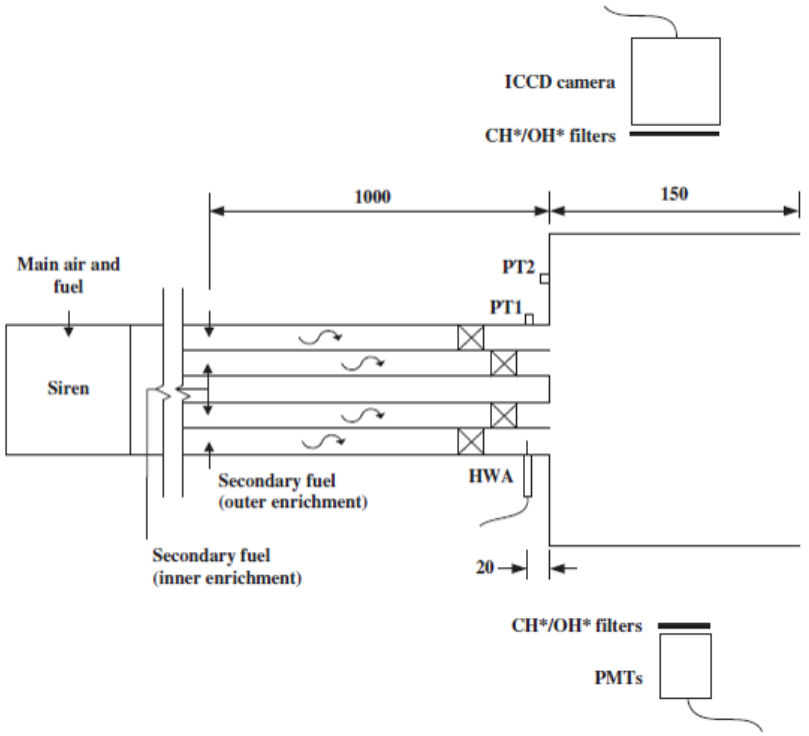
G) Sattelmayer Fully Premixed and Technically Premixed Flames [114]	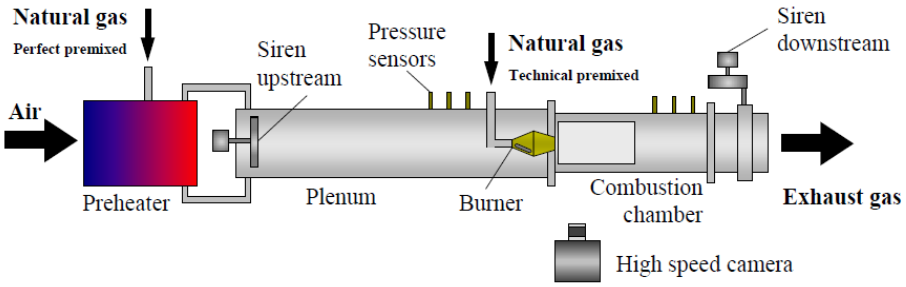
H) Sattelmayer Fully Premixed and Technically Premixed Flames [115]	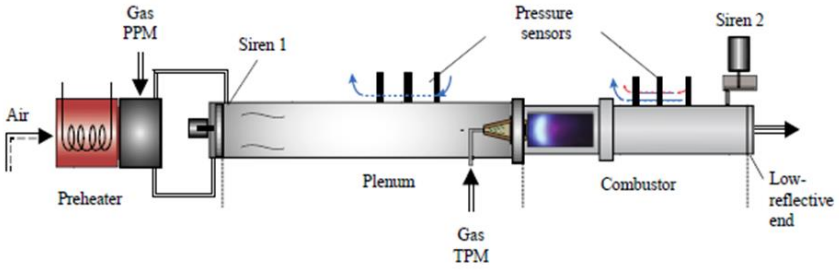

Table 1-1continued

*I) Meier Turbomeca Gas Turbine Model Combustor [65]	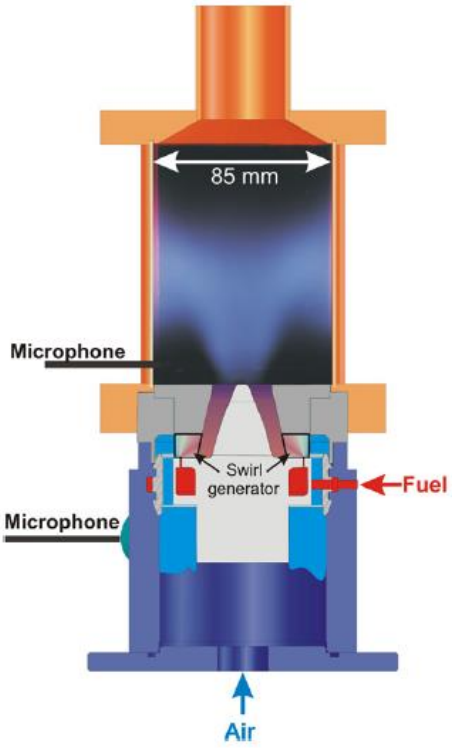
J) Meier Gas Turbine Model Combustor [44]	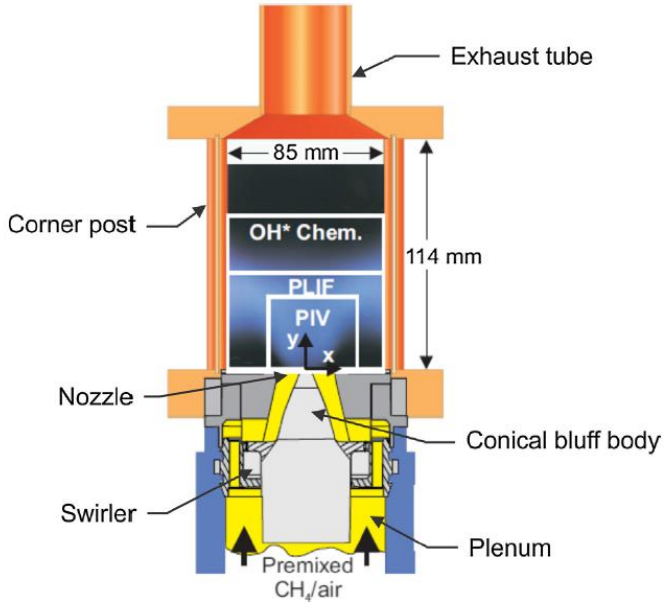

Table 1-1 continued

*K) Meier Gas Turbine Model Combustor [66]	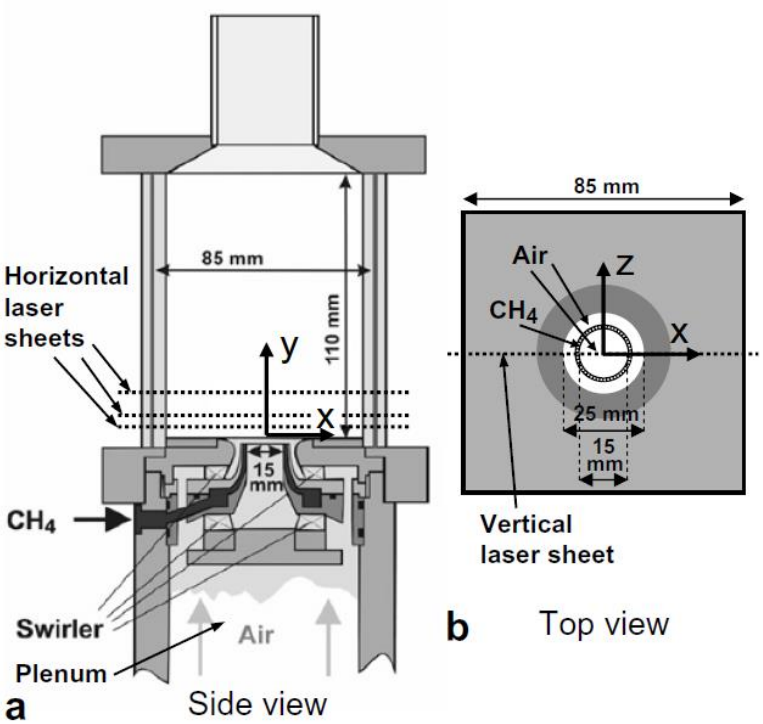
*L) Meier Partially Premixed Flames (fuel stratification) [26]	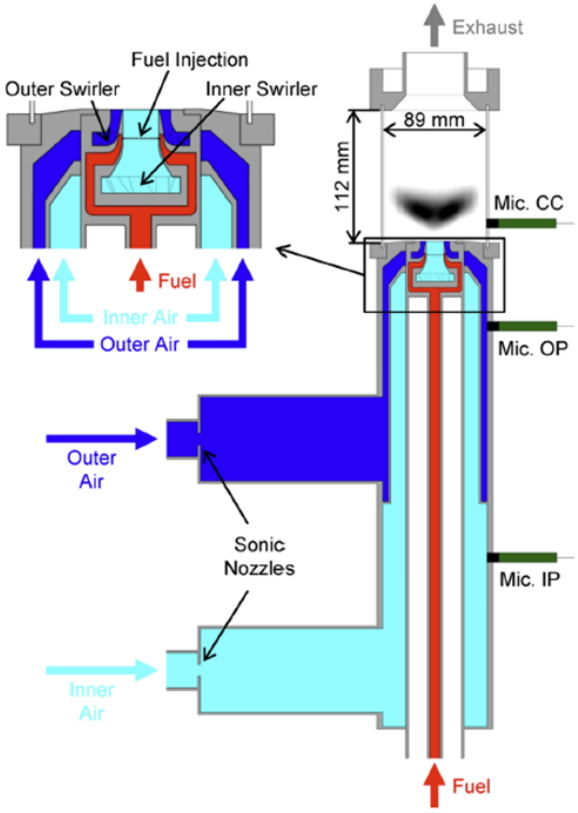

Table 1-1: Some of the main combustor geometries, described in the literature review in Sections 1.1.1. and 1.1.2.2. For the configurations with the asterisk T_{conv}/T_{turb}, fL_{fl}/U and St are estimated in Table 1-2.

	$f\ (Hz)$	T_{conv}/T_{turb}	fL_{fl}/U	$St = fd\ /\ U$
Balachandran Fully Premixed Flames	40.0	83.3	0.2 - 1.8	0.14
Balachandran Fully Premixed Flames	160	83.3	0.2 - 1.8	0.57
Balachandran Imperfectly Premixed Flames	40.0	1.53	0.2 - 1.8	0.14
Balachandran Imperfectly Premixed Flames	160	1.53	0.2 - 1.8	0.57
Santavicca Premixed-Partially Premixed Flames	200	5.37	0.33	0.13
Santavicca Premixed-Partially Premixed Flames	300	7.12	0.5	0.19
Hochgreb Stratified Premixed Flames	60.0	81.8	0.6	0.33
Hochgreb Stratified Premixed Flames	160	81.8	1.6	0.89
Meier Turbomeca Gas Turbine Model Combustor	290	1.10	0.56	0.27
Meier Gas Turbine Model Combustor	290	1.60	1.23	1.16
Meier Partially Premixed flame (fuel stratification)	400	2.84	0.69	0.27

Table 1-2: T_{conv}/T_{turb} (see definition in Section 5.1), fL_{fl}/U and Strouhal number, St for the configurations of Table 1-1 , at which the data for their estimation was available.

2 EXPERIMENTAL METHODS

This chapter describes the experimental configurations, the experimental techniques and the equipment used. Also, the post-processing analysis of the data is presented.

2.1 Description of Burner Configurations

In the present work, different burner configurations were used:

a) a fully premixed burner for the study of self-excited premixed flames
b) a fully premixed burner for the study of forced premixed flames
c) a non-premixed with radial fuel injection burner for the study of forced NPR flames
d) a non-premixed with axial fuel injection burner for the study of forced NPA flames
e) a spray burner for the study of forced spray flames.

Concerning the geometry of systems b-e, the burner configuration was the same with the main difference being the point at which fuel was injected to the system. More details of these systems are presented below.

2.1.1 Fully Premixed Self-Excited (SE) Flames Burner

The experimental apparatus used for the study of self-excited fully premixed flames (Chapter 3) was a 10 kW atmospheric combustor, shown in Figure 2-1. The burner has been developed by Balachandran et al. [40] for the study of the response of fully premixed and imperfectly premixed ethylene flames to acoustic oscillations. The burner consisted of two 300 mm concentric circular ducts. The outer duct (i.d. = 35 mm) housed two pressure taps (axial distance=150 mm), where pressure transducers were mounted flush with the duct internal wall for acoustic pressure measurements. At the exit of the inner duct (i.d. = 6mm), a conical bluff body of diameter 25 mm was mounted for the stabilisation of the flame, giving a blockage ratio of 50%. The flame was also stabilised with a 60-degree vane angle swirler, located 45 mm upstream of the bluff body plane. The swirl number was estimated to be 1.23 based on the expression in [7]. The cold gases flowed through a 200 mm long plenum chamber (i.d.=100 mm). Inside the plenum flow straighteners streamlined the flow. The working section, which involved the reactive part of the flow, included the region immediately downstream of the bluff-body plane. A quartz tube of internal diameter of 70 mm and length of 200 mm enclosed the

working section and provided optical access to the flame. Self-excited acoustic instabilities were induced by extending the length of the duct downstream of the bluff body plane. For the results presented in this chapter, the total length downstream of the bluff body plane was 210 mm, 410 mm or 510 mm, with the former producing very low-amplitude oscillations and the latter producing violent oscillations (discussed in Chapter 3).

In the present work, lean fully premixed methane flames were studied. In order to ensure a fully premixed mixture at the exit of the burner, the air and methane were mixed about 2 m upstream the combustor entrance. The dominant self-excited frequencies of the system varied in the range of 300-400 Hz, the equivalence ratio was between 0.7 and 0.8 and the bulk velocity of the reactants (defined as the total flow rate divided by the open annular area between the bluff body and the outer duct) studied was 10, 12 and 14 m/s. The experiments using this burner configuration were conducted by Dr. Nader Karimi and the post-processing analysis of the experimental data was conducted by the author.

2.1.2 Fully Premixed (P) Burner (Forced Flames)

The experimental apparatus used for the study of forced fully premixed flames (Chapter 4) is demonstrated in Figure 2-2 and Figure 2-3. The burner has been developed by Balachandran et al. [40] and has been used in this study with some modifications. It consisted of two long concentric circular ducts. The outer duct (i.d.=37 mm) housed two pressure taps (axial distance=200 mm), where pressure transducers were mounted flush with the duct internal wall for acoustic pressure measurements. At the exit of the inner duct (i.d. = 6 mm), a conical bluff body of diameter 25 mm was mounted for the stabilisation of the flame (Figure 2-2 b(i), Figure 2-3c). The flame was also stabilised with a 60-degree vane angle swirler (Figure 2-3b), located 41.6 mm upstream of the bluff body plane. The direction of the swirl was clockwise when looking at the nozzle from the combustor chamber. Inside the plenum flow straighteners streamlined the flow. The working section, which involved the reactive part of the flow, included the region immediately downstream of the bluff-body plane. Four quartz plates of 97 mm width and 150 mm length enclosed the working section and provided optical access to the flame, preventing any possible air entrainment from the surroundings. Air and methane were mixed about 1 m upstream of the burner entrance to ensure a fully premixed mixture at the bluff body plane.

In order to perturb the flame and thus, induce heat release fluctuations, acoustic oscillations were imposed to the air mass flow by means of two loudspeakers (Model Pro Signal 55-1205, 60 W, 8 ohm), positioned diametrically opposite each other in a plenum, which was

fitted upstream of the outer duct (see Figure 2-2). The loudspeakers were excited by sinusoidal signals generated using a TTi 40 MHz Arbitrary waveform generator. The signal generated by the waveform generator was amplified by an amplifier (Model IMG Stage Line Power Amplifier STA-700, 800 W) and sent to the speakers. The flames were forced at 160 Hz, which was the main resonant frequency of the burner as was also reported by [40], while the forcing amplitude (peak-to-peak voltage) varied to investigate its effect on the flame response. Between the air mass flow controller and the entrance of the burner, a barrel (190 mm x 75 mm) was used in order to act as a dampener of any potential pressure fluctuations upstream of the burner.

2.1.3 Non-Premixed with Radial Fuel Injection (NPR) Burner (Forced Flames)

As described in Section 2.1.2, in the fully premixed system the acoustic forcing by the loudspeakers resulted in a time-varying velocity field. For the study of forced non-premixed with radial fuel injection (NPR) flames (Chapter 5), the same configuration with the fully premixed system (described in Section 2.1.2) was used, with the main difference being the point at which fuel was injected to the system. Thus, the aerodynamic profile of both systems was very similar. In particular, the bluff body design of the NPR system (Figure 2-2 b(ii), Figure 2-3d) was such that allowed the fuel to be injected radially through a 0.5±0.01 mm circular gap to the main flow at 2 mm upstream of the bluff body plane. The purpose for this was to study the response of a system, where apart from the time-varying velocity field, there was also a time- and space-varying equivalence ratio (the fuel flow could oscillate, since the annular gap at the injection point was not choked). The fact that both systems had an almost identical aerodynamic profile is important in the investigation of the effect of equivalence ratio fluctuations on the flame response. The degree of premixedness of this system lies between the fully premixed and the non-premixed system with axial fuel injection (2.1.4). Figure 2-4 shows an instantaneous stoichiometric mixture fraction iso-surface from an LES/CMC simulation performed by Dr. Andrea Giusti and Dr. Huangwei Zhang for flame NPR-15-055-160-30 (see Section 5.1). It is seen that the stoichiometric mixture fraction (white line) stays very close to the bluff body and is penetrated little inside the burner. The fuel burns as a non-premixed flame, with the reactions mainly occurring along the inner shear layer of the swirling flow.

2.1.4 Non-Premixed with Axial Fuel Injection (NPA) Burner (Forced Flames)

For the study of non-premixed with axial fuel injection (NPA) flames (Chapter 6), the same burner configuration was used with that of the P and NPR Flames (see Section 2.1.2). The main difference was in the bluff body design, which was modified so that a central pipe of diameter 4 mm fed the methane (Figure 2-2 b(iii)). In this system, again there were time- and

space-varying equivalence ratio oscillations, but it is expected that the span of mixture fraction fluctuations at the flame to be larger than in the NPR system. Hence, it could be argued that the P system produces a conventional fully premixed swirl flame, the NPA system a conventional fully non-premixed swirl flame, and the NPR is a nominally non-premixed, but there is quick mixing before the flame (i.e. across the duct and during the 2 mm before the bluff body corner and up to the occasional lift-off height of the flame) so that the base of the flame may resemble the stabilisation point of a lifted jet diffusion flame and the rest of the flame to resemble a stratified premixed flame.

2.1.5 Spray Burner (Forced Flames)

The configuration used for the study of forced ethanol spray flames (Chapter 7) was similar with the previous geometries. In particular, the pressure atomiser (Model Lechler, #212.054.17.AC) was fitted to the conical bluff body holder (Figure 2-2 b(iv)), providing a hollow-cone spray at a 60-degree angle (Figure 2-2d). The orifice diameter of the atomiser nozzle was 0.2 mm [150]. The fuel injection system was connected to a tank of ethanol pressurised by nitrogen. More details on the stable ethanol flame can be found in [151].

2.2 Instrumentation

In this Section, the experimental techniques that were used in this work are discussed, while the error estimates are also stated.

2.2.1 Flow-rate Measurements

The air input to the burner was supplied by the laboratory's compressor, prefiltered for water, particulates and oil content. The air flow rate was controlled by an Air MFC (Alicat, MFC 1000 SLPM), with an uncertainty of $\pm$ (0.8% $of\ Reading\ +\ 0.2\%\ of\ Full\ Scale$) and with a repeatability of $\pm 0.2\%$ Full Scale [152]. The methane (99.999% v/v purity) flow rate was controlled by a Methane MFC (Alicat, MFC 100 SLPM), with an uncertainty of $\pm$ (0.8% $of\ Reading\ +\ 0.2\%\ of\ Full\ Scale$) and with a repeatability of $\pm 0.2\%$ Full Scale. Based on the factory accuracy of the controllers, the uncertainty of the reported velocity, U, and equivalence ratio, φ, is 2.0% and 3.0% respectively.

For the spray experiments, ethanol was pressurized by Nitrogen (99.9995% v/v purity) from a compressed cylinder regulated in the range of 0-6 bar. The ethanol (99.8 + % v/v purity) flow rate was measured using a liquid mass flow controller (Bronkhorst, LIQUI-flow, L30, 0-2 g/s) with an uncertainty of $\pm 0.02\ g/s$ [153]. The flow rate was set and then

controlled by the aforementioned mass flow controller. The mass flow was monitored by a digital readout (Bronkhorst, E-7000), connected to the MFC. For the calibration of the MFC, the weight of the ethanol output with constant flow rate ($\pm 0.1\ g$) was measured and the time taken to discharge a given amount was recorded by a hand-held stopwatch ($\pm 0.01\ s$). The calculated flowrate was then compared to the reading on the MFC.

2.2.2 Acoustic Pressure/Velocity Measurements

For the self-excited system, two Kulite high sensitivity pressure transducers (Model XCS-093 with sensitivities of 4.2857×10^{-3} mV/Pa, and maximum pressure of 5 psi) were mounted flush with the duct internal wall to measure pressure oscillations. For the forced flames, two Kulite pressure transducers (Model XCQ-093, with sensitivities of 2.90598×10^{-3} mV/Pa, and maximum pressure of 5 psid) were used. These pressure signals, after being amplified by a Transducer Amplifier (Model FE-579-TA, Fylde Modular Instrumentation), were used to calculate the velocity fluctuations at the bluff body plane with the two-microphone technique [154]. The two-microphone technique was checked using direct measurements of velocity fluctuations under cold flow conditions with a Dantec hot wire anemometer (Model 55P11), positioned at a radial distance of 15.5 mm from the bluff body centre. The signals from the pressure transducers and the hot wire anemometer were acquired at a sampling rate of 10 kHz with sample lengths of 3.2 s, and digitised using a National Instruments PCI 6034E DAQ card with 16 bits resolution, resulting in a frequency resolution of 0.3 Hz.

2.2.3 OH* Chemiluminescence Measurements

OH* Chemiluminescence constitutes an extremely useful technique to visualise the combustion process and understand its response to acoustic oscillations. It has been used in previous studies to infer the overall or local heat release rate (because the intensity of the chemiluminescence emission from lean premixed flames has been suggested to be an indicator of the heat release rate) and determine the reaction zone location of lean fully premixed flames [40, 87, 155-158]. Chemiluminescence is the radiation emitted from electronically excited species, while decaying back to a lower energy level. The wavelength of this radiation is characteristic of the particular molecule and the transition that it undergoes. For lean hydrocarbon flames a strong chemiluminescence emission is exhibited from OH* at 308 nm. The amount of radiative emission in the flame at a particular wavelength is proportional to the concentration of the associated excited molecule, thus the intensity of the measured chemiluminescence emission can be directly related to the concentration of the excited species [157].

In the self-excited premixed system, OH* chemiluminescence measurements were conducted using full planar view high speed imaging system. For the forced flames, the OH* chemiluminescence measurements were conducted using: a) full planar view high-speed imaging system, and b) a photo-multiplier tube (PMT) unit. In particular, the high-speed imaging system consisted of a LaVision IRO high-speed two stage intensifier (spectral range of 190-800 nm) coupled to a Photron SA1.1 monochrome high-speed CMOS camera with a 1024×1024 pixel resolution up to 5.4 kHz. A UV bandpass filter (270-370 nm) was fitted to the Cerco 2178 UV camera lens. Images were recorded at 5 kHz for 1 s, within the pressure measurement period and the intensifier gated at 190 μs. The projected pixel resolution was approximately 0.14 mm/pixel. The photo-multiplier tube used to measure the global OH* chemiluminescence was a Thorlabs PMT (Model PMM01), fitted with the UV bandpass filter (270-370 nm). It was ensured that light emission was collected from the entire combustion zone. The PMT measurements were recorded simultaneously with the pressure measurements using the aforementioned data acquisition system (Section 2.2.2). The OH* chemiluminescence measurements acquired by the PMT match very closely those acquired by the ICCD camera. Figure 2-6 plots the normalised heat release fluctuations with respect to forcing amplitude, A, of a fully premixed flame forced at 160 Hz, based on OH* chemiluminescence measurements from both PMT and ICCD. It is evident that the maximum deviation is 7%.

In most studies, it is assumed that the overall chemiluminescence emission is proportional to the overall heat release rate. This assumption is valid for constant flame temperature, equivalence ratio, unburned gas temperature, dilution and radiation losses and also for a regime of low strain and curvature [159]. Thus, for flames with time- and space-varying equivalence ratio the OH* chemiluminescence measurements are ambiguous without simultaneous measurements of equivalence ratio fluctuations and they need to be interpreted carefully. In this work, OH* chemiluminescence measurements were used in the absence of other techniques. The normalised global chemiluminescence intensity ($OH^{*\prime}/< OH^{*} >$) was used as a measure of heat release rate in previous studies on the response of stratified premixed flames to acoustic forcing [24], on the investigation of forced imperfectly premixed flames [22] and on the estimation of FTFs of forced spray flames [124]. Finally, the OH* chemiluminescence technique constitutes a line-of-sight measurement (measuring the total emission integrated along the line of sight), thus it cannot capture details of the flame structure. In addition, the signal of the chemiluminescence emission is relatively weak compared with that of the OH PLIF measurement, requiring a longer integration time in order to obtain a strong enough signal.

2.2.4 OH PLIF Measurements

OH PLIF measurements are commonly used during stable and unstable combustion in order to visualise the structure of the flame sheet [40]. Laser-induced fluorescence (LIF) is performed by using laser radiation to excite the species of interest to an upper-electronic state. Then, the excited molecules fluoresce, by emitting photons when they decay back to lower energy states [159]. LIF can be used to make single point measurements with each pulse or to perform two dimensional measurements, at which the laser beam is spread into a thin sheet. The difference between LIF and PLIF lies on the way the fluorescence signal is detected; in a LIF system a photo-multiplier tube can be used and the laser is not turned into a sheet, while in the PLIF system a CCD or an intensified CCD (ICCD) camera is required. In both systems, an interference filter is used to isolate and collect the fluorescence wavelength of interest [159]. In the wrinkled laminar-flame regime, the flame front location can be determined by a steep gradient of OH fluorescence intensity. However, OH radical is relatively long lived, thus it can also be present in regions of high temperature products [159, 160].

In the present study, the OH PLIF system consisted of a SIRAH Credo high speed dye laser (Model 2400), pumped by a high-repetition rate diode solid state laser (532nm, Model JDSU Q201-HD), with a power of 14W at 5 kHz and a pulse length of around 18 ns. The dye laser produced a beam at 566 nm, which was doubled by a BBO crystal to produce a beam with an average power of 300 mW at 5 kHz (60 μJ/pulse). The laser beam was expanded to a 40 mm-height sheet using optics. A LaVision IRO high-speed two stage intensifier was used, coupled to a Photron SA1.1 monochrome high-speed CMOS camera with a 1024×1024 pixel resolution up to 5.4 kHz, fitted with a UV bandpass filter (300-325 nm). Figure 2-5 shows a schematic of the laser and imaging system that was used for the OH PLIF experiments. Images were recorded at 5 kHz for 1 s, within the pressure measurement period, and the intensifier gated at 400 ns. The resolution of OH PLIF images was approximately 0.1 mm/pixel. During processing, each instantaneous OH PLIF image was initially filtered using a 2-D median nonlinear filter for noise reduction (3×3 filter size). Then, the filtered images were corrected for laser sheet profile inhomogeneities with a Gaussian intensity profile.

It should be mentioned that the OH PLIF measurements were used in this study only qualitatively to understand the response of the flame structure and the behaviour of the various parts of the flame, as described in Section 2.3.3. The Flame Surface Density (FSD) results (based on the OH PLIF data, see Section 2.3.2) are used as a surrogate of the heat release for fully premixed flames [40], whereas they can only be used as an indicator of the flame area for the non-premixed flames.

2.3 Data Processing

2.3.1 Determination of the Flame Response based on OH* Chemiluminescence

The time series of acoustic pressure, OH* chemiluminescence and the forcing reference signal measurements were acquired simultaneously for different forcing amplitudes. These signals were analysed spectrally using the Fast Fourier Transform (FFT) technique to determine the complex amplitude of $OH^{*\prime}$ and u' at the forcing frequency. These values were normalised using the respective time averaged values. $OH^{*\prime}(f)/< OH^{*} >$ was used as an estimate of the fluctuating response of the global heat release $Q'(f)/< Q >$. $A = u'(f)/< u >$, $u'(f)$ was the magnitude of the Fourier Transform centred at the forcing frequency, determined from the pressure measurements using the two-microphone technique. From these quantities, the Nonlinear Flame Transfer Function $NFTF = (Q'(f)/< Q >)/(u'(f)/< u >)$ was calculated as a function of A. The acoustic response of the burner was determined by acquiring simultaneous velocity and acoustic pressure measurements, while perturbing the airflow using a constant magnitude sinusoidal input voltage to the speakers at frequencies between 10 and 500 Hz and with a flow velocity of $U = 10$ m/s, shown in Figure 2-7. A good agreement between the two-microphone technique and the hot-wire measurements is shown, as was also reported by [40, 42]. The two-microphone technique slightly overestimates the magnitude of the velocity fluctuation, but the trend of the variation is captured well. Both techniques show a good agreement in the phase of the velocity fluctuations relative to the input forcing signal. Also, three resonant peaks are revealed at 40 Hz, 160 Hz and 320 Hz, from which the frequency at 160 Hz was chosen for the flame forcing in this study because it yielded the highest forcing amplitude. The location of the reference point, at which A is measured is critical for the estimation of a reliable transfer function value. It was reported that if the reference point is not located close to the burner inlet, this would result in uncertainties in the transfer function estimation [161]. In this study, the reference point was located in the inlet of the combustion chamber, which was also the case in [40].

Furthermore, the phase-averaged variation of $Q'(f)/< Q >$ at the forcing frequency was estimated. The 5000 acquired OH* images were separated into a data sets at 15° with respect to the forcing reference signal. Each data set was spatially integrated which provided the phase averaged mean for that set. All the 15° data set was then normalised with the mean value of all the 5000 images, which is referred to the phase-averaged OH* plot.

2.3.2 Estimation of Flame Surface Density (FSD)

The flame surface density (FSD) was estimated using the corrected OH PLIF instantaneous images, following a similar procedure with that described by [40]. In particular, the images were filtered with a Gaussian filter of a width of 3 pixels to remove high frequency noise, and then they were converted into binary images using an intensity thresholding algorithm. Binary values were assigned to the progress variable, which was defined such that it took a value of 0 in fresh reactants and a value of 1 in burnt gases. Also, the magnitude of the 2-D gradient of the progress variable was calculated and the instantaneous flame edge contour was obtained using a threshold on the gradient. The FSD was calculated following a similar approach with others [40, 42, 162], using an interrogation window of 5×5 pixels. In addition, phase-averaged FSD images were calculated at every 15-degree phase angle. The phase-averaged FSD images were also revolved around the central axis of the burner to obtain the cyclic FSD variation. This quantity was compared with the cyclic OH* chemiluminescence variation based on a 40 mm window (40 mm is the height of the OH PLIF laser sheet). The FSD results could be used as a surrogate of the heat release for fully premixed flames [40], whereas they were used only as an indicator of flame area for the non-premixed system with radial fuel injection.

2.3.2.1 Estimation of Lift-off Height

Following the FSD evaluation procedure, the distance of the high gradient of OH regions from the bluff body edge of the left and right branch of the flame was estimated for each image and was referred to as lift-off height, h (Figure 2-8). Also, the probability density function (PDF) of the lift-off height, $P(h)$, ($\int P(h)dh = 1$), with respect to h was calculated and the time average value of h was estimated. For this calculation, the lift-off heights of the left and right branch of the flame in each instantaneous snapshot were considered as two independent samples. The lift-off height timeseries, obtained from the mean lift-off heights of the left and right branches in each instantaneous snapshot, were used in order to obtain the power spectral density (PSD). In this case, the periodicity of the lift-off height signal was examined. In flames at which the PSD exhibited a strong lift-off height periodicity at the forcing frequency, the phase-averaged lift-off height at every 15-degree phase angle was estimated.

2.3.3 Determination of the Behaviour of Different Regions of the Flame based on OH PLIF Imaging

2.3.3.1 Estimation of Flame Angle

The variation of the flame angle during the cycle was estimated based on the phase averaged OH PLIF images. First, for each averaged OH PLIF image at a specific phase angle (Figure 2-9a) an intensity thresholding algorithm was used (Figure 2-9b), after which the magnitude of the 2-D gradient was calculated. Then, the maximum values of the gradient were estimated and the flame edge contour was obtained (Figure 2-9c). A window of 15×25 mm (selected empirically based on the location of the flame edge contour) was used, inside which the point of the maximum gradient was determined. Finally, the flame angle was estimated based on the line, defined from this point and the centre of the annular gap at the bluff body plane, as indicated in Figure 2-9c.

2.3.3.2 Estimation of impingement point

The phase-averaged OH PLIF images were used for the estimation of the impingement point. In particular, for each phase averaged OH PLIF image at every 15-degree phase angle, iso-contour plots of the OH intensity were calculated. The colour contours represent equally spaced thresholds of the OH intensity data, selected carefully based on the range of the OH values, while each colour corresponds to a specific threshold. An example of a phase averaged contour plot at 120-degree phase angle is shown in Figure 2-10. It can be seen that the OH fluorescence signal in the ORZ forms two circular structures, the lower and the upper. The impingement point is defined as the point at which the aforementioned structures separate (indicated by the red arrow in Figure 2-10). During the acoustic cycle, the position of the impingement point moves axially (see Appendix A). Tracking the position of the impingement point during the cycle provides useful insight on the kinematics of the OH structures downstream of the burner exit. Thus, the purpose of the impingement point estimation is to get information about the size of the OH structures that are constrained in the corner of the dump plane.

2.3.3.3 Local response estimation

It has been shown that burners exhibit regions [109] that have different levels of sensitivity to forcing hence, local variations in flame response are present in the flame. A method for quantifying the local response of the flame at the forcing frequency was developed. We define the ratio R_L as the OH fluctuation contribution at 160±3 Hz to the total variance at each pixel. This quantity provides a measure of the energy contained at the forcing frequency

relative to the total energy of the fluctuations, as a function of space. As the number of pixels of an image is very large, this computation can be very long. Therefore, to reduce the computational demand, each OH PLIF image of a 5000-image dataset was divided into 100×100 groups.

The specific steps for the calculation of R_L in each group are:

1) The OH intensity values of all the pixels in that group were summed:

$$f(m) = \frac{\sum_{j=1}^{n}\sum_{i=1}^{n} OH(i,j)}{(n \times n)}$$

Equation 4

where n is the total number of pixels in each group.

2) The timeseries of the vector sum, $F(t)$, were calculated using $t = [1/5000, 2/5000, \dots, 5000/5000]$ and $F = [f(1), f(2), \dots, f(5000)]$.
3) The PSD of $F(t)$ was calculated. Flat Top windowing was used to estimate the PSDs. The Flat Top windowing function shows a good performance for sinewave signals and for applications at which the amplitude accuracy is important.
4) The total variance was estimated by integrating all the spectral components in the frequency domain (0-500 Hz): $\int_0^{500\ Hz} PSD\big(F(t)\big)\, df$.
5)

$$R_L = \frac{\int_{160-3\ Hz}^{160+3\ Hz} PSD\big(F(t)\big)\, df}{\int_0^{500\ Hz} PSD\big(F(t)\big)\, df}$$

Equation 5

for each group was calculated. This ratio varies between 0 and unity and was used as a metric by which local flame sensitivity to the forcing frequency was determined.

These groups were plotted in their respective spatial position, which was a reconstructed image which showed the spatial sensitivity of the flame to forcing (Figure 2-11).

2.3.3.4 $OH/< OH >$ phase-averaged variation estimation

For the fully premixed, NPR and NPA flames, it was identified that there are four main regions of the flame (Figure 2-12a). These regions are:

i. The whole image
ii. The region along the inner shear layer

iii. The upper flame region, referred to as the Top region
iv. The region where the outer recirculation zone resides

These regions were selected based on the annular gap and the angle defined by the bluff body entry length, which is approximately 45 degrees.

For the spray flames, three main regions were selected (Figure 2-12b):

i. The whole image
ii. The inner cone flame region
iii. The outer cone flame region

In each region, the phase-averaged variation of $OH/<OH>$ was evaluated as described below:

1) The OH fluorescence signal of a 5,000-image dataset was phase-averaged at 15 degrees with respect to the forcing signal.
2) Each of the phase-averaged images, corresponding to the studied window, was integrated spatially.
3) The above quantity was normalised with the time-averaged value, which is referred to the phase-averaged OH plot.

2.3.4 Estimation of Centroid

In the case of the self-excited premixed flames, the axial and radial location of the centroid C (x_c, y_c) was calculated for each OH* chemiluminescence image of a 5,000-image dataset using the following equations:

For the centroid along the x-axis,

$$x_c = \frac{\int_s \int xI(x,y)dxdy}{\int_s \int I(x,y)dxdy}$$

Equation 6

For the centroid along the y-axis,

$$y_c = \frac{\int_s \int yI(x,y)dxdy}{\int_s \int I(x,y)dxdy}$$

Equation 7

where $I(x, y)$ is the intensity of OH* at that position.

The power spectrum of the axial and radial centroid locations was then calculated from the respective time series. The calculation of the heat release centroid location provides useful information about the influence of the periodic motions of the system on the global flame motion.

2.3.5 Proper Orthogonal Decomposition (POD) Method

The images were analysed using an in-house developed MATLAB code, based on the principles of Proper Orthogonal Decomposition [136]. The experimental data consists of a number of instantaneous snapshots $Q(x, t)$, which for simplicity is assumed to be a scalar quantity. First of all, the field $Q(x, t)$ is decomposed into mean $\mu(x)$ and time-varying parts $q(x, t)$:

$$Q(x, t) = \mu(x) + q(x, t)$$

Equation 8

After the POD method is applied to a sequence of n temporally resolved heat release-field measurements, an instantaneous realisation at time t, $Q(x, t)$, can be reconstructed in terms of a basis of spatial eigenfunctions $\Phi_i(x)$, such that the POD decomposition can be written as:

$$Q^N(x, t) = a_0\Phi_0(x) + \sum_{i=1}^{N} a_i(t)\,\Phi_i(x)$$

Equation 9

where $a_0\Phi_0(x)$ represents the time averaged (mean) field. Subsequent modes contain the fluctuations and by means of the time coefficients the dynamics can be reconstructed. It should be noted that $\mathrm{Q^N}$ converges to Q when N goes to infinity.

POD can be considered as analogous to Fourier modal analysis. The difference is that in the Fourier decomposition the modes are a priori chosen to be sinusoidal, whereas in POD the basis is empirical, depending on the data [133].

The spatial correlation matrix C of N x N dimensions is calculated from the expression:

$$C = \langle Q(x,t) \cdot Q^T(x,t) \rangle$$

Equation 10

where the superscript T denotes the transposed of the vector and $\langle < \cdot > \rangle$ is the time averaging operator. C is a real and symmetric matrix, therefore it is diagonisable in an orthonormal basis.

The optimal base functions satisfy the eigenvalue problem:

$$C\,\Psi = \lambda\,\Psi$$

Equation 11

where $\Psi = (\psi_1, \psi_2, \ldots, \psi_N)$ are the eigenvectors of the temporal auto-correlation tensor. The calculated eigenvalues (λ_i), which represent the contribution of the modes to the overall energy of the flow, are sorted in decreasing order ($\lambda_i > \lambda_{i+1}$) and thus, the first modes represent the most energetic unsteady structures of the flow. It should be stressed that these eigenvalues should not be interpreted as the real mechanical energy associated with corresponding mode, but only as the energy of the signal that contains this mode.

To solve the eigenvalue problem is computationally expensive as it leads to an M x M eigenvalue, where M is the number of grid points. By applying Sirovich's Method of Snapshots the cost is reduced to an eigenvalue problem of size N x N, where N is the number of snapshots ($M \geq N$).

As a result of the eigenvalue problem N eigenvalues λ_i are obtained. To each eigenvalue λ_i corresponds a mode Φ_i and N eigenvectors ψ_i. Applying this method, the modes are expressed as a linear combination of the snapshots:

$$\Phi_i(x) = \sum_{j=0}^{N} \psi_{i,j} Q\left(x, t_j\right)$$

Equation 12

The projection of the snapshots on each eigenmode leads to the calculation of the associated temporal coefficients $a_i(t)$ of Equation 9. Therefore, the coefficient relative to the i-th mode and the snapshot at time t is expressed by:

$$a_i(t) = \Phi_i(x) \cdot Q(x,t)$$

Equation 13

In this work, the POD has been used for the analysis of OH* chemiluminescence and OH PLIF images of the different systems studied in order to extract the most dominant structures and their periodicity. It should be noted that in the case of forced fully premixed, NPR and Spray flames the POD method was applied to a 5,000-image dataset, while in the case of self-excited premixed flames and forced NPA flames the POD method was applied to a 1,000-image dataset. Since the results of the POD analysis for the studied datasets begin to converge after 500 snapshots, a good statistical representation was achieved.

2.4 Figures of Chapter 2

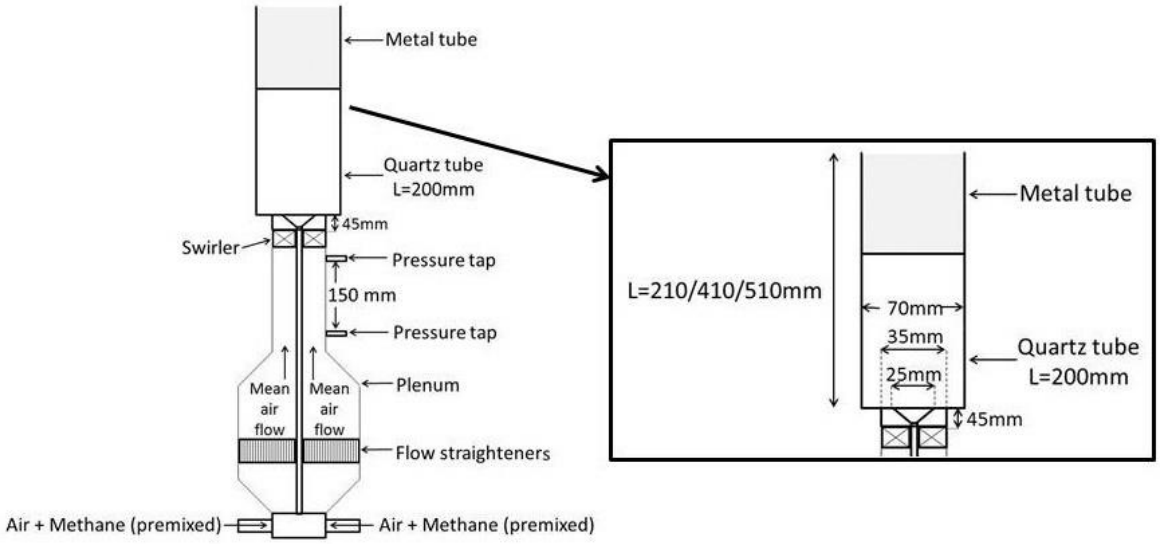

Figure 2-1: Schematic of the fully premixed burner used for the study of self-excited flames.

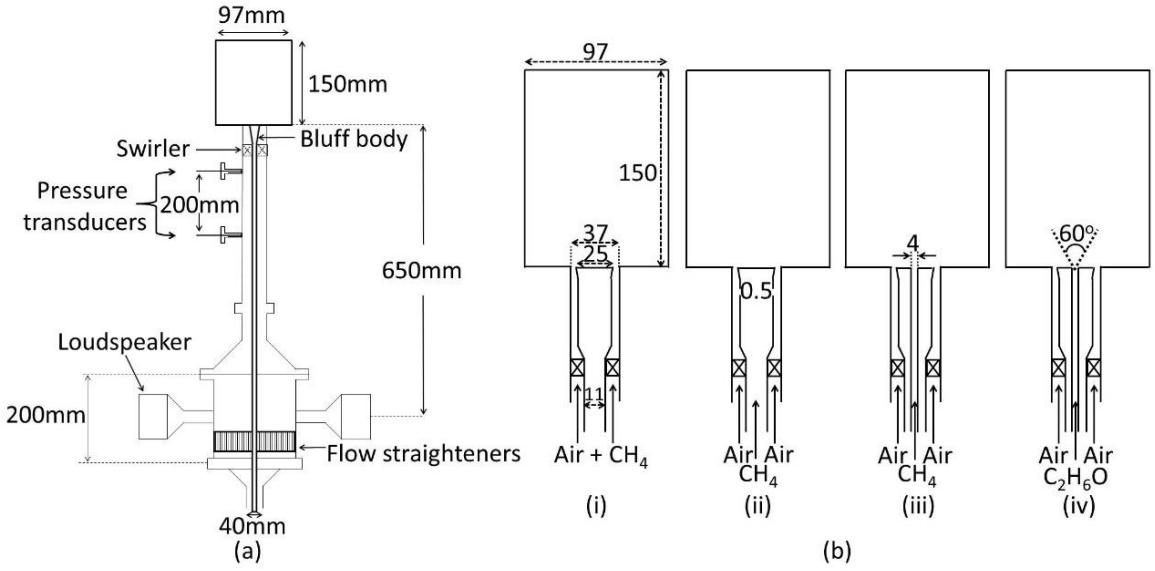

Figure 2-2: Schematic of the burner used for the study of forced (b(i)) fully premixed, (b(ii)) non-premixed with radial fuel injection, (b(iii)) non-premixed with axial fuel injection and (b(iv)) spray flames.

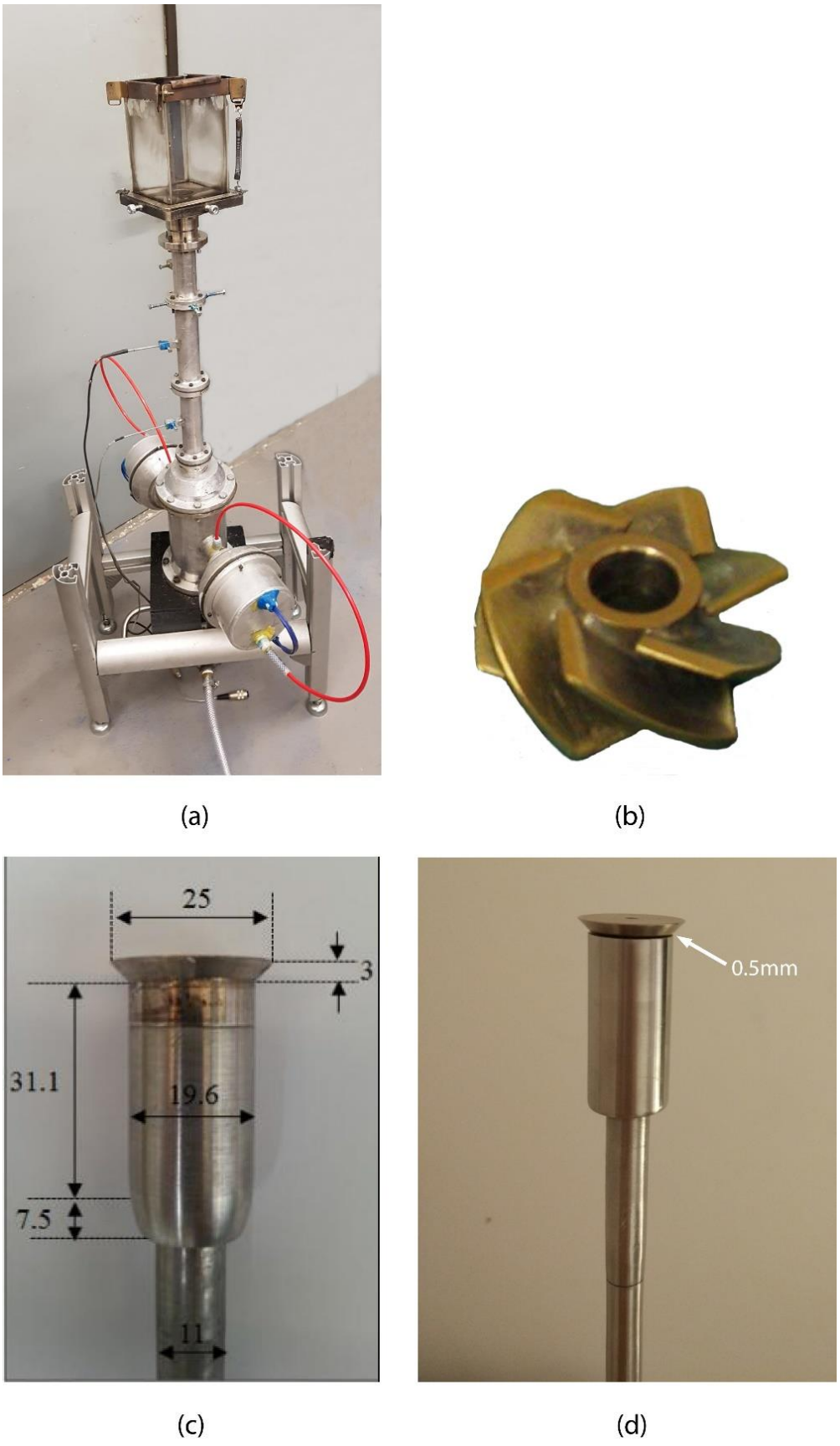

Figure 2-3: Schematic of (a) the burner, (b) swirler, (c) bluff body of premixed, NPA and spray configurations and (d) bluff body of NPR configuration.

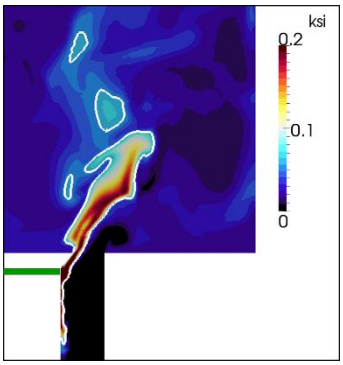

Figure 2-4: Instantaneous mixture fraction field in a streamwise cross section. The white line is the stoichiometric mixture fraction (Dr. Giusti and Dr. Zhang). Flame: NPR-15-055-160-30.

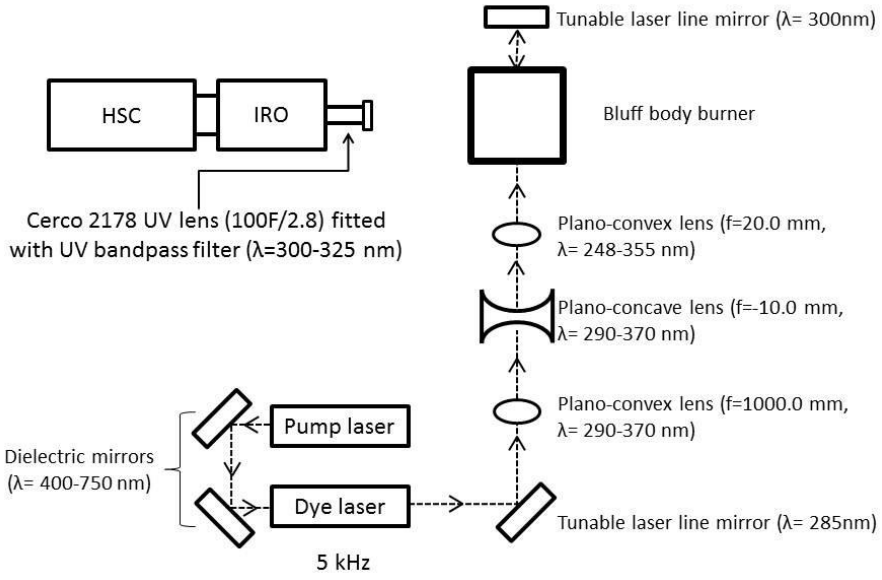

Figure 2-5: Schematic of the laser and imaging system.

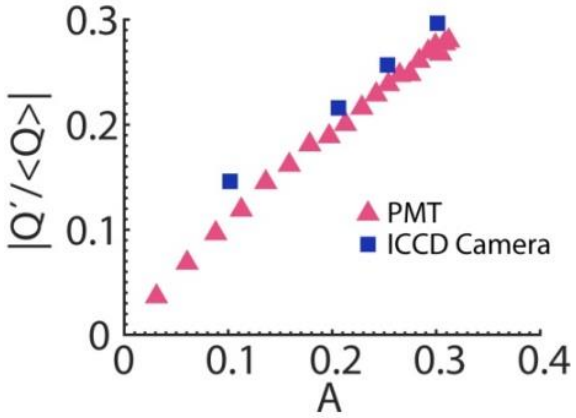

Figure 2-6: Normalised global heat release fluctuations measured as a function of forcing amplitude *A* using OH* chemiluminescence, measured by the ICCD camera and the PMT for a Fully Premixed flame (*U*=15 m/s, *φ*=0.7, forced at 160 Hz).

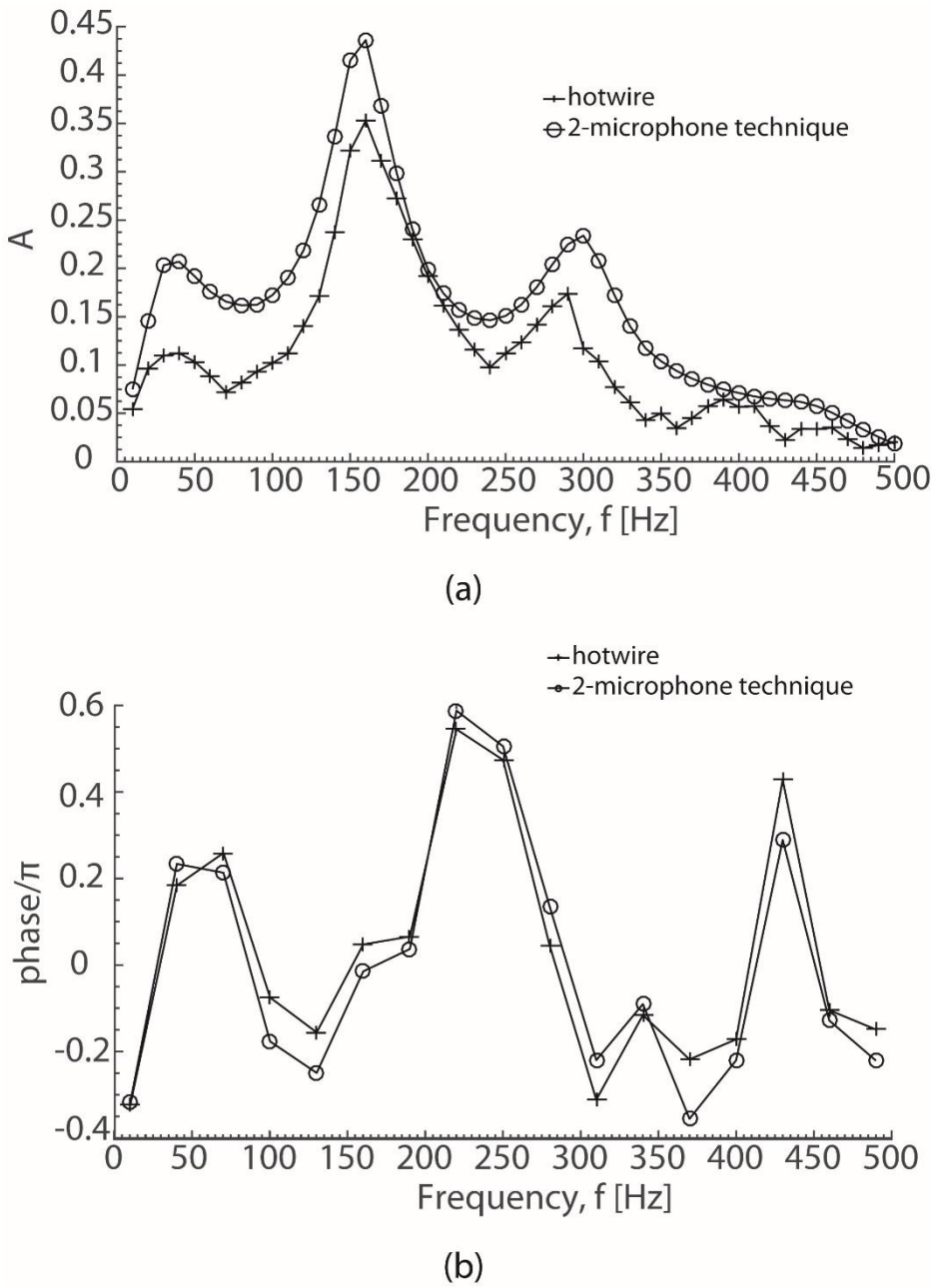

Figure 2-7: Comparison of amplitude and phase of the velocity fluctuation, measured by the two-microphone technique and hotwire located at the centre of the annular gap at the bluff body plane under cold flow conditions, as a function of forcing frequency for a constant peak-to-peak input voltage to the speakers and for U=10 m/s.

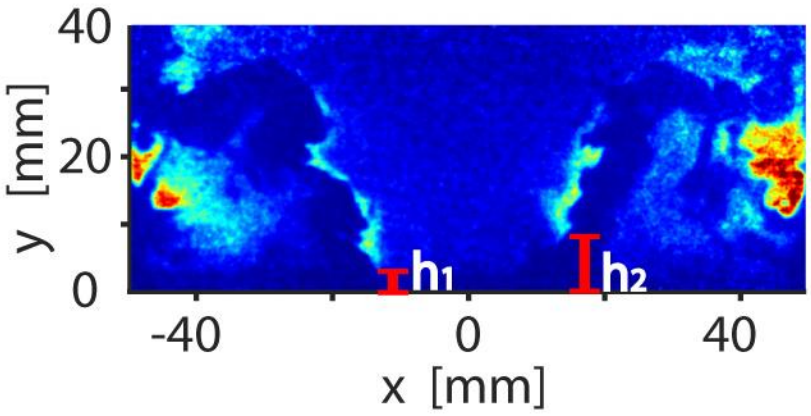

Figure 2-8: Instantaneous OH PLIF snapshot showing the left and right lift-off heights of flame NPR-15-070-160-30.

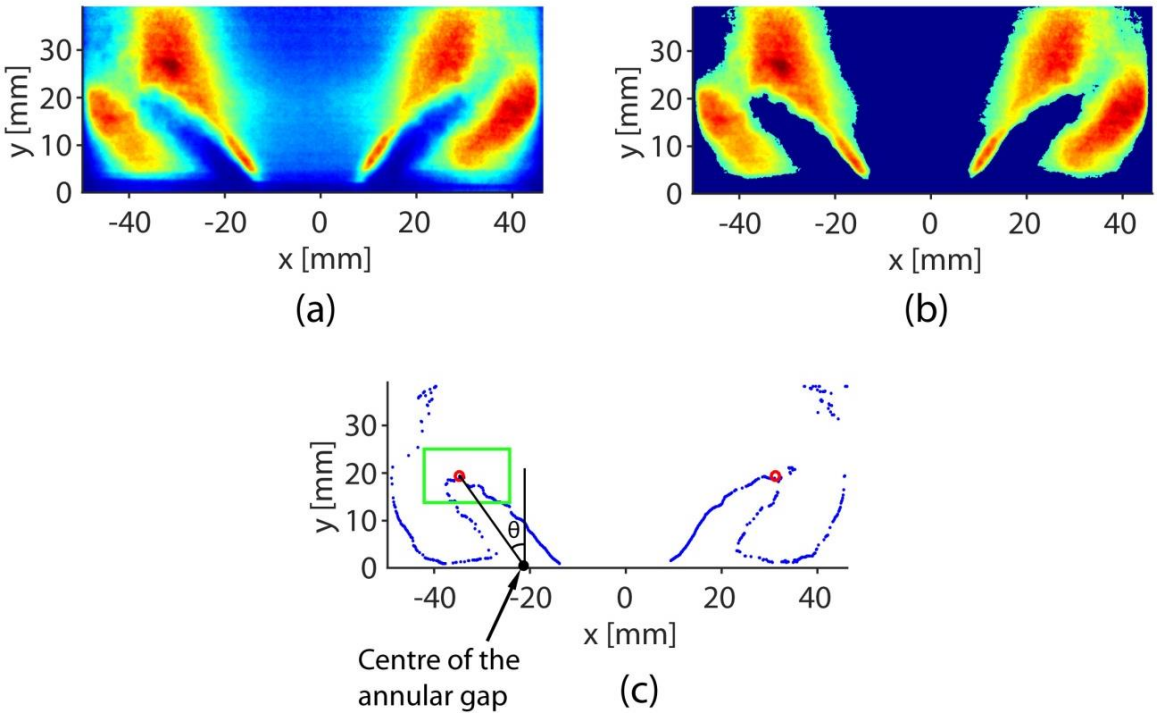

Figure 2-9: (a) Phase-averaged OH PLIF image at 15-degree phase angle, (b) application of an intensity thresholding algorithm, (c) maximum values of the gradient (blue dots), the red circle constitutes the maximum of these values inside the interrogation window (green square), used to determine the flame angle θ.

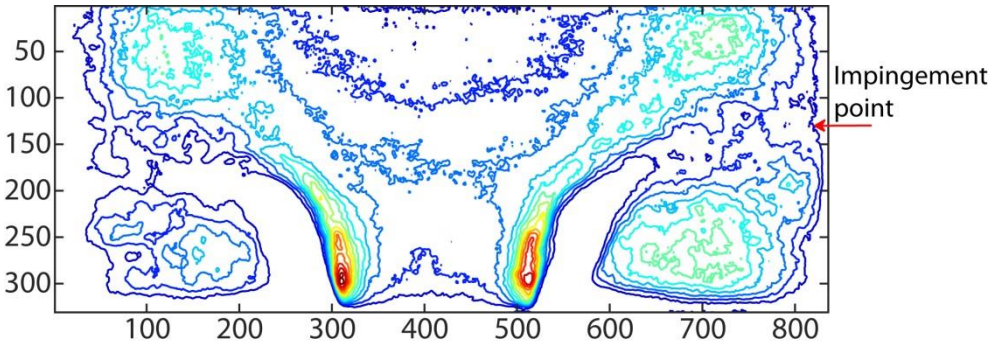

Figure 2-10: Phase-averaged iso-contour plot of OH PLIF for flame NPR-15-055-160-30 at 120 degrees. The impingement point is indicated by the red arrow.

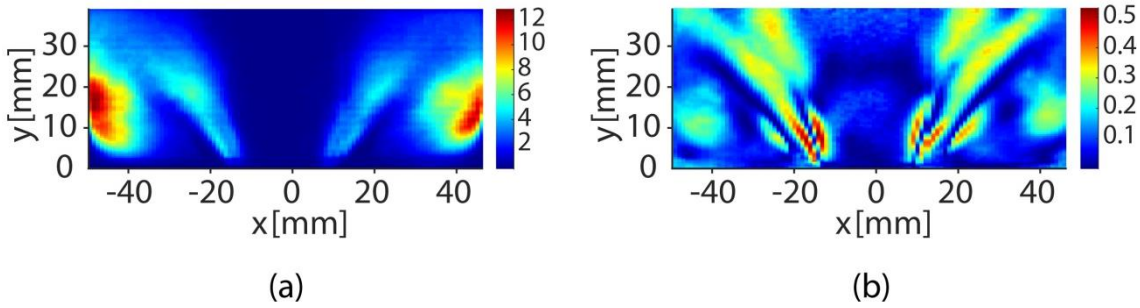

Figure 2-11: An example of (a) the variance of OH and (b) the ratio R_L, described in Section 2.3.3.3. Flame NPR-15-070-160-30.

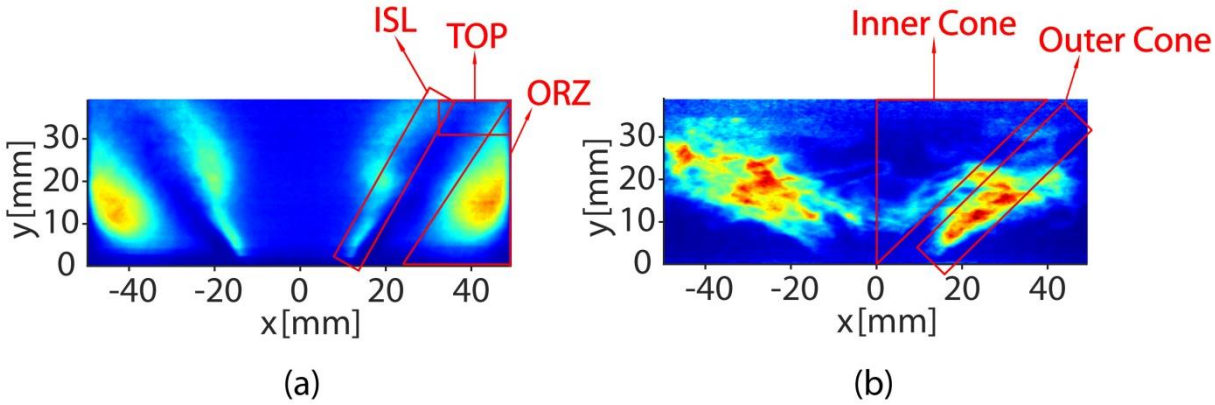

Figure 2-12: Example of phase-averaged OH PLIF image of (a) NPR-15-070-160-30 and (b) S-15-033-160-30. The main regions at which the phase-averaged $OH/< OH >$ was estimated are indicated.

3 SELF-EXCITED FULLY PREMIXED FLAMES

In this chapter, the results from the experiments investigating the behavior of a self-excited fully premixed system are presented. The experiments were conducted by Dr. Nader Karimi and the post-processing analysis of the experimental data was conducted by the author. The experimental conditions are described in Section 3.1. In Sections 3.2 and 3.4, the flame kinematics of the system in terms of spatial structures and their associated frequency components are discussed. In particular, in Section 3.2, the periodic motions of the flames are studied using pressure and heat release spectra, as well as raw OH* chemiluminescence and OH PLIF images. Also, the results from other conventional methods, such as phase-averaged imaging data and tracking the heat release centroid location are discussed in Section 3.4. In addition, in Section 3.3 the heat release fluctuations and flame transfer functions, based on the most pronounced frequencies of the system, are shown. Finally, in Section 3.5 the results from the Proper Orthogonal Decomposition (POD) method are included to give an insight on the dominant flame structures and their periodicity. A novel application of the POD method is proposed to estimate the convection velocity from the most dominant reaction zone structures detected by OH* chemiluminescence imaging.

3.1 Experimental Condition

The results presented in this chapter were acquired by conducting experiments on a fully premixed configuration. Self-excited acoustic oscillations were induced by extending the length of the duct downstream of the bluff body. This system is described in more detail in Section 2.1.1. As seen in Table 3-1, three different duct lengths were investigated: L=210 mm, 410 mm or 510 mm, with the former producing very low amplitude oscillations and the latter producing very violent oscillations. The bulk velocity of the reactants (defined as the total flow rate divided by the open annular area between the bluff body and the outer duct) was U=10 m/s and the equivalence ratio was φ=0.77.

3.2 General Observations

Time series of OH* chemiluminescence images for flame SP-10-077-510 are shown in Figure 3-1. The flame is anchored at the bluff body edge, with some evidence of flame movement into the outer recirculation zone associated with the sudden expansion from the inlet duct to the combustor section. There is evidence of a moving vortex-like OH* chemiluminescence structure in the axial direction, emanating from the interaction of the inlet flow and the bluff body. This interaction causes a flow separation that proceeds downstream. In order to further investigate this, the OH PLIF technique was used to visualise better the flame location. In Figure 3-2 and Figure 3-3 snapshots of flames SP-10-077-410 and SP-10-077-510 respectively are presented. The instant denoted as t=0 was arbitrarily chosen to be 2 ms prior to the peak of the vortex-like structure formation for all conditions. From the observation of the timeframes sequence of the OH PLIF images for L=510 mm, it is evident that the vortex structure is very pronounced. In addition, in the case of L=510 mm at t=2ms, the phenomenon of local flame annihilation is noted, as indicated by the red circle in Figure 3-3. This occurs as the inner and outer flame fronts are brought together and it ultimately leads to an overall decrease in flame surface area and hence local heat release rate, as it has been reported before in externally forced flames [40, 163]. In these studies, the magnitude of flame annihilation was found to be dependent on the amplitude of the induced forcing. In contrast, in the L=410 mm case, the vortex-like OH structures are not fully formed and the OH intensity appears to be more concentrated in the region above the bluff body. Comparing flames from the same duct length condition but of different equivalence ratios (Figure 3-4), it is found that the equivalence ratio has an impact on the morphology of the flame roll-up. At low φ, roll-up is incomplete, while at higher φ the diameter of the flame roll-up around the vortex core is found to be decreased. This is in agreement with previous results [164].

In order to study the periodicity of the aforementioned vortex-like structure in more detail and the effect of the equivalence ratio and of the duct length on its oscillation frequency, different operating conditions were examined. It was found that depending on the equivalence ratio, the pressure and heat release spectra can exhibit multiple peaks with significantly different frequencies, single peaks or not very clear peak structures. For example, it is interesting to observe that in the case of the longest duct length flame SP-10-077-510, the pressure spectrum exhibits pressure fluctuations at 372 Hz (f_1) and 263 Hz (f_2), whereas the heat release spectrum exhibits heat release fluctuations at the same frequencies and at 109 Hz, which is the difference of the other frequencies ($f_1 - f_2$) (Figure 3-5). The frequency at f_1=372 Hz constitutes the dominant peak of both the pressure and the heat release spectrum and corresponds to the

thermo-acoustic oscillation. This phenomenon and its effects on the flame kinematics is investigated in more detail in Section 3.4. Operation at lower φ results in a single peak, which appears at the same frequency in both spectra. In addition, for some other conditions no definite peak structures are found. At higher φ multiple peaks are revealed in the pressure and heat release spectra. Concerning the effect of the duct length, in the case of the shortest duct length, 210 mm, both spectra show low amplitudes and appear noisy with no distinct peak structures, implying that the flame is thermo-acoustically stable. At 410 mm two noisy peaks around 395 and 265 Hz of higher amplitude are observed, while at 510 mm distinct and high amplitude peaks are seen, as explained above (Figure 3-5), denoting strong self-excited oscillations.

3.3 Estimation of Heat Release Fluctuations and FTFs

The normalised global heat release fluctuations and FTFs based on the most pronounced frequencies are estimated and presented below. As mentioned above, at lower φ values the pressure and heat release spectra exhibited only one dominant frequency, while at higher φ multiple peaks were revealed. Also, it was found that the longer the duct length and the higher the equivalence ratio, the stronger the self-excited oscillations were, with the effect of duct length being much stronger.

Figure 3-6a shows the most dominant frequency, f_1, exhibited by the pressure and heat release spectra (the pressure and heat release dominant peaks were revealed at similar frequencies with the maximum deviation being ±20 Hz) for flames with U=10 m/s, L=510 mm and φ=0.7-0.8. As discussed in Section 3.2, these peaks correspond to the thermo-acoustic frequency. It is clear that the dominant oscillation frequency f_1 increases from 310 to 380 Hz with φ, which could be due to the increase in laminar flame speed with the equivalence ratio. Figure 3-6b plots the amplitude A with respect to φ, which corresponds to the respective dominant frequency f_1 presented in Figure 3-6a (The acoustic velocity, calculated from acoustic pressure measurements, using the two-microphone technique, was used to quantify the velocity amplitude at the burner exit, as described in Section 2.2.2). It can be seen that A varies between 0.03 and 0.1. Furthermore, the time series of OH* chemiluminescence were analysed spectrally to obtain the complex amplitude of the fluctuation at the dominant oscillation frequency f_1 of the experimental condition studied (Section 2.3.1). The normalised global heat release fluctuation shows an increasing trend with φ (Figure 3-6c), while the values of the transfer function based on f_1 oscillate around NFTF=1.3 (Figure 3-6d).

In Figure 3-7a, the second highest peak, f_2, revealed by the pressure and heat release spectra, is plotted with respect to φ, for flames with U=10 m/s, L=510 mm and φ=0.76-0.79.

In this case, a frequency at 263 Hz is shown, which is not altered by the change in φ. This peak at f_2=263 Hz was suggested to correspond to the PVC frequency (see Section 3.4). The amplitude A based on f_2 increases between 0.03 and 0.11 with φ (Figure 3-7b). Also, the normalised heat release fluctuation on f_2 exhibits an increasing trend with φ (Figure 3-7c), however the values of $<Q'/<Q>$ are very small (0.06-0.21). The transfer function (Figure 3-7d) stays relatively constant around NFTF=1.7.

3.4 Effect of simultaneous periodic motions on flame kinematics

As mentioned above, it was found that for some conditions the system develops three simultaneous periodic motions, where the third motion oscillates at a frequency equal to the difference of the other two frequencies. This interesting phenomenon is analysed in this Section. A brief discussion of similar findings reported in the literature is followed by the investigation of the effect of this phenomenon on the global flame motion by calculating the heat release centroid location. Finally, the way these frequency components influence the associated oscillation flame patterns is studied using phase-averaged OH* chemiluminescence and OH PLIF images. This analysis is based on flame SP-10-077-510.

The peak at 109 Hz ($f_1 - f_2$), in Figure 3-5, was found to be consistent with results reported in the previous studies that are presented below. Steinberg et al. [41] and Boxx et al. [57] investigated the flow-flame interactions of a flame with a degree of premixedness in a gas turbine model combustor exhibiting self-excited thermo-acoustic oscillations at 308 Hz. Using POD, it was found that the flow field revealed, apart from the thermo-acoustic frequency at f_1=308 Hz, two other peaks at f_2=515 Hz and at f_3=207 Hz ($f_2 - f_1$). The former peak corresponded to the precession vortex core (PVC) and the latter, which was at the difference between the PVC and the thermo-acoustic frequency, represented their interaction. The global heat release and pressure PSDs revealed peaks that corresponded only to the thermo-acoustic oscillations. From the OH* chemiluminescence images it was shown that the axial motion of the heat release centroid corresponded to thermo-acoustic oscillations, whereas the dominant peak of the centroid radial location spectrum corresponded to the interaction of the flame with the PVC. Doubly phase resolved statistics based on the phase of both the acoustic cycle and the PVC motion showed that the PVC was axially stretched and contracted by the thermo-acoustic oscillation. Thus, it was concluded by the authors that this was causing the appearance of the frequency at $f_2 - f_1$, In another study [58], the heat release PSD revealed three peaks which corresponded to the thermo-acoustic oscillation (f_a), to the helical mode (f_h) and to their interaction ($f_h - f_a$). This observation was made both at self-excited thermo-acoustic

oscillations and at stable conditions with external forcing. This interaction has also been observed in [165].

Based on the above findings, it could be speculated in this study that the peak at 263 Hz (f_2) corresponds to a precessing vortex core (PVC), whereas the peak at 109 Hz ($f_1 - f_2$) represents the interaction between the acoustic oscillation and the PVC. A more detailed analysis including PIV measurements would be necessary to prove the aforementioned suggestion and understand the mechanisms of this coupling, however this is not the focus of this work.

In order to shed more light on the way the aforementioned frequency components affect the overall heat release kinematics, the global flame motion was described by tracking the location of the heat release centre over the measurement time. The axial and radial location of the centroid $C\ (x_c\ , y_c)$ of the OH* chemiluminescence signal was calculated for a dataset of 5000 images (flame SP-10-077-510).

In Figure 3-8, both spectra of the axial and radial centroid location reveal three peaks at f_1=372 Hz (thermo-acoustic oscillation), f_2=263 Hz (PVC) and $f_1 - f_2$=109 Hz (thermo-acoustic oscillation-PVC interaction). Therefore, it is evident that these three mechanisms, which were previously described, influence both the axial and radial heat release location. The magnitude of the peaks of the axial centroid location, representing the axial displacement of the centroid, is greater than that of the peaks of the radial centroid location, implying that the fluctuation of the axial location is much more significant than that of the radial location. It is interesting to observe that in the axial centroid spectrum the magnitude of the PVC frequency is greater than that of the thermo-acoustic oscillation, which is unlike that shown in the integrated OH intensity spectrum. This suggests that the centroid axial location is less affected by the thermo-acoustic oscillation than the PVC. On the other hand, the PVC disturbance fluctuates over a larger magnitude about the axial centroid location. It is also worth noting that the magnitude of the peak of the radial centroid location at 372 Hz is much greater than the others, denoting that the effect of the thermo-acoustic oscillation on the fluctuation of the radial location is more dominant.

Having described the global motion of the flame, it is important to investigate the way these frequency components influence the associated oscillation flame patterns. Figure 3-9 shows phase-averaged OH* chemiluminescence images of flame SP-10-077-510 with respect to the frequency of the thermo-acoustic oscillation, the PVC and the interaction component respectively. In order to investigate further the underlying mechanisms that are associated with

the thermo-acoustic oscillation frequency component, Figure 3-10 shows phase-averaged OH PLIF images of the flame examined at this frequency.

The phase-averaged images at the thermo-acoustic frequency (f_1=372 Hz) reveal the strong axial motion (puffing) of the flame. The nearly even and equal distributions of the integrated heat release reveal that the flame has a symmetric structure with respect to the centre axis of the burner. From the phase-averaged OH PLIF images of the same flame condition, it is evident the formation of vortex-like OH structures. In particular, an inward rolling vortex-like structure is formed by the inner shear layers at the central recirculation zone (CRZ), whereas an outwardly rolling vortex-like structure is created by the outer shear layers at the outer recirculation zone. From the roll-up of the flame, illustrated by the OH PLIF measurement, it is assumed that these two concentric vortex rings are advected downstream as two counter-rotating vortex pairs. The vortex-like OH rings grow in size as they are moving downstream, after which a new pair is formed at the bluff body plane. The formation of these structures is almost symmetric and their propagation downstream happens without a phase lag between the left and right side of the flame. This axisymmetric response to self-excited oscillations is similar to the response of premixed flames to acoustic forcing [40].

The phase-averaged OH* chemiluminescence images corresponding to the PVC (f_2=263 Hz) (Figure 3-9b) show a less pronounced axial flame motion, where the heat release rate distribution oscillates non-symmetrically around the axis. This asymmetry is typical of the presence of helical flow structures [166]. It should be noted that the Strouhal number of the PVC for this case was estimated to be 1.05, while the values of Strouhal number for the PVC in [10] were ~2.

Finally, the phase-averaged OH* chemiluminescence images at the interaction frequency ($f_1 - f_2$=109 Hz) in Figure 3-9c shows an asymmetric heat release distribution pattern. It is interesting to notice that the axial motion of the flame is less pronounced than that shown in Figure 3-9a. Also, the series of the phase-averaged images appear to have a less smooth transition unlike those of the other two modes. These observations are probably attributed to the fact that this mode oscillates at the periodicity of the interaction of the other two modes and thus, the heat release distribution is determined by the area where the other two modes intersect. As a result, the heat release oscillation area of the interaction mode is determined by the PVC mode. The lack of smoothness could be explained by the fact that the phase-averaged images may represent the interaction of a series of phenomena taking place.

3.5 POD Analysis

3.5.1 OH* Chemiluminescence and OH PLIF POD Analysis

Having described the parameters that affect the flame-vortex interaction using conventional methods (Section 3.2) and the way the multi-frequency components affect the flame kinematics (Section 3.4), a further investigation of these phenomena is attempted by using the Proper Orthogonal Decomposition method. In fact, information about both the spatial structure and the periodicity of the vortex-like structure is acquired from the shape of the POD modes and the PSD of the POD time coefficients respectively.

Figure 3-11 (a) and (b) shows POD Modes and their respective PSD for flame SP-10-077-210. No strong self-excited oscillations are identified in the PSD of POD time coefficients, denoting a thermo-acoustically stable flame, while the POD modes indicate that the flame has no strong features. Figure 3-11 (c) and (d) shows data for flame SP-10-077-510. In this case, the PSD shows the strong self-excited oscillations of the flame, and the multi-frequency components observed correspond to the dominant frequencies and to their linear combinations. In particular, the PSD of the POD time coefficients reveals the same peaks (372 Hz (f_1), 263 Hz (f_2) and 109 Hz ($f_1 - f_2$)) that were exhibited in the heat release spectrum (Figure 3-5), while the pressure spectrum shows only f_1 and f_2. In all three spectra, f_1=372 Hz constitutes the dominant peak and corresponds to the thermo-acoustic oscillation. It should be noted that frequencies f_1, f_2 and $f_1 - f_2$ are revealed in the PSD of POD time coefficients of the first four POD Modes. f_1 is the highest frequency exhibited by the PSD of POD Modes 1 and 2, however in the PSD of Modes 3 and 4 f_1 is significantly reduced (by two orders of magnitude). f_2 is the second highest frequency shown in the PSD of Modes 1 and 2, and the highest peak in the PSD of Mode 3, while the magnitude of the peak has the same order of magnitude in the PSD of all 4 POD Modes. Frequency $f_1 - f_2$ is one order of magnitude greater in the PSD of POD Modes 1 and 2 than that of Modes 3 and 4. The POD Modes reveal a strong axial motion of the flame with little radial dependence. As the mode index increases, the wavelength of this motion decreases. Thus, the POD method and the PSD of the POD time coefficients reproduce what the pressure and OH* signal give. Also, Modes 1 and 2 constitute a pair and have similar POD energy values, as it will be discussed below. From the experiments, it was found that the higher the equivalence ratio and the longer the duct length, the stronger the self-excited oscillations were. For the majority of the cases exhibiting strong self-excited oscillations, the mode shapes appeared to be in pairs and they usually had similar energy values.

Figure 3-11e, f show the cumulative energy spectrum of the OH* chemiluminescence and OH PLIF data for flames SP-10-077-210, SP-10-077-410 and SP-10-077-510. For the OH* chemiluminescence data, it is evident that up to mode 150, for a given mode number the longer the duct, the higher the cumulative energy is. This energy difference is much greater in the first few modes, the energy contribution of which is significantly larger than that of the successive modes. The first 200 modes capture 90.5%, 89% and 95.5% of the total energy for a dataset of 1000 images for flames SP-10-077-210, SP-10-077-410 and SP-10-077-510 respectively. Concerning the OH PLIF data, the cumulative energy contained in the first 200 modes is 89% for Flame SP-10-077-410 and 88% for SP-10-077-510, which is similar with the POD energy of the OH* chemiluminescence data. However, the first few modes in the OH* chemiluminescence data contain significantly greater energy than those of the OH PLIF data. For example, for SP-10-077-510 the energy contained in the first two modes of the OH* chemiluminescence data is 63.5%, while that for the OH PLIF data is 11.5%.

Figure 3-12 presents the relative energy content of each of the first 10 POD Modes for SP-10-077-210 (a) and SP-10-077-510 (b), which have the same equivalence ratio (φ=0.77). Modes 1 and 2 are the most energetic ones containing 3.8% and 3.2% respectively for SP-10-077-210, and 34.1% and 29.8% respectively for SP-10-077-510. So, in the case of SP-10-077-510 the total energy content of the first 2 modes is 9 times higher than that of the SP-10-077-210 flame. This is attributed to the fact that the energy is concentrated in a dominant structure, which is shown in the case of an axially moving vortex-like structure for SP-10-077-510, while there is a lack of such a structure in case of SP-10-077-210. Another striking feature is that the energy contained in Mode 3 is constant (2.8%) for flames SP-10-077-210 and SP-10-077-510. This indicates that the dominant oscillating mechanism is captured mainly by the first two Modes. Also, it is worth noting that in the case of SP-10-077-510, the modes appear to be in pairs of similar energy contents (1-2, 3-4, 5-6 and so forth). This observation, which has been reported before [167-169], constitutes a characteristic of single-frequency oscillations and has been attributed to vortex advection.

Having presented the different aspects of the POD analysis individually, graphs of the predominant oscillation frequency from the POD time coefficients, pressure and integrated OH* intensity spectra, as well as of the pressure root mean square (RMS) values with respect to the parameters that influence them the most are presented and discussed collectively (Figure 3-13). The purpose of this analysis is to examine the interaction between the heat release and the acoustics.

Figure 3-13 shows the dominant frequency captured in the aforementioned PSDs with respect to the equivalence ratio for different duct lengths. As shown in Figure 3-13 (a) the predominant oscillation frequency, as obtained from the PSD of the POD time coefficients, increases with φ in a range between 310 and 380 Hz. This might be attributed to the increase in laminar flame speed with the equivalence ratio. Figure 3-13 (b) and (c) show that the flame appears to be stable in the case of SP-10-077-210, as the lack of acoustic resonance manifests itself in a stable heat release. The matching of the pressure, heat release and PSD of POD time coefficients spectrum denotes a strong interaction between the pressure and the heat release fluctuation. From Figure 3-13 (d), which plots the RMS of the pressure fluctuation with respect to φ, a maximum is observed at φ=0.77 for L=510 mm. This corresponds to a self-excited oscillation of 370 Hz and its RMS value is approximately 60% greater than that at φ=0.7. At this point, taking into consideration that a cold flow velocity experiment using loudspeakers to induce a pressure fluctuation in the burner suggests that the burner exhibits a natural frequency at approximately 370 Hz, it is possible that the aforementioned RMS peak value is amplified due to the resonance of the burner. As for L=210 mm, the RMS values are grouped into two clusters and they seem to be independent of φ.

Concerning the effect of cold flow velocity, Figure 3-13 (a) shows that the dominant oscillation frequency, as obtained from the PSD of the POD time coefficients, takes greater values for U=14 m/s than those observed at U=10 m/s. Figure 3-13 (d) shows that for the case of U=10 m/s, a maximum of the RMS amplitude of the acoustic pressure, with peak amplitude of 40 Pa occurring at φ=0.77, which might correspond to the resonant frequency of the burner, as mentioned previously. For U=14 m/s the RMS amplitude of the pressure is greater than that for U=10 m/s between φ=0.70 and φ=0.74. This is probably due to the fact that at higher flame speed the heat release oscillations induce greater pressure fluctuations in the flow field. Also, for a given velocity, the RMS amplitude of the pressure increases with the duct length. This was expected from the previous deduction that the longer duct length is linked to stronger self-excited oscillations and stronger patterns of the POD mode shapes.

3.5.2 Estimation of Convection Velocity

As described in Section 3.5.1, flame SP-10-077-510 exhibited a strong self-excited oscillation at 372 Hz (see PSD of POD time coefficients in Figure 3-11b), while the OH* chemiluminescence POD Modes revealed a banded structure with little radial dependence, associated with a strong axial motion of the flame. The energy contribution of Modes 1 and 2

was 34.1% and 29.8% of the total POD energy respectively, implying that the dominant mechanism was mainly captured by them.

The convection velocity of the aforementioned OH* chemiluminescence structure is estimated from the simultaneous examination of the most dominant POD Modes and the respective PSD of POD time coefficients. In particular, the convection velocity, based on the first POD Mode, was determined by multiplying the characteristic heat release wavelength, λ, measured from the first POD Mode, as shown in Figure 3-11c, with the dominant frequency, exhibited by the respective PSD of POD time coefficients (f=372 Hz). In this study, the dominant oscillation frequency, obtained from the PSD of POD time coefficients was found to take values between 310 Hz and 380 Hz for U=10, 14 m/s and φ=0.7-0.8 (Figure 3-13). Figure 3-14 (a), which plots the convection velocity (calculated from the first POD Mode) with respect to equivalence ratio for different bulk velocities, shows a positive correlation between the bulk velocity and the convection speed. As far as the effect of equivalence ratio is concerned, no unifying trend can be observed, as the dominant frequency showed an increase with φ, however the wavelength was found to be negatively correlated with the equivalence ratio. In Figure 3-14c, the ratio of the convection velocity to the bulk velocity with respect to φ was found to take values in the narrow range of 1.40-1.66 for conditions with φ=0.70-0.87 and U=10, 12, 14 m/s. The ratio of the convection velocity and the mean velocity was found to be between 0.6 and 1.7 by Karimi et al. [81], while it was 1.13 and 1.02 at 35 Hz and 70 Hz respectively on a conical Bunsen flame [94]. This ratio was estimated to be 0.5 at 150 Hz in an axisymmetric wedge flame [43]. The ratio of the mean velocity to the convection velocity was found to be in the range 1-1.8 for Strouhal numbers St=0.4-2.6 [147]. More details on previous studies estimating the convection velocity were presented in Section 1.1.4.

It is worth noting that the convection velocities, estimated from the first four POD Modes were relatively close, as both the wavelength of the dominant OH* chemiluminescence structure and the respective dominant frequency had similar values. The estimated convection velocities based on the first and second POD Modes show a maximum deviation of 27% (Figure 3-14).

Similar banded shape OH* chemiluminescence structures were found by Sieber et al. [146]. It was reported that the wavelengths of the velocity spectral Proper Orthogonal Decomposition (sPOD) Modes did not match with those of the respective OH* chemiluminescence Modes, implying that the heat release structures cannot be directly compared with velocity data acquired with PIV. However, it was claimed that the OH* chemiluminescence Modes demonstrated clear structures, that have the same spatial

symmetries with the velocity Modes. A direct comparison between the velocity and OH* Modes could be possible by applying a tomographic reconstruction of the OH* chemiluminescence Modes [58].

In the above analysis, a novel application of the Proper Orthogonal Decomposition method was proposed to estimate the convection velocity from the most dominant OH* chemiluminescence structures of a complex burner geometry system.

3.6 Conclusions

In this chapter, an experimental investigation of a self-excited fully premixed system is performed. OH* chemiluminescence (ICCD camera) and OH PLIF measurements were acquired. The flame kinematics were examined in terms of spatial structures and their associated frequency components. In an effort to understand the periodic motions of the flames, conventional methods, such as pressure and heat release spectra, phase-averaged images and the heat release centroid location tracking were used. In addition, the heat release fluctuations and flame transfer functions, based on the most pronounced frequencies of the system, were estimated. The dominant structures of the flames and their periodicity were further characterised using the Proper Orthogonal Decomposition (POD) method. Finally, a novel application of the POD method was proposed to estimate the convection velocity in self-excited swirl premixed flames from the most dominant reaction zone structures detected by OH* chemiluminescence imaging.

It was found that the longer the duct length and the higher the equivalence ratio, the stronger the self-excited oscillations were, with the effect of duct length being much stronger. The equivalence ratio had an impact on the morphology of the flame roll-up. The POD analysis revealed that the POD energy was mainly concentrated in a dominant structure, which was shown in the case of an axially moving vortex-like structure.

The correspondence of the spectra of the pressure, heat release and the PSD of the POD time coefficients denoted a strong interaction between the pressure and the heat release fluctuations. The dominant frequencies were found to increase with equivalence ratio and bulk velocity and decrease with duct length. Furthermore, depending on the equivalence ratio, the spectra showed a difference in the number of observed peaks. In most cases, at low φ, only one dominant frequency, f_1, was exhibited, which was associated with the thermoacoustic frequency. However, at greater φ values, the system revealed up to three simultaneous periodic motions, which were suggested to correspond to the thermoacoustic frequency (f_1), PVC (f_2) and their interaction ($f_1 - f_2$). The heat release fluctuations and flame transfer functions were

estimated based on the most pronounced frequencies f_1 and f_2. In particular, the thermoacoustic frequency f_1 increased from 310 to 380 Hz with φ, while the PVC frequency f_2=263 Hz was not altered by φ. In both cases, the forcing amplitude A varied between 0.03 and 0.1 and the global heat release showed an increasing trend with φ. The transfer function values based on f_1 and f_2 oscillated around 1.3 and 1.7 respectively.

Frequencies f_1, f_2 and f_3 influenced both the axial and radial location of the heat release centroid, with the displacement of the radial location leading to a periodic heat release asymmetry in the flame. Phase-averaged OH* chemiluminescence and OH PLIF images showed that the thermo-acoustic frequency resulted in a strong axial motion of the flame, during which two vortex-like structures were convected downstream. However, the PVC could be associated with a non-symmetrical oscillation of the heat release rate distribution around the centre of the burner and the interaction component might be linked to an asymmetric heat release distribution pattern.

For the majority of the cases exhibiting strong self-excited oscillations, the POD Mode shapes appeared to be in pairs and they usually had similar energy values. The POD energy captured in the OH* chemiluminescence Modes was greater than that in the respective OH PLIF Modes. Finally, the convection velocity, estimated from the POD method, was positively correlated to bulk velocity, however the effect of equivalence ratio was more complex. This was due to the fact that the dominant frequency increased with φ, however the wavelength was negatively correlated to the equivalence ratio. For a range of conditions, the convection velocity was found to be in the range of 1.4-1.7 bulk flow velocities at the inlet of the combustor.

3.7 Figures of Chapter 3

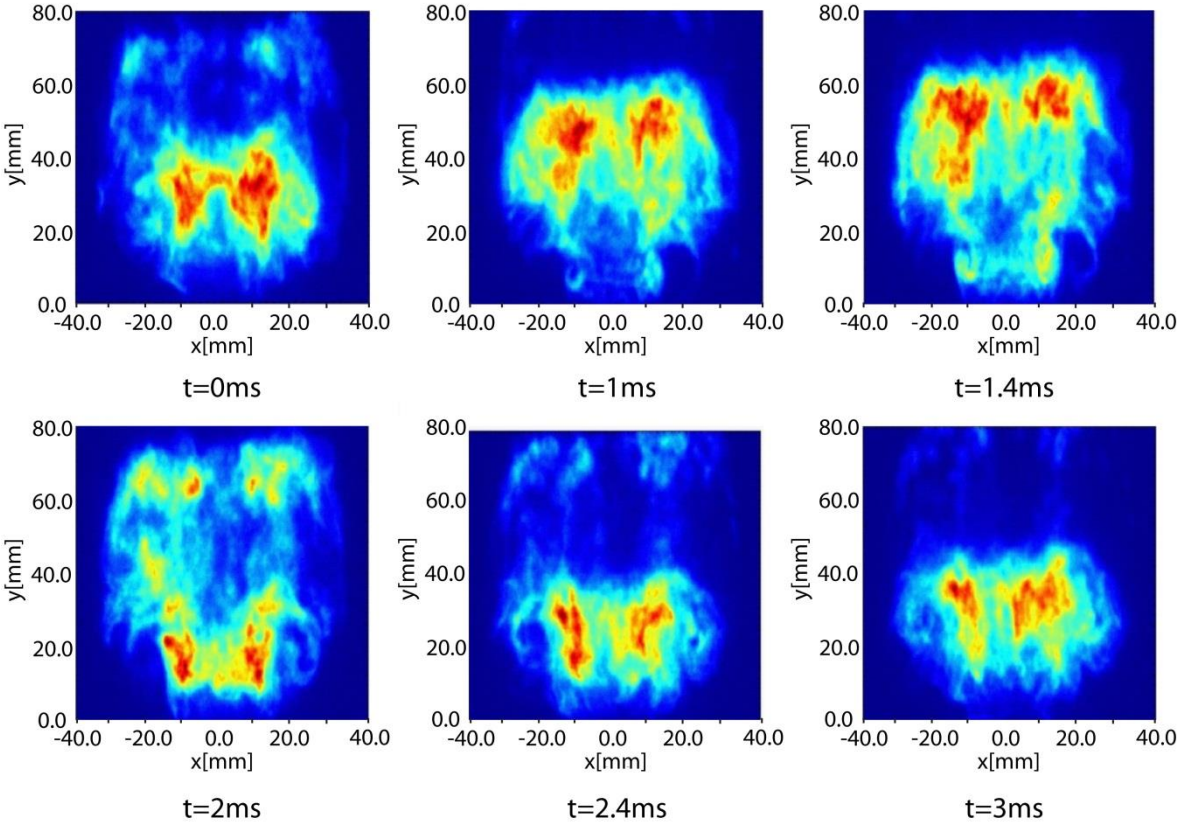

Figure 3-1: Instantaneous OH* chemiluminescence images of flame SP-10-077-510 (*t*=0 ms was arbitrarily chosen to be 2 ms prior to the peak of the vortex formation).

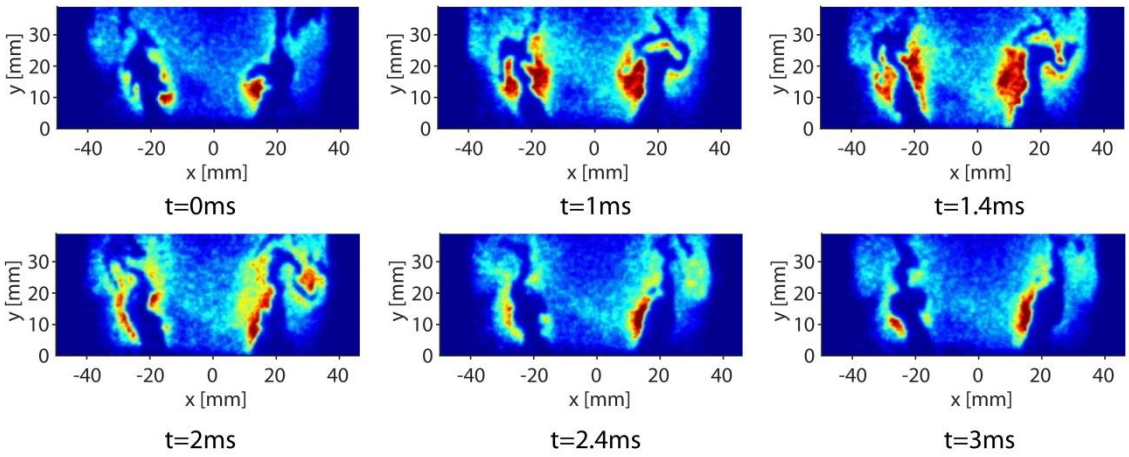

Figure 3-2: Instantaneous OH PLIF images of flame SP-10-077-410 (*t*=0 ms was arbitrarily chosen to be 2 ms prior to the peak of the vortex formation).

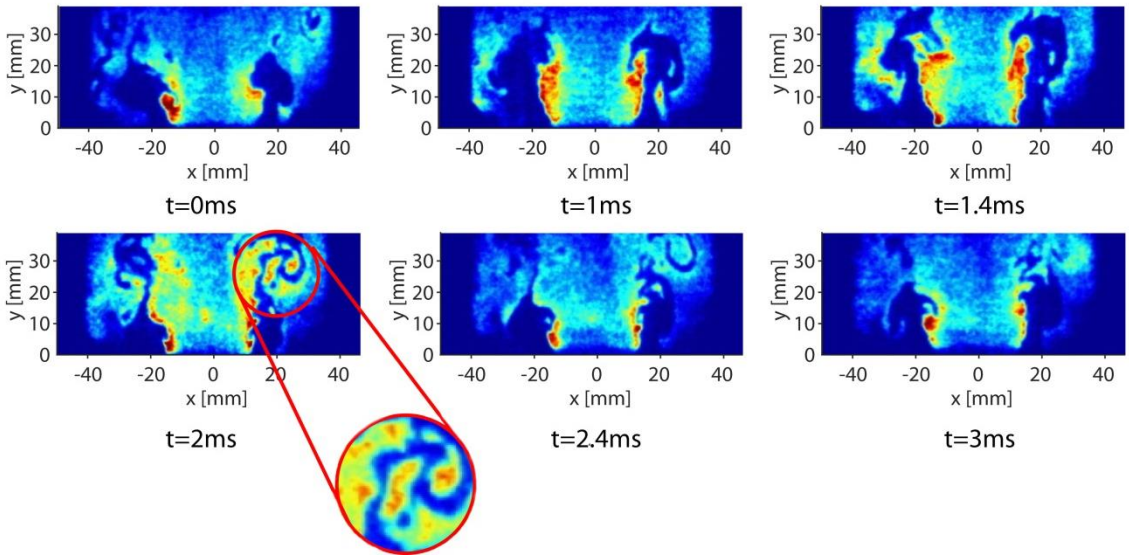

Figure 3-3: Instantaneous OH PLIF images of flame SP-10-077-510 (*t*=0 ms was arbitrarily chosen to be 2 ms prior to the peak of the vortex formation). The detail at *t*=2 ms shows the area where local flame annihilation was found.

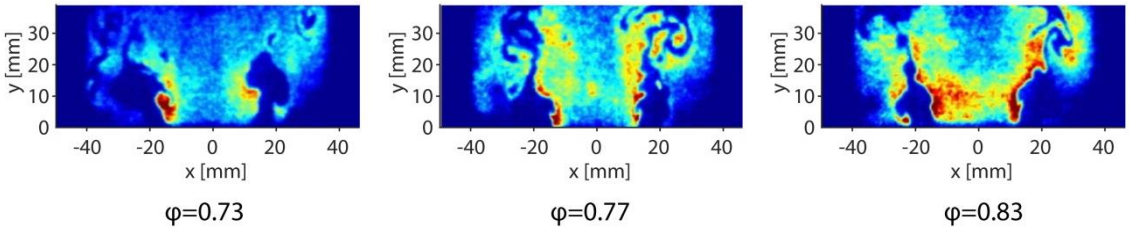

Figure 3-4: Instantaneous OH PLIF images corresponding to the time of the peak vortex-like structure formation for conditions: *U*=10 m/s, *L*=510 mm and *φ*=0.73 (left), *φ*=0.77 (middle) and *φ*=0.83 (right)

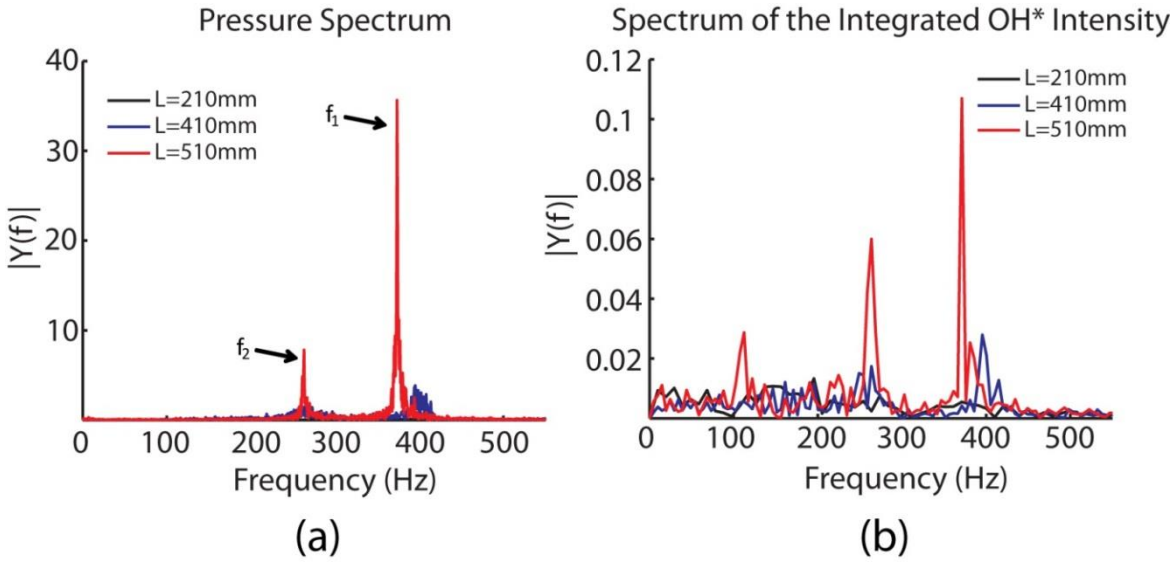

Figure 3-5: (a) Pressure spectrum and (b) spectrum of integrated OH* intensity for flames SP-10-077-210 (L=210 mm), SP-10-077-410 (*L*=410 mm) and SP-10-077-510 (*L*=510 mm).

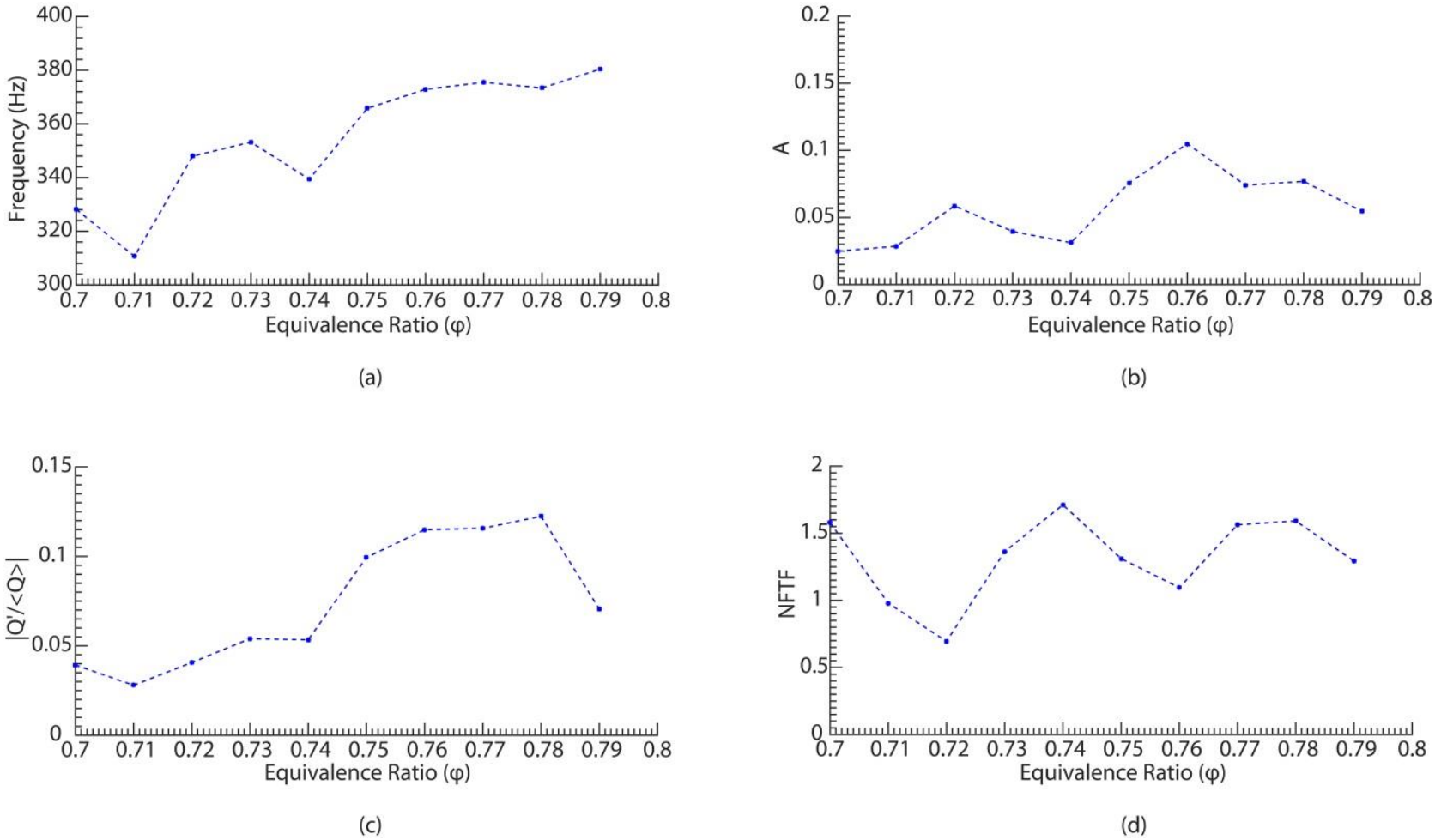

Figure 3-6: Dominant frequency, f_1, exhibited by the pressure and heat release spectra with respect to φ (a), amplitude A, corresponding to f_1, as a function of φ (b), normalised global heat release fluctuations based on f_1, using OH* chemiluminescence plotted with φ (c) and the respective NFTF with respect to φ (d). Flames with U=10 m/s, L=510 mm and φ=0.7-0.8.

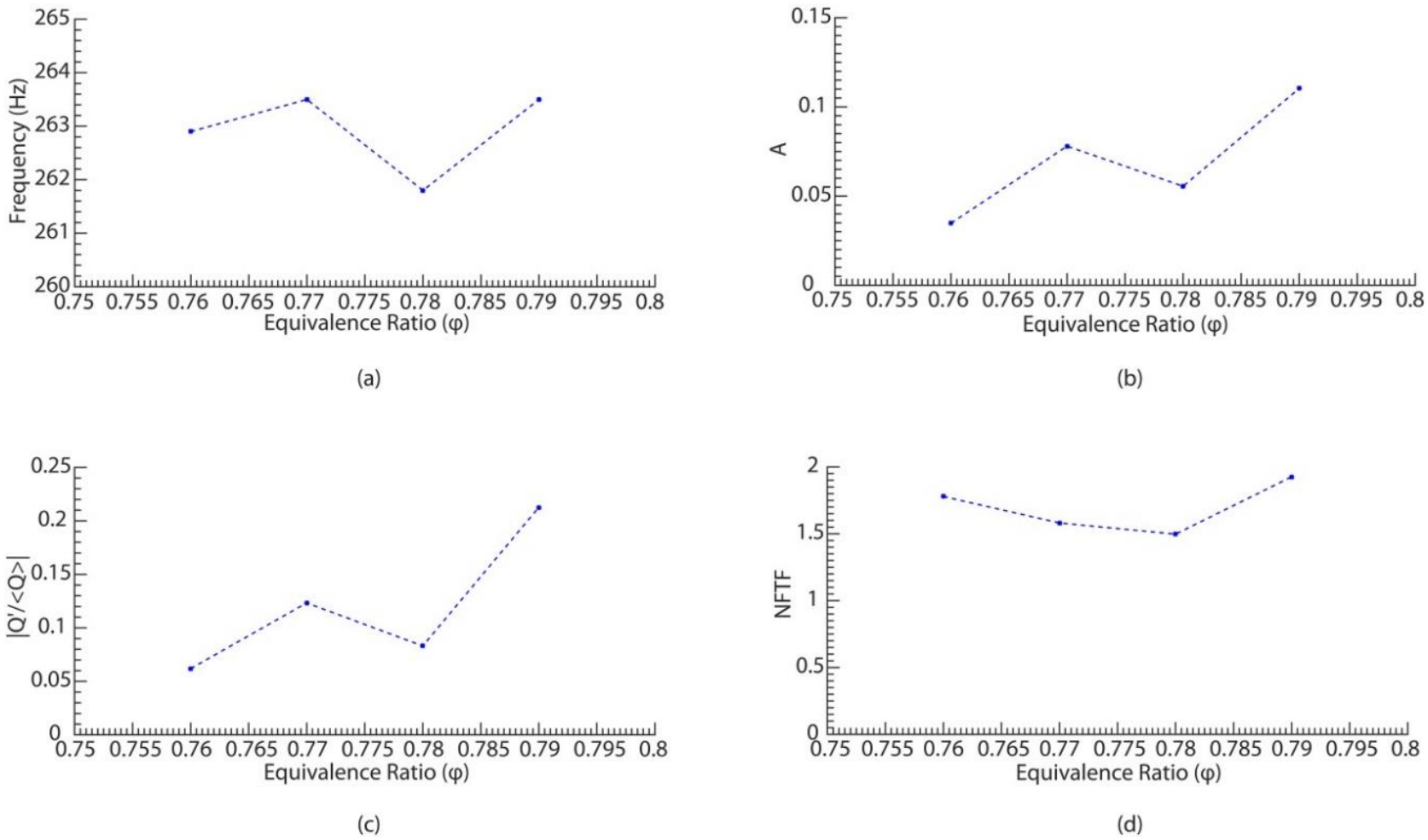

Figure 3-7: Second dominant frequency, f_2, exhibited by the pressure and heat release spectra with respect to φ (a), Amplitude A, corresponding to f_2, as a function of φ (b), Normalised global heat release fluctuations based on f_2, using OH* chemiluminescence plotted with φ (c) and the respective NFTF with respect to φ (d). Flames with U=10 m/s, L=510 mm and φ=0.76-0.79.

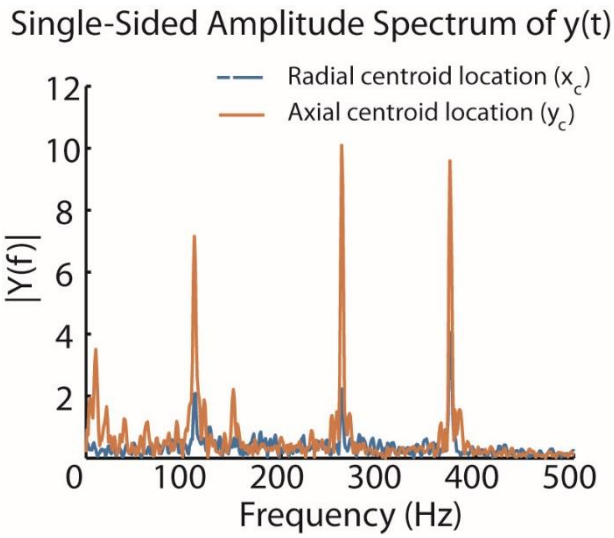

Figure 3-8: Spectra of axial and radial centroid locations for flame SP-10-077-510.

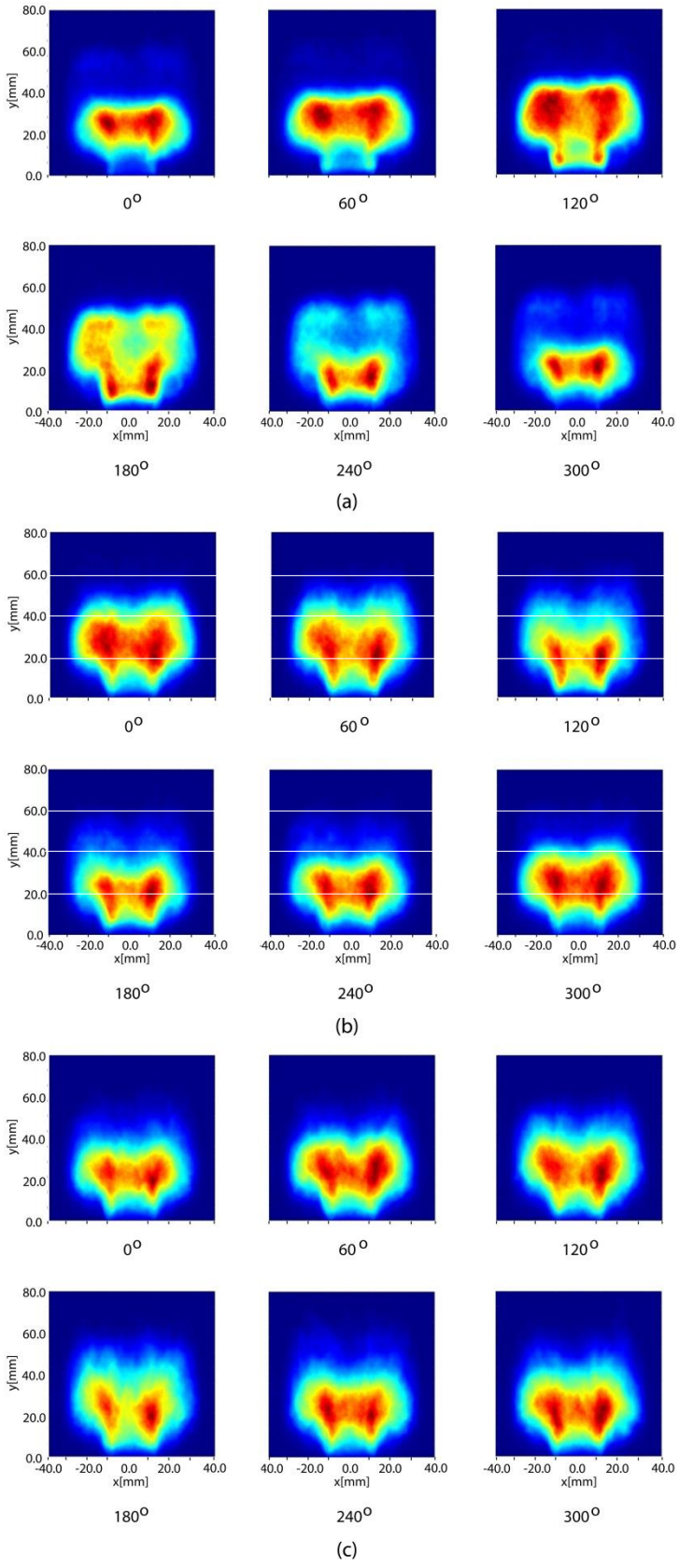

Figure 3-9: Phase-averaged OH* chemiluminescence images of the flames SP-10-077-510 with respect to the frequency of (a) the thermoacoustic oscillation, (b) the PVC frequency and (c) the frequency interaction component.

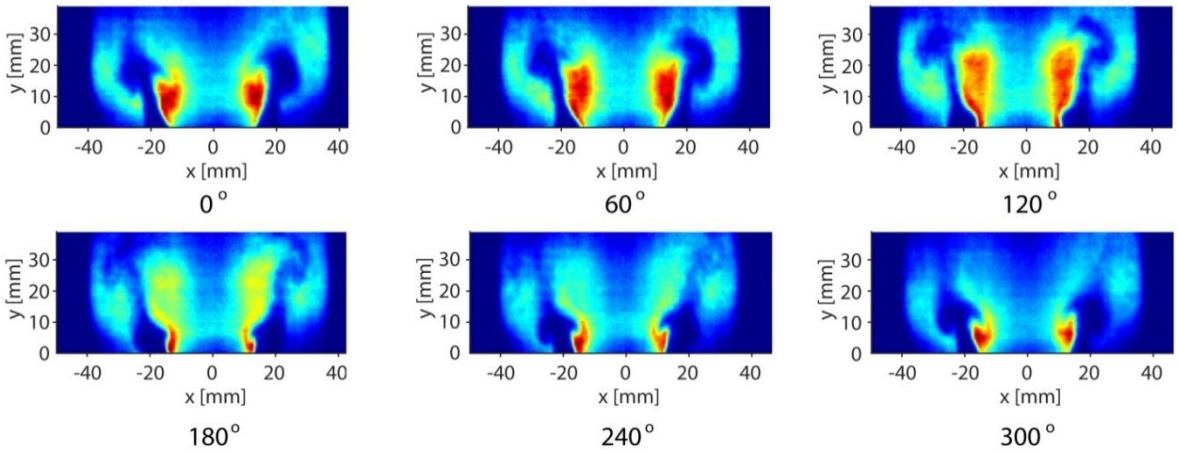

Figure 3-10: Phase-averaged OH PLIF images of flame SP-10-077-510 with respect to the frequency of the thermoacoustic oscillation.

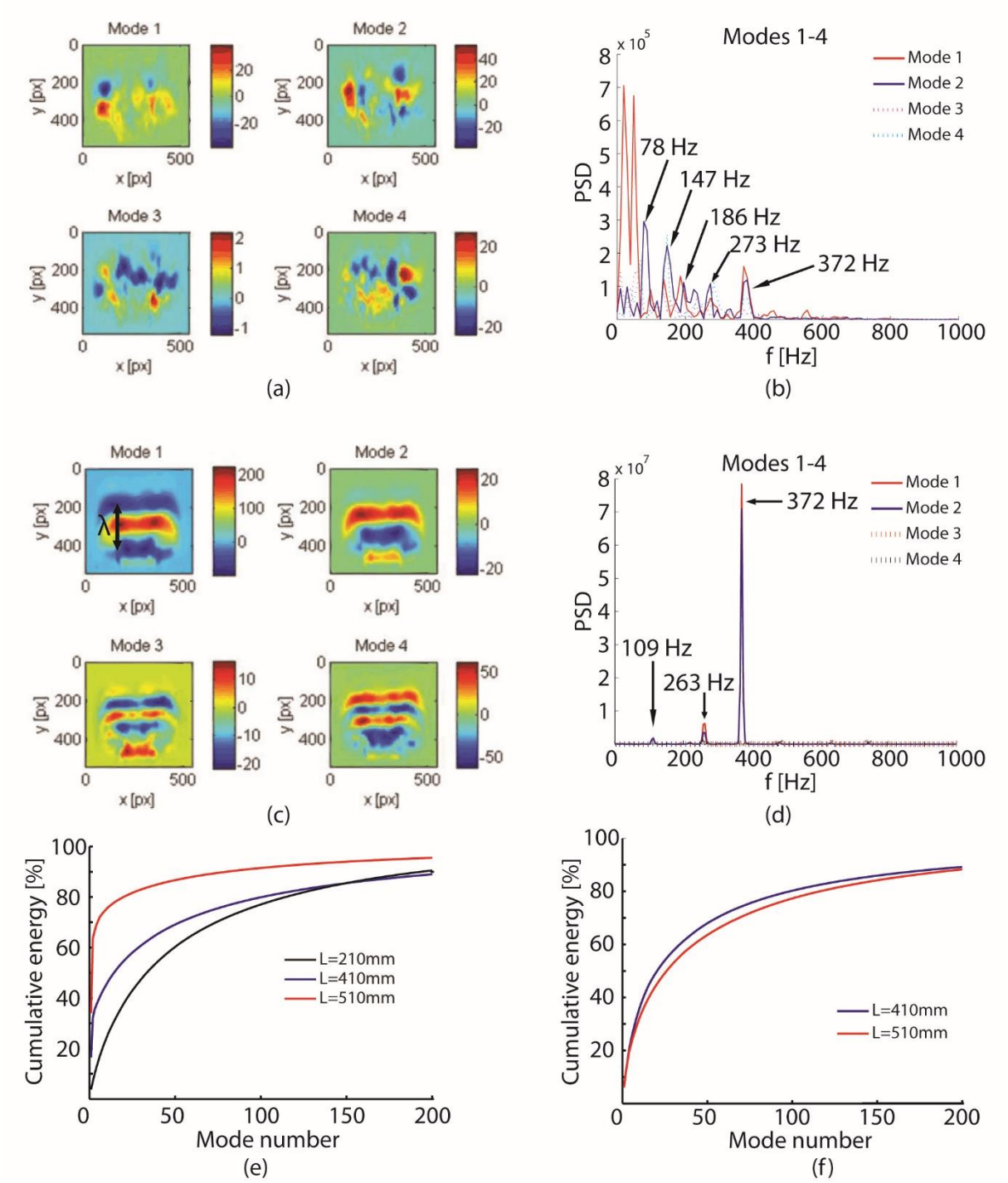

Figure 3-11: OH* chemiluminescence POD Modes, their respective PSD of POD time coefficients for SP-10-077-210 (a, b) and SP-10-077-510 (c, d) and the cumulative energy of OH* chemiluminescence (e) and OH PLIF (f) POD Modes for different duct lengths of SP-10-077.

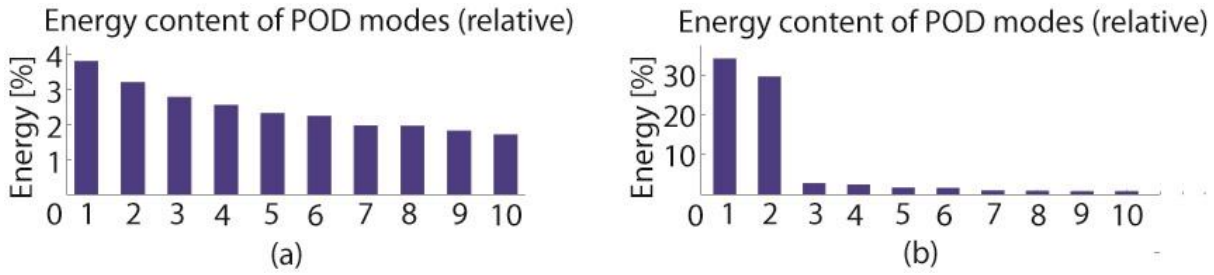

Figure 3-12: POD energy content (%) of the first 10 OH* chemiluminescence POD Modes for flames (a) SP-10-077-210 and (b) SP-10-077-510.

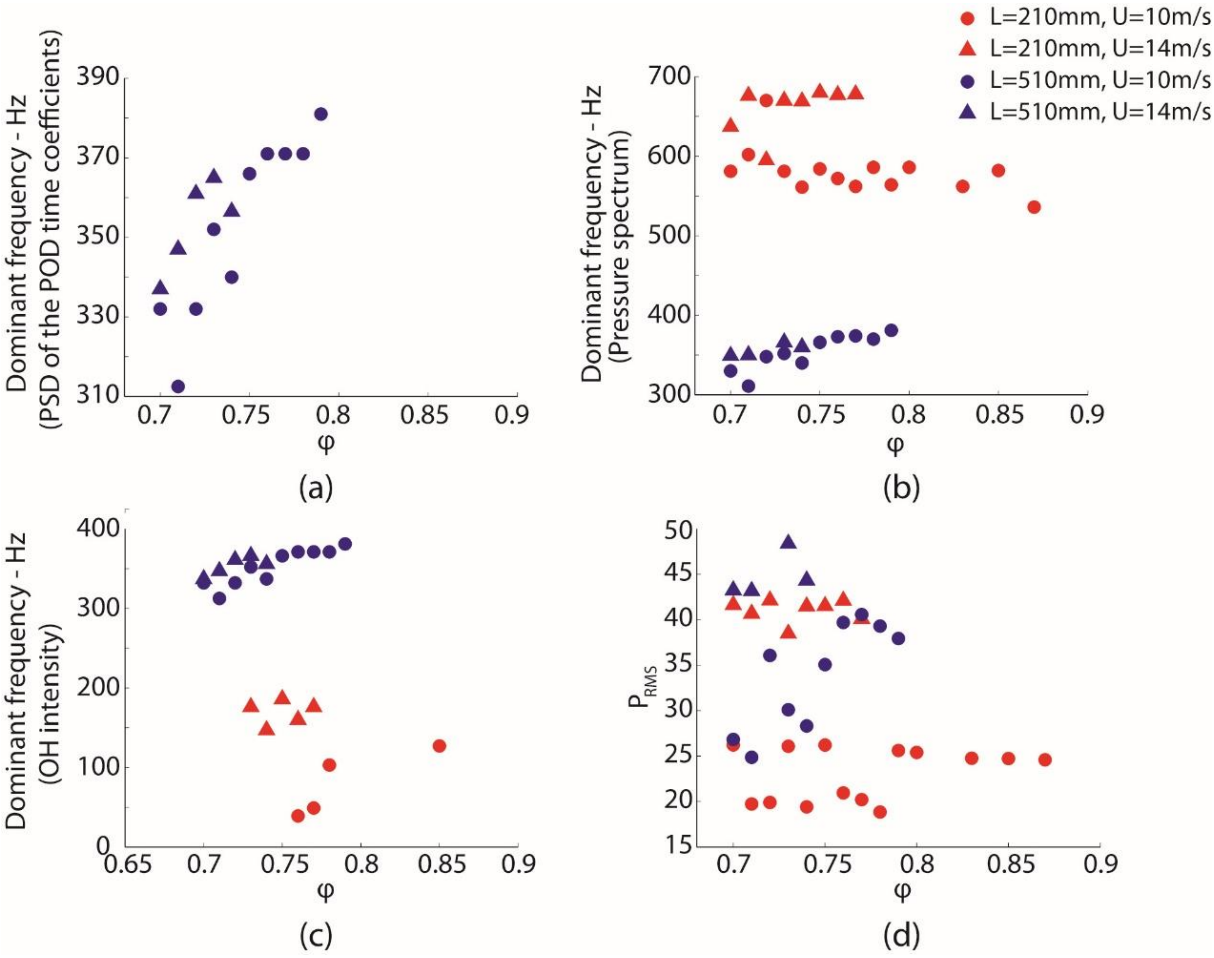

Figure 3-13: Dominant frequencies acquired from the spectra of: (a) PSD of POD time coefficients, (b) pressure and (c) integrated OH intensity, and (d) pressure root mean square as a function of equivalence ratio φ for various flames with L=210 mm, L=510 mm, U=10 m/s and U=14 m/s.

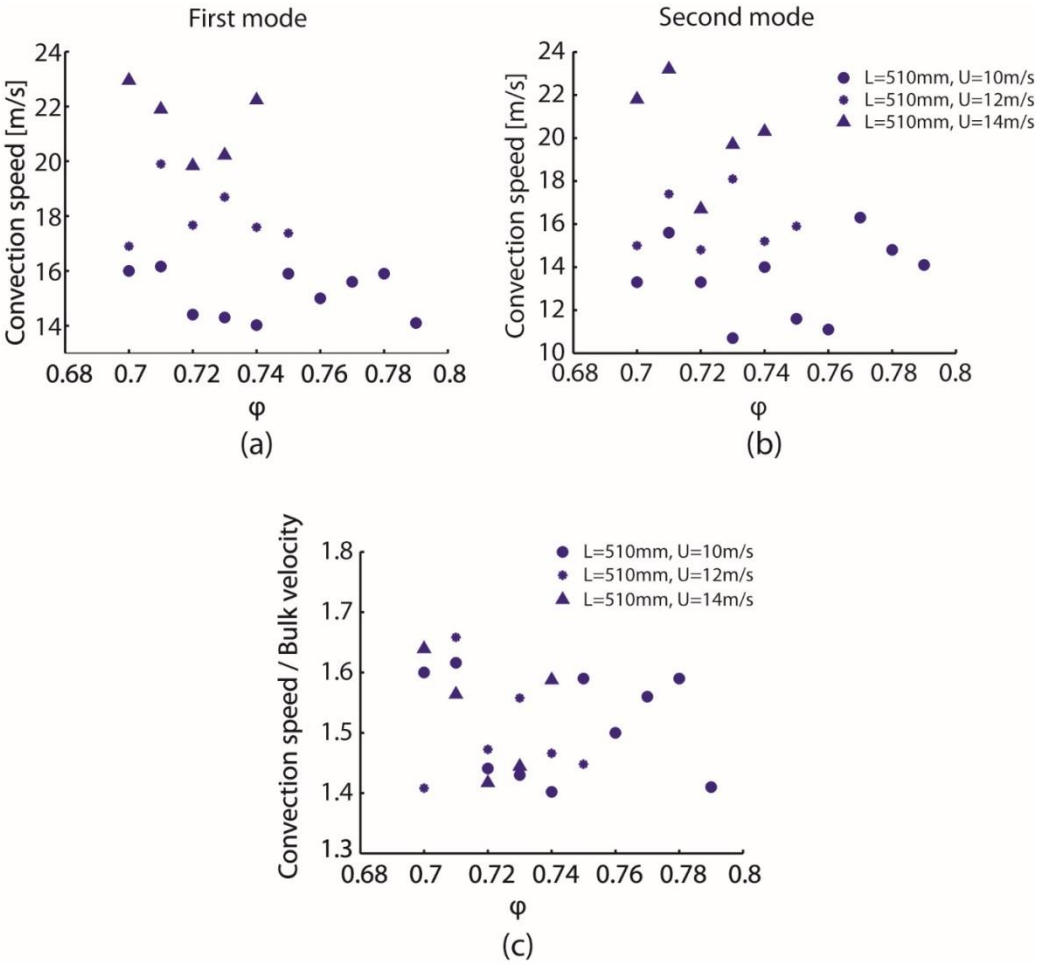

Figure 3-14: Convection velocity as a function of equivalence ratio, φ, for L=510 mm and U=10, 12, 14 m/s based on (a) the first and (b) second OH* chemiluminescence POD Modes. (c) Ratio of convection velocity to bulk velocity, U, with respect to equivalence ratio, for the same conditions, based on the first OH* chemiluminescence POD Mode.

3.8 Tables of Chapter 3

Condition	$\boldsymbol{U}$ $(\boldsymbol{m/s})$	$\boldsymbol{\varphi}$	**Duct Length,** $\boldsymbol{L}$ $(\boldsymbol{mm})$
SP-10-077-210	10	0.77	210
SP-10-077-410	10	0.77	410
SP-10-077-510	10	0.77	510

Table 3-1: Flame codes and corresponding conditions of some of the methane self-excited premixed flames.

4 RESPONSE OF FORCED FULLY PREMIXED FLAMES

The response of fully premixed flames has been studied extensively both experimentally and computationally in the literature [40, 89, 92, 158, 170]. In this chapter, the results from the experiments studying the response of the methane fully premixed flames are presented briefly. The flow and acoustic conditions at which the experiments were conducted are described in Section 4.1. In Section 4.2 the results of the experiments are discussed. These include the qualitative description of the flame kinematics of one experimental condition, based on OH* chemiluminescence and OH PLIF measurements, as well as the estimation of the amplitude dependence of the transfer function. Also, the flame surface density (FSD), calculated from OH PLIF images, was used as a surrogate of the heat release, as well as qualitatively as an indicator of the flame area. Finally, the results from the Proper Orthogonal Decomposition (POD) analysis are included to give an insight on the basic structures of the flame and their periodicity, while the convection velocity of the most dominant structures of the system was estimated.

4.1 Experimental Condition

The results presented in this chapter were acquired by conducting experiments using the fully premixed configuration, described in detail in Section 2.1.2. The premixed air-methane mixture was forced at 160 Hz (main resonant frequency of the burner) and at forcing amplitudes, A, up to 54% of the velocity mean value. In this system, the acoustic oscillations imposed at the inlet result in time varying velocity field, while there is no temporal or spatial variation in equivalence ratio. The base case flame P-15-070 with air velocity U_{air}=15 m/s and equivalence ratio φ=0.7 (Air Flow Rate=530 lpm and Methane Flow Rate=39 lpm) is studied in this chapter.

4.2 Results

4.2.1 Flame Kinematics

In this study, all the experiments were conducted with the use of a strong swirler, thus it is important to examine its influence on the response of the flames to high amplitude acoustic oscillations. Figure 4-1 and Figure 4-2 show the evolution of flame P-10-080-160-50 without and with swirler respectively, using phase-averaged OH* chemiluminescence images at every 15-degree phase angle. In the non-swirling flame, a vortex-like OH* chemiluminescence structure is formed at the bluff body edge, and is convected downstream, while growing in size. This is consistent with previous experiments on forced premixed ethylene flames [40]. However, in the case of the swirling flame (Figure 4-2), the observed vortex-like OH* chemiluminescence structure is less coherent than that formed in the non-swirling flame. Also, with the use of swirl, the flame brush thickness is greater and the flame is shorter than that without swirl. Figure 4-3 shows that the use of the swirler affects greatly the flame response, as in the non-swirling flame the peak-to-peak variation between the trough and the peak value of the heat release cycle is greater than that of the swirling flame.

The time-averaged OH* chemiluminescence images (Figure 4-4) show that the flame has a cylindrical shape, while the highest heat release is concentrated close to the wall. From the mean OH PLIF images, low OH intensity is observed in the inner shear layer (ISL) region, suggesting that the flame branches are anchored at the bluff body edge, whereas significantly greater OH intensity is seen in the outer recirculation zone (ORZ) region. From the comparison between the forced and unforced flames, a change in the flame shape can be seen. The flame branches in the ISL region of P-15-070-160-30 are much thicker than those of P-15-070, while the OH seen in the ORZ of the forced case is greater than that of the unforced. Also, P-15-070-160-30 is 7 mm shorter than P-15-070.

Instantaneous OH* chemiluminescence and OH PLIF images of P-15-070-160-30, during a cycle (Figure 4-5) demonstrate high heat release close to the wall, and wrinkling along the flame front, as well as vortex-like OH structures. Occasionally, attachment and lift-off -with relatively small lift-off heights- at the bluff body edge can be observed. The evolution of P-15-070-160-30 during the cycle is presented by using phase-averaged OH* chemiluminescence (Figure 4-6) and OH PLIF (Figure 4-7) images. Figure 4-6 shows a change in the flame shape and in particular, a downstream motion of the heat release zone during the cycle, with the main heat release being concentrated close to the wall. Figure 4-7 reveals that the flame impinges on the wall, while a change in the flame angle is observed.

During the acoustic cycle, the flame angle changes between 32 and 55 degrees, with the maximum value being revealed around 0 degrees and the minimum approximately at 200 degrees of the forcing cycle (Figure 4-8). A fluctuating flame angle, varying between the annular jet and the ORZ regions was reported by Thumuluru and Lieuwen [88]. The flame angle estimation data is very useful for the validation of models based on a kinematic description of the flame (eg. G-equation) [171]. From the phase-averaged Flame Surface Density (FSD) images of P-15-070-160-30 (Figure 4-9), it can be seen that the flame area modulation is mainly associated with a change in the angle of the flame front. The phase-averaged FSD images were revolved around the central axis of the burner and were used to obtain the cyclic FSD variation. In Figure 4-10, this quantity is compared with the cyclic OH* chemiluminescence variation, based on a 40 mm-window (40 mm is the height of the OH PLIF laser sheet). The comparison between Figure 4-8 and Figure 4-10 shows that the cyclic flame angle variation is almost in anti-phase with the FSD variation, which is consistent with Figure 4-9, at which it can be seen that the area of the flame front increases as the flame angle becomes steeper. In Figure 4-10, a relatively good agreement is observed between the cyclic OH* chemiluminescence and FSD variation, with a slight difference in amplitude and phase. Thus, it could be deduced that the heat release modulation is mainly through flame surface modulation for P-15-070-160-30. Also, this agreement suggests that the FSD can capture the global heat release well, despite the reservation of it being a planar measurement and the possibility of the flame speed varying along the flame. The agreement between FSD and OH* chemiluminescence phase-averaged variation was previously reported by [23, 40, 158, 172, 173]. Balachandran et al. [23], in their study of forced premixed ethylene flames without swirl, deduced that the flame area modulation was the most important mechanism affecting the heat release fluctuations [40]. The slight difference in phase and amplitude between the FSD and OH* chemiluminescence (Figure 4-10) could probably be attributed to the increased wrinkling in the third dimension due to the presence of the strong swirler. Concerning the influence of the flame burning rate fluctuations along the flame, despite the possibility of them being present (they could account for the difference in FSD and OH* chemiluminescence data), they are of smaller significance than the magnitude of the FSD and how it is altered by the flame angle. In order to investigate the influence of burning rate fluctuations along the flame, quantitative reaction rate (RX) measurements should be conducted, however this is not in the scope of this work.

In Figure 4-11, the local response of the flame at the forcing frequency is quantified based on OH PLIF images. The total variance, determining the OH fluctuations in the frequency range of 0-500 Hz, is the greatest in the near wall region. The metric of local flame sensitivity

to the forcing frequency, R_L (Figure 4-11), defined in Section 2.3.3.3, is much lower in the ISL region than in large zones on the downstream side of the OH PLIF plane, in spite of the fact that the acoustic oscillations gradients are stronger close to the annular passage than those in the downstream locations of the combustion chamber. This could be attributed to the fact that the reaction zone in the ISL region, close to the bluff body plane, is much weaker than that in the downstream region. High values of R_L are also seen in the IRZ and ORZ regions, while zero-value regions exist adjacent on both sides of the ISL zone. A zero value, either reflects the absence of OH, or it indicates that zero OH fluctuations at the forcing frequency are exhibited. In this case, considering the phase-averaged OH PLIF images (Figure 4-7) and the angle variation during the cycle (Figure 4-8), which changes between 32 and 55 degrees, it could be speculated that these zero-value zones constitute the extremes on either side of the flame angle variation region, between which the flame angle is modulated during the cycle. The high-value zones, observed adjacent to the aforementioned zero-value locations, are possibly part of the inner and outer recirculation zones and might be associated with the penetration of unburnt reactants to the outer and inner recirculation zones. The above pattern is also revealed in the second OH PLIF POD Mode of the flame, as described in Section 4.2.3.3, implying that the respective characteristics that it represents constitute one of the most dominant mechanisms of the flame kinematics of the system.

To investigate the behaviour of the various parts of the flame to forcing, the $OH/< OH >$ phase-averaged variation of the main flame regions (see Section 2.3.3.4) is presented in Figure 4-12a, from which the sequence of the OH intensity peaks in the ISL-Top-ORZ regions (Table 4-1) is estimated using the impingement point (see Section 2.3.3.2) as a reference. The phase difference of the $OH/< OH >$ peak between the ISL and Top region is 40 degrees, whereas the ORZ is delayed 175 degrees with respect to that in the Top region. In addition, the angle variation and the $OH/< OH >$ in the ISL region are almost in phase during the cycle. From Figure 4-12a, it can be seen that even though relatively high OH fluctuations are revealed in the individual regions, a low $OH/< OH >$ variation is observed in the total OH PLIF window. This can be explained by the phase difference observed among the $OH/< OH >$ curves of the different regions, which has an evening-out effect.

Concerning the impingement point position, it was found to move axially during the cycle (Figure 4-12b). Occasionally, it can be also observed at the OH* chemiluminescence snapshots, as indicated by the red arrow in Figure 4-5a. The position of the impingement point (Figure 4-12b) exhibits a sinusoidal trend with the peak revealed at 257 degrees and the trough at 77 degrees. The velocity fluctuations (Figure 4-12a) exhibit a sinusoidal trend with the peak

revealed at approximately 330 degrees. The phase difference between the peak of the velocity signal and the impingement point peak is 73 degrees (Figure 4-12a).

Figure 4-13 plots the probability density function of the lift-off height, P(h), with respect to h for both forced and unforced flames. The average lift-off height of P-15-070-160-30 is much lower than that of the unforced P-15-070 ($\bar{h}$=0.68 mm and $\bar{h}$=1.4 mm respectively), suggesting that in this case forcing influences the flame lift-off behaviour. The PDFs of both P-15-070-160-30 and P-15-070 show that approximately 50% of the samples exhibit a lift-off height below 0.13 mm and 0.3 mm respectively, while the positive tail of P-15-070-160-30 is shorter than that of P-15-070 (up to around 4.3 mm and 8.6 mm respectively). From Figure 4-14, it can be seen that the lift-off height of P-15-070-160-30 shows a small periodicity at 160 Hz, because apart from the peak at 160 Hz, other peaks at lower frequencies are revealed, while no peak is exhibited at 320 Hz. The phase-averaged lift-off height shows that the values are very small, however it should be noted that the data points exhibit a sinusoidal shape. Flames P-10-070 and P-10-070-160-30 have a similar average lift-off height ($\bar{h}$=0.33 mm and $\bar{h}$=0.30 mm respectively), suggesting that the forcing at A=30% hardly affects the lift-off behaviour, while the PDF peaks reveal that 71% of the samples exhibit a lift-off height below 0.15 mm. On the contrary, close to blow-off, at a high forcing amplitude of A=0.5, the lift-off behaviour is very different. In particular, the average lift-off height of P-10-070-160-50 is significantly greater ($\bar{h}$=2.6 mm) than that at lower A. Also, P-10-070-160-50 has the longest positive tail of all flames studied. The above imply that the greater the destabilisation of the flame (as the flame approaches blow-off) with the increase in forcing amplitude, the greater the lift-off heights variation observed. Figure 4-14b depicts that the lift-off periodicity at the forcing frequency of P-10-070-160-50 is very pronounced, as the lift-off spectrum exhibits a dominant peak at 160 Hz, while a small periodicity is observed at 320 Hz and 480 Hz, as well as at low frequencies. The phase-averaged lift-off height reveals that the data points exhibit a sinusoidal shape.

4.2.2 Amplitude Dependence of the Flame Response

Following the previous analysis on the flame kinematics at a specific forcing amplitude (A=30%), the overall flame response as a function of forcing amplitude is presented below for P-15-070, P-15-060, P-10-070 and P-10-080.

In the fully premixed system, the results suggest that the general trend is that at low forcing amplitudes $<Q'/<Q>$ increases linearly with A, and with a further increase in A, the heat release response continues to rise at a reduced rate, until it starts saturating at higher amplitudes. The maximum value of the normalised OH* chemiluminescence intensity

($<Q'/< Q >$) is 29%, observed in case of P-15-070-160-30, while the magnitude at which the heat release response starts deviating from linearity varies between A=11% and A=20%. Close to blow-off, P-15-060, does not follow the aforementioned trends, as the magnitude of its response is almost zero.

Concerning the effect of equivalence ratio on the flame response, it is shown that the normalised global heat release of P-10-080 is greater than that of P-10-070 at lower A, but from A=31% the difference in their response becomes smaller and eventually both curves meet at A=50% (Figure 4-15a). The high response of P-10-080 at low A might possibly be associated with the fact that this condition has a greater equivalence ratio (thus, a greater fuel flow rate, since U is kept constant) than that of P-10-070, thus it could be conjectured that the premixed system is sensitive to changes in the equivalence ratio. It is worth noting that a high sensitivity to the fuel flow rate was also observed in the Spray and NPA systems. On the contrary, at greater A the system is not sensitive to changes in equivalence ratio, since both curves show similar $<Q'/< Q >$ values. Also, Figure 4-15a shows that the normalised heat release response of P-10-080 increases nonlinearly with A, while that of P-10-070 shows a more linear dependence on A. This could probably be explained by the fact that both conditions when forced at low amplitudes are far from blow-off, and thus the rate at which $<Q'/< Q >$ increases with A is relatively high, but at higher A, as the flame is gradually approaching blow-off, the chaotic radial flame motion observed is more violent and as a result, the rate at which $<Q'/< Q >$ increases with A is reduced. This behaviour is more prominent for P-10-080, which is farther from blow-off than P-10-070. In addition, a vortex-like OH* chemiluminescence structure was formed, especially at high forcing amplitudes, as seen in Figure 4-2 for P-10-080-160-50. However, condition P-15-070, which showed a relatively linear heat release response with A, a vortex-like OH* chemiluminescence structure could barely be seen. Balachandran et al. [40], in the study of the forced response of turbulent flames, suggested that the non-linear heat release response of the system with A was attributed to flame roll-up, whereas the linear response was associated with the absence of flame roll-up.

The transfer function measurements show a nonlinear amplitude dependence (Figure 4-15b). In particular, for P-15-070 and P-10-080, a gradual decrease in the transfer function can be observed with A, which is greater at lower A, whereas at higher A the changes in the transfer function are reduced. The greatest NFTF reduction in the premixed system is exhibited by P-10-080 (from 0.77 to 0.4). For P-10-070, the transfer function increases linearly up to A=0.24, after which it remains almost constant, while the NFTF of P-10-060 is almost zero. Figure 4-15c

shows a little dependence on the forcing amplitude. As a general trend, for most conditions there is a slight gradual increase in the NFTF phase with A.

The power spectrum of the OH* chemiluminescence signal of P-15-070-160-30 (Figure 4-16c) shows that apart from the strong response at 160 Hz, the flame also responds at the first harmonic frequency, at 320 Hz (the 320 Hz peak magnitude is smaller by one order of magnitude compared with that at 160 Hz). Figure 4-16a shows that the harmonic frequency content of the heat release signal at 320 Hz, in spite of the fact that the velocity signal did not show any significant harmonic contents (Figure 4-16b), results in some nonlinearities in the heat release response. In order to investigate this nonlinear behaviour, the response of flame P-10-070 at the first harmonic was studied and the inlet velocity measurements were analysed to determine the amount of harmonic content using the two-microphone technique. An almost linear increase in harmonic content at 320 Hz is observed with the increase in forcing amplitude (Figure 4-17a). However, the ratio of heat release fluctuation at the first harmonic frequency to that at the forcing frequency (Q_h'/Q') with respect to forcing amplitude shows a highly nonlinear variation (Figure 4-17b). This relative response to 320 Hz increases linearly up to A=11%, after which it decreases also linearly until A=31%. Then the proportional harmonic response remains almost constant up to A=48%, while a peak is exhibited at A=53%. At A=11%, which is the forcing amplitude at which the peak of the relative response to 320 Hz is revealed, the normalised heat release response showed a slight deviation from linearity (Figure 4-15a). It was found that this nonlinearity occurred with the appearance of a vortex-like OH* chemiluminescence structure, suggesting that the response to the harmonic frequency was suppressed with the appearance of this structure. These findings are consistent with the results of Balachandran et al. [40], based on unswirled forced premixed ethylene flames. In their study, the peak of the relative response was revealed at A=15%, and it was also linked with a nonlinearity in the normalised heat release, which occurred with the appearance of flame roll-up. In addition, at A=53%, at which the second peak of the relative response to 320 Hz is revealed (Figure 4-17b), the normalised heat release exhibited a drop (Figure 4-15a). Similar observations were reported in previous studies based on forced turbulent premixed flames [68, 92, 158, 165, 174], where the nonlinearity was speculated to be due to a nonlinear evolution of flame surface area. Apart from vortex roll-up, flame lift-off [89-91] was also reported to be an important mechanism of nonlinearity.

4.2.3 Proper Orthogonal Decomposition Analysis (POD)

In this section, the POD results of OH* chemiluminescence and OH PLIF images are discussed. The OH* chemiluminescence POD results presented below consist of the first few modes, the PSDs of POD time coefficients, the instantaneous OH* chemiluminescence images and their reconstruction based only on a small number of modes, as well as the relative cumulative energy content of POD modes. The OH PLIF POD results are also presented in a similar way. The following discussion focuses on: a) the basic structure of the flame extracted from POD, b) its temporal evolution, c) the difference between the forced and unforced flame and d) the estimation of the convection velocity of the most dominant structures of the system.

4.2.3.1 OH* Chemiluminescence POD Analysis

As far as the spatial structure of the flame is concerned, Mode 1 exhibits a roughly antisymmetric structure of heat release fluctuations (Figure 4-18a), which is associated with a left-right oscillating motion, as well as an axial dependence of the flame shape on the left side of the flame, which suggests a slight axial motion of the flame, as seen in the respective reconstructed image in Figure 4-18b. A similar behaviour is also exhibited from the other POD Modes and from the reconstructed images of the added Modes 1-4. These antisymmetric heat release fluctuations cannot be seen easily in the raw OH* chemiluminescence snapshots, because of the underlying small-scale fluctuations. The PSD of POD time coefficients of a mode reveals the periodicity associated with the respective motion of the flame. In Figure 4-18a, the PSD of Mode 1 reveals a peak at 25 Hz, while the PSDs of Modes 2-4 exhibit many peaks at different frequencies. To investigate the mechanism associated with the peak at 25 Hz, image recording for a much longer duration, such that to capture a sufficient number of cycles is necessary.

For P-15-070-160-30, Modes 1 and 2 show a banded shape (Figure 4-19), which is representative of the pronounced axial flame motion. As demonstrated by the respective reconstructed images (Figure 4-20), in case of Mode 1, the flame moves axially in the downstream direction, whereas in case of Mode 2, the heat release contracts at the point at which the flame impinges on the wall (impingement point, see Figure 4-5a), and subsequently from this point it expands simultaneously in both the upstream and downstream directions. In both Modes, the heat release is mainly concentrated close to the wall. The respective PSDs of POD time coefficients exhibit one dominant peak at 160 Hz, and a smaller one at 320 Hz. The PSD of Mode 3 exhibits one dominant peak at 320 Hz and other smaller peaks at lower frequencies, while the PSD of Mode 4 shows many peaks. The signal to noise ratio in the PSD

of Modes 3 and 4 is much lower than that of the PSD of Modes 1 and 2. The structure of Modes 3 and 4 represents a combination of a transverse and axial motion.

Concerning the POD energy, the energy contribution of Modes 1 and 2 is significantly larger than that of the successive modes (Table 4-2), implying that the dominant mechanism is captured mainly by the first two modes. In particular, the first two Modes of P-15-070-160-30 contain approximately 58.5% of the total energy, while the energy of Modes 3 and 4 is much lower (4.8%). This is consistent with the results of the self-excited flame SP-10-077-510, at which the POD energy content of the first two Modes was 63.9%, while that of Modes 3-4 was only 5.3%. In both cases, this was attributed to the fact that the energy was concentrated in a dominant structure, associated with the pronounced axial flame motion. Figure 4-21 shows the cumulative POD energy distribution of the first 200 Modes of P-15-070 and P-15-070-160-30. The cumulative energy of the forced flame is greater than that of the unforced condition, while their energy difference becomes smaller at higher modes. The cumulative energy content of the first four Modes of P-15-070-160-30 is 63.3%, while that of P-15-070 is 29.3% of the total energy. This suggests that the effect of forcing on the flame structure is important. Also, both curves, exhibit a much steeper slope at lower mode numbers than at higher modes.

4.2.3.2 Estimation of Convection Speed

In this section, the convection velocity of the most dominant OH* chemiluminescence structure of P-15-070-160-30 is estimated using the OH* chemiluminescence POD method. As described in Section 4.2.3.1, the structure of the first POD Mode reveals a banded shape, which is representative of the axial motion of the flame, and is associated with a dominant peak at 160 Hz (as shown by the PSD of the POD time coefficients in Figure 4-19). This Mode contains 48.2% of the total POD energy, implying that the dominant mechanism is mainly captured by it. The convection velocity was determined by multiplying the characteristic heat release wavelength, λ, of the first POD Mode, as shown in Figure 4-19, with the dominant frequency (160 Hz), exhibited by the respective PSD of POD time coefficients. Thus, the ratio of the convection velocity to the bulk velocity was estimated to be approximately 1. This value is lower than the estimated ratio (1.40-1.66) in the case of the self-excited premixed system (Section 3.5.2). Similar banded shape OH* chemiluminescence structures were found by Sieber et al. (11). In particular, the first seven OH* POD Modes and spectral OH* POD Modes were presented, the analysis of which revealed three dominant structures: the actuation mode, PVC-I and PVC-II. It was reported that the energy of the actuation mode increased with the increase in forcing amplitude. The first pair of POD Modes revealed a banded shape, while the structure of higher modes was characterised as ‘mode clutter’, revealing multiple wavelengths with no

clear symmetries. This is consistent with the findings of the present work, where at higher Modes more details of the flame structure where shown.

4.2.3.3 OH PLIF POD Analysis

The first OH PLIF POD Mode of P-15-070 (Figure 4-22a) shows an antisymmetric OH structure, which corresponds to the left-right oscillating motion (Figure 4-22b), and is associated with many frequencies. Modes 2-4 exhibit more details of this transverse motion, while the PSD of POD time coefficients also reveal many frequencies. The time evolution of the reconstructed images of Modes 1 to 4 with their modal time coefficients also show the left-right flame motion, with the OH close to the wall being greater than that in the ISL region. Also, a change in the flame angle can be barely seen (Figure 4-22b).

In contrast, for the forced flame P-15-070-160-30, the first two Modes show strong features of the flame structure and are almost purely associated with the forcing frequency. In particular, the structure of both modes is representative of the angle variation, as demonstrated by the respective reconstructed images (Figure 4-24). Also, the structure of Mode 2 is similar with that of Figure 4-11, showing the boundaries between which the flame angle varies, while the banded shape, seen on the right side of the ORZ region, is typically characteristic of OH fluctuations in the axial direction. The reconstructed images of the first 4 POD Modes added together reveal a combination of flame angle variation and transverse motion (Figure 4-24).

The relative energy contained in the first four OH PLIF Modes and the energy distribution in the individual modes are greater in case of P-15-070-160-30 than those of P-15-070 (Table 4-3). In addition, for P-15-070-160-30, the cumulative energy contained in the first 50 OH* chemiluminescence POD Modes is significantly greater (86.5%) than that in the first 50 OH PLIF Modes (56.7%) (Figure 4-21). The reduced energy values of the OH PLIF data imply that the structures captured by the planar measurement constitute a good representation of the structures revealed by the line-of-sight measurement, however OH PLIF cannot capture fully all the OH* chemiluminescence features, possibly due to the strong swirl.

4.3 Conclusions

In this chapter, the experimental investigation of the response of the fully premixed system (i.e. no temporal or spatial variation in equivalence ratio) is presented briefly. OH* chemiluminescence measurements, acquired with a photomultiplier tube (PMT) and an ICCD camera, were used to study qualitatively the heat release response of the flames, while OH PLIF measurements were used to understand the response of the flame structure and the behaviour

of the various parts of the flame. Apart from the flame kinematics analysis, the amplitude dependence of the transfer function was estimated. Also, the flame surface density (FSD), calculated from OH PLIF images, was used as a surrogate of the heat release, as well as qualitatively as an indicator of the flame area. The dominant structures of the flames and their periodicity were characterised using the Proper Orthogonal Decomposition (POD) method, while the convection velocity of the most dominant structures of the system was estimated.

First of all, the effect of the swirler on the flame response was found to be very important, with a non-swirling flame exhibiting a greater response than a swirling flame. Concerning the amplitude dependence of the fully premixed flame response, a high, nonlinear response was observed in the flames studied (the maximum normalised global heat release fluctuation was 29%). The general trend was that at low forcing amplitudes $<Q'/<Q>$ increased linearly with A, and with a further increase in A, the heat release response continued to rise at a reduced rate until it started saturating at higher amplitudes. Close to blow-off, the flame response was significantly reduced compared with that farther from blow-off. In addition, at low A, the fully premixed system showed an increased sensitivity to equivalence ratio, whereas at greater A the system was not sensitive to changes in equivalence ratio. As far as the influence of forcing amplitude on the heat release response is concerned, at low forcing amplitudes A and far from blow-off, the rate at which $<Q'/<Q>$ increased with A was relatively high, but at greater A and as the flame was approaching blow off, more violent chaotic radial flame motion was observed and thus, the rate at which $<Q'/<Q>$ increased with A was reduced. Also, the nonlinear heat release response of the system with A was associated with the formation of a vortex-like OH* chemiluminescence structure, while a more linear response was linked to the absence of OH*-vortex structures. A source of nonlinearity in the heat release response was associated with the fact that part of the energy was transferred to the first harmonic (320 Hz), while the velocity signal did not show any significant harmonic contents. This response to the harmonic frequency was suppressed with the appearance of a vortex-like OH* chemiluminescence structure.

Concerning the flame kinematics, a novel method for quantifying the local response of the various parts of the flame at the forcing frequency was developed. This was achieved by using the ratio R_L defined as the OH fluctuation contribution at 160±3 Hz to the total variance based on groups of pixels from the OH PLIF images. R_L was found to be much lower in the ISL region than in large regions on the downstream side of the OH PLIF plane, in spite of the fact that the acoustic oscillation gradients were stronger closer to the annular passage than those in the downstream locations of the combustion chamber. This was probably attributed to the fact

that the reaction zone in the ISL region, close to the bluff body plane was much weaker than that in the downstream region. A pattern with zero-value regions was revealed adjacent on both sides of the high ISL R_L values, which represented the extremes between which the flame angle was modulated during the cycle. The above patterns were also seen in the second OH PLIF POD Mode, implying that these characteristics constitute dominant mechanisms of the premixed system.

During the acoustic cycle, the change in the angle of the flame that was observed followed a sinusoidal trend. Another important feature of the flame was the impingement point, the position of which showed an axial movement during the cycle, exhibiting a sinusoidal trend. The impingement point was used as a reference point in the analysis of the sequence at which the OH intensity peaks in the ISL-Top-ORZ regions were revealed. The phase difference among the curves of the OH signal in the different regions of the flame was found to change in the various flames. Also, it was found that the angle variation and the $OH/<OH>$ in the ISL region were almost in phase during the cycle. Even though relatively high OH fluctuations were revealed in the individual regions, a low $OH/<OH>$ variation was observed in the total OH PLIF window, due to the phase difference among the $OH/<OH>$ curves of the different regions, which had an evening out effect. In addition, it was suggested that forcing influenced the flame lift-off height behaviour and in particular, the greater the destabilisation of the flame with the increase in forcing amplitude, the greater the lift-off heights observed. The lift-off height periodicity at the forcing frequency was very pronounced, especially at greater forcing amplitudes. It was shown that the flame angle variation was almost in anti-phase with the FSD variation. Finally, a relatively good agreement was reported between the cyclic OH* chemiluminescence and FSD variation with a slight difference in amplitude and phase, from which it could be deduced that the heat release modulation was mainly through flame surface modulation and also that the FSD could capture the global heat release well. The difference in phase and amplitude was probably attributed to the increased wrinkling in the third dimension due to the presence of the strong swirler.

From the POD analysis, the first two OH* chemiluminescence POD Modes revealed a banded shape, which represented the axial motion of the flame and was associated with the forcing frequency at 160 Hz. The fact that the energy contribution of the first two Modes was significantly greater than that of the successive modes implied that the dominant mechanism was captured mainly by the first two modes. The OH PLIF POD results, apart from the aforementioned features, revealed the angle variation of the flame. The ratio of the convection

velocity to the bulk velocity was estimated to be unity, which is lower than that of self-excited premixed flames (Chapter 3).

4.4 Figures of Chapter 4

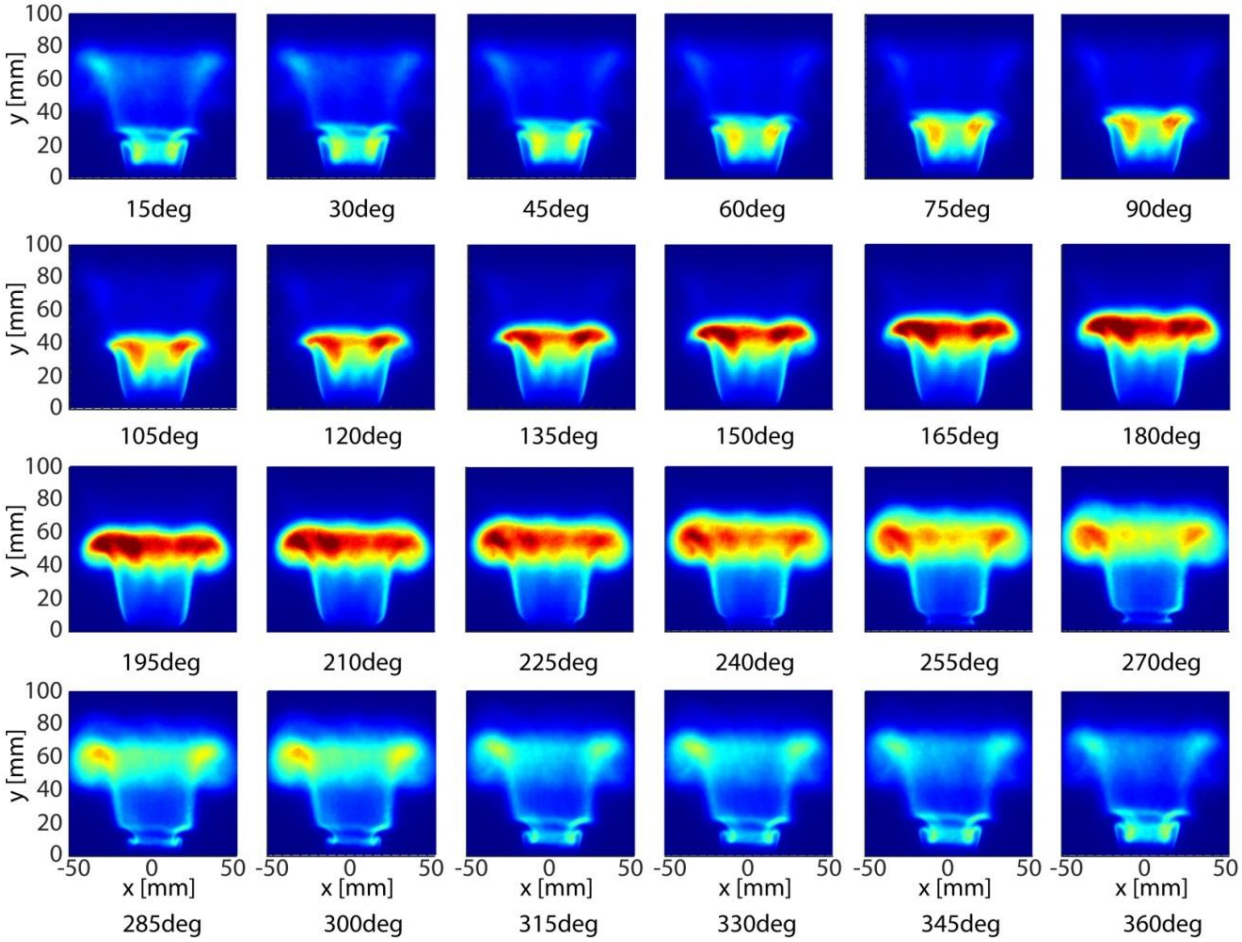

Figure 4-1: Phase-averaged OH* chemiluminescence images of P-10-080-160-50 without swirler.

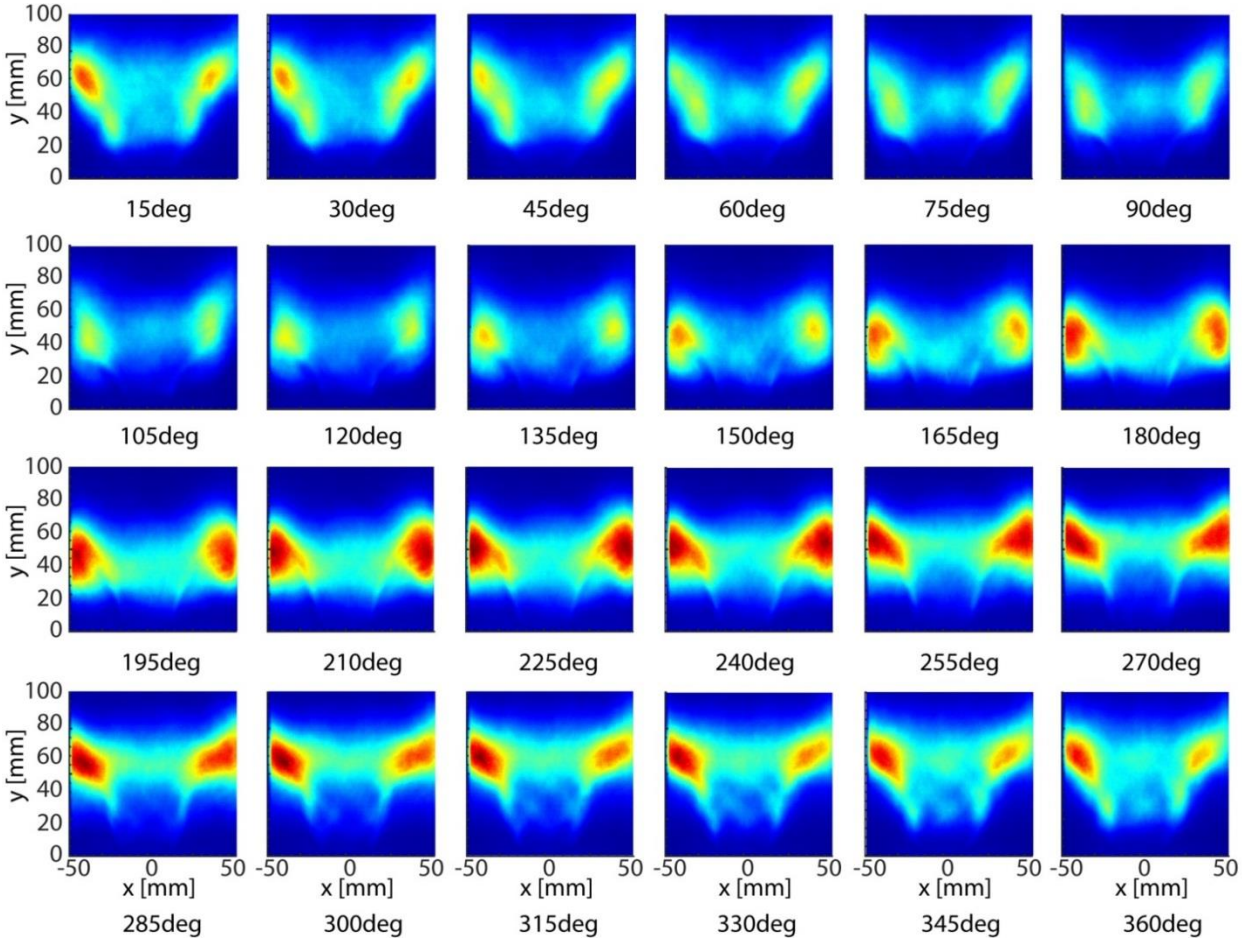

Figure 4-2: Phase-averaged OH* chemiluminescence images of P-10-080-160-50 with swirler.

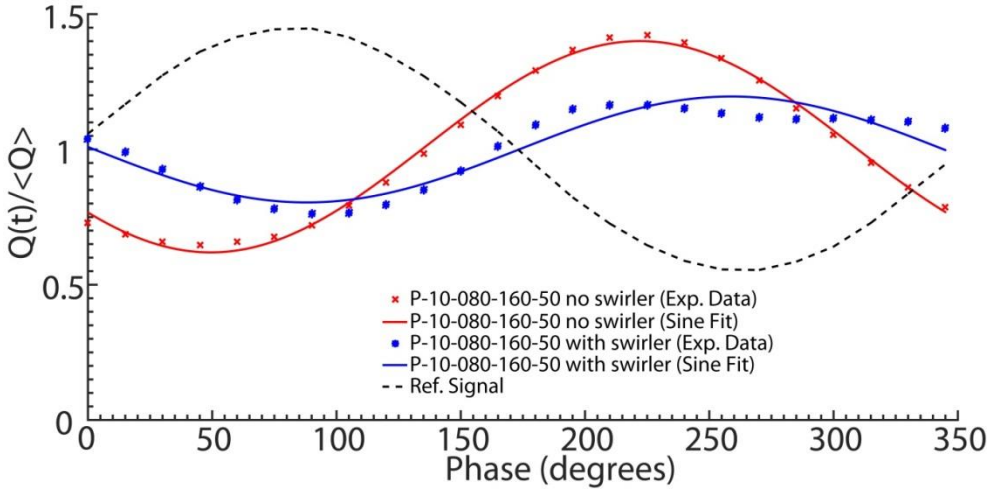

Figure 4-3: Comparison of cyclic OH* chemiluminescence variation between non-swirling P-10-080-160-50 and swirling P-10-080-160-50.

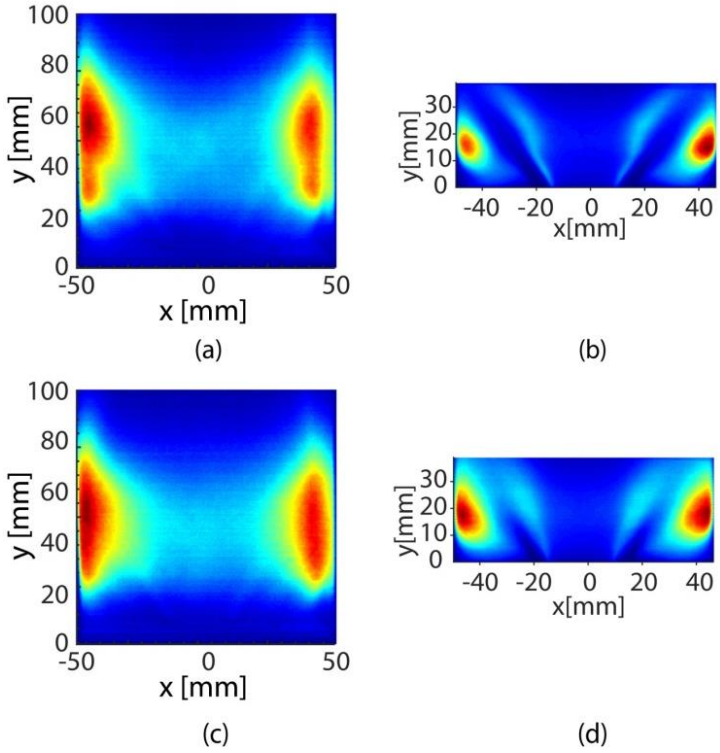

Figure 4-4: Time-averaged (a) OH* chemiluminescence and (b) OH PLIF image of unforced fully premixed P-15-070 and (c) time-averaged OH* chemiluminescence and (d) OH PLIF image of forced P-15-070-160-30.

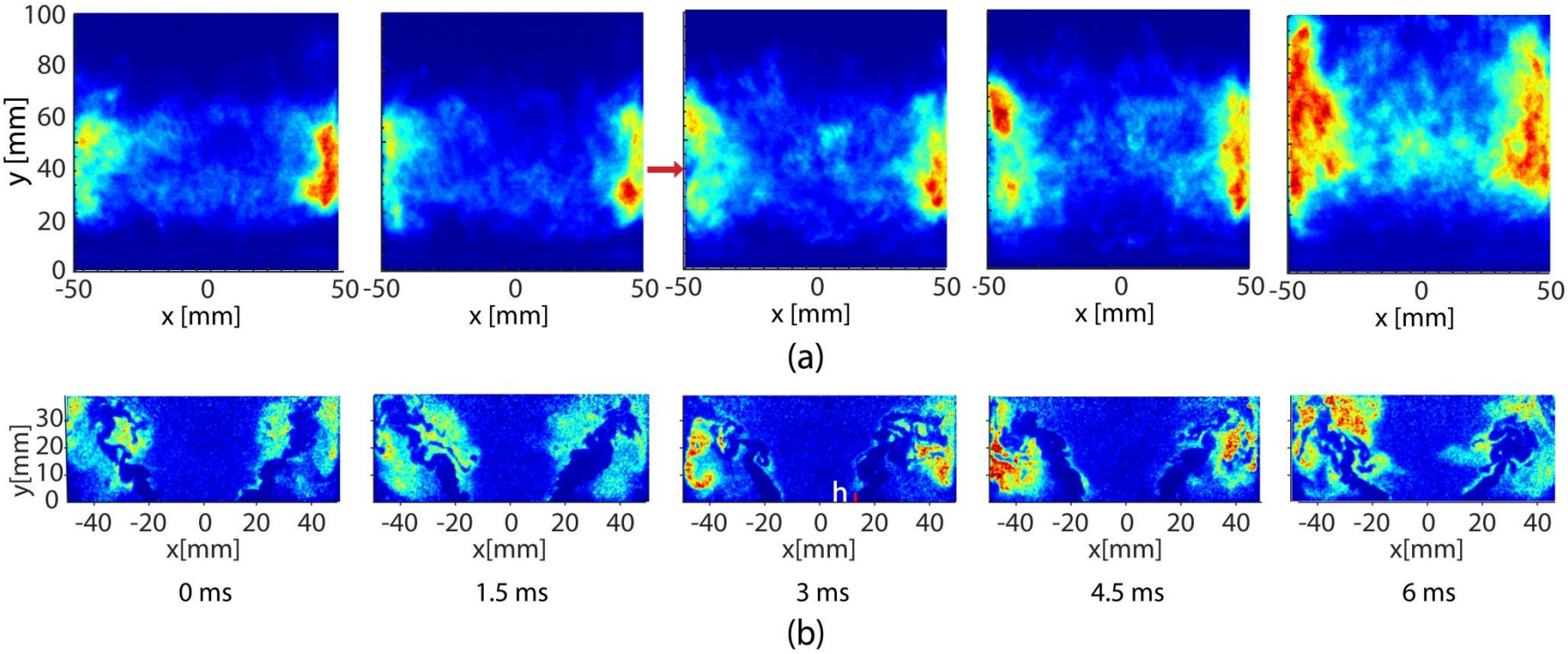

Figure 4-5: (a) Instantaneous OH* chemiluminescence and (b) OH PLIF images of P-15-070-160-30 (not recorded simultaneously during a cycle, *t*=0 ms corresponds to the beginning of the cycle). The same colormap for each image was used. The main features of the flame behaviour are highlighted: red arrow: the point at which the flame branch in the ISL impinges on the wall, while the heat release extends in both downstream and upstream directions, red line: lift-off height h at the bluff body edge.

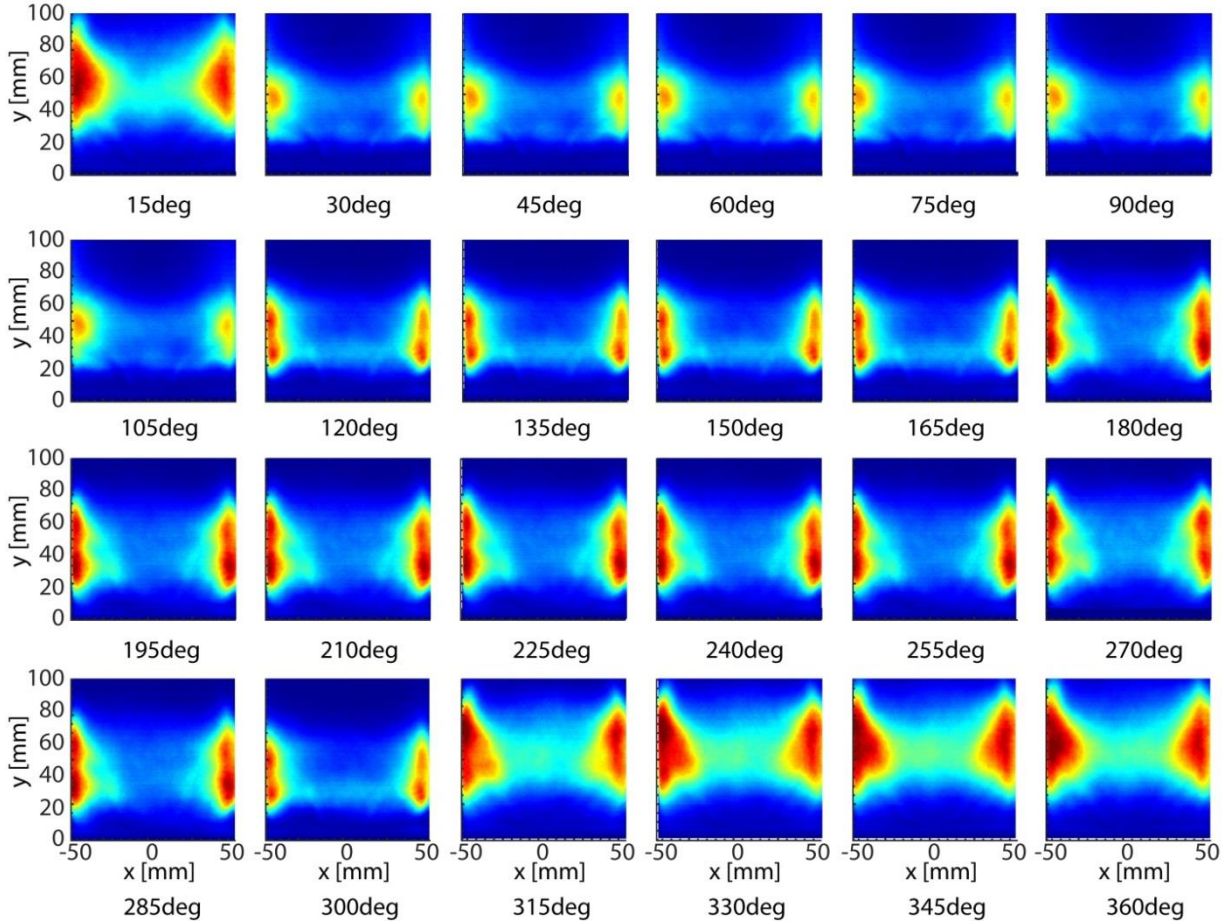

Figure 4-6: Phase-averaged OH* chemiluminescence images of P-15-070-160-30.

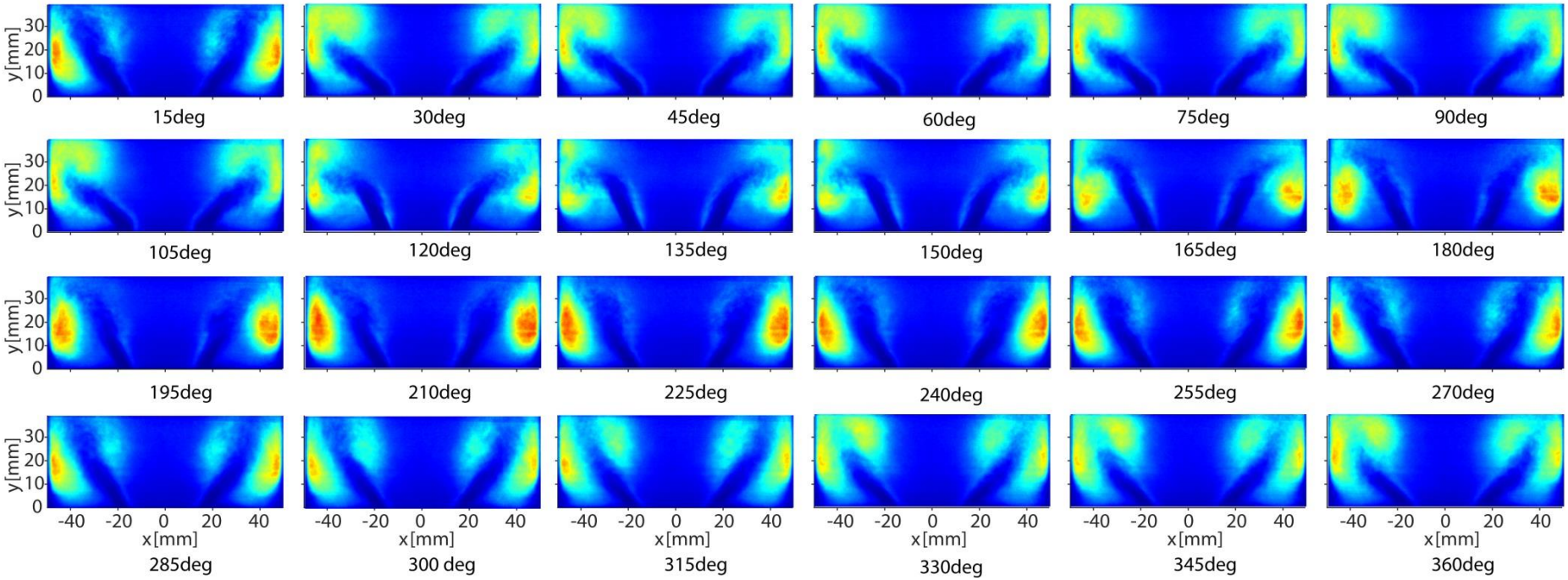

Figure 4-7: Phase-averaged OH PLIF images of P-15-070-160-30.

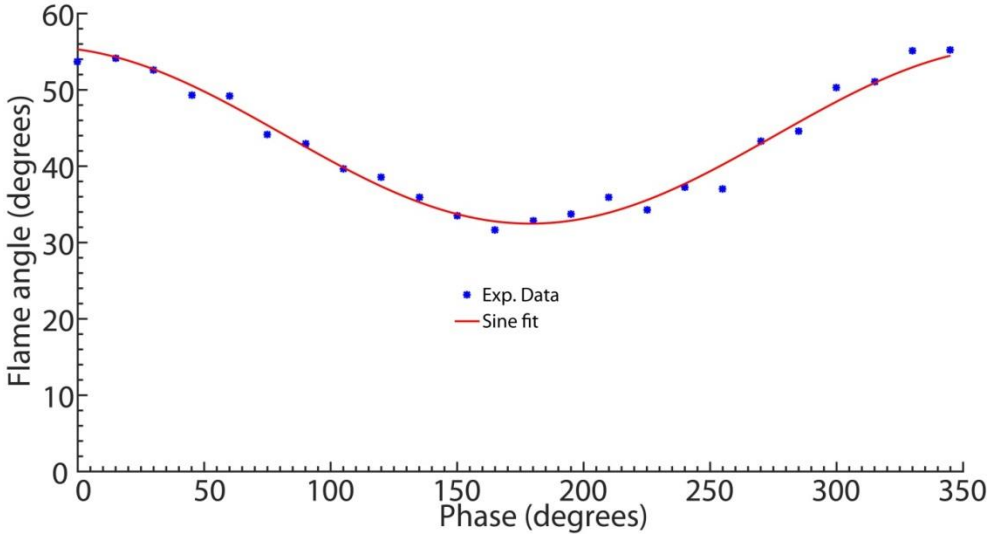

Figure 4-8: Flame angle variation with respect to phase of the acoustic cycle, based on phase-averaged OH PLIF images (Figure 4-7). Flame: P-15-070-160-30.

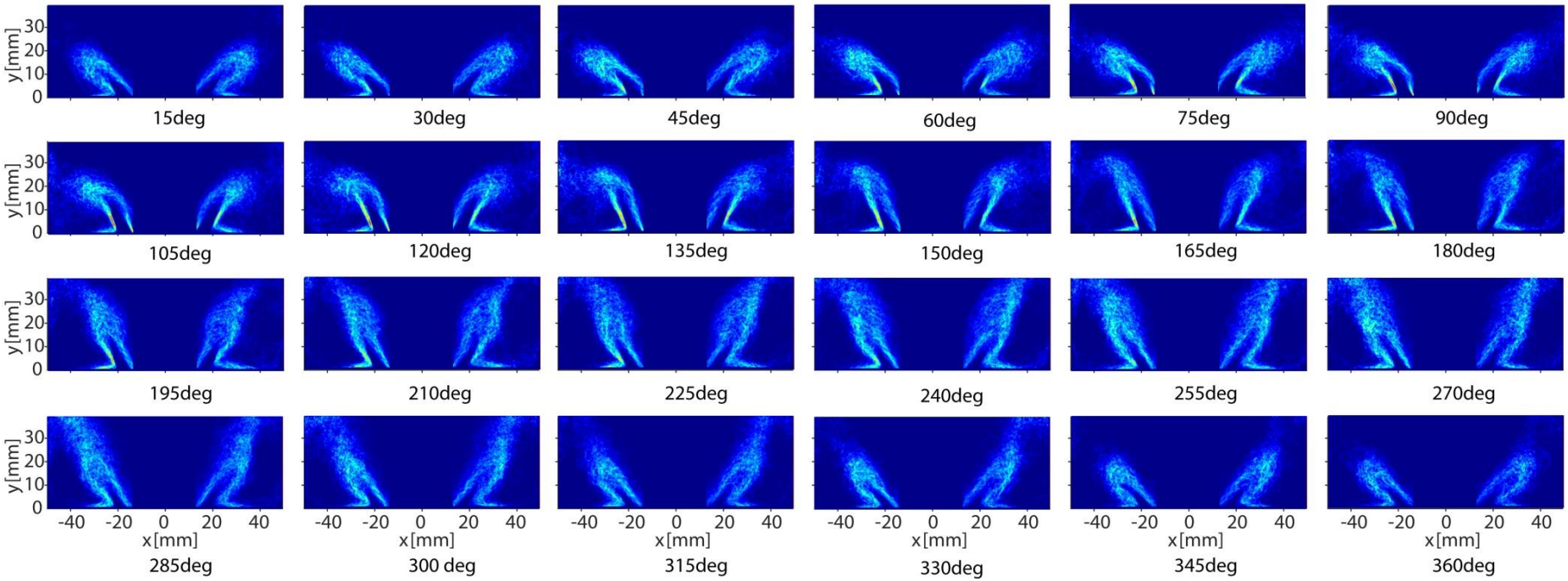

Figure 4-9: Phase-averaged FSD images of P-15-070-160-30.

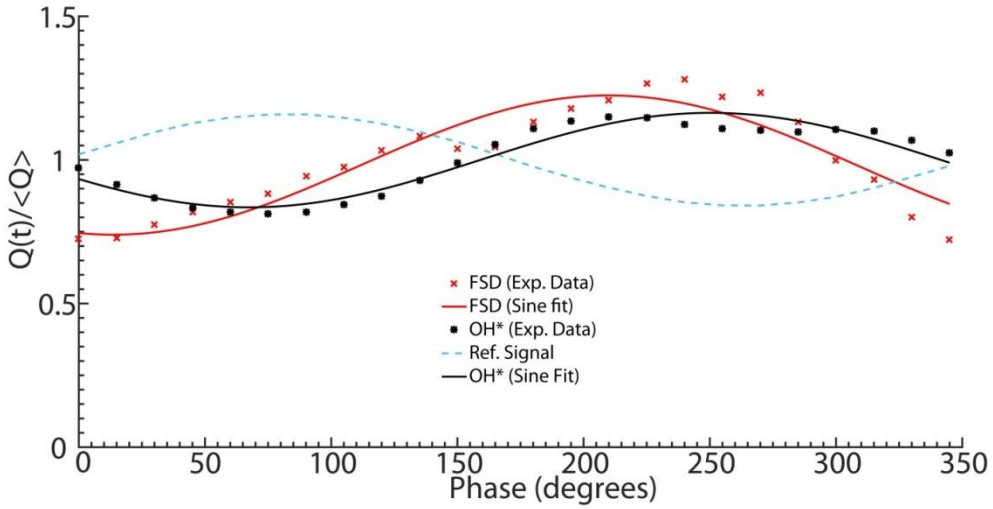

Figure 4-10: Comparison of the cyclic FSD variation, evaluated from the phase-averaged FSD images presented in Figure 4-9, revolved around the burner central axis, and the cyclic OH* chemiluminescence variation based on a 40 mm window (40 mm is the height of the OH PLIF laser sheet) for P-15-070-160-30.

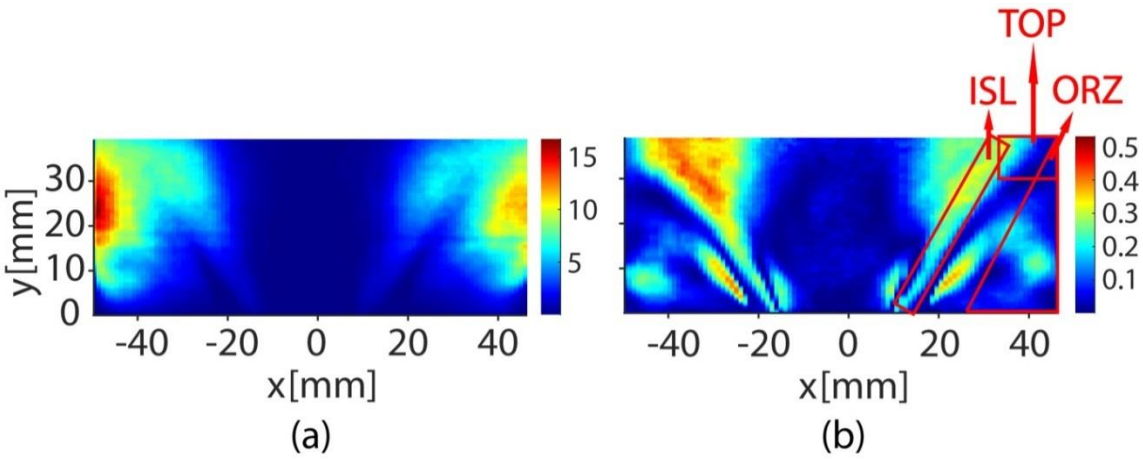

Figure 4-11: (a) Variance of OH and (b) ratio R_L (OH fluctuation at 160 Hz to the total variance of OH) for P-15-070-160-30.

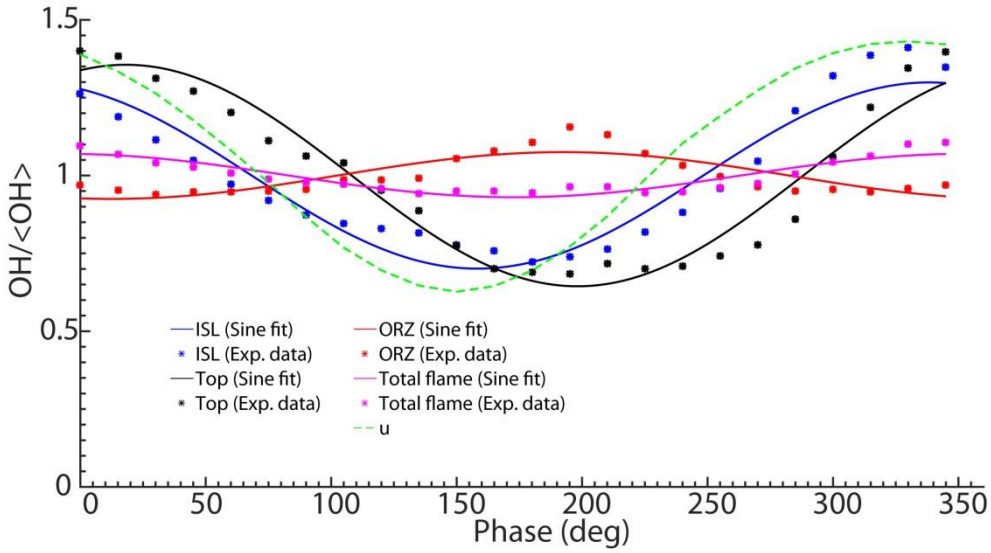

(a)

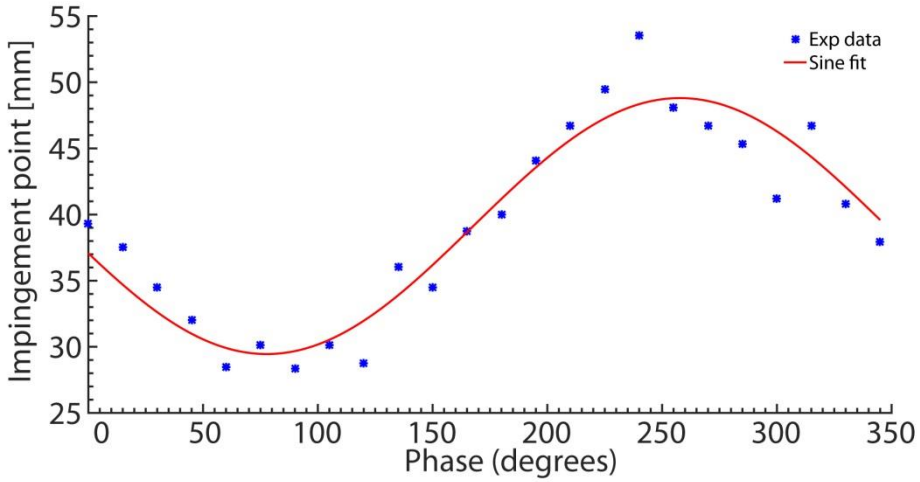

(b)

Figure 4-12: (a) $OH/< OH >$ variation during the cycle, evaluated from phase-averaged OH PLIF images (data presented in Figure 4-7), calculated from the ISL, Top, ORZ and the whole OH PLIF window. The green dashed line represents the normalised acoustic velocity fluctuations. (b) Impingement point position variation with respect to phase of the acoustic cycle. Flame: P-15-070-160-30.

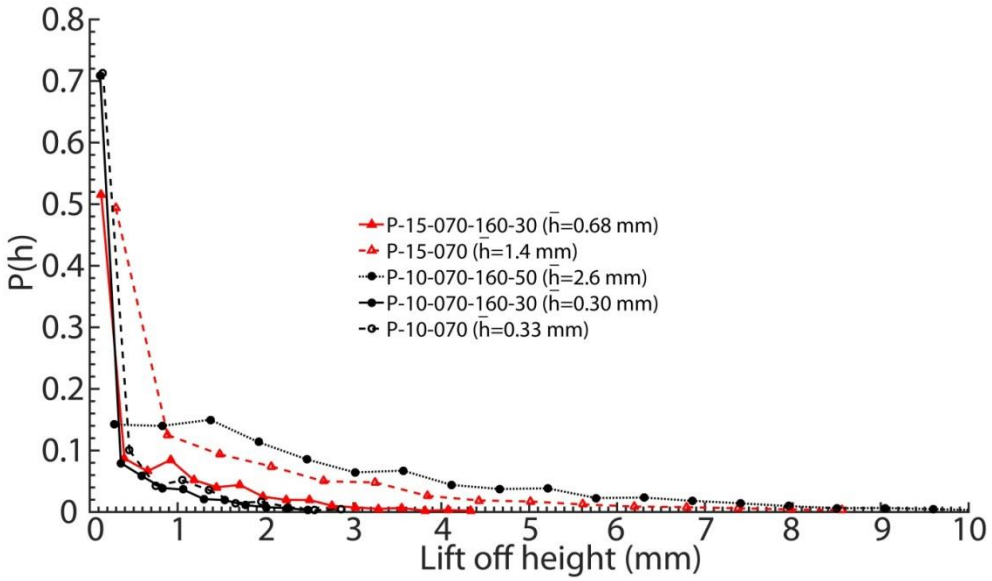

Figure 4-13: Probability density function of the lift-off height, $P(h)$, with respect to h for forced and unforced flames. The average lift off height $\bar{h}$ is indicated.

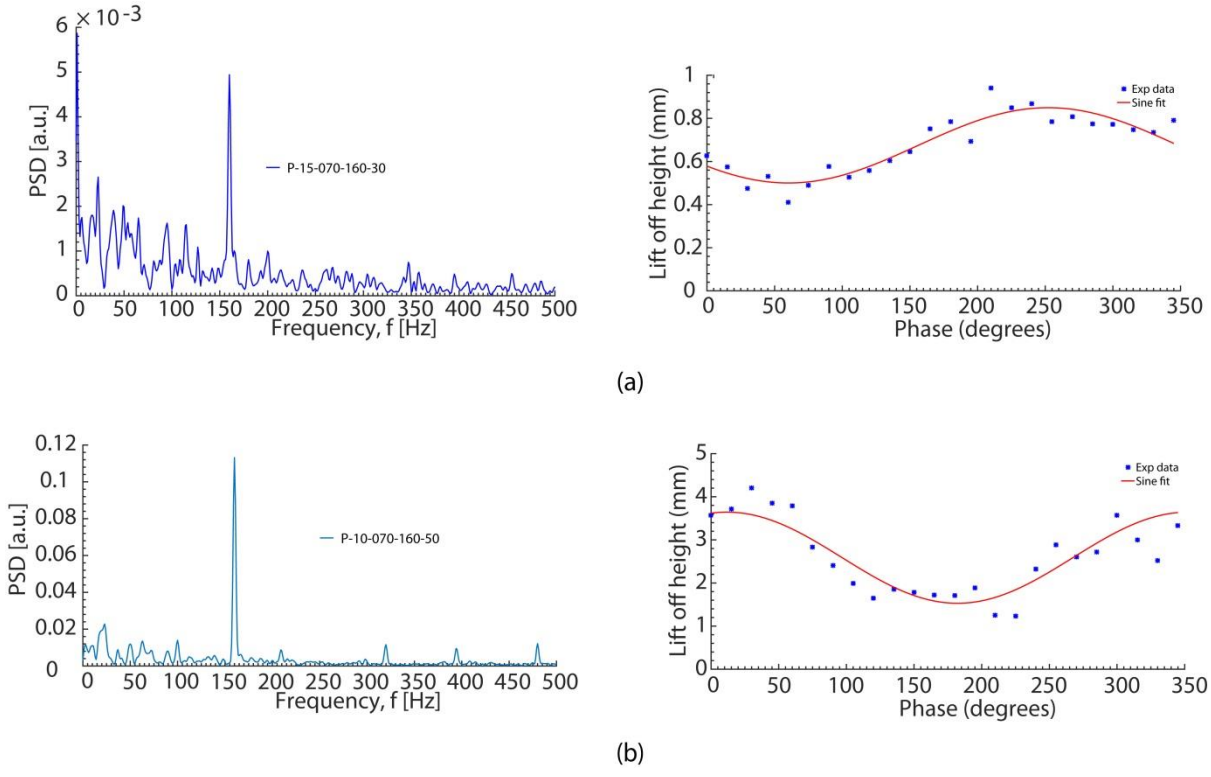

Figure 4-14: Power spectra of lift-off height and lift-off height with respect to phase for (a) P-15-070-160-30 and (b) P-10-070-160-50.

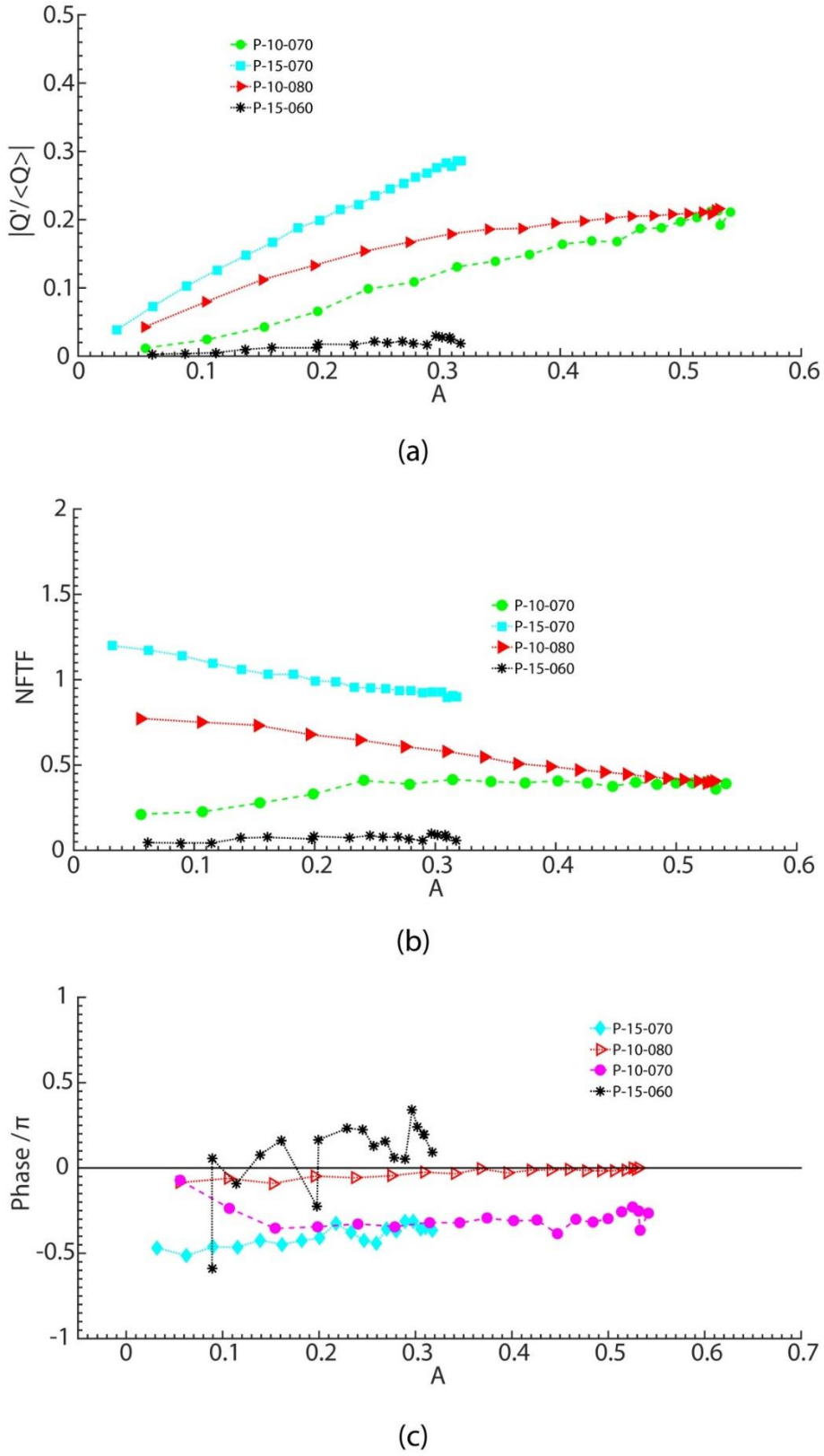

Figure 4-15: (a) Normalised global heat release fluctuations of flames P-15-070, P-10-070, P-10-080 and P-15-060 measured as a function of *A* using OH* chemiluminescence, (b) the corresponding transfer function and (c) its phase evaluated from the data of (a).

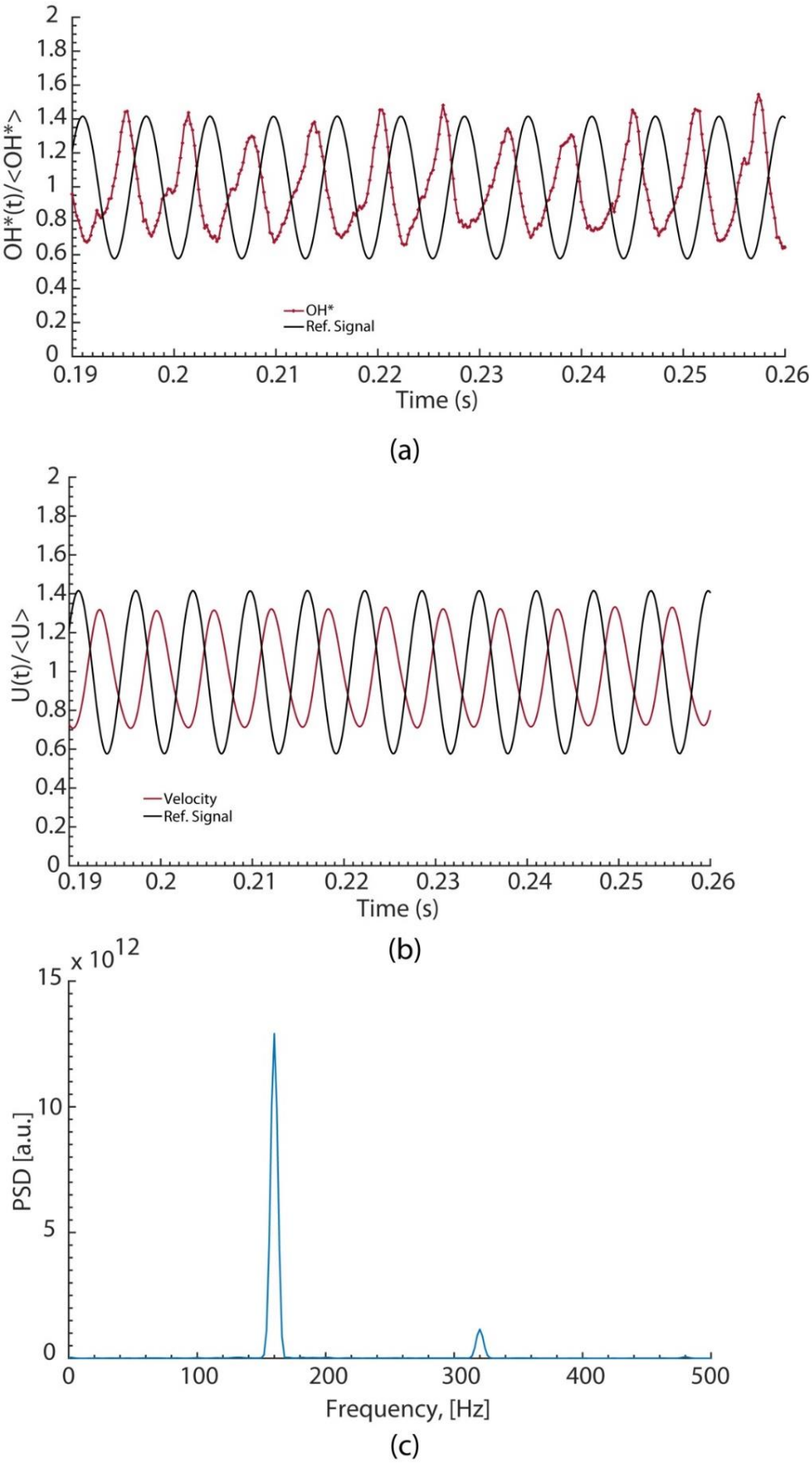

Figure 4-16: Time series of (a) OH* chemiluminescence, (b) the corresponding inlet velocity data, calculated from the two-microphone technique, and (c) power spectrum of OH* chemiluminescence signal of P-15-070-160-30.

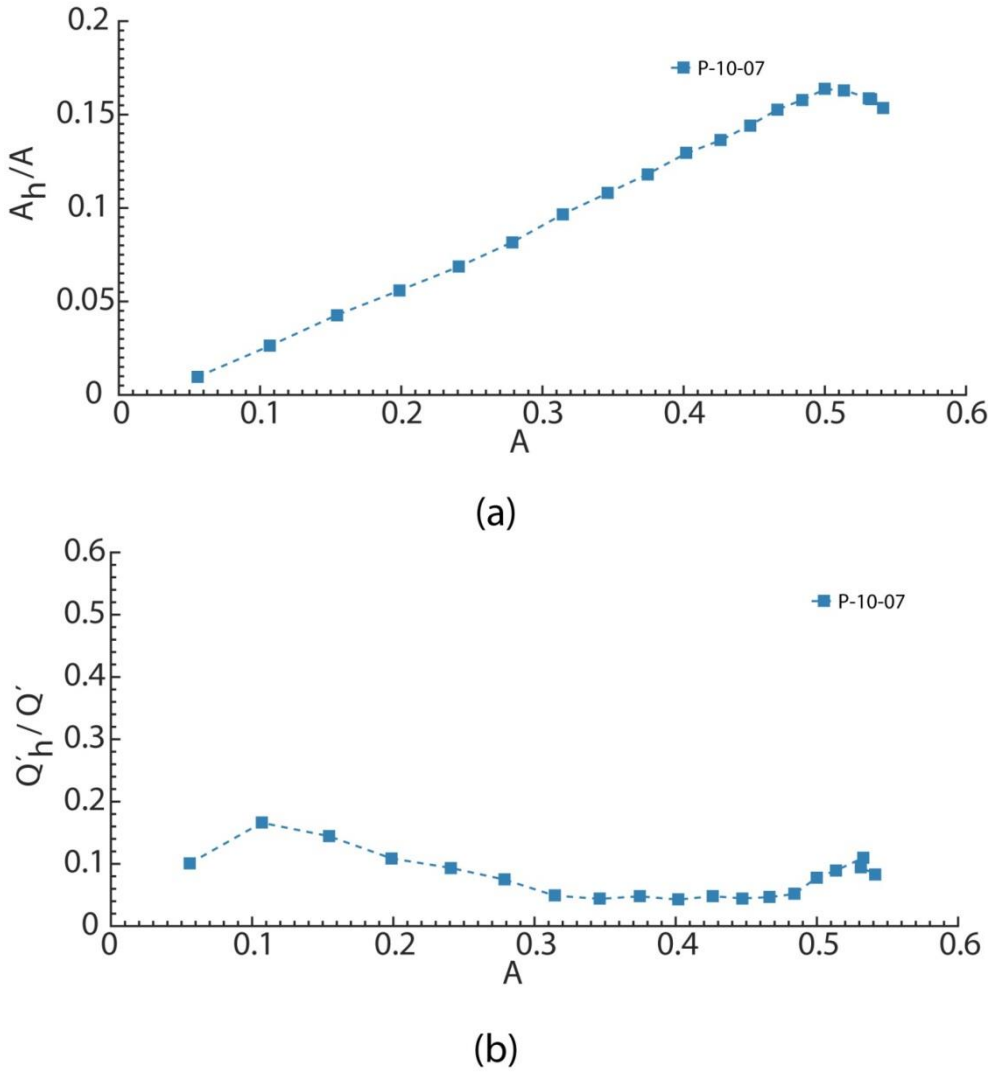

Figure 4-17: Variation of (a) ratio of amplitude of inlet velocity fluctuation at first harmonic of the forcing frequency (320 Hz) A_h, to that at the forcing frequency (160 Hz), A, with respect to A, and (b) ratio of heat release fluctuation at the first harmonic (320 Hz) to that at the forcing frequency (160 Hz), (Q'_h/Q') , as a function of A. Flame: P-10-070.

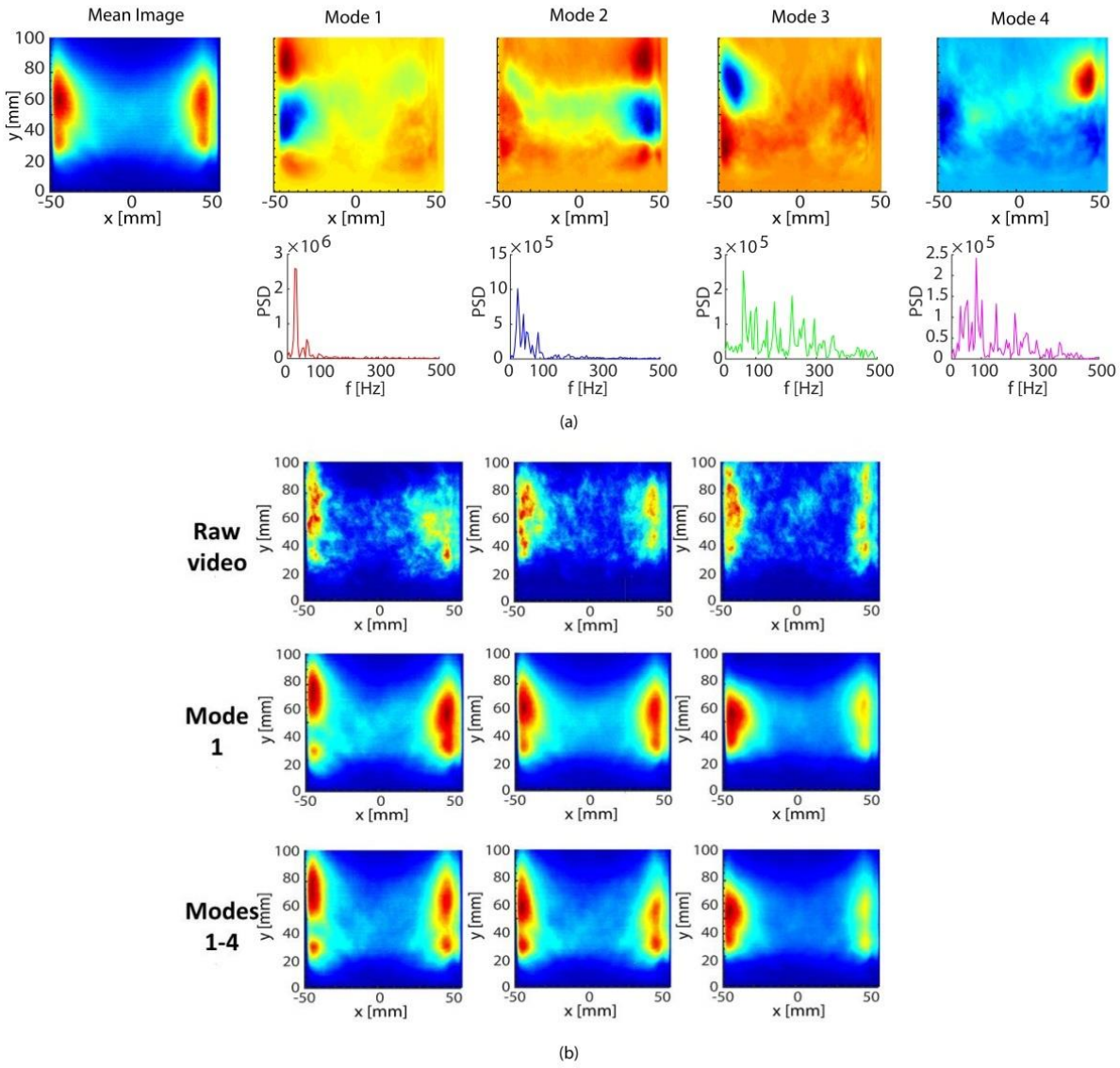

Figure 4-18: (a) Mean image and first four OH* chemiluminescence POD Modes and the respective PSD of POD time coefficients. (b) Instantaneous OH* chemiluminescence images, and snapshots at the same times from reconstructed OH* movie using the mean and Mode 1 only and the mean and Modes 1 to 4. Flame: P-15-070.

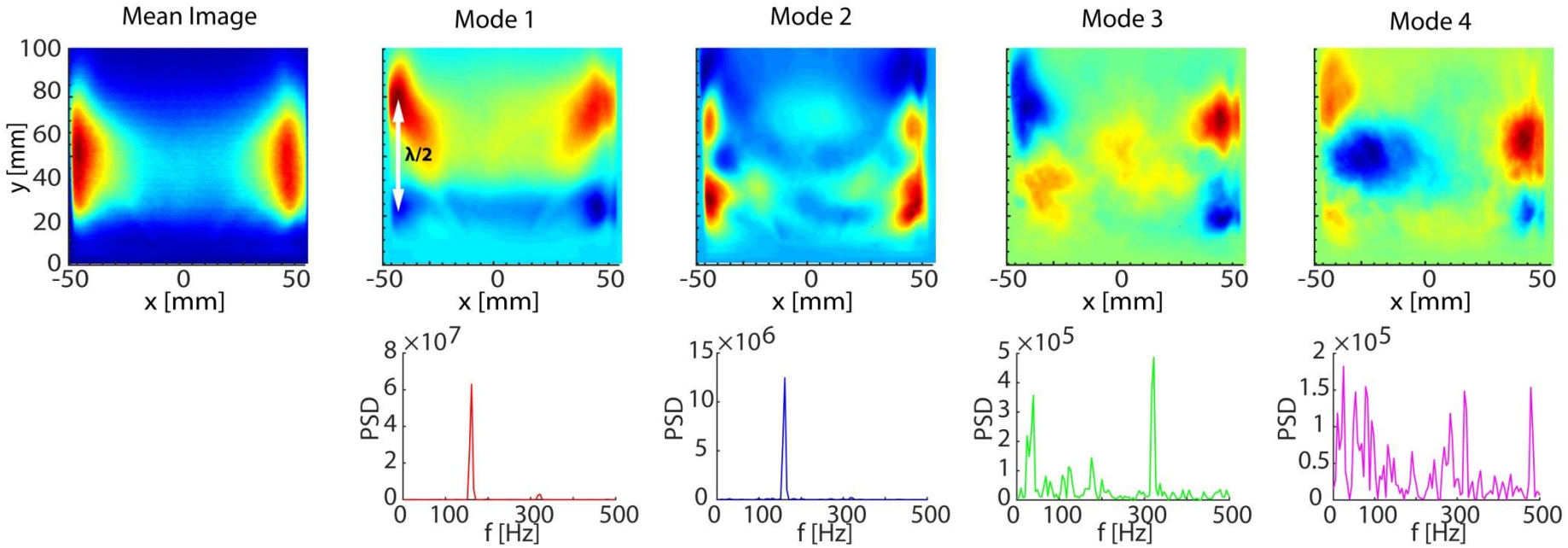

Figure 4-19: Mean Image and first four OH* chemiluminescence POD Modes and respective PSD of POD time coefficients of P-15-070-160-30.

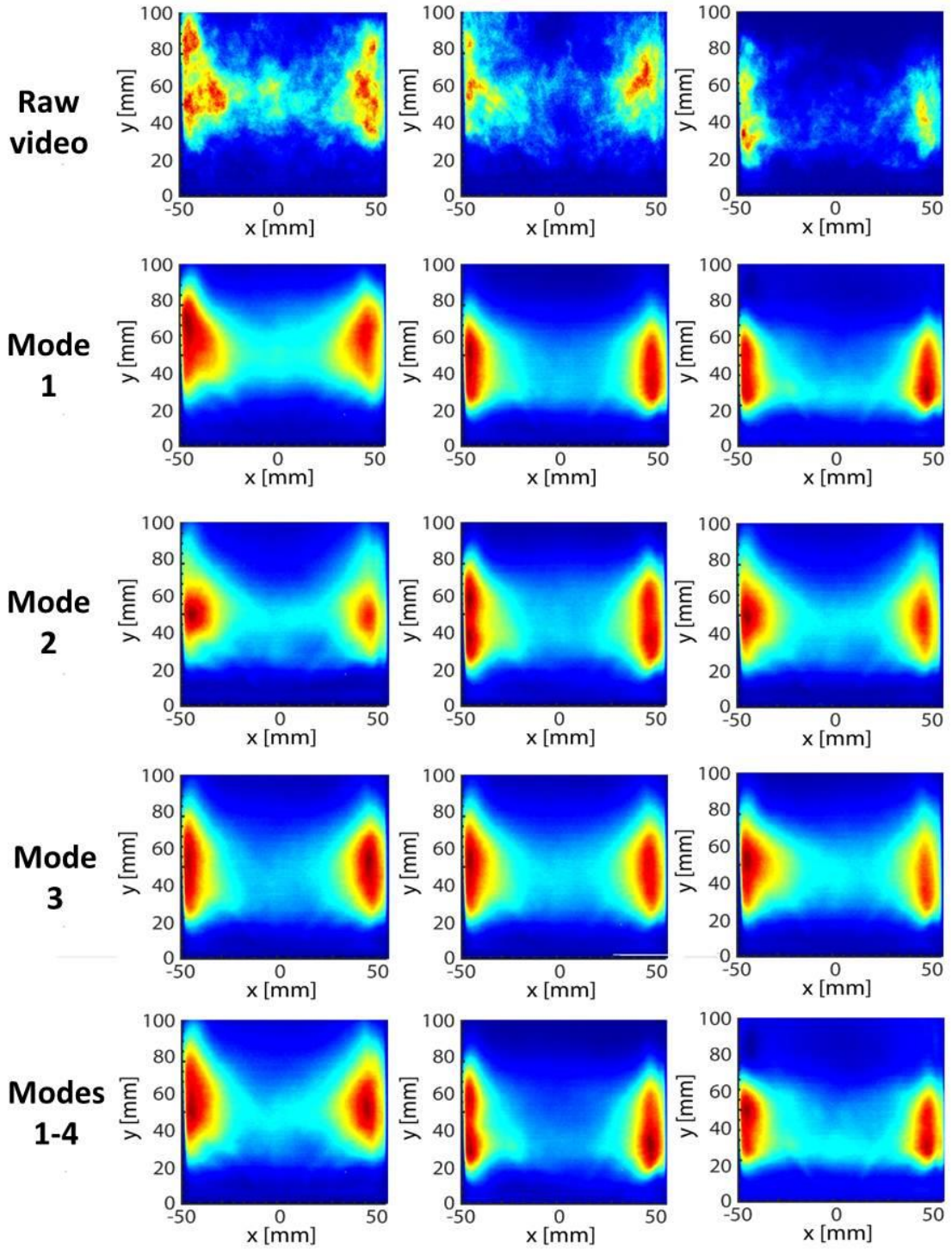

Figure 4-20: Instantaneous OH* chemiluminescence images (first row), and snapshots at the same times from reconstructed OH* movie using the mean and Mode 1 only (second row), the mean and Mode 2 only (third row), the mean and Mode 3 only (fourth row) and the mean and Modes 1 to 4 (fifth row) of P-15-070-160-30.

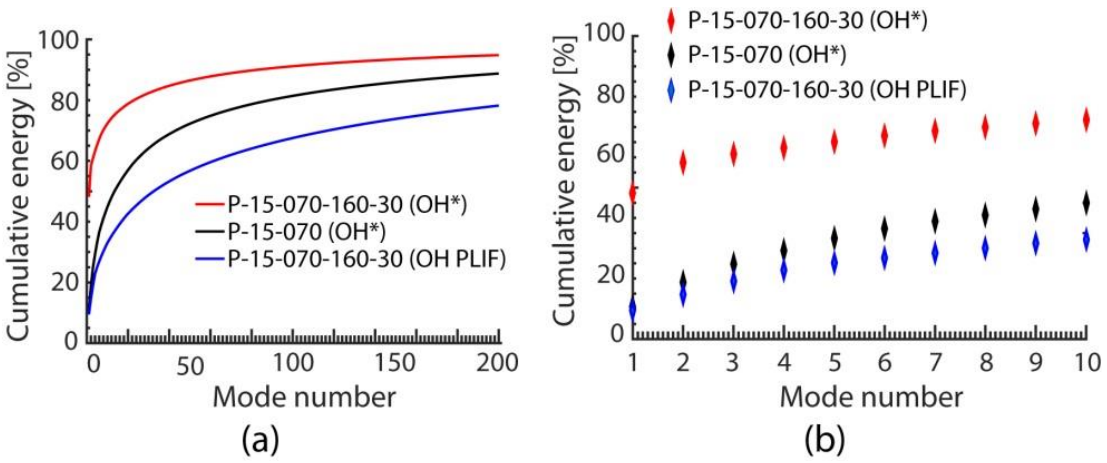

Figure 4-21: Cumulative energy of POD Modes of OH* chemiluminescence of flames P-15-070 (unforced), and P-15-070-160-30 and of OH PLIF POD Modes of flame P-15-070-160-30.

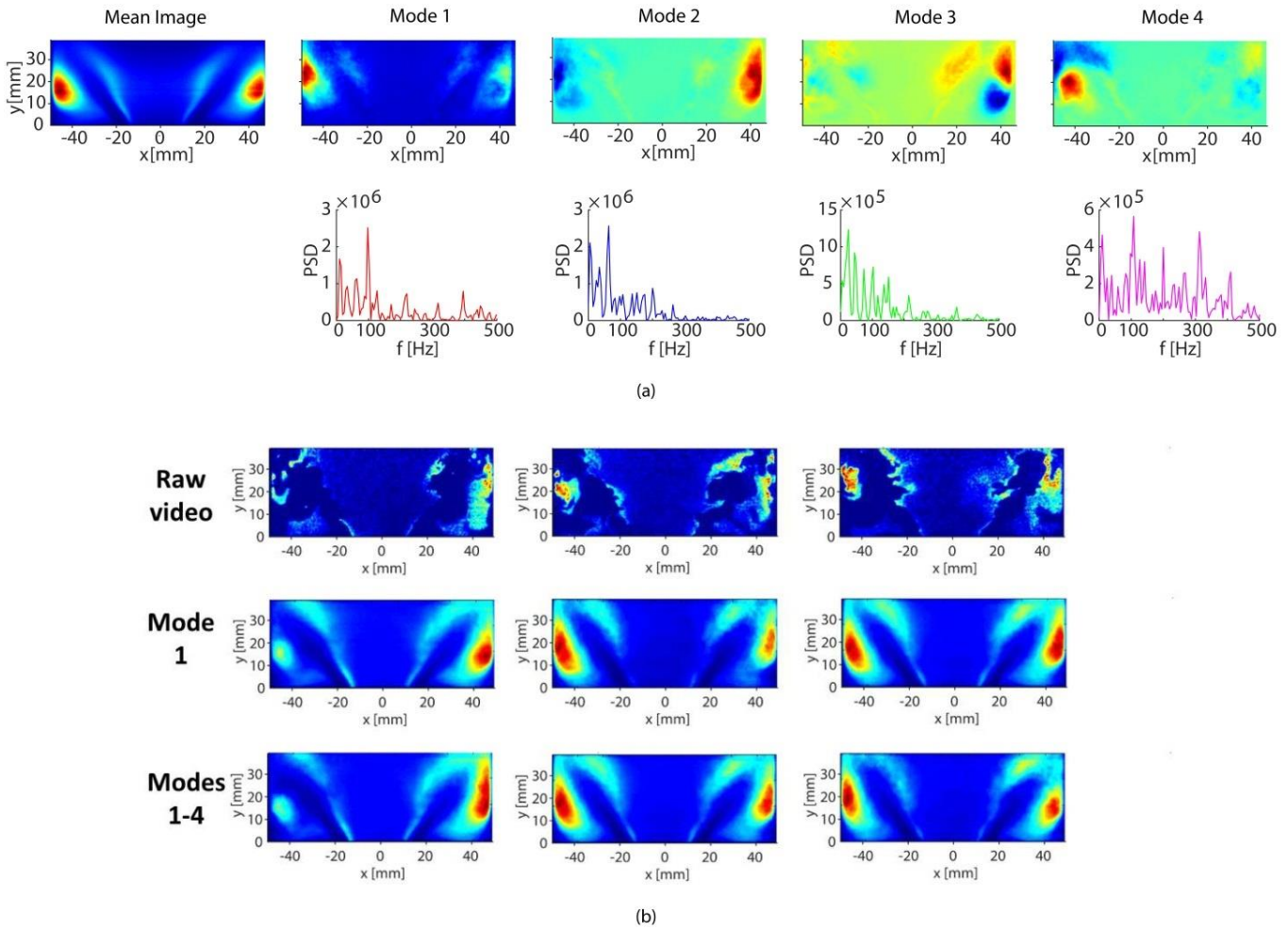

Figure 4-22: (a) Mean Image and first four OH PLIF POD Modes and respective PSD of POD time coefficients. (b) Instantaneous OH PLIF images (first row), and snapshots at the same times from reconstructed OH PLIF movie using the mean and Mode 1 only (second row) and the mean and Modes 1 to 4 (third row). Flame: P-15-070.

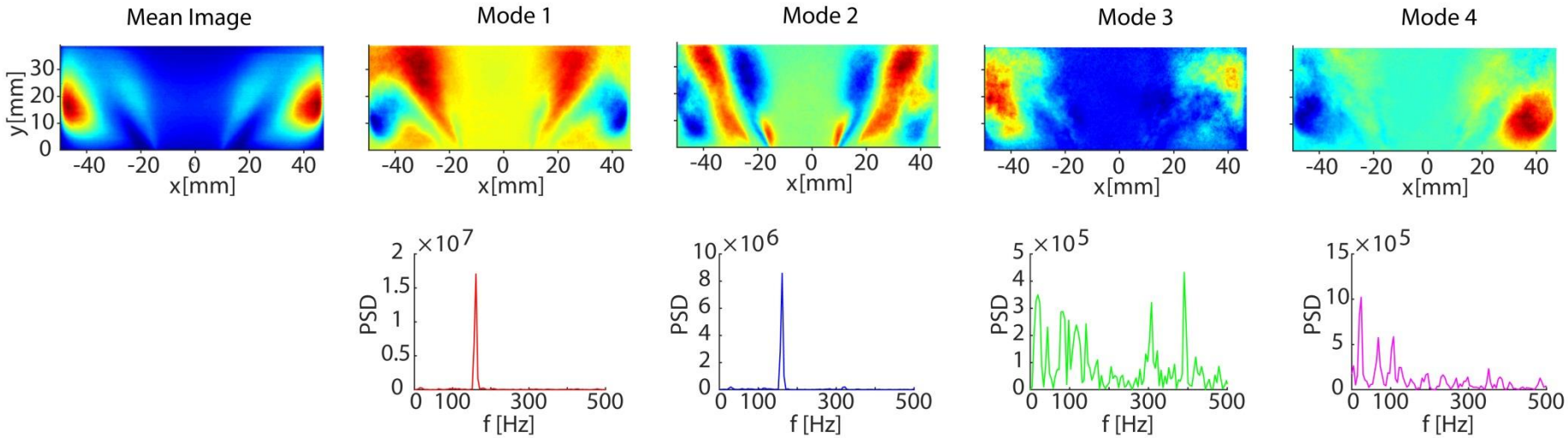

Figure 4-23: Mean Image and first four OH PLIF POD Modes and respective PSD of POD time coefficients of P-15-070-160-30.

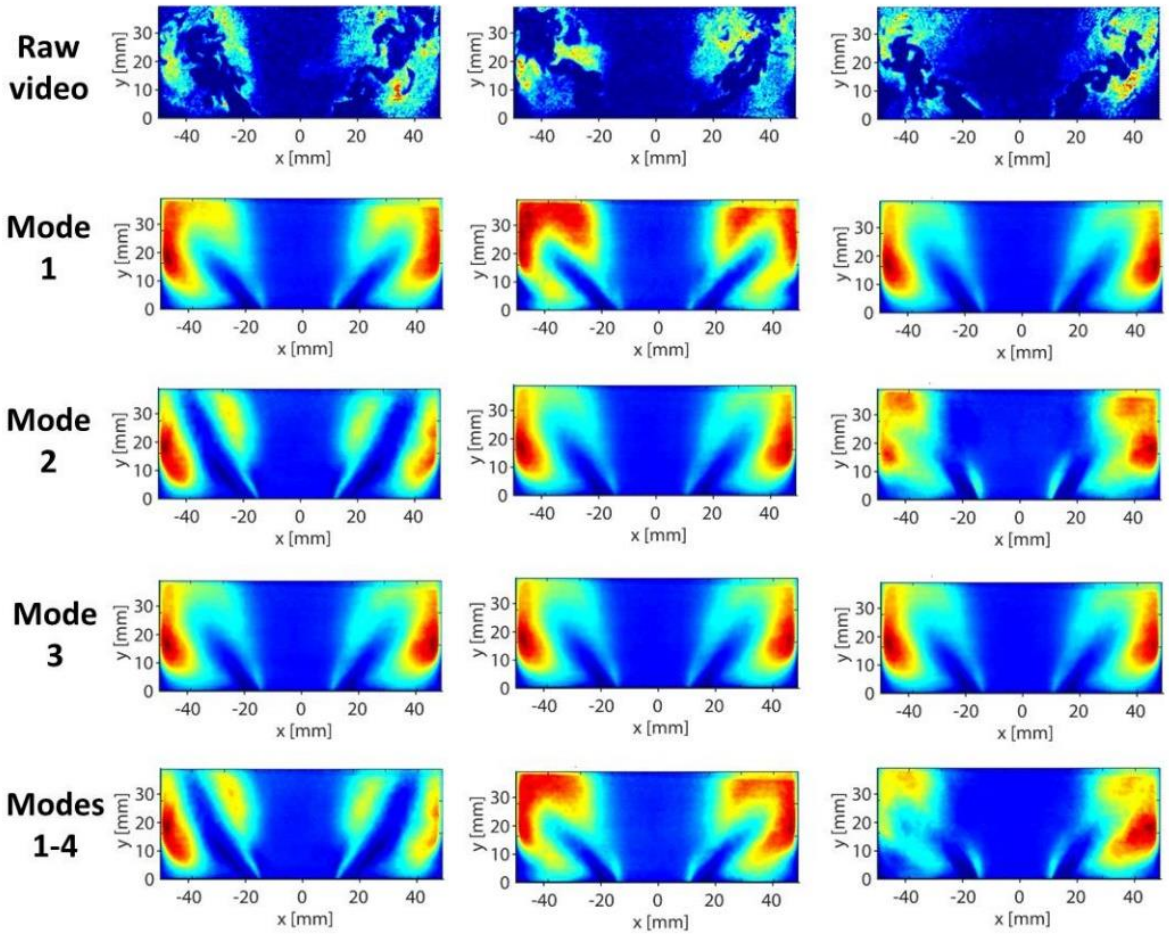

Figure 4-24: Instantaneous OH PLIF images (first row), and snapshots at the same times from reconstructed OH PLIF movie using the mean and Mode 1 only (second row), the mean and Mode 2 only (third row), the mean and Mode 3 only (fourth row) and the mean and Modes 1 to 4 (fifth row) of P-15-070-160-30.

4.5 Tables of Chapter 4

Signals	φ (degrees)	$\Delta\varphi$ (degrees)
Total	353	96
ISL	338	81
Top	18	121
ORZ	193	296
u	330	73
Impingement point	257	0

Table 4-1: Phase angle of $OH/<OH>$ peak values for ISL, Top, ORZ regions, velocity signal and impingement point. Flame: P-15-070-160-30.

OH* Chemiluminescence	P-15-070	P-15-070-160-30
Mode	**Energy (%)**	**Energy (%)**
1	10.6	48.2
2	8.2	10.3
3	6.2	2.5
4	4.3	2.3
1-4	29.3	63.3

Table 4-2: POD energy content of the first four OH* chemiluminescence POD Modes of P-15-070 and P-15-070-160-30.

OH PLIF	P-15-070	P-15-070-160-30
Mode	**Energy (%)**	**Energy (%)**
1	6.1	9.5
2	3.9	5.2
3	3.1	4.4
4	2.9	3.8
1-4	16.0	22.9

Table 4-3: POD energy content of the first four OH PLIF POD Modes of P-15-070 and P-15-070-160-30.

5 RESPONSE OF NON-PREMIXED FLAMES WITH RADIAL FUEL INJECTION

In this chapter, the results from the experiments investigating the response of the methane non-premixed flames with radial fuel injection (NPR) are presented. The flow and acoustic conditions at which the experiments were conducted are described in Section 5.1. In Section 5.2, the results of the experiments are presented and discussed. These include a qualitative description of the flame kinematics, based on OH* chemiluminescence and OH PLIF measurements, as well as the estimation of the amplitude dependence of the transfer function. The flame surface density (FSD), calculated from OH PLIF images, was used qualitatively as an indicator of the flame area. Moreover, special attention was given to the study of the effect of different parameters, such as air velocity, global equivalence ratio and forcing amplitude on the flame response, as well as the behaviour of forced flames when the blow off condition is approached. In addition, the results from the Proper Orthogonal Decomposition (POD) analysis are included to give an insight into the basic structures of the flames and their periodicity. Finally, in Section 5.3 the NPR fully premixed flames are compared in terms of their kinematics and response.

5.1 Experimental Conditions

The results presented in this chapter were acquired by conducting experiments using the non-premixed with radial fuel injection (NPR) configuration (Section 2.1.3). The aim of this design was to achieve a degree of premixing that lay between the fully premixed (i.e. no temporal or spatial variation in equivalence ratio) and the non-premixed systems with very large mixture fraction fluctuations at the flame location. The air stream was forced at 160 Hz and at forcing amplitudes up to 50% of the velocity mean value.

The flames studied in this chapter are presented in Table 5-1. The base unforced experimental condition is NPR-15-055 with air velocity U_{air}=15 m/s (U_{air} was defined as the air flow rate divided by the open annular area between the bluff body and the outer duct at the

exit of the burner inlet) and global equivalence ratio φ=0.55. The effect of global equivalence ratio and air velocity on the flame response were also investigated and analysed. As seen Table 5-1, the base case and flame NPR-10-055 when forced at 160 Hz and A=30% are relatively close to blow-off (the air velocity is 93% and 91% respectively of the velocity at the blow-off condition). Flame NPR-15-077-160-30 is farther from blow-off (U_{air}=74%U_B) compared with the base case.

5.2 Results

5.2.1 Effect of Forcing Amplitude on Lean Blow-off Limits

Figure 5-1 shows the lean blow-off limits of forced NPR flames at 160 Hz. In order to determine the blow-off point, for a constant air flow rate and a given forcing amplitude, A, the fuel flow rate was decreased gradually in steps of 0.1 lpm every 40 seconds until blow-off occurred, recording the fuel blow-off flow rate. At each air flow rate, an average fuel blow-off flow rate of 10 individual measurements was calculated. The fuel velocity (U_f was calculated as the fuel flow rate divided by the area of the fuel nozzle exit) at blow-off constitutes the average value of ten blow-off events, while the standard deviation of these measurements normalised by the mean value was approximately 0.03. It should be noted that this low value was made possible because the step of fuel flow rate reduction was very small (0.1 lpm) and a large number of blow-off measurements were conducted. From this figure, it can be deduced that forcing reduces the stability of the flame, which decreases with increasing forcing amplitude. In particular, for a constant U_{air} at blow-off, the greater the forcing amplitude A, the greater the U_f at blow off, whereas for a constant U_f, the greater the forcing amplitude, the lower the U_{air} at blow-off. Also, for a given forcing amplitude A, as the U_f increases, the U_{air} increases. This is consistent with the findings of previous studies on the blow-off behaviour of forced premixed flames [120, 175] as well as with fundamental studies on laminar counterflow diffusion flames [176-178] . It was deduced that the acoustic forcing had a great influence on blow-off equivalence ratios, which was found to depend on the modulation frequency and mixture velocity. In addition, another study on blow-off of forced premixed flames with spatial mixture gradients [123] reported that the blow-off equivalence ratio increased with forcing amplitude for f=100 Hz and f=200 Hz. This was associated with the greater unsteadiness at the flame base, in agreement with the results of Balachandran et al. [23].

Table 5-2 gives an estimation of time scales of different processes for the studied conditions. The timescales in Table 5-2 are estimated using the following equations:

$$T_{conv} = \frac{L_{conv}}{U}$$

where L_{conv} is the distance from the fuel injection point to the bluff body plane.

$$T_{turb} = \frac{L_{turb}}{u'}$$

where the turbulence length scale

$$L_{turb} \sim \frac{0.3\ (D_{out} - D_{in})}{u'}$$

D_{out} = 37 mm is the outer diameter and D_{in} = 20 mm is the inner diameter of flow path and the turbulence velocity scale u' [179]

$$u' = 0.1U$$

$$T_{chem} = \frac{v_{turb}}{{S_L}^2(\varphi = 1)}$$

$$v_{turb} = C.L_{turb}.u'$$

$$C \sim O(0.1)$$

$$T_{diff} = \frac{(D_{out} - D_{in})^2}{D_{turb}}$$

$$D_{turb} = \frac{v_{turb}}{Sc_t}$$

where Sc_t =0.7 is the turbulent Schmidt number [179]

$$T_f = \frac{1}{f}$$

The ratio of convection to turbulent timescale (T_{conv}/T_{turb}) gives an indication of the degree of premixedness of the reactants at the exit of the burner. This ratio is estimated to be around 0.08, which means that convection is faster than turbulent mixing by one order of magnitude. Thus, it could be suggested that the reactant mixture is not fully premixed by the time it reaches the burner exit, leading to a space-varying equivalence ratio. The acoustic oscillations imposed at the inlet result in time-varying velocity field and global equivalence ratio, because the air flow is oscillating, and the fuel flow could in principle oscillate, since the annular gap at the injection point was not choked. The instantaneous fuel flow rate at the annular gap, where the fuel is injected radially is determined by the instantaneous pressure drop across the fuel nozzle. Thus, it could be reasonable to assume that a low air velocity at the bluff body plane would correspond to a high equivalence ratio at the same location, whereas a higher air velocity would correspond to a lower equivalence ratio.

5.2.2 Kinematics of a Forced Non-Premixed with Radial Fuel Injection Flame

For flame NPR-15-055 the mean OH fluorescence signal is concentrated mainly in a thin zone, located in the inner shear layer (ISL) region, suggesting that the flame branches are anchored at the bluff body edge, whereas relatively low OH intensity is observed in the outer recirculation zone region (ORZ). The OH* chemiluminescence image demonstrates that the flame impinges on the wall, close to which the highest heat release is revealed (Figure 5-2). From the comparison between the forced and unforced condition (Figure 5-2 a and b and Figure 5-2 c and d), significant changes are observed in the flame shape. The flame branches in the ISL region of NPR-15-055-160-30 are much thicker than those of NPR-15-055, while the OH seen in the ORZ region of the former is greater than that of the latter flame. For NPR-15-055-160-30 high heat release is observed both in the ISL region and close to the wall. It is worth noting that with forcing the heat release close to the wall is concentrated in a much greater region than that without forcing, extending both downstream and upstream of the point at which the flame (Figure 5-2c).

A sequence of instantaneous OH* chemiluminescence and OH PLIF images show important features of NPR-15-055-160-30 (Figure 5-3). The red arrow demonstrates the point at which the flame branch in the ISL region impinges on the wall, while the heat release extends from this point in both the downstream and upstream directions. The position of this point (called impingement point) during the cycle will be analysed below using phase-averaged OH PLIF contour plots. The OH PLIF images reveal a highly variable behaviour of the OH region with the OH signal intensity varying significantly among the snapshots. The OH zone is

occasionally fragmented in different regions, complete or partial absence of the flame branch in the ISL and/or wall region, and attachment and lift-off at the bluff body edge can be seen (Figure 5-3). Phase-averaged OH* chemiluminescence images show a significant modulation of the flame shape, and specifically a downstream movement of the heat release zone during the acoustic cycle (Figure 5-4). OH* chemiluminescence is a line-of-sight measurement and thus, no individual regions of the flame can be isolated. However, the parts of the images closer to the wall capture mainly the behaviour of the edge of the flame, as they constitute a line-of-sight integration of OH* chemiluminescence emitted only from that part of the flame. This part of the images shows that the flame impinges on the wall, while a change in the flame angle can be seen, which is also revealed more clearly in the phase-averaged OH PLIF images in Figure 5-5. In this figure, apart from the variation in the flame angle, the OH intensity seen at the base of the flame is much greater than that in the downstream part of the flame or in the ORZ region. In particular, between 165 and 240 degrees, during which the flame angle is relatively small, high OH intensity is observed at the base of the flame, whereas the OH intensity in the downstream region is much lower. The OH intensity in the downstream region increases with the increase in the flame angle (i.e. between 255 and 360 degrees). During the acoustic cycle the flame angle varies between approximately 33 and 47 degrees (Figure 5-6). The maximum value is revealed at 0 degrees and the minimum at 225 degrees.

In Figure 5-7, the local response of the flame at the forcing frequency is quantified based on OH PLIF images. The variance and thus, the level of OH fluctuations associated with the whole frequency range (0-500 Hz), is the greatest in the near wall region. The metric of local flame sensitivity to the forcing frequency, R_L, defined in Section 2.3.3.3, is greater in the branches of the flame in the ISL region, downstream of the annular air passage than in the other parts of the flame. In particular, in the ISL region, R_L is much greater between the bluff body edge and 20 mm downstream than at greater heights. This could probably be explained by the fact that the velocity fluctuations are expected to be stronger close to the annular air passage than in the downstream locations of the combustion chamber. R_L is low in the ORZ region and downstream of the bluff body.

To investigate the behaviour of the various parts of the flame to forcing, the $OH/< OH >$ phase-averaged variation of the main flame regions (see Section 2.3.3.4) is presented in Figure 5-8, from which the sequence of the OH intensity peaks in the ISL-Top-ORZ regions (Table 5-3) is estimated using the impingement point as a reference. The phase difference of the $OH/< OH >$ peak between the ISL and Top region is 70 degrees, whereas the peak in the ORZ is delayed 242 degrees with respect to that in the Top region. The flame angle variation

during the cycle (Figure 5-6) is almost in phase with the $OH/<OH>$ variation in the Top region, suggesting that as the flame angle increases, the OH in the Top region also increases. $OH/<OH>$ in the ISL region and angle variation have a phase difference of approximately 60 degrees. From Figure 5-8, it can be seen that even though relatively high OH fluctuations are revealed in the individual regions, a low $OH/<OH>$ variation is observed in the total OH PLIF window. This can be explained by the phase difference observed among the $OH/<OH>$ curves of the different regions, which has an evening out effect.

All the figures concerning phase-averaged variation are plotted using the sinusoidal forcing signal as a reference, i.e. at 0 degrees the forcing signal is zero and at 90 degrees the forcing signal is maximum. Concerning the impingement point position, a sinusoidal axial movement is observed (Figure 5-9) with the peak revealed at 300 degrees (black arrow) and the trough at 120 degrees. The velocity fluctuations (Figure 5-8) exhibit a sinusoidal trend with the peak revealed at 270 degrees. The phase difference between the peak of the velocity signal and the impingement point peak is 30 degrees, while the $OH/<OH>$ in the ORZ is almost in phase with the velocity signal.

5.2.3 Effect of Air Velocity, Global Equivalence Ratio and Forcing Amplitude

After the description of the kinematics of the base case NPR-15-055-160-30, it is important to investigate the influence of global equivalence ratio, air velocity and forcing amplitude on the flame response. For this purpose, conditions NPR-15-070-160-30, NPR-10-055-160-30 and NPR-10-055-160-50 (Table 5-1) were selected to discuss the most striking differences.

As far as global equivalence ratio is concerned, the comparison between NPR-15-055-160-30 and NPR-15-070-160-30 (Figure 5-2b and Figure 5-10a) shows a change in the mean flame shape. In particular, NPR-15-055-160-30, which is closer to blow-off than NPR-15-070-160-30, reveals relatively high heat release both in the ISL and the near wall regions. The mean OH PLIF image also demonstrates high OH in these parts of the flame. However, in NPR-15-070-160-30, the highest mean heat release is revealed in the near wall region, while it is particularly low up to approximately 17 mm from the bluff body plane. The mean OH PLIF image shows clearly that the OH in the ORZ is significantly greater than that in the ISL region. Also, NPR-15-055-160-30 is approximately 40 mm shorter than NPR-15-070-160-30. The above suggests that the influence of global equivalence ratio on flame response is important, since it affects the location of the main heat release zones. For NPR-10-055-160-30, the highest mean heat release (Figure 5-10b) appears close to the wall, whereas, unlike NPR-15-055-160-

30 (Figure 5-2b), relatively low heat release is revealed close to the bluff body edge. Also, NPR-10-055-160-30 is around 30 mm shorter than NPR-15-055-160-30. Finally, NPR-10-055-160-30 and NPR-10-055-160-50 (Figure 5-10b,c) have a similar overall mean flame shape.

From OH* chemiluminescence and OH PLIF snapshots (Figure 5-11) of NPR-15-070-160-30, high heat release is observed close to the wall, while the OH PLIF images show wrinkling along the flame front, as well as the formation of a vortex-like OH structure at the base of the flame. Also, the OH zone is less fragmented than that of NPR-15-055-160-30 (Figure 5-3), while attachment and lift-off at the bluff body edge can be seen.

Phase-averaged OH* chemiluminescence images (Figure 5-12) demonstrate a change in the shape of NPR-15-070-160-30 during the cycle, with the main heat release appearing in the downstream region close to the wall. Concerning the influence of the global equivalence ratio, the peak-to-peak variation between the trough and the peak value of the heat release cycle is greater for NPR-15-070-160-30 than that of NPR-15-055-160-30 (Figure 5-13). In fact, $<Q'/< Q >$ (Section 2.3.1) is 49% and 37% for the former and the latter flame respectively.

In order to better understand the cyclic OH* chemiluminescence behaviour of these flames, four main regions of the OH* chemiluminescence image were selected: a) 0-20 mm (lower 20 mm), b) 20-40 mm (middle 20 mm), c) 40-60 mm (upper 20 mm) and d) total 0-60 mm bands, downstream of the bluff body plane. In each region, $Q(t)/< Q >$ was calculated: a) the OH* chemiluminescence signal of a 5,000-image dataset was phase-averaged at 15 degrees with respect to the forcing signal, b) Each of the phase-averaged images corresponding to the studied region was integrated spatially and c) this quantity was then normalised with the time-averaged value (Figure 5-12). For NPR-15-055-160-30, the heat release variation of the various bands is very similar both in amplitude and phase (Figure 5-14a), suggesting that the global heat release response to acoustic forcing is similar with the local heat release response. For NPR-15-070-160-30, the curve of the middle 20 mm-band has a bimodal shape, whereas the lower and upper bands have a unimodal shape (Figure 5-14b). The cyclic $Q(t)/< Q >$ variation of the total 60 mm window, constitutes the result of the evening out-like effect due to the phase difference between the $Q(t)/< Q >$ variation of these 20mm-bands. Figure 5-15 presents the phase-averaged images that correspond to the marked points of the curves of NPR-15-070-160-30 in Figure 5-14b. In the lower 20mm-band (Figure 5-15a), the phase-averaged images show that the flame angle variation is very pronounced, suggesting that it may have a great influence on the distribution of the OH* chemiluminescence signal, especially in the ORZ region. The peak $Q(t)/< Q >$ value is revealed at 225 degrees, at which the flame angle is such that the flame close to the wall takes the lowest position during the cycle. Thus, it could

be suggested that the unimodal shape is attributed mainly to the change in the flame angle. In the upper band, the much greater $Q(t)/< Q >$ variation is probably linked with the pronounced axial flame motion (Figure 5-15c). The peak value at 255 degrees corresponds to the highest downstream position of the flame. In the middle band (Figure 5-15b), at 150 degrees (peak of first mode) high heat release is observed close to the wall, while the flame angle in this window is almost negligible. At 240 degrees (peak of second mode) the flame angle is clearly defined, implying that the second mode is associated with the flame angle variation. The trough at 195 degrees, shows features from both the aforementioned mechanisms, suggesting that at this point the two mechanisms are balancing each other. Therefore, the bimodal shape of the middle 20mm-band, implies that the heat release response in this region has contributions through two kinematic mechanisms: the axial flame motion (first mode) and the change in the flame angle (second mode). Based on the above, it is evident that the global heat release modulation is determined by the balance between the fluctuations in local heat release by the axial motion and the angle variation. The axial flame motion was also observed in previous studies, which investigated the response of imperfectly premixed ethylene flames to acoustic forcing at 160 Hz [23]. It was suggested that the flame response was dominated by the vortex roll-up and shedding, which was more pronounced than the vortex-like structures observed in the present results, mainly due to the absence of swirl.

The phase-averaged OH PLIF images of NPR-15-070-160-30 (Figure 5-16) show clearly the flame impingement on the wall and the flame angle variation. Unlike the OH intensity at the base of the flame, which is relatively high for all phase angles, the OH intensity in the downstream part of the ISL region has a different behaviour. In this region, the OH intensity and thickness varies during the cycle, leading to different shapes of the mean OH PLIF image. For instance, at 180-210 degrees, which corresponds to a steeper flame angle than that in the other phases, the mean OH intensity in the upper part of the ISL region is relatively low, at 225-315 degrees a gradual increase in the thickness of the mean OH is observed, and at 330-105 degrees the thickness of the mean OH decreases, while the OH intensity between the upper ISL and ORZ regions increases, 'bridging' these two regions. Also, the size and intensity of the OH zone in the ORZ region is modulated during the cycle.

The phase-averaged FSD images of NPR-15-070-160-30 (Figure 5-17) show that the flame area modulation is mainly associated with a change in the angle of the flame front. The cyclic OH* chemiluminescence variation shows a similar phase, but a greater magnitude than the cyclic FSD variation (Figure 5-18). It is worth noting that the cyclic flame angle variation (Figure 5-19) is almost in anti-phase with the FSD variation (the 200-degree phase angle

corresponds to the maximum FSD value and to the minimum flame angle). In fact, the area of the flame front increases as the flame angle became steeper (Figure 5-17). The difference in magnitude (Figure 5-18) suggests that apart from the flame area, other mechanisms might also contribute to the heat release modulations.

The evolution of flame NPR-10-055-160-30 (Figure 5-20 and Figure 5-21) is similar with that of NPR-15-055-160-30 (Figure 5-4 and Figure 5-5). NPR-10-055-160-30 is close to blow-off (U_{air}=91% of U_B), but with the increase in forcing amplitude the flame further approaches blow-off. The phase-averaged OH* chemiluminescence and OH PLIF images of NPR-10-055-160-30 (Figure 5-20 and Figure 5-21) and NPR-10-055-160-50 (Figure 5-22 and Figure 5-23) reveal a similar behaviour, however in the latter flame, both heat release and OH intensity are significantly reduced. The OH intensity in the ORZ is relatively low, while high OH is only observed at the base of the flame. It is worth noting that a vortex-like OH* chemiluminescence structure is formed at the bluff body edge and is convected downstream between 270 and 360 degrees (Figure 5-22). During the acoustic cycle, the angle of NPR-15-070-160-30 varies between 36 and 53 degrees (Figure 5-19), while the angle modulation of NPR-10-055-160-30 and NPR-10-055-160-50 is very similar (23-44 degrees and 21-44 degrees respectively) (Figure 5-24).

The time series of OH* (PMT) and the corresponding inlet velocity measurements are investigated. For NPR-15-070-160-30, the global OH* signal exhibits a nearly sinusoidal response with small variations in amplitude (Figure 5-25a). The distortion of the waveform, suggests a strong response at a harmonic frequency, while the velocity signal does not show any significant harmonic contents. In fact, the power spectrum of the OH* chemiluminescence signal reveals one dominant peak at 160 Hz, a smaller -by one order of magnitude compared with that at 160 Hz- peak at 320 Hz, and a very small peak at the second harmonic at 480 Hz (by two orders of magnitude smaller than that at 160 Hz). The OH* chemiluminescence snapshots (Figure 5-11) demonstrate the oscillatory motion of the flame, without any evidence of isolated flame regions. However, the OH* signal of NPR-15-055-160-30 (Figure 5-25b) reveals a large distortion of the waveform, with regions of the heat release cycles reaching very high and low values, but with the heat release remaining nonzero throughout the cycle. The velocity signal is almost a pure sinewave. This suggests that the heat release response is not subject purely to the forcing frequency at 160 Hz, but multiple frequencies are involved. The power spectrum of the OH* signal exhibits one dominant peak at 160 Hz, a smaller peak at 20 Hz, which is of the same order of magnitude with the dominant one, and other very small peaks in the range of 20-160 Hz. The irregular variation of the heat release of NPR-15-055-160-30 is

explained by the instantaneous OH* chemiluminescence images (Figure 5-3a), which as described in Section 5.2.2, revealed a great variation of the heat release, during which isolated flame regions could be also observed, but without the flame blowing out completely during the cycle. Therefore, the reduced response of NPR-15-055-160-30, compared with that of NPR-15-070-160-30, is associated mainly to the fact that the flame is very close to the blow-off condition, which results in an increased chaotic radial flame motion and possibilities of local extinctions.

The influence of forcing amplitude on the OH* chemiluminescence time series of NPR-10-055 is examined (Figure 5-26). At A=0.2, a small distortion of the waveform is observed (Figure 5-26a), while the PSD exhibits a dominant peak at 160 Hz, and two smaller peaks at 24 Hz and 320 Hz. It is interesting to note that at A=0.5 the PSD reveals a dominant peak at 160 Hz, and smaller peaks at 6 Hz and 30 Hz, however no peak at 320 Hz can be seen. The increase in A, results not only in a nonlinear increase in the peak-to-peak values of the OH* chemiluminescence signal (Figure 5-26), but also in a greater variation of the heat release signal amplitude through the cycle, reaching values that are much greater or lower than the mean. Concerning the 6 Hz frequency, the phase-averaged OH* chemiluminescence images at 6 Hz show a chaotic radial flame motion, revealed in the form of isolated high heat release regions on either side of the flame (Figure 5-27). In order to check that this chaotic radial flame motion is associated with the frequency at 6 Hz, phase-averaged OH* chemiluminescence images at 59 Hz are presented. In this case, the flame shape does not change greatly during the cycle. The above findings are consistent with the fact that during the experiments a violent chaotic radial flame motion was observed when the flame was close to blow-off. In order to investigate in more depth the mechanism associated with the frequency 6 Hz, image recording for a much longer duration, such that to capture a sufficient number of cycles at this frequency, is necessary. The low frequency peaks that were exhibited when the flame was approaching blow-off were previously observed [180] and were associated with the increased unsteadiness close to blow-off. High-speed imaging revealed near total flame extinction, followed by reignition events, the occurrence and duration of which (a few milliseconds) increased when blow-off was approaching [180].

Concerning the local response of the flame at the forcing frequency, for NPR-15-070-160-30, R_L takes the greatest values in the ISL region, downstream of the annular passage (Figure 5-28a). Specifically, R_L is much greater between the bluff body edge and 20 mm downstream, than that at greater heights. Unlike NPR-15-055-160-30, R_L is relatively high also in the ORZ region, because of the penetration of unburnt reactants to the ORZ. Adjacent on

both sides of the high R_L values in the ISL zone, zero-value regions can be seen. A zero value, either reflects the absence of OH, or it indicates that zero OH fluctuations at the forcing frequency are revealed. In this case, taking into account the phase-averaged OH PLIF images and the angle variation during the cycle, which changes between 36 and 53 degrees (Figure 5-16 and Figure 5-19 respectively), it could be speculated that these zero-value regions constitute the extremes on either side of the flame angle variation region, between which the flame angle is modulated during the cycle. In addition, R_L takes high values in the regions adjacent to the aforementioned zero-value locations, which are possibly part of the inner and outer recirculation zones and might be associated with the penetration of unburnt reactants. Relatively high R_L values are also observed in similar locations for NPR-15-055-160-30 (Figure 5-7), but they are less pronounced. For NPR-10-055-160-30 (Figure 5-28b) very high R_L values are observed along the ISL region which, unlike the previous cases, they extend up to the top of the OH PLIF window. The zero-value region pattern, defining the boundaries between which the flame angle varies, as described above, can be seen, however it is less pronounced than in the previous cases. From these observations, it seems that for NPR-10-055-160-30 the 160 Hz forcing is 'felt' globally by the flame. Flame NPR-10-055-160-50 (Figure 5-28c) exhibits a similar pattern, however R_L takes lower values in the ISL region, which is expected due to its proximity to blow-off. In the aforementioned flames, the total variance, determining the OH fluctuations in the frequency range of 0-500 Hz, is the greatest in the near wall region.

As far as the individual parts of the flame are concerned, for NPR-15-070-160-30 (Figure 5-29), the phase difference of the $OH/< OH >$ variation between the ISL and Top region is 87 degrees, whereas the signal in the ORZ is delayed 163 degrees with respect to that in the Top region (Table 5-4). The $OH/< OH >$ in the ISL region (Figure 5-29) and the angle variation (Figure 5-19) have similar phases during the cycle. The velocity fluctuations exhibit a sinusoidal trend with the peak revealed at 285 degrees. From Figure 5-30, it is evident that the position of the impingement point exhibits a sinusoidal trend with the peak revealed at 255 degrees and the trough at 80 degrees. The phase difference between the peak of the velocity signal and that of the impingement point is 330 degrees.

Flame NPR-10-055-160-30 is very interesting, because unlike the previous conditions, the curves of the $OH/< OH >$ signal for all regions studied (Figure 5-31a), including the impingement point distance from the bluff body plane cycle variation are very close in both amplitude and phase, with the maximum revealed between 350 and 36 degrees (Table 5-5a). This suggests that the forcing at 160 Hz is 'felt' globally by the flame, which was previously revealed from Figure 5-28b. This behaviour is characteristic of convectively compact flames,

where the flame length is much smaller than the convective wavelength [96], and as a result a convective disturbance, such as an equivalence ratio oscillation can be felt globally, leading to heat release disturbances at different locations of the flame being in phase with each other. However, this flame cannot be described as convectively compact, because the convective wavelength is comparable with the time averaged flame length (L=72 mm). For Flame NPR-10-055-160-30 the velocity fluctuations show a sinusoidal trend with the peak exhibited at 220 degrees. The position of the impingement point exhibits a sinusoidal trend with the peak revealed at 23 degrees and the trough at 210 degrees (Figure 5-32a). The phase difference between the peak of the velocity signal and that of the impingement point is 163 degrees.

Comparing the $OH/< OH >$ signal variation of NPR-10-055-160-30 and NPR-10-055-160-50 (Figure 5-31), it is evident that the increase in forcing amplitude leads to greater phase differences between the various parts of the flame (Table 5-5b). Thus, at different forcing amplitudes, the OH signal cycle variation changes in the different regions, so do cancellation effects. For NPR-10-055-160-50, the velocity fluctuations exhibit a sinusoidal trend with the peak revealed at 255 degrees. The position of the impingement point exhibits a sinusoidal trend with the peak revealed at 50 degrees and the trough at 230 degrees (Figure 5-32b). The phase difference between the peak of the velocity signal and that of the impingement point is 155 degrees.

For flames NPR-15-055-160-30 and NPR-15-055 (base case), the peaks of the probability density functions PDFs of the lift-off heights reveal that 32% and 36% respectively of the samples exhibit a lift-off height of around 0.8 mm, with the average lift-off height being 2.2 mm and 1.3 mm respectively (Figure 5-33). The lift-off of the forced flame shows small periodicity at 160 Hz, because apart from the peak at 160 Hz, many noisy peaks are also revealed in the PSD (Figure 5-34). Far from blow-off, flames NPR-15-070-160-30 and NPR-15-070 show a similar average lift-off height ($\bar{h}$=1.9 mm and $\bar{h}$=1.8 mm respectively), suggesting that forcing hardly affects the lift-off behaviour of the flame far from blow-off. The peaks reveal that 26% and 19% respectively of the samples exhibit a lift-off height of approximately 1.5 mm. The lift-off exhibited by the forced flame shows a slight periodicity at 160 Hz and at 320 Hz, as concluded by the fact that in PSD of the lift-off height (Figure 5-34), apart from these peaks, more dominant peaks are observed at lower frequencies. The reduced periodicity of this flame is expected, since from the PDF it was evident that forcing has a negligible impact on the lift-off behaviour of the flame. While NPR-10-055 is less lifted than the other unforced cases (average lift-off height h=0.9 mm), NPR-10-055-160-30 and NPR-10-055-160-50 are lifted more than all other forced flames and specifically, the lift-off height of

the latter flame, which has the highest forcing amplitude, is significantly more pronounced than that of the other flames (average lift-off heights $\bar{h}$=2.7 mm and $\bar{h}$=4.4 mm respectively). This implies that the greater the destabilisation of the flame (as the flame approaches blow-off) with the increase in forcing amplitude, the greater the lift-off heights observed. Concerning the peaks of the PDFs, for NPR-10-055, 25% of the samples show a lift-off height below 0.4 mm, while for NPR-10-055-160-30 and NPR-10-055-160-50, 35% and 27% of the samples reveal a lift-off height below 0.4 mm. In case of NPR-10-055-160-30 and NPR-10-055-160-50, the lift-off periodicity at the forcing frequency is very pronounced, especially at the greater forcing amplitude, as in both flames the lift-off spectrum shows a dominant peak at 160 Hz (Figure 5-34). The phase-averaged lift-off height of flames NPR-15-055-160-30, NPR-10-055-160-30 and NPR-10-055-160-50 exhibit a sinusoidal shape (Figure 5-35). Also, NPR-15-055-160-30, NPR-10-055-160-30 and NPR-10-055-160-50 have longer positive tails than the respective unforced cases. The PDFs of NPR-15-070-160-30 and NPR-15-070 reveal the shortest positive tails (up to around 4 mm). From the above analysis, it is suggested that the forced flames tend to have increased average lift-off heights compared to the unforced.

5.2.4 Amplitude Dependence of the Flame Response

Following the previous analysis on the flame kinematics at a specific forcing amplitude (A=30% or A=50%), the overall flame response as a function of forcing amplitude is presented below for NPR-15-055, NPR-10-055 and for NPR-15-051 and NPR-10-46, which are closer to blow-off than the former flames.

The results suggest that the heat release response of the NPR flames to the inlet forcing amplitude is very high with the maximum value being approximately 46% for NPR-10-055 (Figure 5-36). Concerning the base case, NPR-15-055, $<Q'/<Q>$ increases linearly with A up to $A{\sim}10\%$, and subsequently it continues rising but with a reduced slope, until it starts saturating at $A{\sim}33\%$. For NPR-10-055, $<Q'/<Q>$ increases linearly with A up to $A{\sim}16\%$, then it continues rising with an increased slope up to $A{\sim}32\%$, and afterwards it increases further but with a reduced slope, until it stabilises at $A{\sim}46\%$. It is interesting to observe that between $A = 46\%$ and $A = 53\%$, the $<Q'/<Q>$ values oscillate around $<Q'/<Q> = 43\%$. During the experiments, it was observed that the amplitude A at which the normalised heat release started oscillating coincided with the initiation of a chaotic radial flame motion, which became more intense with the further increase in A, indicating that the flame was gradually approaching blow-off. Comparing the heat release response of NPR-15-055 and NPR-10-055, the response of the former flame is greater than that of the latter. In particular, at low A both flames have a

similar response, then between A=6-16% the difference in their response increases, and subsequently it gradually decreases until the two curves meet at A=35%. The heat release response of NPR-15-051 and NPR-10-046, which are closer to blow-off than the other flames, is very similar with that of NPR-15-055. $<Q'/<Q>$ increases almost linearly with A, until blow-off occurs around A=18%. The most striking feature of the aforementioned curves is that they exhibit a similar gradient before their deviation from linearity, implying the low sensitivity of the system towards a change in the operating conditions.

The NFTF of NPR-15-055 decreases gradually from approximately 1.9 to 1.2, having a similar slope with that of NPR-15-051 and NPR-10-046, the NFTF of which reduces from 1.9 to 1.6 and from 1.8 to 1.3 respectively (Figure 5-36b). The NFTF of NPR-10-055 has a decreasing trend up to $A\sim$16%, where it levels off, while at $A\sim$32% it starts decreasing again. The NFTF values vary between 1.52 and 0.66. NPR-15-055 exhibits a greater reduction in NFTF compared with that of NPR-10-055, with the NFTF of the former decreasing from 1.89 (A =4%) to 1.16 (A=35%), and that of the latter decreasing from 1.52 (A=6%) to 1.1 (A=35%). Concerning the NFTF phase (Figure 5-36c), small changes are observed with the forcing amplitude. In particular, for NPR-15-051 and NPR-10-046 the phase slightly increases almost linearly with A, whereas for NPR-15-055 and NPR-10-055 it exhibits an increasing trend, followed by a slight decrease.

The harmonic frequency content at 320 Hz of the heat release signal, despite the fact that the velocity signal did not show any significant harmonic contents (as described in Section 5.2.3), results in a nonlinear heat release response. In order to better understand this nonlinear behavior, the inlet velocity measurements were analysed to determine the amount of harmonic content. An almost linear increase in harmonic content at 320 Hz is observed with the increase in forcing amplitude (Figure 5-37a). However, the ratio of heat release fluctuation at the first harmonic frequency to that at the forcing frequency (Q'_h/Q') with respect to forcing amplitude shows a highly nonlinear variation (Figure 5-37b). This relative response to 320 Hz increases linearly up to A=16%, after which it decreases also linearly until A=0.29. Then the proportional harmonic response stays almost constant up to A=0.46, while a sudden increase is observed at A=49%, after which it decreases again. At A=16%, which is the forcing amplitude at which the peak of the relative response to 320 Hz is revealed, the normalised heat release response (Figure 5-36a) exhibits a deviation from linearity. An analysis of the aforementioned relative response at 320 Hz, based on fully premixed bluff body stabilised ethylene flames [40], showed similar trends. In particular, the peak of the relative response was observed at A=15%, and it was also linked with a nonlinearity in the normalised heat release. A deviation from linearity at A=15%

was also observed in previous studies based on forced turbulent premixed flames [158, 174], where it was speculated that it was due to a non-linear evolution of flame surface area, and the need for optical measurements was suggested for this to be confirmed. Balachandran et al. [40] suggested that this nonlinearity occurred with the appearance of flame roll up, which is also the case in this study with the difference that the vortex-like OH* chemiluminescence structure is less coherent due to the high swirl. Therefore, it could be conjectured that the response to the harmonic frequency was suppressed with the appearance of the aforementioned vortex-like structure. In addition, at A=49%, when the peak of the relative response is revealed, the normalised heat release (Figure 5-36a) exhibited a drop. From the above analysis, it can be deduced that the large distortion of the waveform at greater A is due to the presence of other frequencies, apart from the forcing frequency, in the heat release signal. At greater A, a greater variation of the heat release is observed, while isolated parts of the flame are seen more frequently. Also, it is suggested that the nonlinear increase in the heat release with A (Figure 5-36a) is associated with the irregular variation of the amplitude of the heat release signal, observed at higher A, as the flame approaches blow-off. A further nonlinearity occurs close to the blow-off condition, due to the fact that the heat release signal exhibits a periodicity not only at the forcing frequency and occasionally its harmonic at 320 Hz, but also at other frequencies.

5.2.5 Proper Orthogonal Decomposition (POD) Analysis

In this section, the POD results of OH* chemiluminescence and OH PLIF images are discussed. The OH* chemiluminescence POD results presented below consist of the first few modes, the PSDs of POD time coefficients, the instantaneous OH* chemiluminescence images and their reconstruction based only on a small number of modes, as well as the relative cumulative energy content of POD modes. The OH PLIF POD results are also presented in a similar way. The following discussion focuses on: a) the basic structure of the flame extracted from POD, b) its temporal evolution and c) the difference between the forced and unforced flame and d) the estimation of the convection velocity of the most dominant structures of the system.

5.2.5.1 OH* Chemiluminescence POD Analysis

Concerning the spatial structure of the unforced flame NPR-15-055, Mode 1 exhibits a roughly antisymmetric pair of heat release fluctuations, which is characteristic of the left-right motion of the flame (Figure 5-38a), as it is demonstrated by the time evolution of the reconstructed image of Mode 1 with its modal time coefficients (Figure 5-38b). Similar behaviour is also exhibited from the other POD Modes and from the reconstructed images of

the added Modes 1-4. As the POD mode number increases, more details of the flame structure are revealed. These antisymmetric heat release fluctuations cannot be seen easily in the raw OH* chemiluminescence snapshots because of the underlying small-scale fluctuations. The PSD of POD time coefficients of a mode reveals the periodicity associated with the respective motion of the flame. In Figure 5-38a, the PSDs of Modes 1, 2 and 4 exhibit dominant peaks mainly below 50 Hz, while the PSD of the third Mode reveals, apart from the low frequencies, peaks at frequencies greater than 50 Hz.

In terms of spatial features of NPR-15-055-160-30, Modes 1 and 2 show an axial dependence of the flame shape (Figure 5-39), which suggests the axial motion of the flame, as seen by the respective reconstructed images (Figure 5-40). The respective PSDs reveal that 160 Hz is the main frequency content associated with this motion, implying that forcing affects significantly the behaviour of the flame. A relatively small peak is also exhibited at 320 Hz. The shapes of Modes 3 and 4 show a combination of axial and radial heat release variation, which represents an axial and transverse oscillating flame motion (Figure 5-40), while in the PSDs, apart from the main peak at 160 Hz, other peaks -of the same order of magnitude- are also revealed at lower frequencies and at the first harmonic at 320 Hz.

Concerning the POD energy, Figure 5-41 shows that the cumulative energy of the forced flame is greater than that of the unforced, while their energy difference becomes smaller at higher modes. Also, both curves exhibit a much steeper slope at lower mode numbers than at higher modes, as the energy contribution of the first few modes is much larger than that of the successive modes. In particular, the cumulative energy content of the first four Modes of NPR-15-055-160-30 is 48.1%, while that of NPR-15-055 is 25.6% of the total energy. For the former flame the energy content of Mode 1 is 25.6%, whereas for the latter flame it is only 9.6% (Table 5-6). This is attributed to the fact that POD energy is concentrated in a dominant structure, which is shown in the case of the axial motion of the flame, as described previously, while there is lack of such a structure in the unforced case. Also, the first 100 Modes of the forced condition contain 89.0% of the total energy, as opposed to 81.1% of the unforced flame. From the above, it is clear that the effect of forcing on the flame structure is important.

Below, the POD results of NPR-15-070-160-30 are discussed, to evaluate the effect of forcing on the basic structure of the flame and its temporal evolution without the additional contribution of the blow-off kinematics. The shapes of the POD modes of NPR-15-070-160-30 (Figure 5-42) is more well-defined than that of NPR-15-055-160-30, indicating that the flame has stronger features, which is consistent with the stronger response to acoustic oscillations that was discussed in Section 5.2.4. In particular, Modes 1 and 2 reveal a strong axial dependence,

which is characteristic of the pronounced axial flame motion, also demonstrated by the respective reconstructed images (Figure 5-43). Additionally, these images reveal a change in the flame angle, however this will be addressed more clearly in Section 5.2.5.3. The respective PSDs exhibit one dominant peak at 160 Hz, which is much stronger than that of NPR-15-055-160-30, implying the greater influence of forcing on the flame response. Apart from the 160 Hz, a peak at 320 Hz is shown, which is one order of magnitude smaller than that at 160 Hz. The PSD of Mode 3 exhibits one dominant peak at 320 Hz and two much smaller ones at 160 Hz and 480 Hz. Both the respective Mode and the reconstructed image show an outward movement of the flame towards the wall. In Mode 4, a roughly antisymmetric pair of heat release fluctuations is seen, which represents the left-right motion of the flame. The respective PSD shows a peak at 320 Hz, but the signal to noise ratio is much smaller than that of the PSDs in the previous modes.

Concerning the POD energy of NPR-15-070-160-30 (Table 5-6), the energy contribution of Modes 1 and 2 is significantly larger than that of the successive modes (45.8% and 22.4% of the total energy respectively). This implies that the dominant mechanism is captured mainly by the first two modes. In addition, the fact that the cumulative energy content of the first two Modes is almost two times greater than that of the close to blow-off flame NPR-15-055-160-30, suggests that the flame structures that are associated with forcing are much more pronounced when the flame is farther from blow-off. Figure 5-44a shows the cumulative POD energy distribution of the different modes of NPR-15-070 and NPR-15-070-160-30. The slope of these curves is much steeper than that of NPR-15-055 and NPR-15-055-160-30 (Figure 5-41). For NPR-15-070-160-30, 90% of the total energy is captured by the first 32 Modes, whereas the same energy content is contained in 88 Modes in case of NPR-15-055-160-30. Thus, it can be conjectured that the effect of forcing is greater at conditions that are far from blow-off, leading to stronger features of the flame structure than those at a closer proximity to blow-off. On the contrary, close to the blow-off condition, the blow-off kinematics affect dramatically the flame structure and as a result, the influence of forcing on the flame structure decreases. This is an important factor that explains the greater response of NPR-15-070-160-30 than that of NPR-15-055-160-30, shown in Section 5.2.4.

The OH* chemiluminescence POD data of NPR-10-055-160-30 and NPR-10-055-160-50 (not presented here) are similar with that of Flame NPR-15-055-160-30. In both flames, the PSDs of Modes 1 and 2 exhibit a dominant peak at 160 Hz, and the POD modes show a banded shape, which is representative of the axial motion, while in the PSDs of Modes 3 and 4 the 160 Hz peak is not dominant, and many other peaks are revealed. In this case, the POD

modes show an almost antisymmetric structure, which is characteristic of the left-right motion of the flame. The cumulative energy content of NPR-15-055-160-30, NPR-10-055-160-30 and NPR-10-055-160-50 is very similar (Figure 5-44b), suggesting that the effect of forcing on the flame structure is similar.

5.2.5.2 Estimation of Convection Speed

In this section, the convection velocity of the most dominant OH* chemiluminescence structure of NPR-15-070-160-30 is estimated using the OH* chemiluminescence POD method. As described in Section 5.2.5.1, the structure of the first POD Mode reveals a banded shape, which is representative of the axial motion of the flame, and is associated with a dominant peak at 160 Hz. This Mode contains 45.8% of the total POD energy, implying that the dominant mechanism is mainly captured by it. The convection velocity was determined by multiplying the characteristic heat release wavelength, λ, of the first POD Mode, as shown in Figure 5-42, with the dominant frequency (160 Hz), exhibited by the respective PSD of POD time coefficients. Thus, the ratio of the convection velocity to the bulk velocity was estimated to be approximately 0.54. This value is lower than the estimated ratio in the case of the self-excited premixed system (1.40-1.66) and that of P-15-070-160-30 (1.00).

5.2.5.3 OH PLIF POD Analysis

The first OH PLIF POD Mode of NPR-15-055 (Figure 5-45a) shows an antisymmetric OH structure, which corresponds to the left-right oscillating motion (Figure 5-45b), and is associated mainly with a frequency at 38 Hz. The OH in the ISL region forms a thin zone (Figure 5-45b), which suggests that the angle of the flame barely changes. Modes 2, 3 and 4 exhibit more details of this transverse motion, while the PSD reveals many frequencies, the most dominant of which are: 88 Hz (Mode 2), 49 Hz and 5 Hz (Mode 3), and 38 Hz (Mode 4). The time evolution of the reconstructed images of Modes 1 to 4 with their modal time coefficients also show the left-right flame motion, with the OH in the ISL region being greater than that close to the wall.

Concerning NPR-15-055-160-30, the structure of POD Modes 1 and 2 (Figure 5-46a) consists of an antisymmetric pair of OH close to the wall, and thicker ISL regions than those of the unforced case. The reconstructed snapshots describe the respective flame motion (Figure 5-46b). The periodicity linked with this motion consists of various peaks: 5 Hz, 38 Hz, 160 Hz (Mode 1) and 10 Hz, 107 Hz, 160 Hz (Mode 2). In addition, Mode 3 shows a similar structure with that revealed by Figure 5-7, which seems to be characteristic of the flame angle variation, as is also shown in Figure 5-46b. In particular, the maximum OH zones, observed at the base

of the bluff body in the ISL and ORZ regions of the POD Mode, probably indicate the extremes between which the flame angle is modulated. The respective PSD reveals a dominant peak at 160 Hz, but also two other peaks at 38 Hz and 122 Hz. It is worth noting that the 122 Hz peak constitutes the difference between the forcing frequency at 160 Hz and the frequency at 38 Hz. The peak at 38 Hz was also exhibited by the PSD of Mode 1 of the unforced case. The main features of the reconstructed images of Modes 1-4 are the transverse motion and the angle variation of the flame.

The relative energy contained in the first four OH PLIF POD Modes and the energy distribution in the individual modes are greater in the forced than those in the unforced flame (Table 5-7). This is attributed to the fact that the energy is concentrated in a dominant structure, which is shown in the forced case, as opposed to the lack of such a structure in the unforced flame. In addition, for NPR-15-055-160-30, the cumulative energy contained in the first 50 OH* chemiluminescence POD Modes is greater (82.4%) than that in the respective OH PLIF Modes (68.9%). The reduced energy values of the OH PLIF data suggest that the structures captured by the planar measurement constitute a good representation of those revealed by the line of sight measurement, without capturing fully though all the OH* chemiluminescence features.

For NPR-15-070-160-30, POD Modes 1 and 2 show strong features of the flame structure and are almost purely associated with the forcing frequency (Figure 5-47a). In particular, both modes structure is representative of the angle variation, shown more clearly in the respective reconstructed images (Figure 5-47b). Also, the structure of Mode 2 is similar with that of Figure 5-28a, showing clearly the boundaries between which the angle varies, while a banded shape is exhibited mainly on the right side of the ORZ region, which is typically characteristic of OH fluctuations in the axial direction. The reconstructed images of Mode 2 reveal that the banded shape could be attributed to a change in the size of the circular structure, shown by the OH fluorescence fluctuations in the ORZ region. Also, these images demonstrate that the behaviour of the ISL region is directly related to that of the ORZ region. In fact, when the OH fluctuations in the ISL form a straight zone, the size of the circular structure in the ORZ is big, extending farther downstream than the OH PLIF frame size. On the contrary, a much smaller size is observed when the OH fluctuations on the inner side of the ISL region form an inwardly curved zone. The above behavior of the OH profile could possibly be explained by the speculation that the OH fluorescence signal follows the streamlines of the flow in the inner and outer recirculation zones, the height and width of which could change during forcing, as a result of the change in the aerodynamic profile. This speculation is consistent with the axial

movement of the impingement point, following a sinusoidal trend during the cycle, described in Section 5.2.3. Smoke visualization experiments conducted in previous studies [23] suggested that under some conditions (forcing at 40 Hz) a significant change in the size and width of the central recirculation zone was observed during the cyclic variation. In order to verify with certainty the above speculation, flow field PIV measurements are required. The structure of Modes 3 and 4 shows a combination of transverse motion and angle change features. The PSD of Mode 3 exhibits many noisy peaks with the dominant being at 44 Hz and the PSD of Mode 4 apart from the dominant peak at 160 Hz, shows one peak at 320 Hz and others mainly at lower frequencies. The reconstructed images of the first 4 POD Modes added together reveal all the aforementioned trends, with the most striking features being the flame angle variation and the change in the size of the OH structures in the IRZ and ORZ regions.

The cumulative energy content of flames NPR-15-055-160-30, NPR-10-055-160-30 and NPR-15-070-160-30 is similar, while flame NPR-10-055-160-50 has a greater energy content (Figure 5-48).

5.3 Comparison Between Fully Premixed and Non-Premixed Flames with Radial Fuel Injection

In this Section, fully premixed (P) and non-premixed with radial fuel injection (NPR) forced flames are compared in terms of their kinematics and NFTFs.

Concerning the geometry of the two systems, the main difference was the fuel injection point, thus the aerodynamic profile of both systems was very similar. It could be argued that the Premixed system produced a conventional fully premixed swirl flame, while the NPR system was nominally non-premixed but with a degree of premixing between the fully premixed and the non-premixed systems with very large mixture fraction fluctuations at the flame location. The design of these experiments aimed to study and compare the response to acoustic oscillations of the former system, where there was no temporal or spatial variation in equivalence ratio, with the latter system, where apart from the time-varying velocity field, there was also a time- and space-varying equivalence ratio (the fuel flow could in principle oscillate since the annular gap at the injection point was not choked). The fact that both systems have an almost identical aerodynamic profile is important in the investigation of the effect of equivalence ratio fluctuations on the flame response.

For the flame kinematics discussion, P-15-070-160-30 and NPR-15-070-160-30 are compared. The most striking difference of NPR-15-070-160-30 and P-15-070-160-30 is seen in the inner shear layer (ISL) region downstream of the annular passage, between the bluff body plane and 15 mm downstream (Figure 4-11, Figure 5-28a). In particular, at this zone R_L values are significantly greater in case of NPR-15-070-160-30 than that of P-15-070-160-30. This is attributed to the equivalence ratio modulation through the cycle, since as mentioned above, the fuel injection point constitutes the main factor that differentiates these systems. Another difference of NPR-15-070-160-30 and P-15-070-160-30 is the following: in the NPR system, the greater values of R_L are concentrated in the shear layer zones, mainly closer to the bluff body plane. On the contrary, in P-15-070-160-30, even though the acoustic oscillations are expected to be greater at the burner exit than further downstream, the values of R_L are greater in large regions on the downstream side of the OH PLIF plane than those in the ISL region. In the P-15-070-160-30 system, high R_L values are also seen in the IRZ and ORZ regions. The above could probably be explained by the fact that for P-15-070-160-30, the reaction zone is stronger in the downstream region and close to the wall than in the ISL region, while for NPR-15-070-160-30, the reaction zone in the ISL region is very strong (Figure 5-49). Apart from the aforementioned differences, some similar patterns are observed, the most prominent being the R_L zero-value regions, adjacent on both sides of the ISL zone (Figure 4-11, Figure 5-28a). The

above pattern is also revealed in the second OH PLIF POD Mode of P-15-070-160-30 and NPR-15-070-160-30 (Figure 4-23 and Figure 5-47a respectively), implying that the respective characteristics that it represents constitute one of the most dominant mechanisms of the flame kinematics of both systems.

For both P-15-070-160-30 and NPR-15-070-160-30, the $OH/< OH >$ variation shows many similarities, especially in the Top and ORZ regions. The phase difference of $OH/< OH >$ variation between the Top and the ORZ regions is similar in both P-15-070-160-30 and NPR-15-070-160-30 flames (175 and 163 degrees respectively) (Figure 4-12 and Figure 5-29). Also, the impingement point variation with respect to phase showed a similar trend in both flames, which was also the case with the flame angle variation during the cycle. In addition, the angle variation and the $OH/< OH >$ in the ISL region were almost in phase during the cycle. However, the main difference observed in Figure 5-29 and Figure 4-12 is that the phase difference of $OH/< OH >$ variation between the ISL and Top region is much greater for NPR-15-070-160-30 ($\Delta\varphi$=87 degrees) than that for P-15-070-160-30 ($\Delta\varphi$=40 degrees). This greater $\Delta\varphi$ of the NPR system could probably be associated with the fact that in that system the reaction zone is stronger in the ISL region closer to the bluff body plane than further downstream due to the cyclic variation of equivalence ratio.

Figure 5-50 suggests that the peak-to-peak variation between the trough and the peak value of the heat release cycle is greater for NPR-15-070-160-30 than that of P-15-070-160-30. In fact, $<Q'/< Q >$ is 49% and 29% for the former and the latter flame respectively. Also, the phase difference between $<Q'/< Q >$ and u is approximately 30 and 120 degrees for NPR-15-070-160-30 and P-15-070-160-30 respectively (Figure 5-50).

For Flame P-15-070-160-30, the phase-averaged OH* chemiluminescence variation agrees relatively well with the FSD variation, with a small difference in amplitude and phase (Figure 5-51). This suggests that in the fully premixed system, the heat release modulation is mainly through flame surface area modulation. It should be noted that the slight difference in the phase and amplitude between the FSD and OH* chemiluminescence for P-15-070-160-30, might also be attributed to increased wrinkling in the third dimension, due to the presence of the strong swirl. The cyclic FSD variation of NPR-15-070-160-30 and P-15-070-160-30 is very similar in amplitude and phase, with the maximum value revealed at around 200 degrees (Figure 5-51). Also, in both conditions the cyclic flame angle variation was almost in anti-phase with the FSD variation, with the minimum angle exhibited at approximately 200 degrees (Figure 4-8 and Figure 5-19). In fact, as shown in Figure 5-17, the area of the flame front increased as the flame angle became steeper. The agreement between the FSD variation of both flames, implies

that the flame area modulation mechanism, and how it is influenced by the change in the flame angle, are common in both the Premixed and NPR systems. Since both systems have a similar geometry and hence, almost identical aerodynamic profiles, it could be speculated that the flame area modulation is mainly dependent on the time-varying velocity field, while the effect of equivalence ratio fluctuations on the flame area seems to be of smaller importance. For NPR-15-070-160-30, the cyclic OH* chemiluminescence variation shows a similar phase, but a greater magnitude than the respective FSD variation. This difference in magnitude is mainly attributed to the equivalence ratio fluctuations constituting an important mechanism of the NPR system. The similar phase suggests that this contribution of the equivalence ratio fluctuations to the heat release modulation is mainly in the magnitude and less in phase. Therefore, from the above analysis it can be conjectured that in the NPR system both the flame area and the equivalence ratio modulations constitute important mechanisms of the heat release modulations.

NPR-15-070-160-30 and P-15-070-160-30 exhibit a significantly different lift-off behaviour. From the PDF of the lift-off height (Figure 5-52a), it can be seen that the average lift-off height of NPR-15-070-160-30 is $\bar{h}$=1.9 mm, while the peak demonstrates that 26% of the samples exhibit a lift-off height approximately at 1.5 mm. Also, the PDF of NPR-15-070-160-30 reveals a short positive tail (up to around 4 mm). The lift-off exhibited by NPR-15-070-160-30 shows a slight periodicity at 160 Hz and at 320 Hz. The average lift-off height of flame P-15-070-160-30 is much lower ($\bar{h}$=0.68) than that of NPR-15-070-160-30. It should be noted that the average lift-off height of the premixed flames is lower than that of the respective NPR conditions. The PDF of P-15-070-160-30 shows that approximately 50% of the samples exhibit a lift-off height below 0.13 mm, while the positive tail of P-15-070-160-30 is up to around 4.3 mm. The lift-off height periodicity at 160 Hz of P-15-070-30 is greater than that of NPR-15-070-160-30 (Figure 5-52b). Unlike NPR-15-070-160-30, in this case no peak is revealed at 320 Hz. The phase-averaged lift-off heights (Figure 5-52c), reveal that the data points of P-15-070-160-30 exhibit a sinusoidal shape, whereas in case of NPR-15-070-160-30, the data points are not a good fit to the sinusoidal line, which is expected due to the reduced periodicity at 160 Hz.

The curves of the normalised heat release response with respect to forcing amplitude of the NPR system are much greater than those of the premixed system (Figure 5-53). In the case of the fully premixed system, the maximum normalised OH* chemiluminescence intensity ($Q'/< Q >$) is 29%, whereas in the NPR system the respective value is 46%. In both systems, the general trend is that at low forcing amplitudes $Q'/< Q >$ increases linearly with A, and with a further increase in A, the heat release response continues to rise at a reduced rate, until it starts

saturating at higher amplitudes. The magnitude at which the heat release response starts deviating from linearity varies between A=11% and A=20%. The NPR flames show a low sensitivity towards a change in the operating conditions, particularly when they are close to the blow-off condition. However, in the fully premixed system, as far as the effect of equivalence ratio on the flame response is concerned, Figure 5-53 reveals that the normalised global heat release of P-10-080 is greater than that of P-10-070 at lower A, but from A=31% the difference in their response becomes smaller and eventually both curves meet at A=50%. Thus, it could be conjectured that the premixed system is sensitive to changes in the equivalence ratio at low A, whereas at greater A the system is not sensitive to changes in equivalence ratio. The normalised heat release response of P-10-080 increases nonlinearly with A, while that of P-10-070 shows a more linear dependence on A (Figure 5-53).

The transfer function measurements show a nonlinear amplitude dependence: at lower amplitudes the transfer function drops rapidly with A and once the magnitude reaches a certain value, with further increase in A there is little change in transfer function (Figure 5-53). The magnitude of the transfer function of the NPR flames is much greater than that of the premixed flames, which also suggests a very high response of the former. Another striking feature is that the NFTF reduction of the NPR flames is much greater than that of the fully premixed flames. The greatest NFTF reduction in the premixed system is exhibited by P-10-080 (from 0.77 to 0.4), whereas in the NPR system is shown by NPR-10-055 (from 1.52 to 0.66). A possible explanation for this response could be that both conditions when forced at low amplitudes are far from blow-off, and thus the rate at which $Q'/< Q >$ increases with A is relatively high, but as A increases, the chaotic radial flame motion increases and the flames are approaching blow-off, resulting in $Q'/< Q >$ increasing with A at a reduced rate.

The power spectra of the OH* chemiluminescence signal of NPR-15-070-160-30 and P-15-070-160-30 (Figure 5-54) show that apart from the strong response at 160 Hz, they also respond at the first harmonic frequency, at 320 Hz (the magnitude of the 320 Hz is smaller by one order of magnitude compared with that at 160 Hz). Also, a very low peak is observed at the second harmonic frequency (480 Hz). The harmonic frequency content of the heat release signal at 320 Hz, despite the fact that the velocity signal did not show any significant harmonic contents (see Section 4.2.2 and Section 5.2.4), results in some nonlinearities in the heat release response. The response of P-10-070 and NPR-10-055 at the first harmonic shows similar trends. In particular, concerning the harmonic content at 320 Hz in the inlet velocity measurements, both systems exhibit an almost linear increase with forcing amplitude, with the values being very similar (Figure 5-55a). Also, in both flames the ratio of the fluctuation of heat release at

the first harmonic frequency to that of the forcing frequency, Q'_h/Q', with respect to forcing amplitude shows a highly nonlinear variation, with the trend being almost identical, but the values of the NPR system being greater than that of the premixed (Figure 5-55b). The relative response to 320 Hz increases linearly up to A=16% and A=11% for NPR-10-055 and P-10-070 respectively, after which it decreases also linearly until A=29% and A=31% respectively. Then, the proportional harmonic response stays almost constant up to A=46% and A=48% respectively, while a sudden increase is revealed at A=49% and A=53% for NPR-10-055 and P-10-070 respectively. At A=16% and A=11%, which is the forcing amplitude of NPR-10-055 and P-10-070 respectively at which the peak of the relative response to 320 Hz is revealed, the normalised heat release response exhibited a deviation from linearity (Figure 5-53a), which was more pronounced in the NPR system than that in the premixed. In both systems, it was observed that this nonlinearity occurred with the appearance of a vortex-like OH* chemiluminescence structure, suggesting that the response to the harmonic frequency was suppressed with the appearance of this structure. These findings are consistent with the results of Balachandran et al. [40], based on fully premixed bluff body stabilised ethylene flames. Finally, at A=49% and A=53% (NPR-10-055 and P-10-070 respectively), at which the second peak of the relative response to 320 Hz is revealed (Figure 5-55b), the normalised heat release exhibited a drop (Figure 5-53a).

The comparison between the POD analysis of NPR-15-070-160-30 and P-15-070-160-30 present many similarities. In both systems, the first two OH* chemiluminescence POD Modes reveal a strong axial dependence, which is characteristic of the pronounced axial flame motion. The respective PSDs of POD time coefficients exhibit one dominant peak at 160 Hz and a smaller one -by one order of magnitude- at 320 Hz. It should be mentioned that these peaks are much stronger in the NPR than in the premixed system, implying the greater influence of forcing on the flame response. The energy content of the first Mode is 45.8% and 48.2% for NPR-15-070-160-30 and P-15-070-160-30 respectively, whereas that of Mode 2 is 22.4% and 10.3% respectively (see Section 4.2.3.1 and Section 5.2.5.1). In both flames, the energy contribution of the first two modes is significantly larger than that of the successive modes, suggesting that the dominant mechanism is captured mainly by the first two modes. The structure of the first two OH PLIF POD Modes reveals a change in the flame angle, with Mode 2 showing a similar structure with that of Figure 4-11 and Figure 5-28a, where the boundaries between which the angle varies can be seen.

In Figure 5-56, the normalised heat release response and the transfer function are plotted with respect to the non-dimensional frequency fL_{fl}/U for the fully premixed and NPR

systems. In particular, the frequency of forcing was normalised with the convection time, estimated by dividing the length of the flame, L_{fl}, with the bulk velocity, U. The flame length was defined as the distance between the edge of the bluff body and the highest position of the flame, based on the time-averaged OH* chemiluminescence intensity. The flame boundary was determined using a threshold value which was chosen to separate flame regions from the background noise of the image. A flame whose length is much smaller than an acoustic/convective wavelength is referred to as acoustically/convectively compact [181]. The figure suggests that the response of the NPR system was greater than that of the fully premixed system in the whole range of fL_{fl}/U. As discussed above, in the fully premixed system the heat release modulations are mainly dominated by flame area variations, whereas in the NPR system both the flame area and the equivalence ratio modulations constitute important mechanisms of the heat release modulations. The close to zero values are attributed to the fact that close to blow-off the flame response is significantly reduced compared with that farther from blow-off. These results are consistent with the findings of a previous study on forced fully premixed and imperfectly premixed forced ethylene flames [22], which also suggested that the response of imperfectly premixed flames was greater than that of fully premixed flames, but only when the flame was compact (fL_{fl}/U<1). However, for fL_{fl}/U≥1, the fully premixed and imperfectly premixed flames exhibited a similar response.

5.4 Conclusions

Detailed experimental studies were performed to investigate the response of overall lean turbulent methane non-premixed flames with radial fuel injection to acoustic forcing. In this system, the degree of premixing was between the fully premixed (i.e. no temporal or spatial variation in equivalence ratio) and the non-premixed systems with very large mixture fraction fluctuations at the flame location, and apart from the time-varying velocity field, there was also a time- and space-varying equivalence ratio. OH* chemiluminescence measurements, acquired with a photomultiplier tube (PMT) and an ICCD camera, were used to study qualitatively the heat release response of the flames, while OH PLIF measurements were used also qualitatively to understand the response of the flame structure and the behaviour of the various parts of the flame. Apart from the flame kinematics analysis, the amplitude dependence of the transfer function was estimated. Also, the flame surface density (FSD), calculated from OH PLIF images, was used qualitatively as an indicator of the flame area. Special attention was given to the study of the effect of air velocity and global equivalence ratio on the flame response, as well as the behaviour of forced flames when blow-off is approached. The dominant structures of the flames and their periodicity were characterised using the Proper Orthogonal Decomposition (POD) method, while the convection velocity of the most dominant structures of the system was estimated. Finally, a comparison between forced fully premixed and non-premixed with radial fuel injection flames was performed in terms of their response.

Concerning the amplitude dependence of the non-premixed with radial fuel injection flame response, a very high, nonlinear response was observed in the flames studied (the maximum normalised global heat release fluctuation was approximately 49%). The general trend was that at low forcing amplitudes $Q'/< Q >$ increased linearly with A, and with a further increase in A, the heat release response continued to rise at a reduced rate, until it started saturating at higher amplitudes. It was found that forcing reduced the stability of the flames, which decreased with the increase in forcing amplitude, thus the investigation of the influence of forcing on the flame kinematics close to blow-off is also important. Close to blow-off, the NPR system showed a low sensitivity towards a change in the operating conditions. It was suggested that the proximity of the forced flames to blow-off condition was critical in their heat release response. In particular, studying the effect of the global equivalence ratio on the flame response (U_{air} constant and different global φ), flames that were close to blow-off exhibited a significantly reduced heat release response compared with those far from blow-off. This could be associated with the increased chaotic radial flame motion and possibilities of local extinctions, resulting in isolated flame regions closer to blow-off. For instance, unlike the far

from blow-off flames, close to blow-off the OH* chemiluminescence signal revealed a large distortion of the waveform, reaching very high and low values, while the frequency content of the signal consisted of multiple frequencies, apart from the forcing frequency. As far as the influence of forcing amplitude on the heat release response, it was deduced that at greater A, a greater variation of the heat release was observed, while isolated parts of the flame were seen more often as blow-off was approached. In addition, it was suggested that at greater A, as the flame was approaching blow-off, the nonlinear increase in the heat release with A was also associated with the irregular variation of the amplitude of the heat release signal. Finally, in some NPR flames, a source of nonlinearity in the heat release response was associated with the fact that part of the energy was transferred to the first harmonic (320Hz), while the velocity signal did not show any significant harmonic contents. It was observed that this response to the harmonic frequency was suppressed with the appearance of a vortex-like structure.

As far as the flame kinematics are concerned, the following conclusions were reached. It was revealed that the various parts of the flame responded differently to acoustic forcing. A novel method for quantifying the local response of the various parts of the flame at the forcing frequency was developed based on OH PLIF images. From this, it was shown that the ISL region, downstream of the annular passage -and especially between the bluff body edge and 20 mm downstream- constituted the location of the highest R_L values, whereas R_L was very low farther downstream. A pattern with zero-value regions of R_L was observed adjacent on both sides of the high ISL proportion values, which represented the extremes between which the flame angle was modulated during the cycle. The above patterns were revealed in the second OH PLIF POD Mode, implying that these characteristics constitute dominant mechanisms of the NPR system. During the acoustic cycle, the change in the angle of the flame that was observed followed a sinusoidal trend. Another important feature of the flame was the impingement point (the point at which the flame branch in the ISL region impinges on the wall), which was calculated from phase-averaged OH PLIF contour plots. The position of the impingement point showed an axial movement during the cycle, also exhibiting a sinusoidal trend, and it was used as a reference in the analysis of the sequence at which the OH intensity peaks in the ISL-Top-ORZ regions were revealed. The phase difference among the curves of the OH signal in the different regions of the flame was found to change in the various flames. Even though relatively high OH fluctuations were revealed in the individual regions, a low $OH/<OH>$ variation was observed in the total OH PLIF window, due to the phase difference among the $OH/<OH>$ curves of the different regions, which had an evening out effect. Also, it was deduced that far from blow-off, the lift-off behaviour of the flame was hardly affected

by forcing. However, closer to blow-off, the forced flames exhibited increased average lift-off heights compared to the unforced conditions. In particular, the greater the destabilisation of the flame (as the flame was approaching blow-off) with an increase in forcing amplitude, the greater the observed lift-off heights. The lift-off height periodicity at the forcing frequency was very pronounced, especially at greater forcing amplitudes. Finally, it was suggested that the cyclic OH* chemiluminescence variation showed a similar phase, but a greater amplitude than the cyclic FSD variation, implying that apart from the flame area, other mechanisms might also contribute to the heat release modulations. The area of the flame front was increasing as the flame angle was becoming steeper.

From the POD analysis, the first two OH* chemiluminescence POD Modes revealed a banded shape, which represented the axial motion of the flame and was associated with the forcing frequency at 160 Hz. The fact that the POD energy content of the first four Modes of the forced flames was greater than that of the respective unforced, suggested that forcing affected significantly the flame structure. Also, it was conjectured that the influence of forcing on the flame response was greater for flames that were far from blow-off, leading to more pronounced features of the POD Modes and to stronger peaks at 160 Hz in the PSDs than those at a closer proximity to blow-off. Closer to blow-off, the blow-off kinematics affected dramatically the flame structure and as a result, the influence of forcing on the flame structure was found to decrease. The OH PLIF POD results, apart from the aforementioned features, revealed the angle variation of the flame. Overall, POD was found to be a useful tool in the identification of dominant features and their periodicity in forced NPR flames, even at conditions that were close to blow-off.

From the comparison between the NPR and the fully premixed flames, the main conclusions are the following. First of all, the response of the NPR system was greater than that of the fully premixed system in the range of fL_{fl}/U studied, however, in both systems, close to blow-off the flame response was significantly reduced compared with that farther from blow-off. The curves of the heat release response as a function of forcing amplitude had a similar general trend. Unlike the NPR system, where a low sensitivity was observed towards a change in the operating conditions, the premixed showed an increased sensitivity to φ, particularly at low A. In addition, in both systems it was shown that for some flames, a source of nonlinearity in the heat release response was associated with the fact that part of the energy was transferred to the first harmonic (320 Hz), while the velocity signal did not show any significant harmonic contents. The response of both flames at the first harmonic showed similar trends with the response of the NPR flame being greater than that of the premixed. While for the NPR flame

R_L was greater in the region downstream of the annular passage, close to the bluff body edge, than that in the other flame regions, in the premixed flame higher R_L values were seen in large regions on the downstream side of the OH PLIF plane. In addition, in the fully premixed system, the good agreement between the OH* chemiluminescence and FSD variation implied that the heat release modulation was mainly through flame surface area modulation. Also, the agreement between the FSD variation of the premixed and NPR flames suggested that the flame area modulation mechanism, and how it was influenced by the flame angle, was common in both systems. Thus, in the NPR Flame, the difference in the magnitude between the OH* chemiluminescence and FSD variation, previously mentioned, was mainly attributed to the equivalence ratio fluctuations constituting an important mechanism of the system. Therefore, in the NPR system, both the flame area and the equivalence ratio modulations constitute important mechanisms of the heat release modulations. Unlike NPR, in the premixed flame, forcing influences the lift-off behaviour, however the average lift-off height of the premixed flames was lower than that of the respective NPR conditions. Finally, concerning the POD analysis, in both systems, the first two OH* chemiluminescence POD Modes revealed an axial motion of the flame, associated with the forcing frequency at 160 Hz, which was significantly more pronounced in the NPR system than that in the premixed, while the structure of the first two OH PLIF POD Modes revealed a change in the flame angle. Based on the first OH* POD Mode, the ratio of the convection velocity to the bulk velocity was estimated to be 0.54 for the NPR flame, while that of the respective fully premixed flame was unity.

5.5 Figures of Chapter 5

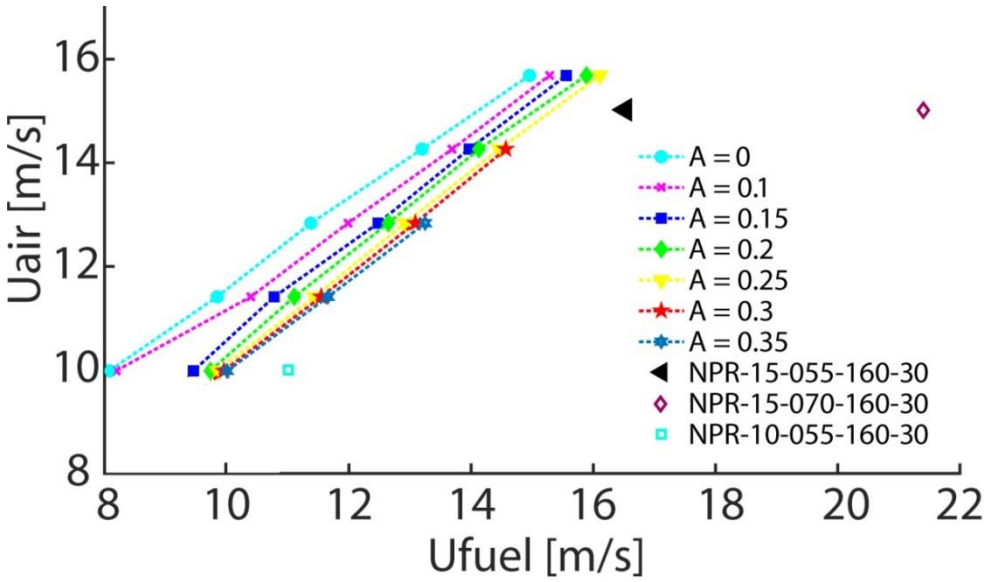

Figure 5-1: Air blow-off velocity, U_{air}, as a function of fuel blow-off velocity, U_f, (calculated at the exit of the fuel nozzle) for various forcing amplitudes A, for the NPR configuration. The studied experimental conditions (Table 5-1) are also indicated.

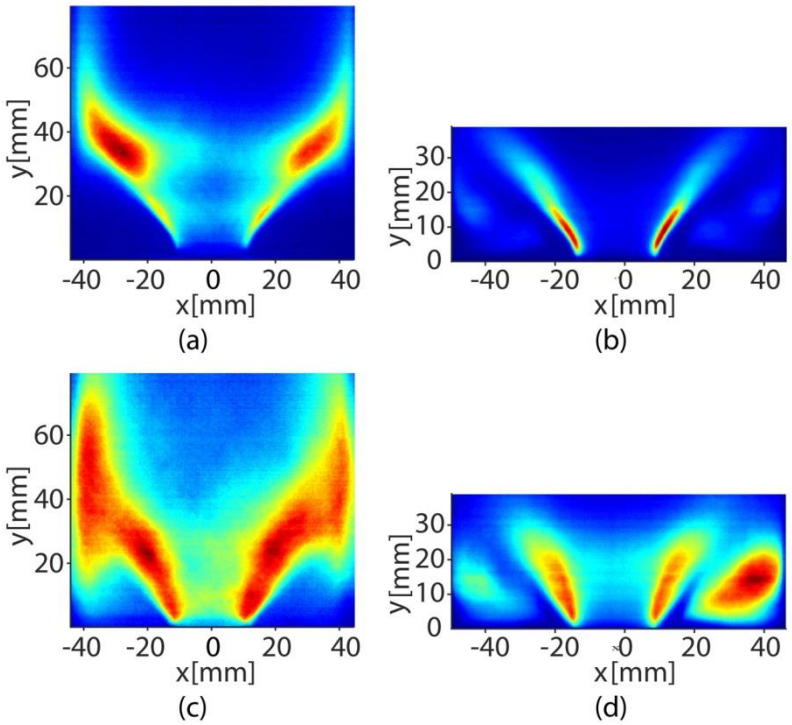

Figure 5-2: Time-averaged OH* chemiluminescence and OH PLIF images of NPR-15-055 (a, b respectively) and of NPR-15-055-160-30 (c, d respectively).

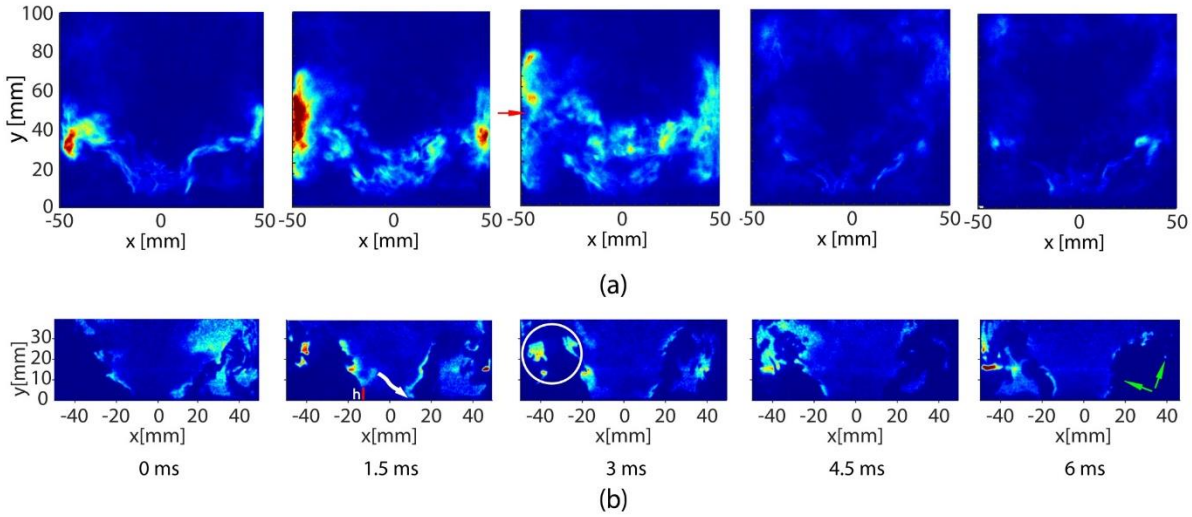

Figure 5-3: (a) Instantaneous OH* chemiluminescence and (b) OH PLIF images of NPR-15-055-160-30 (not recorded simultaneously during a cycle, *t*=0 ms corresponds to the beginning of the cycle). The same colormap for each image was used. The main features of their behaviour are highlighted: red arrow: impingement point, red line: lift-off height *h* at the bluff body edge, white curved arrow: flame attached to the bluff body edge, green arrow: flame branch in the ISL or wall region missing, white circle: breaks of the OH zone.

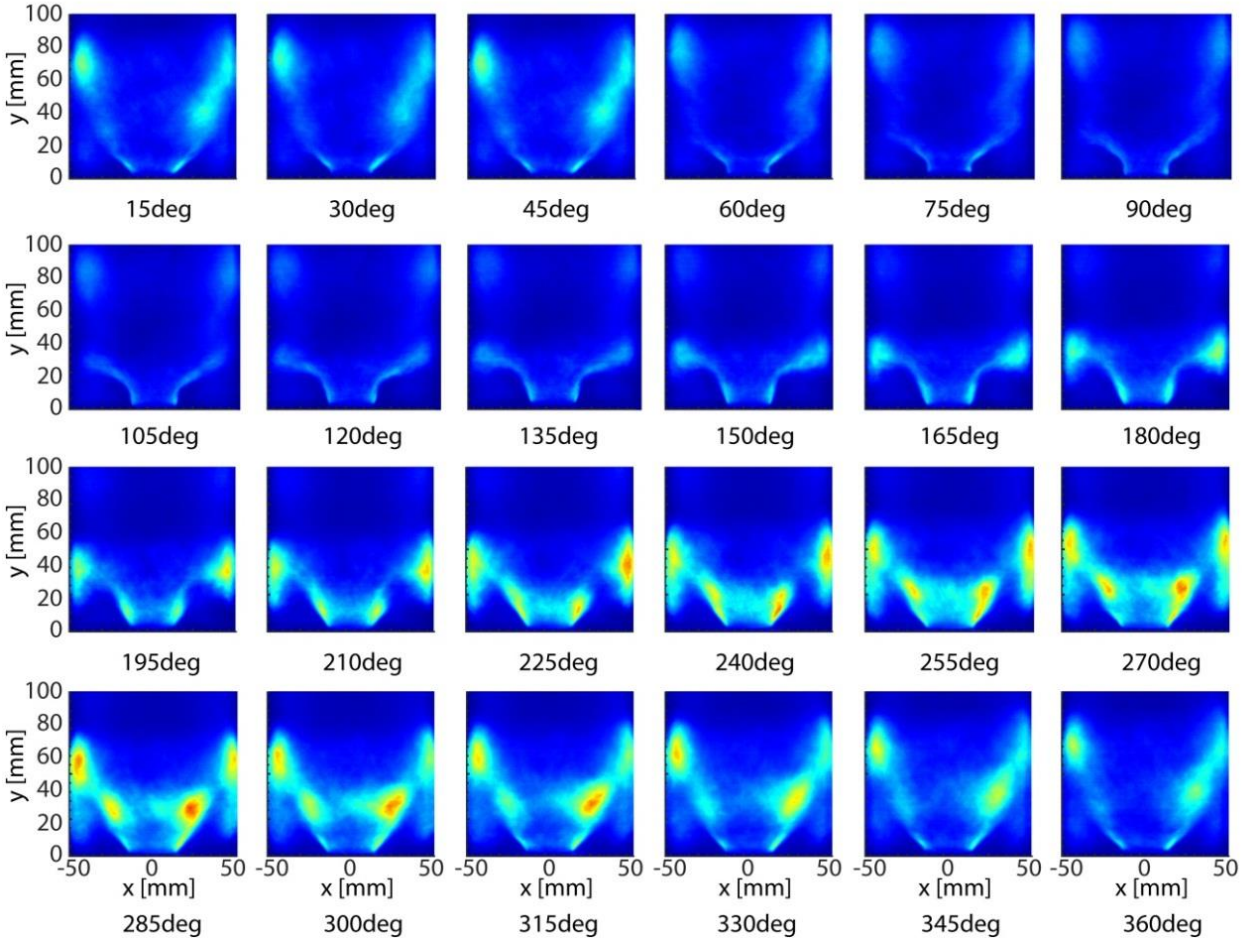

Figure 5-4: Phase-averaged OH* chemiluminescence images of NPR-15-055-160-30.

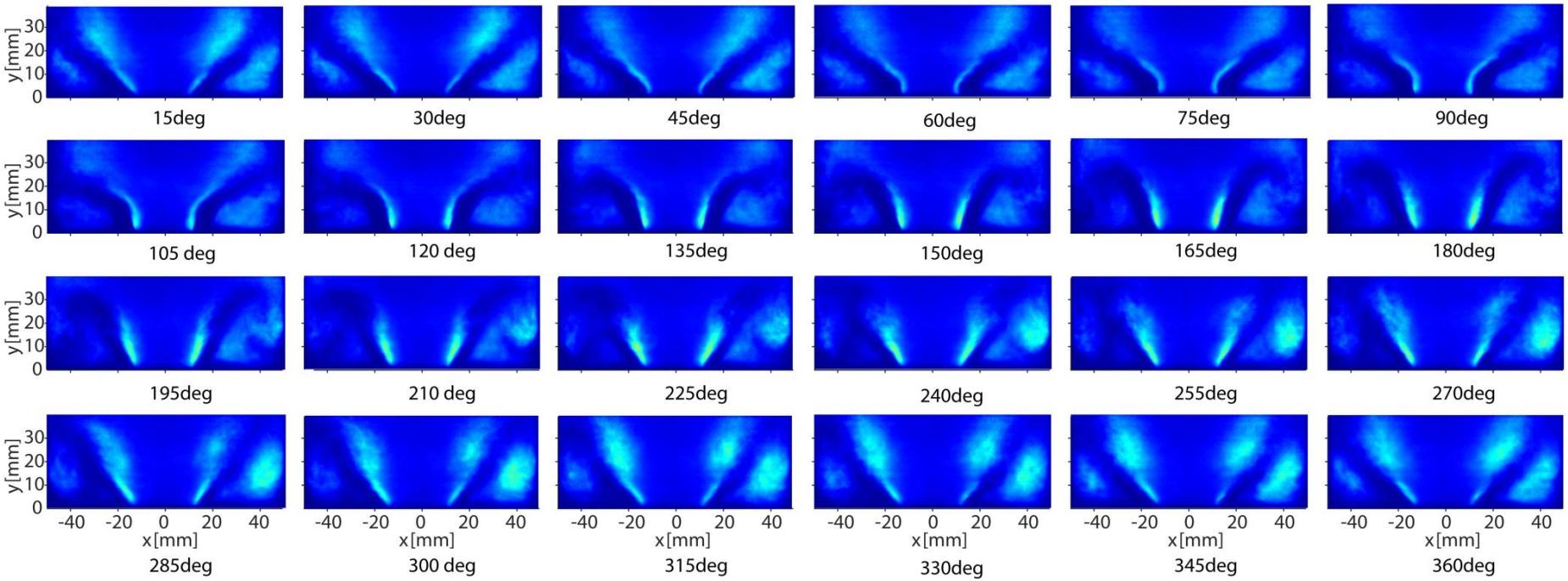

Figure 5-5: Phase-averaged OH PLIF images of NPR-15-055-160-30.

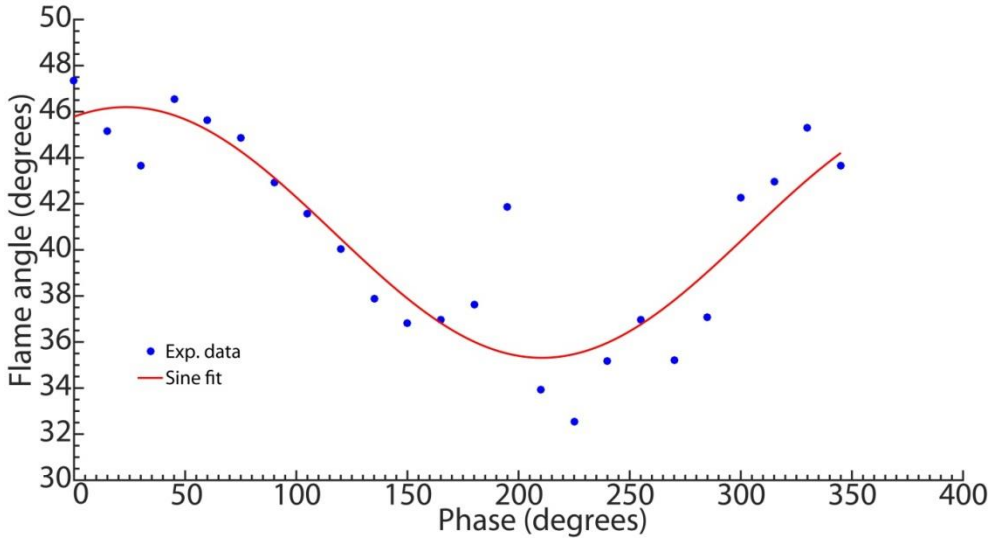

Figure 5-6: Flame angle variation with respect to phase of the acoustic cycle for NPR-15-055-160-30.

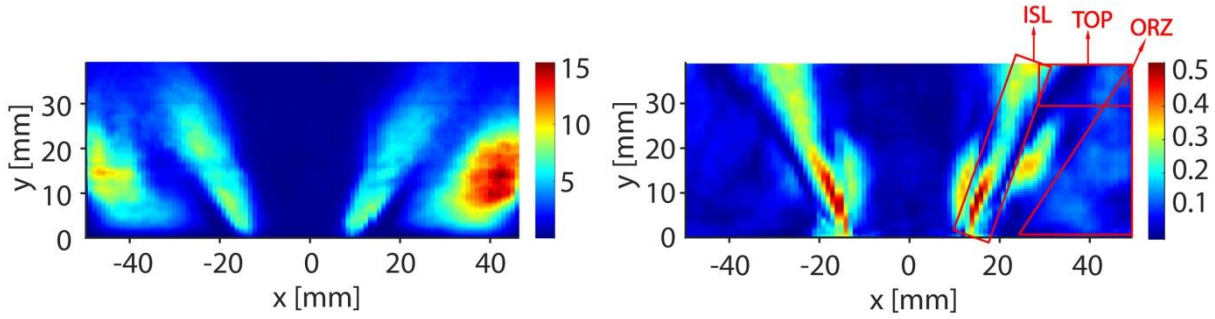

Figure 5-7: (a) Variance of OH and (b) ratio R_L (OH fluctuation at 160 Hz to the total variance of OH) for NPR-15-055-160-30.

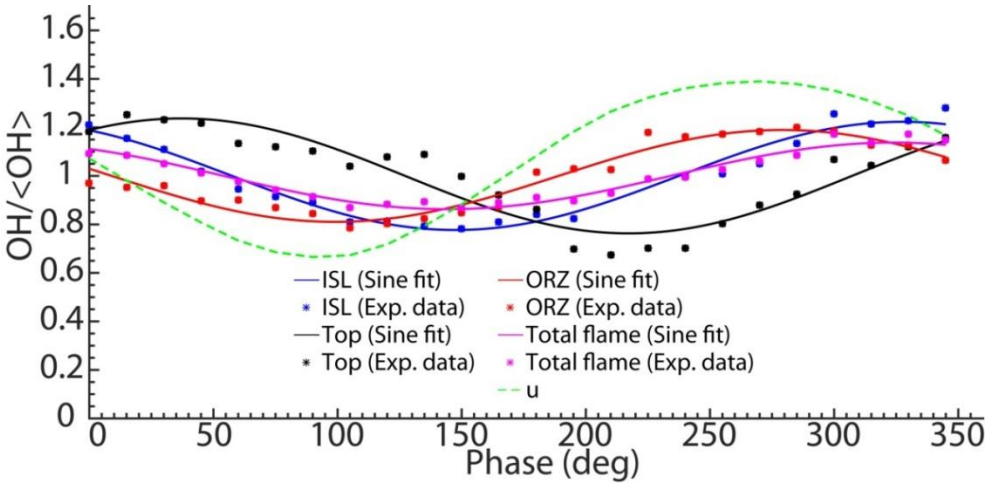

Figure 5-8: $OH/< OH >$ variation during the acoustic cycle, evaluated from phase-averaged OH PLIF images (data presented in Figure 5-5), calculated from the ISL, Top, ORZ and whole OH PLIF window. The green dashed line represents the normalised acoustic velocity fluctuations. Flame: NPR-15-055-160-30.

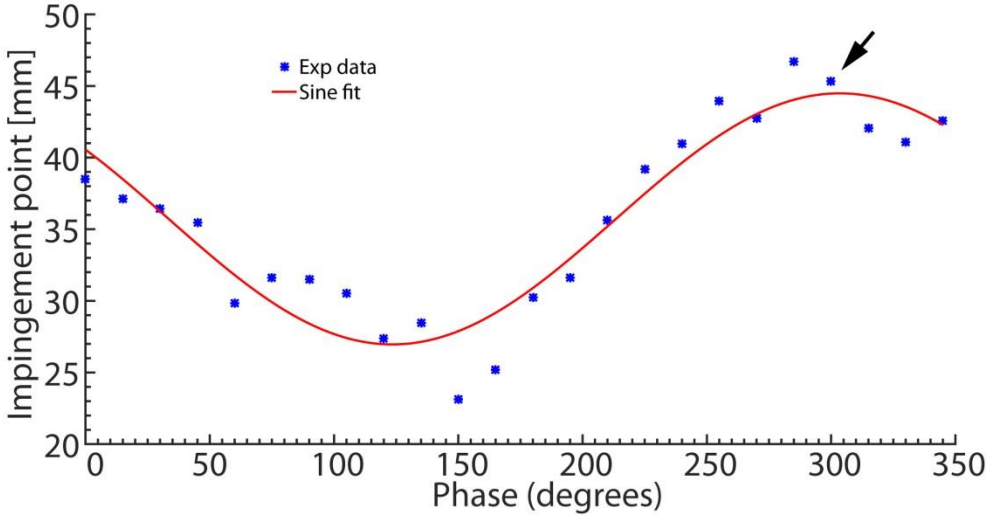

Figure 5-9: Impingement point position variation with respect to phase of the acoustic cycle for NPR-15-055-160-30.

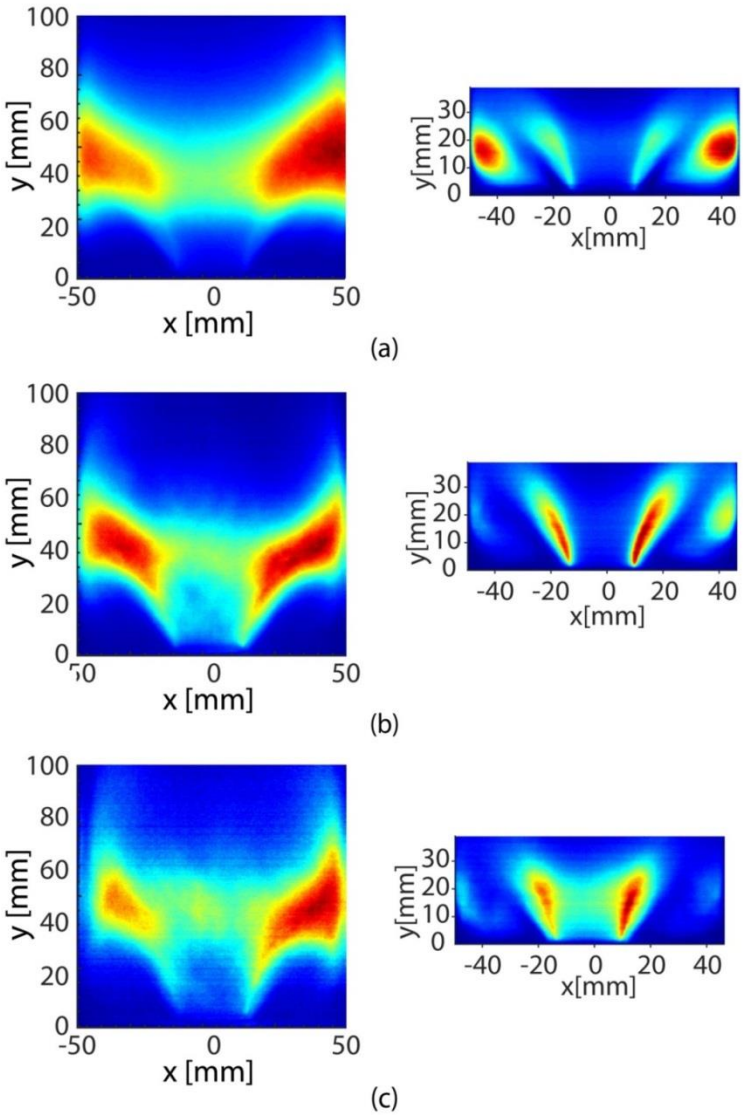

Figure 5-10: Time-averaged OH* chemiluminescence (left) and OH PLIF images (right) of (a) NPR-15-070-160-30, (b) NPR-10-055-160-30 and (c) NPR-10-055-160-50.

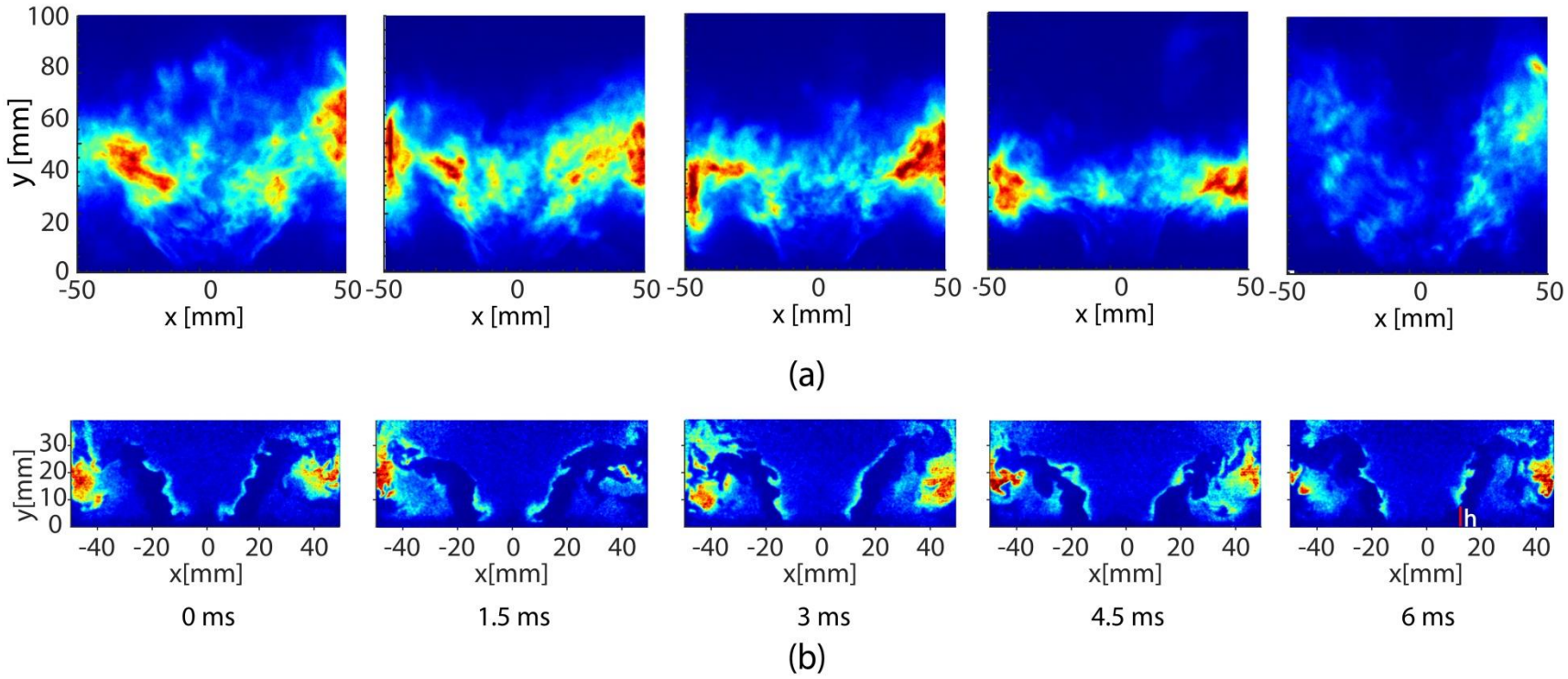

Figure 5-11: (a) Instantaneous OH* chemiluminescence and (b) OH PLIF images of NPR-15-070-160-30 (not recorded simultaneously during a cycle, *t*=0 ms corresponds to the beginning of the cycle). The same colormap for each image was used. Red line: lift-off height *h* at the bluff body edge.

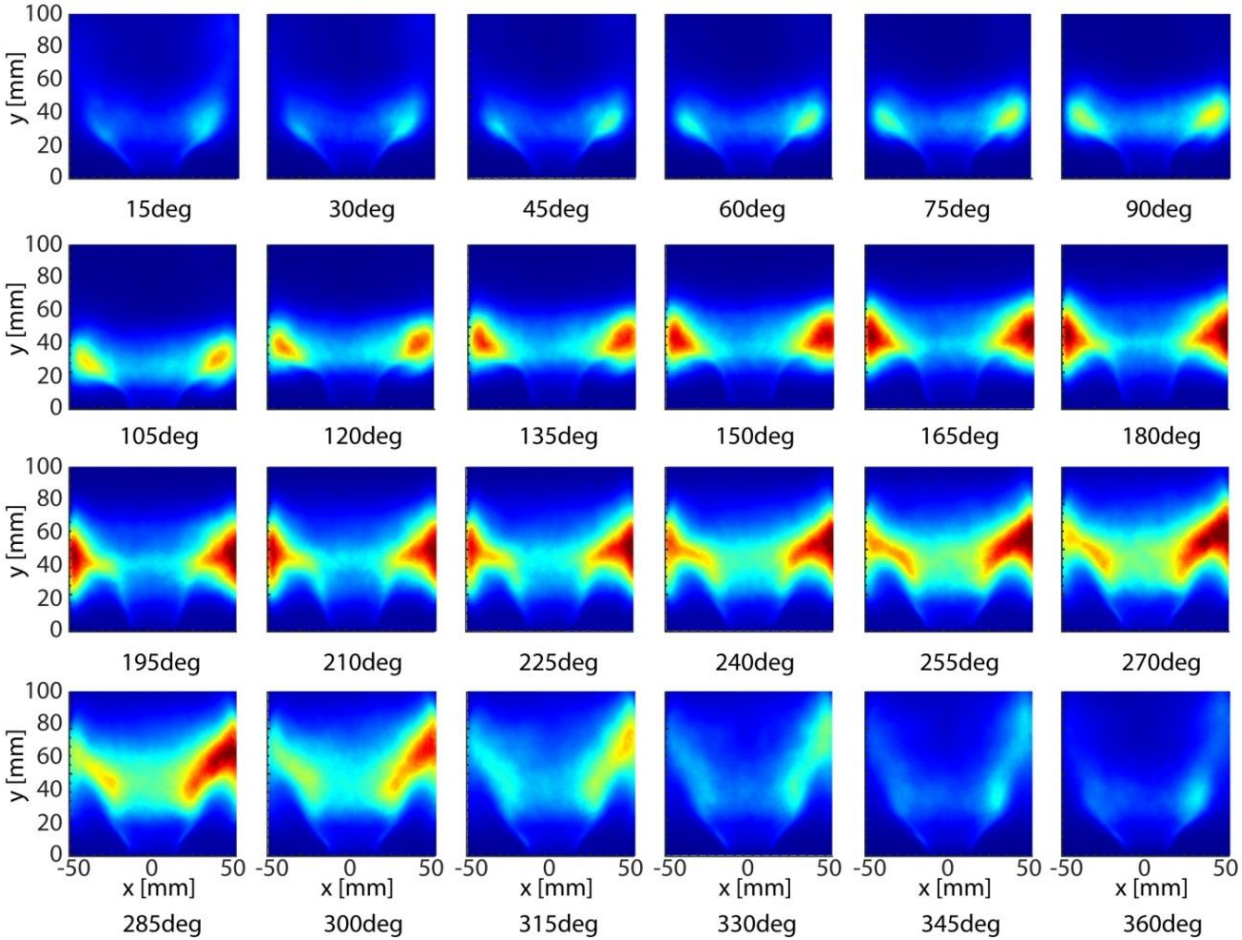

Figure 5-12: Phase-averaged OH* chemiluminescence images of NPR-15-070-160-30.

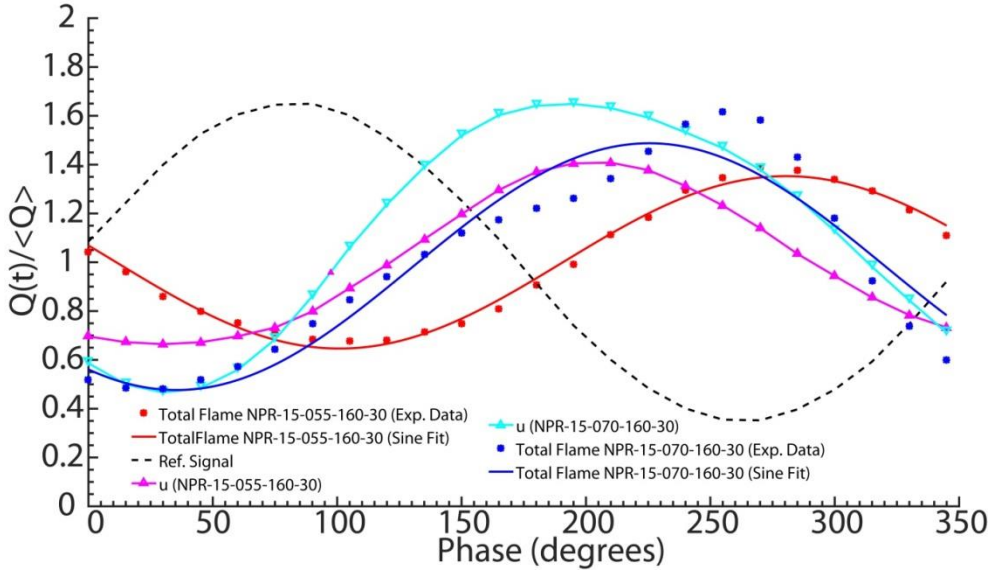

Figure 5-13: Comparison of the normalised global heat release variation evaluated from OH* chemiluminescence images for flames NPR-15-055-160-30 and NPR-15-070-160-30 (data presented in Figure 5-4 and Figure 5-12 respectively). The normalised acoustic velocity fluctuations are also presented.

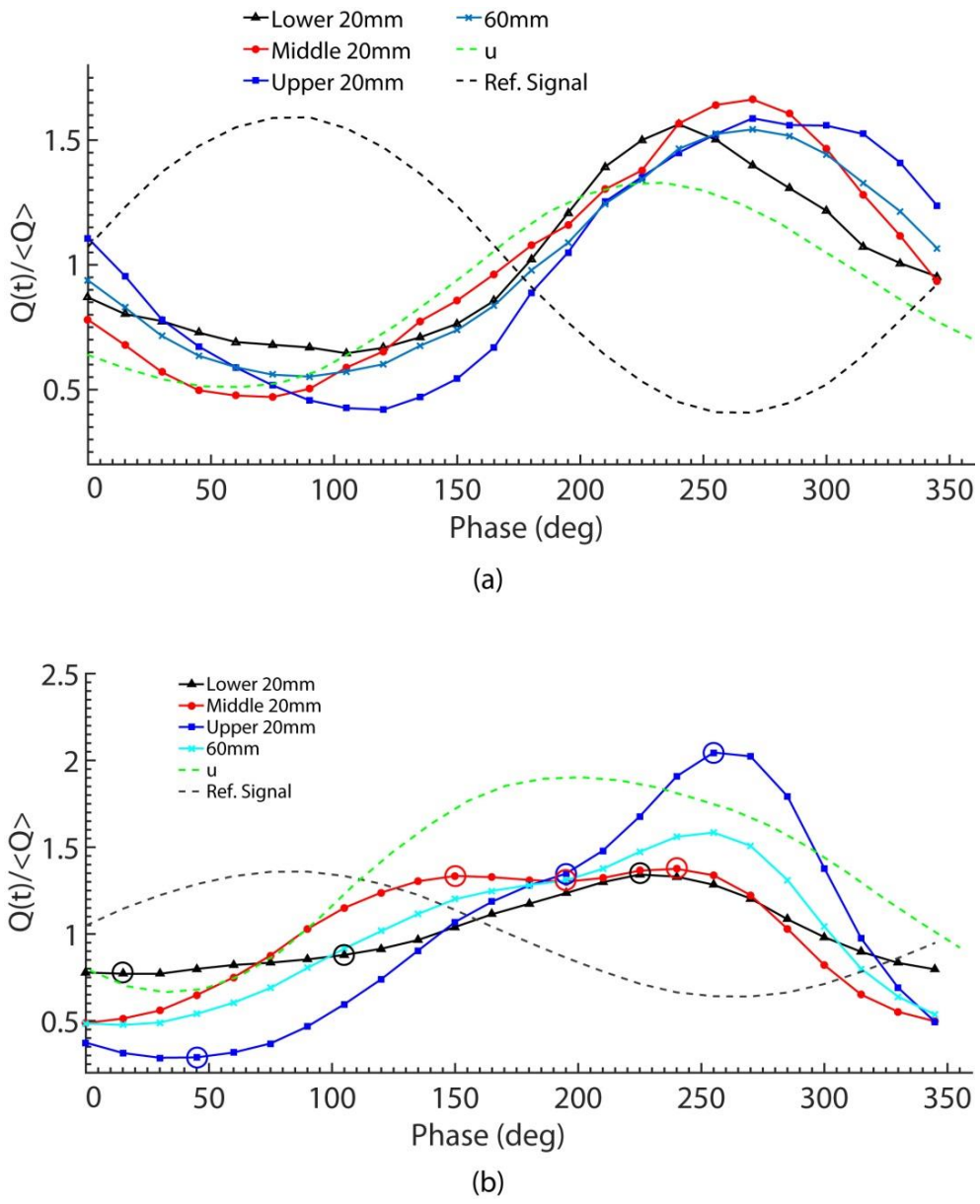

Figure 5-14: Global heat release cycle variation for (a) NPR-15-055-160-30 and (b) NPR-15-070-160-30, evaluated from phase-averaged OH* chemiluminescence images (data presented in Figure 5-12) based on four windows: 0-20 mm (lower 20 mm), 20-40 mm (middle 20 mm), 40-60 mm (upper 20 mm) and total 0-60 mm downstream of the bluff body plane. The phase-averaged images that correspond to the marked points of the curves are presented in Figure 5-15.

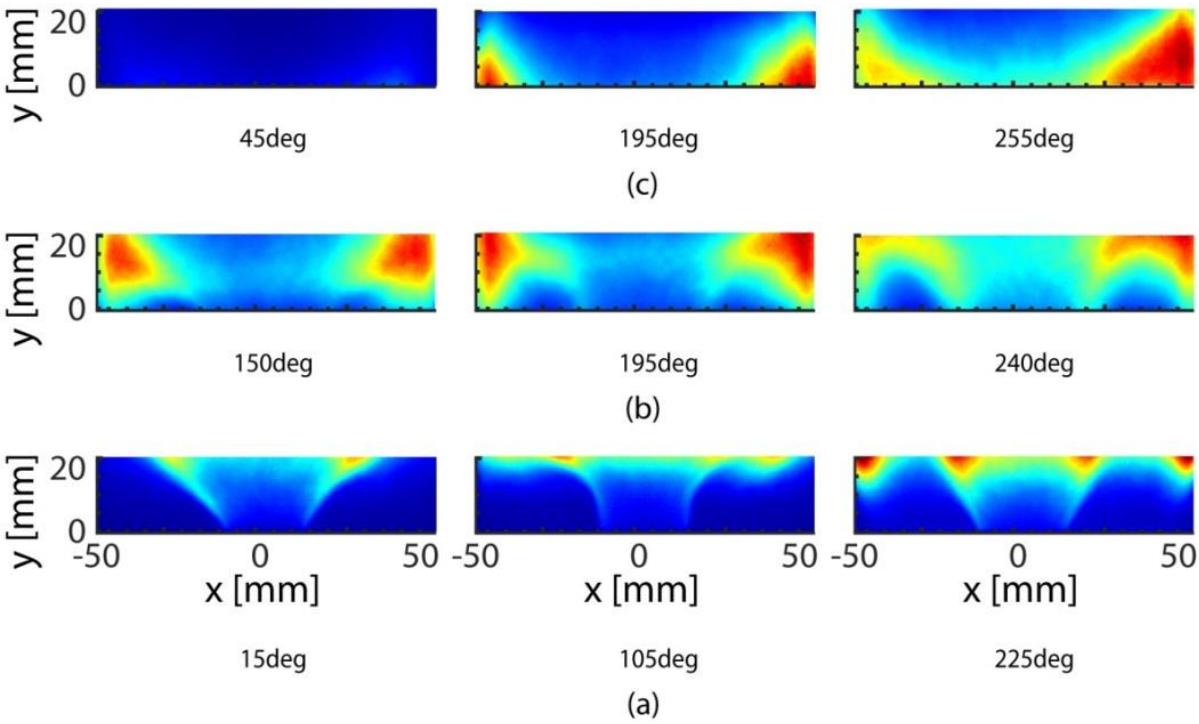

Figure 5-15: Phase-averaged OH* chemiluminescence images that correspond to the marked points of the curves of NPR-15-070-160-30 plotted in Figure 5-14b.

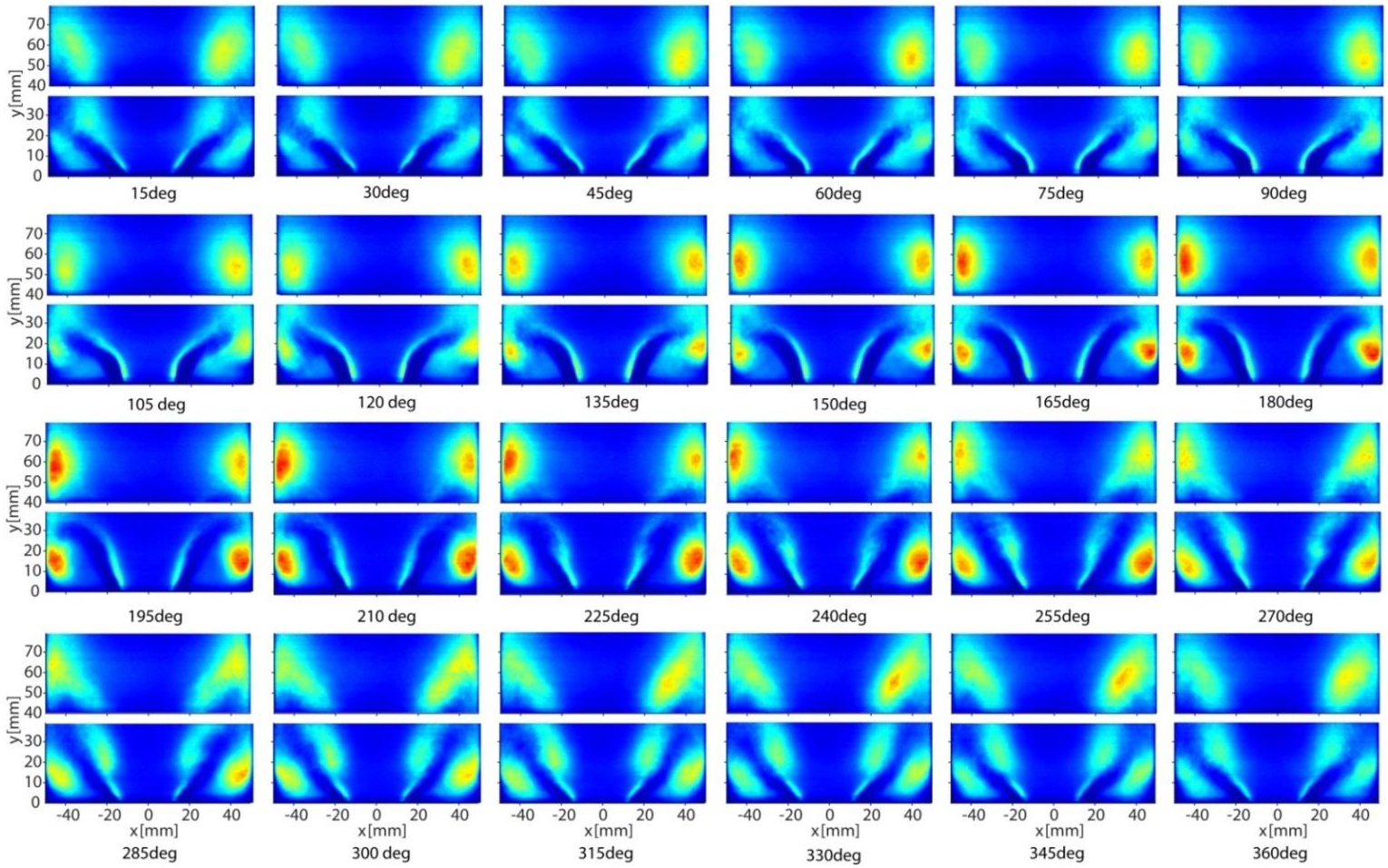

Figure 5-16: Phase-averaged OH PLIF images, based on both lower and upper OH PLIF laser sheet, of NPR-15-070-160-30.

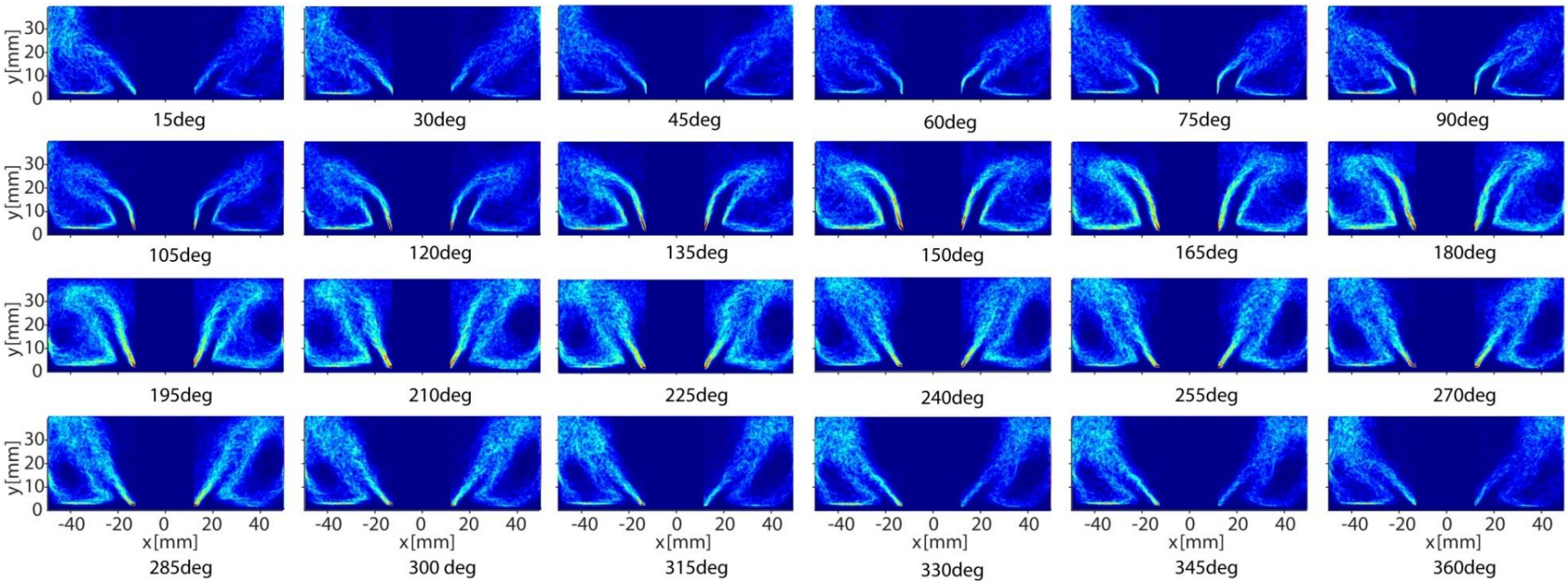

Figure 5-17: Phase-averaged FSD images of NPR-15-070-160-30.

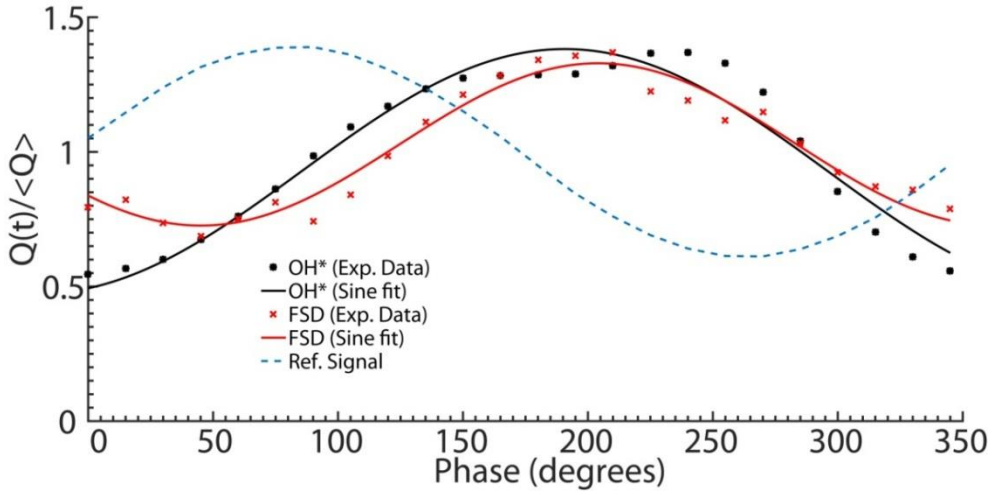

Figure 5-18: Comparison of the cyclic FSD variation, evaluated from the phase-averaged FSD images presented in Figure 5-17, revolved around the burner central axis, and the cyclic OH* chemiluminescence variation for NPR-15-070-160-30, both based on a 40 mm-window (40 mm is the height of the OH PLIF laser sheet).

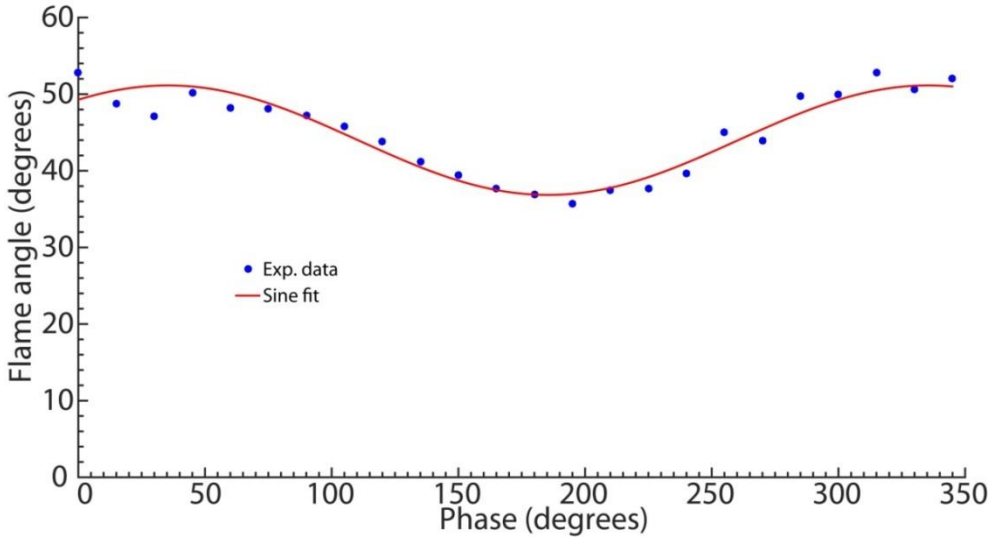

Figure 5-19: Flame angle variation with respect to phase of the acoustic cycle for NPR-15-070-160-30.

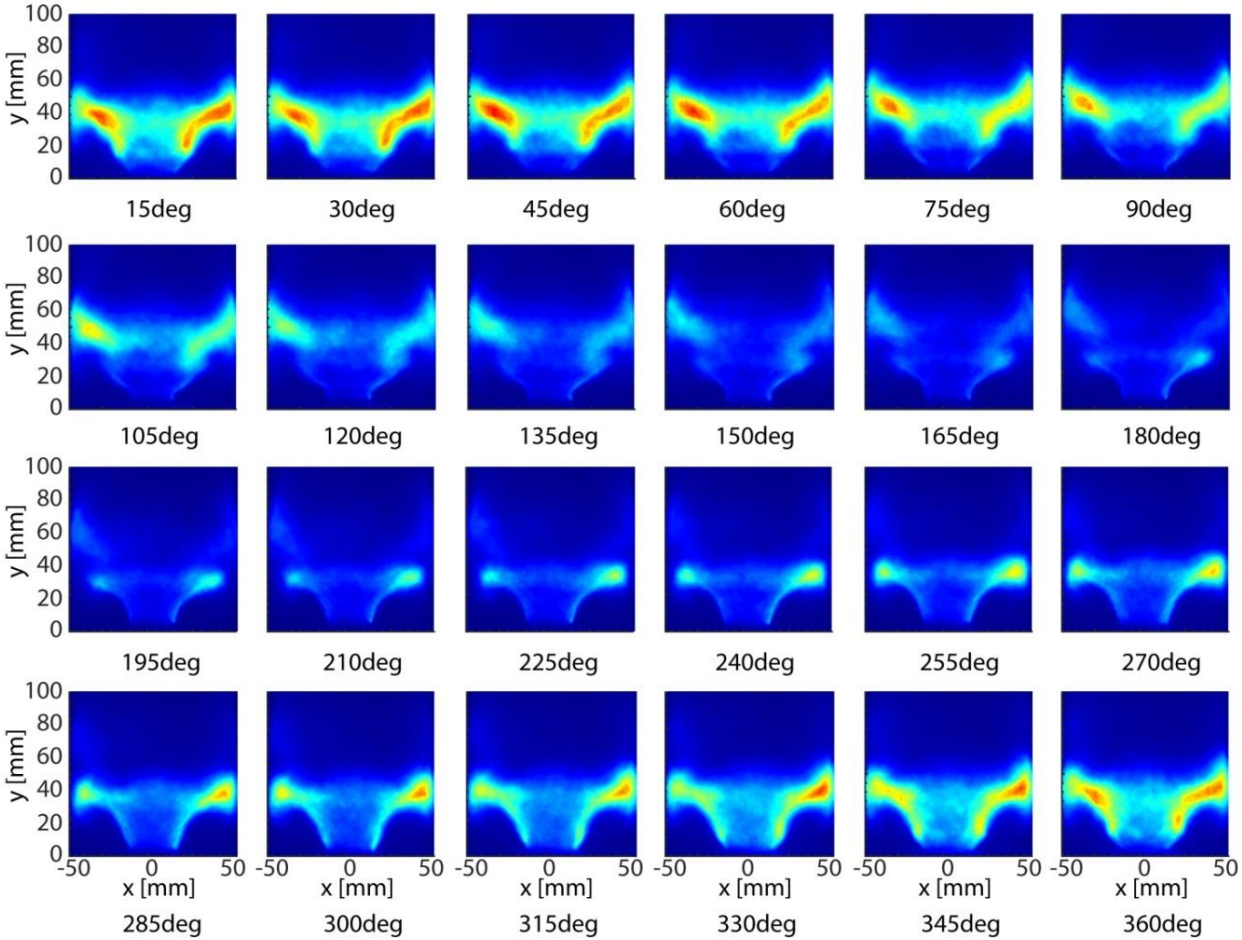

Figure 5-20: Phase-averaged OH* chemiluminescence images of NPR-10-055-160-30.

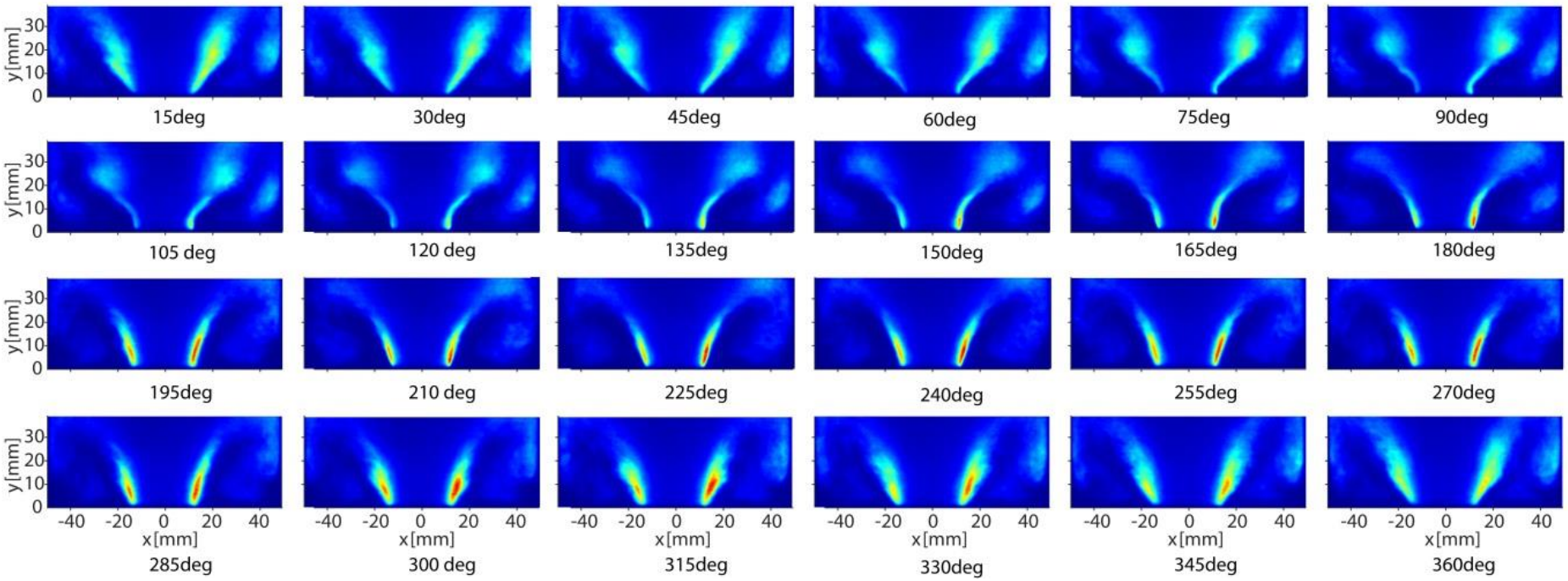

Figure 5-21: Phase-averaged OH PLIF images of NPR-10-055-160-30.

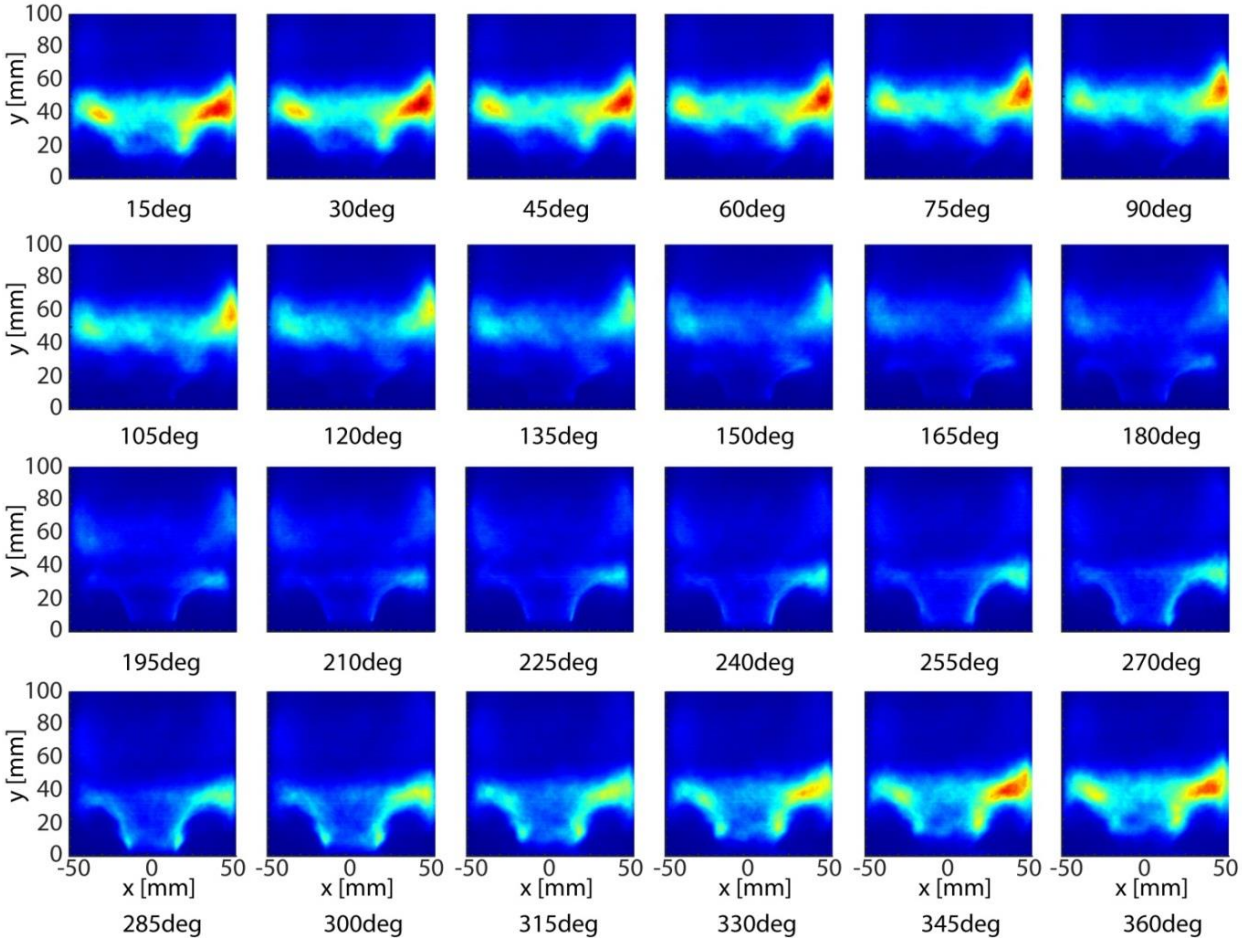

Figure 5-22: Phase-averaged OH* chemiluminescence images of NPR-10-055-160-50.

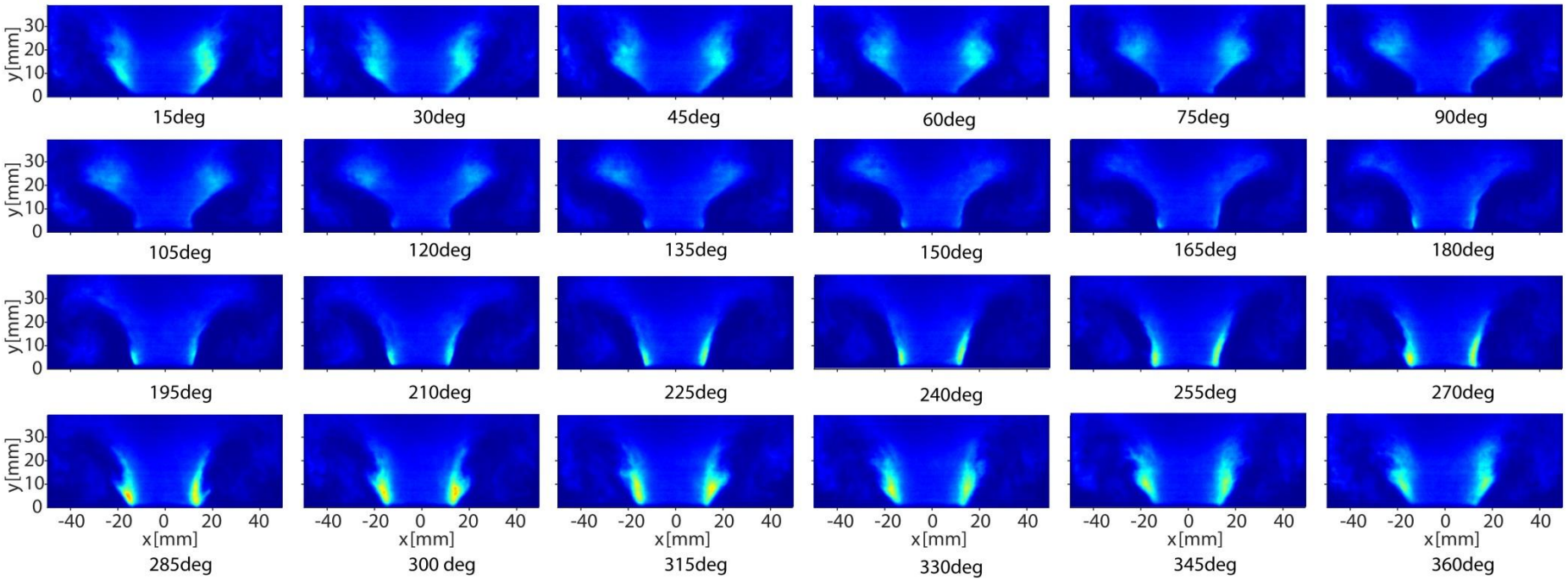

Figure 5-23: Phase-averaged OH PLIF images of NPR-10-055-160-50.

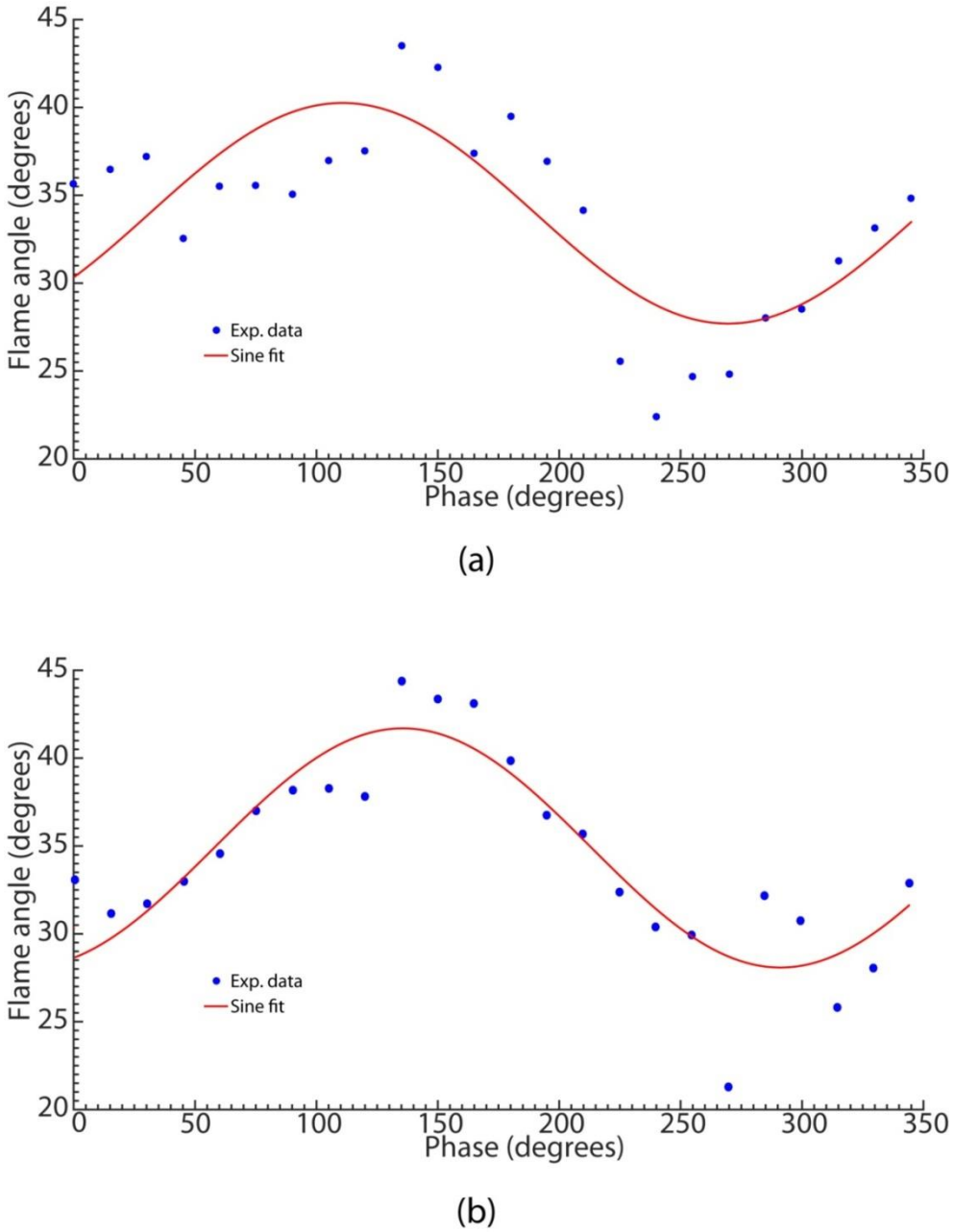

Figure 5-24: Flame angle variation with respect to phase of the acoustic cycle for (a) NPR-10-055-160-30 and (b) NPR-10-055-160-50.

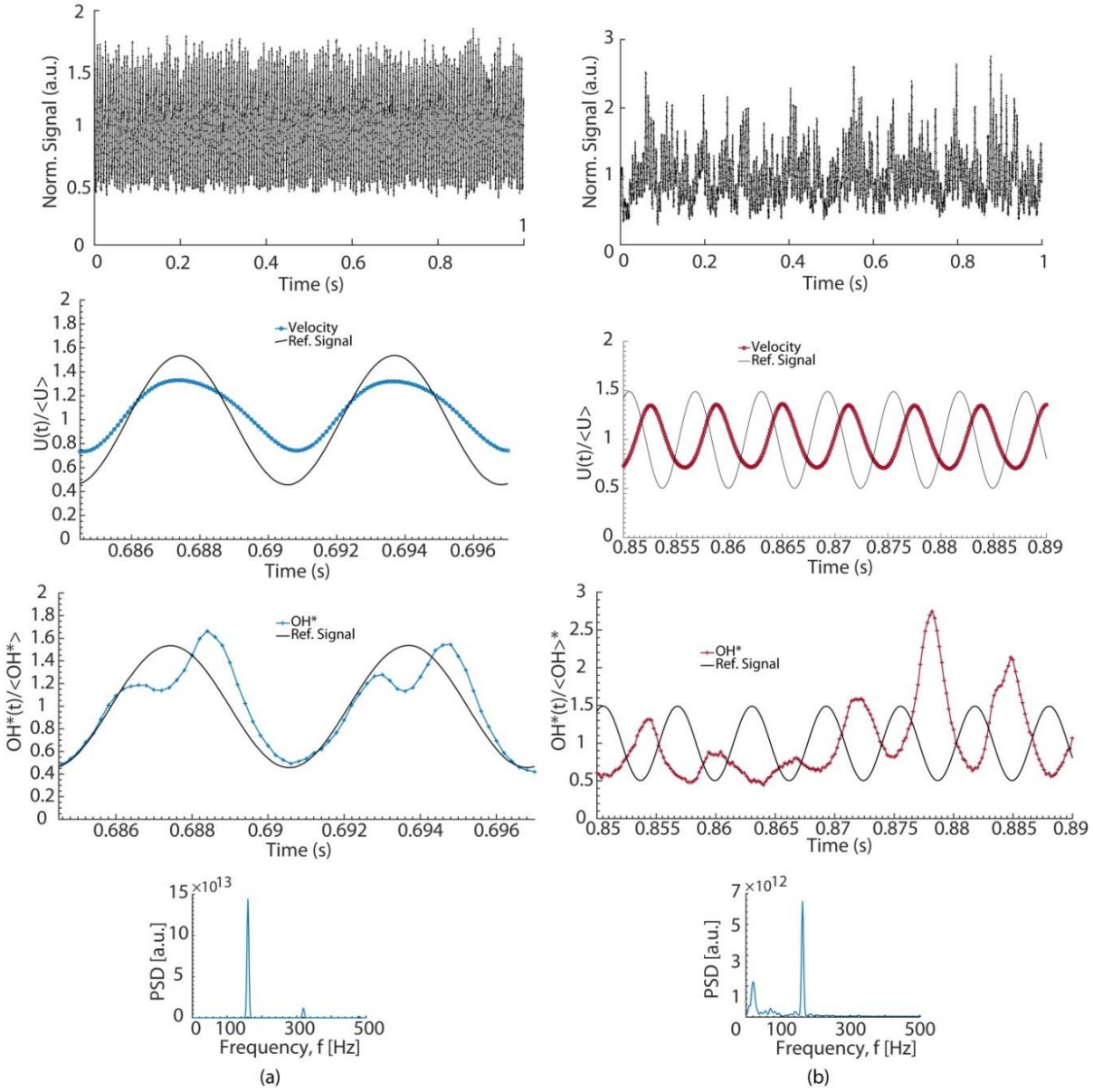

Figure 5-25: Time series of OH* chemiluminescence, the corresponding inlet velocity data, and the PSD of OH* chemiluminescence signal for (a) NPR-15-070-160-30 and (b) NPR-15-055-160-30.

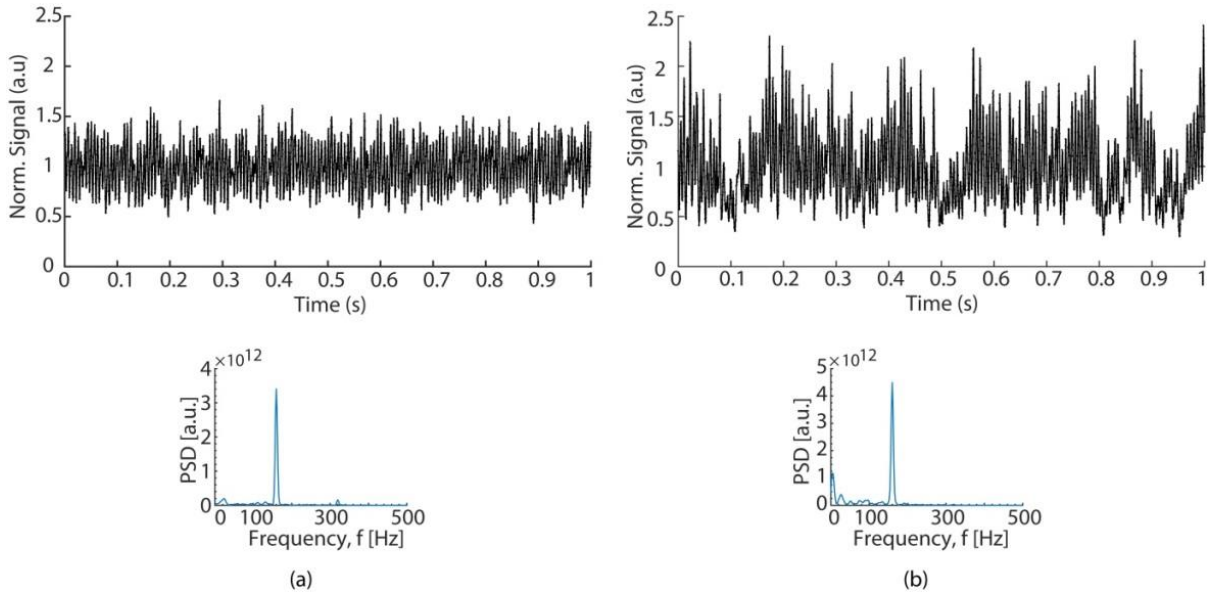

Figure 5-26: OH* chemiluminescence time series and power spectra of OH* chemiluminescence signal for (a) *A*=0.2 and (b) *A*=0.5 for NPR-10-055 forced at 160 Hz.

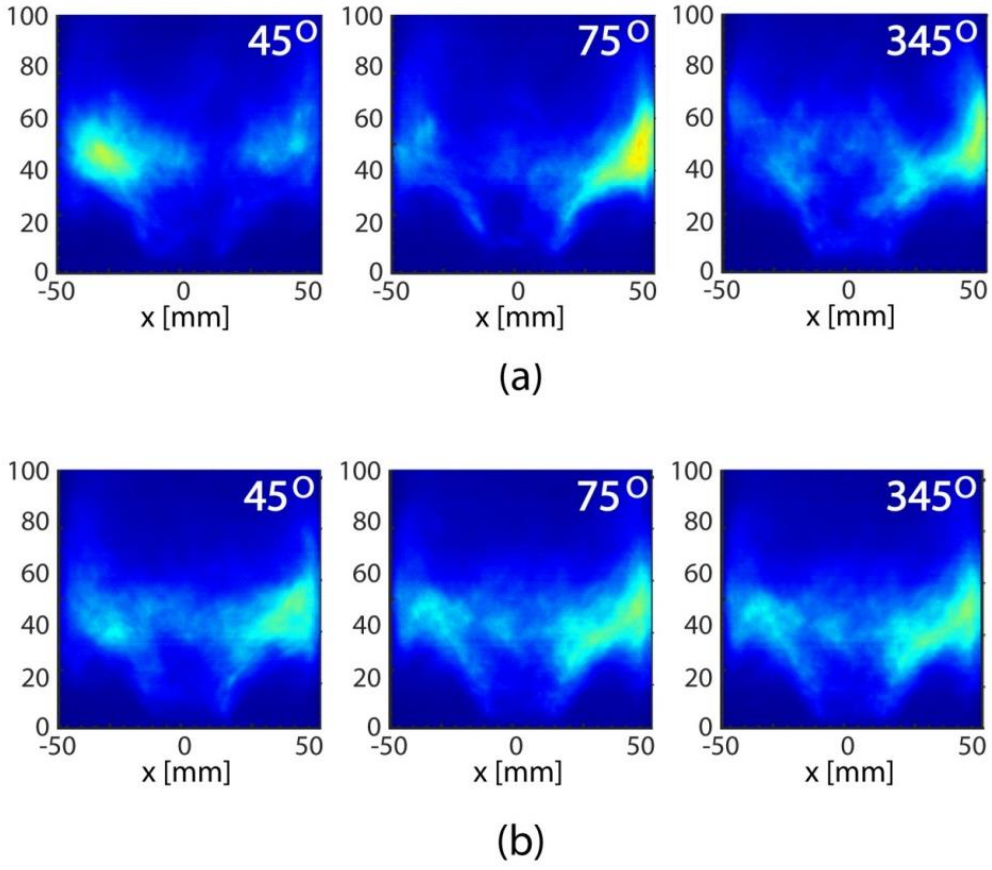

Figure 5-27: Phase-averaged OH* chemiluminescence images of NPR-10-055-160-50 at (a) 6 Hz and (b) 59 Hz.

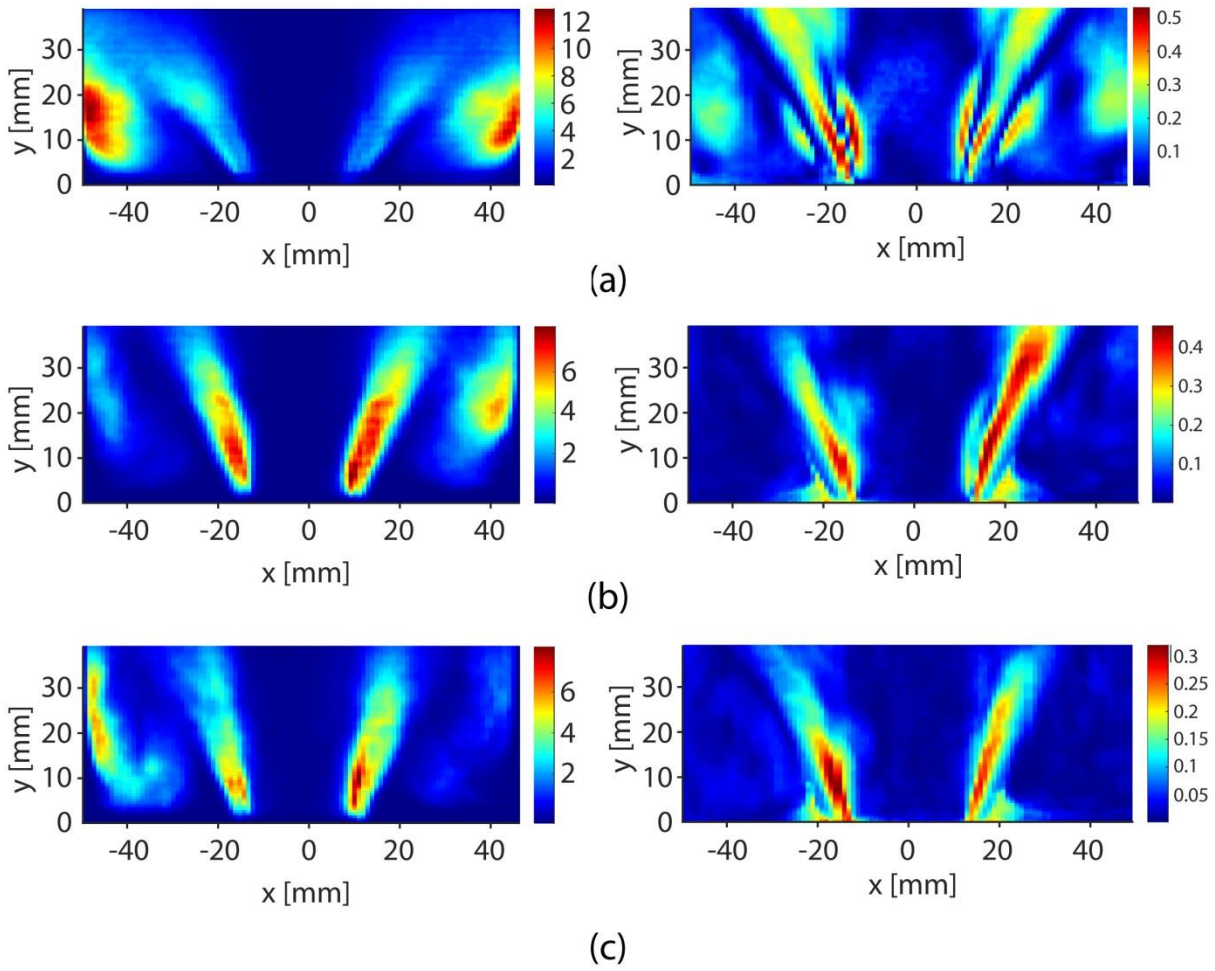

Figure 5-28: Variance of OH (left) and ratio R_L (OH fluctuation at 160 Hz to the total variance of OH) (right) for (a) NPR-15-070-160-30, (b) NPR-10-055-160-30 and (c) NPR-10-055-160-50.

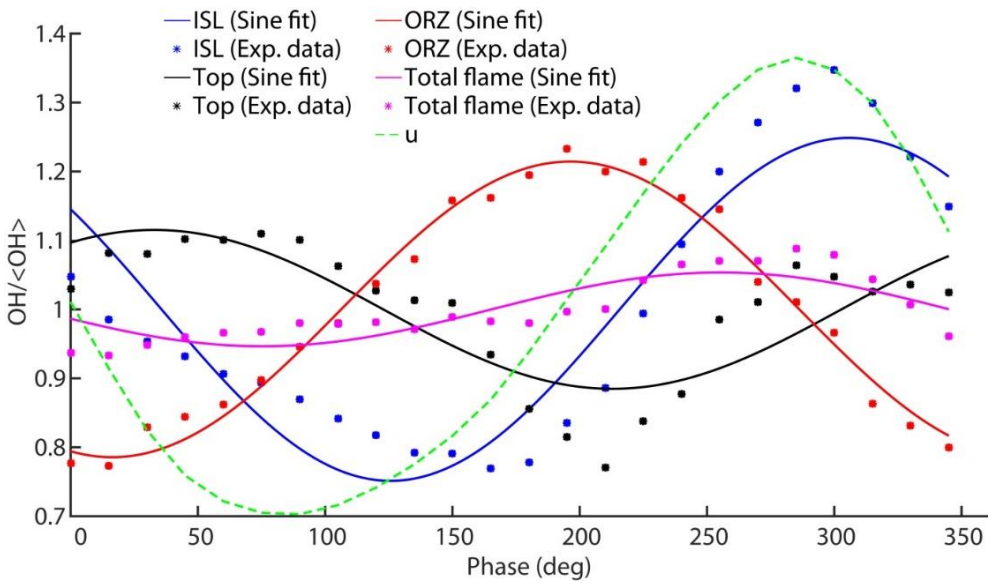

Figure 5-29: $OH/< OH >$ variation during the acoustic cycle, evaluated from phase-averaged OH PLIF images (data presented in Figure 5-16), calculated from the ISL, Top, ORZ and whole OH PLIF window. The green dashed line represents the normalised acoustic velocity fluctuations. Flame: NPR-15-070-160-30.

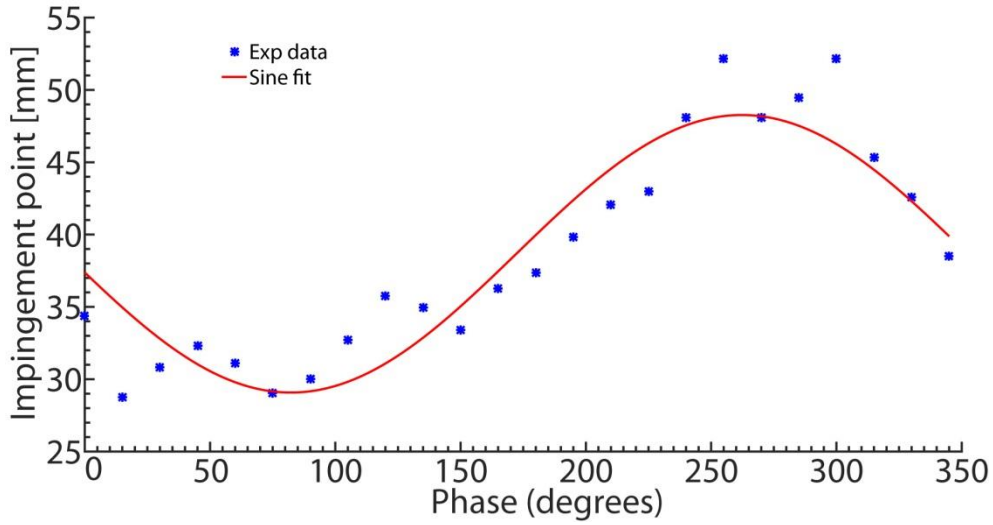

Figure 5-30: Impingement point position variation with respect to phase of the acoustic cycle for NPR-15-070-160-30.

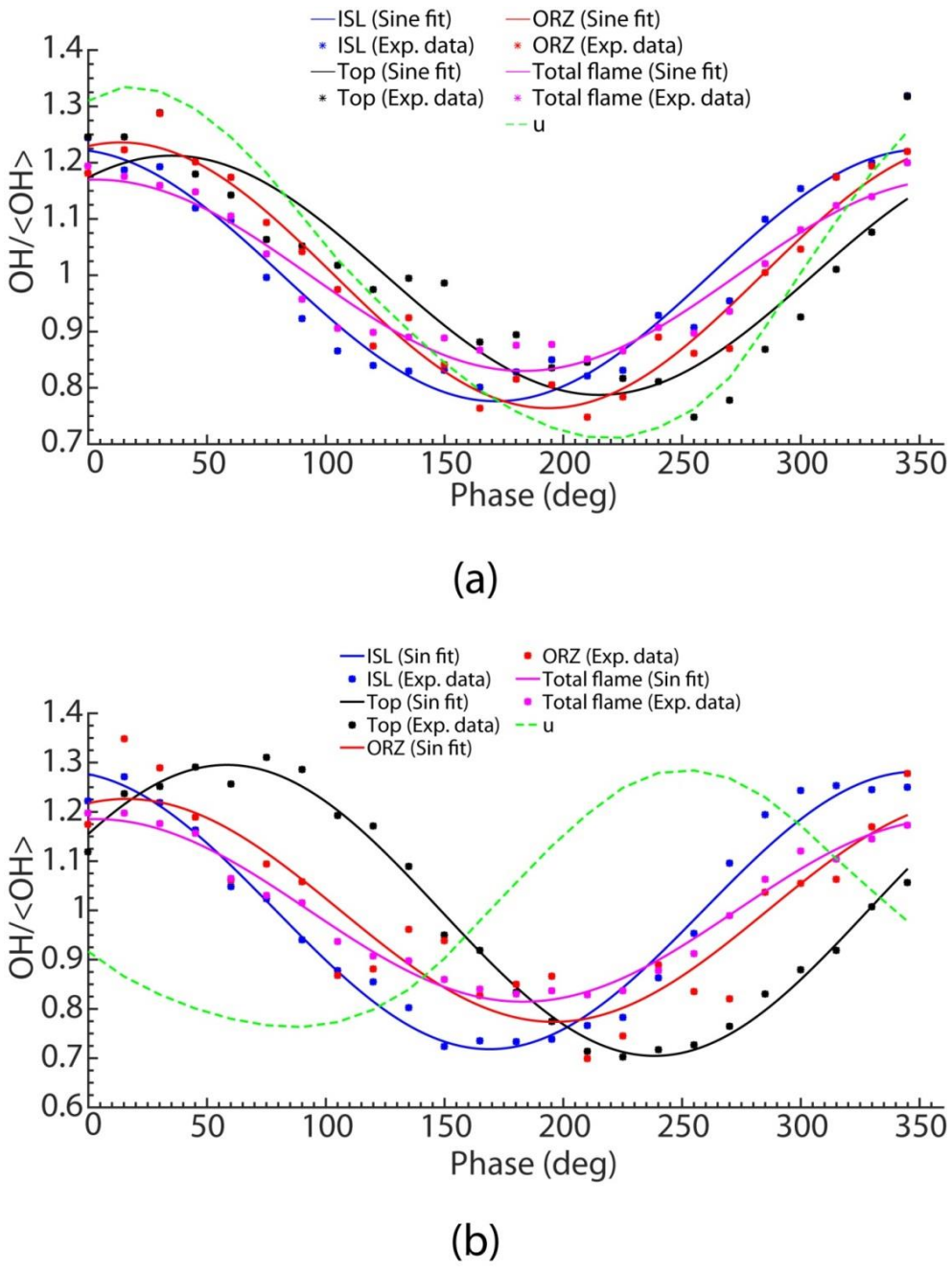

Figure 5-31: $OH/< OH >$ variation during the acoustic cycle, evaluated from phase-averaged OH PLIF images (data presented in Figure 5-21 and Figure 5-23), calculated from the ISL, Top, ORZ and whole OH PLIF window. The green dashed line represents the normalised acoustic velocity fluctuations for (a) NPR-10-055-160-30 and (b) NPR-10-055-160-50.

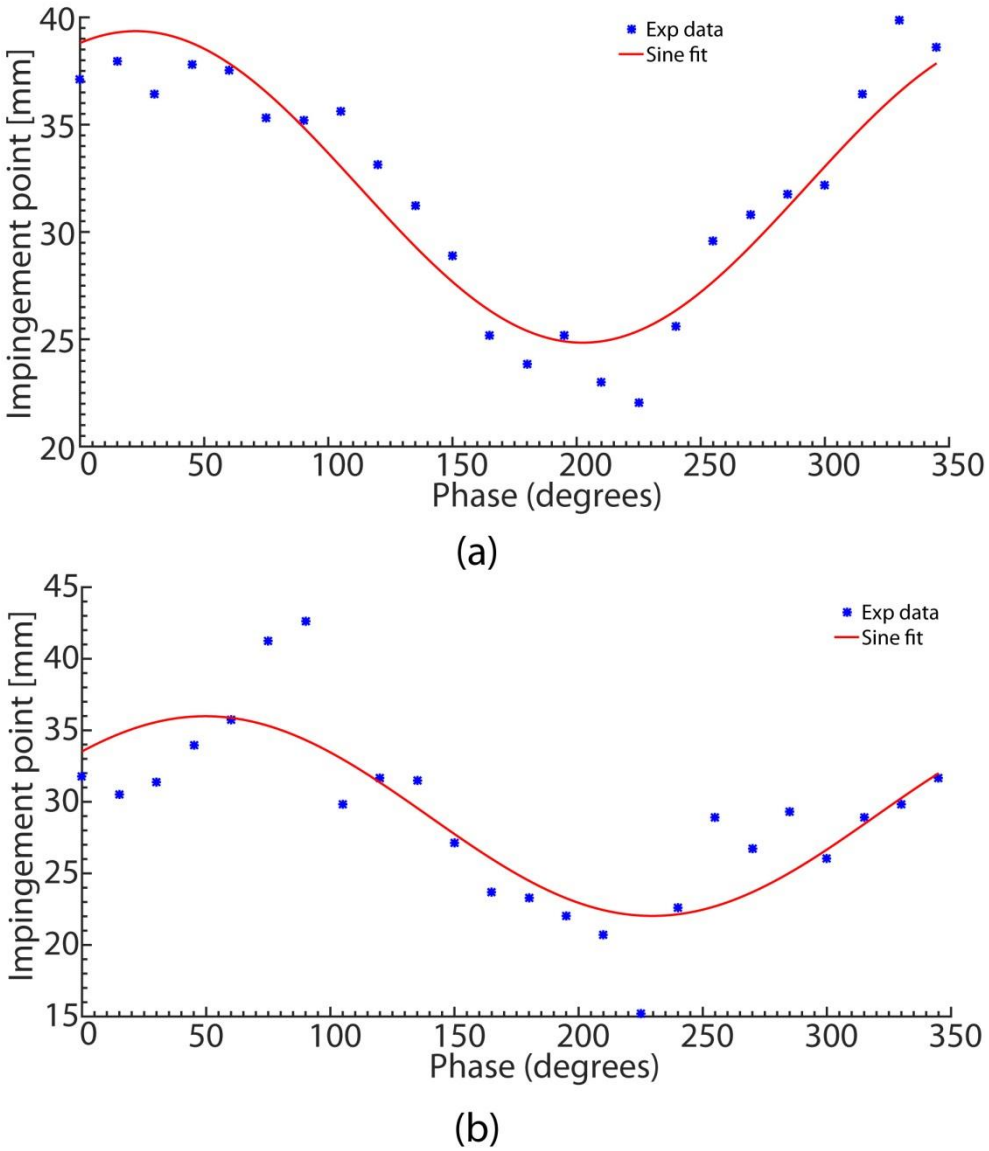

Figure 5-32: Impingement point position variation with respect to phase of the acoustic cycle for (a) NPR-10-055-160-30 and (b) NPR-10-055-160-50.

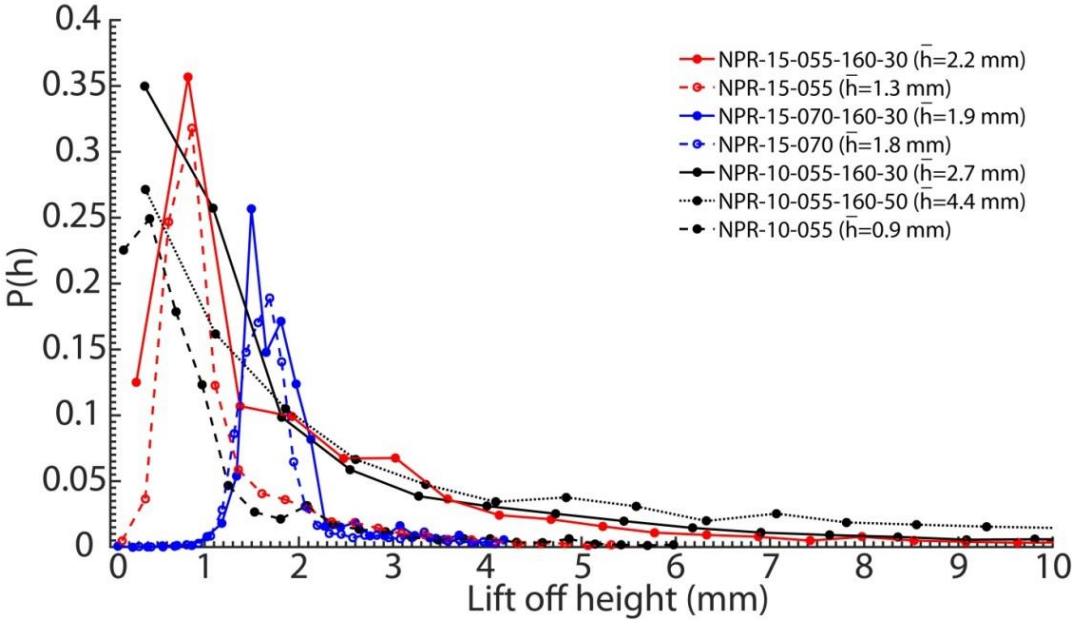

Figure 5-33: Probability density function of the lift-off height, $P(h)$, with respect to h for both the forced and unforced flames presented in Table 5-1. The average lift-off height $\bar{h}$ is indicated.

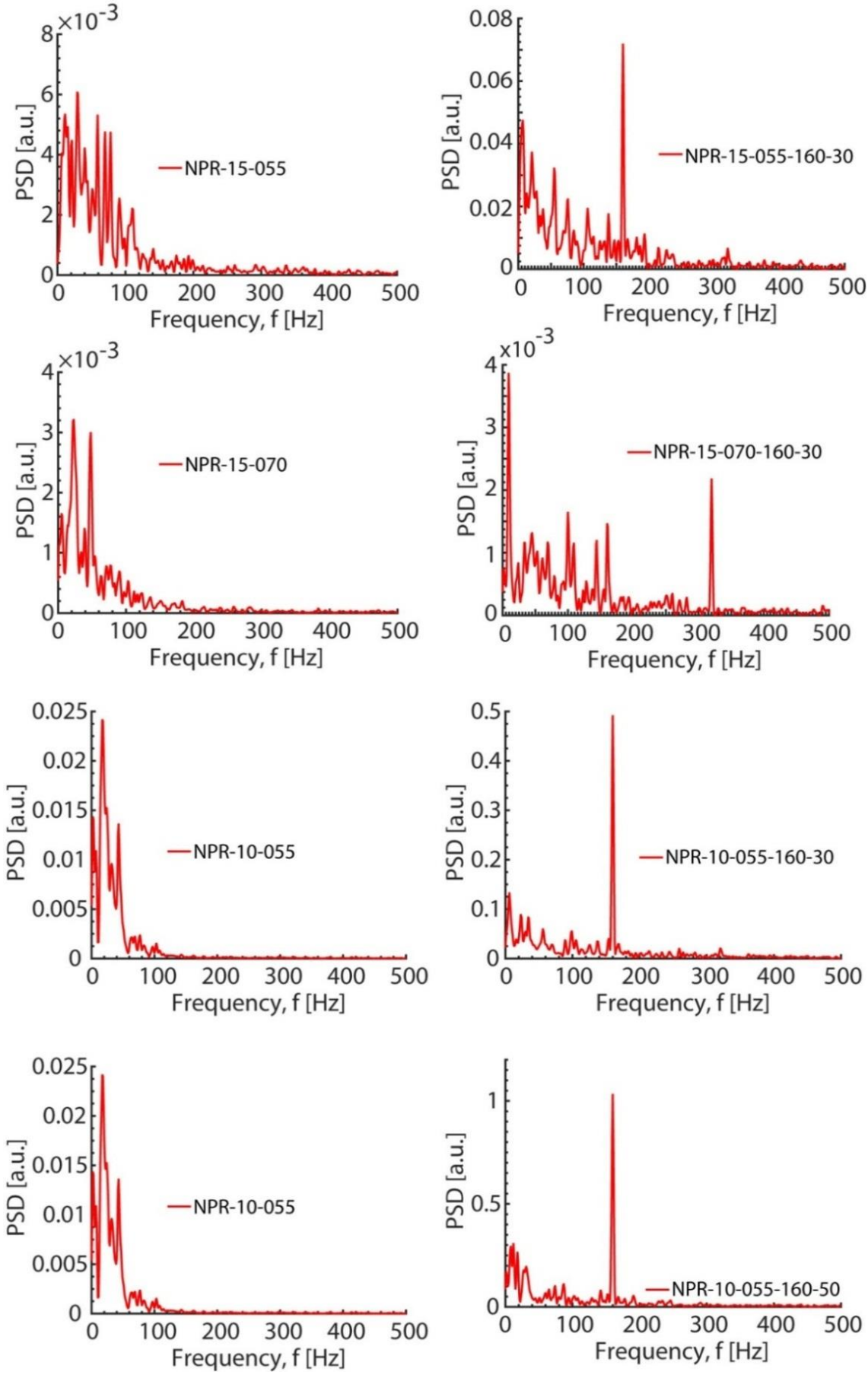

Figure 5-34: Power spectra of lift-off height.

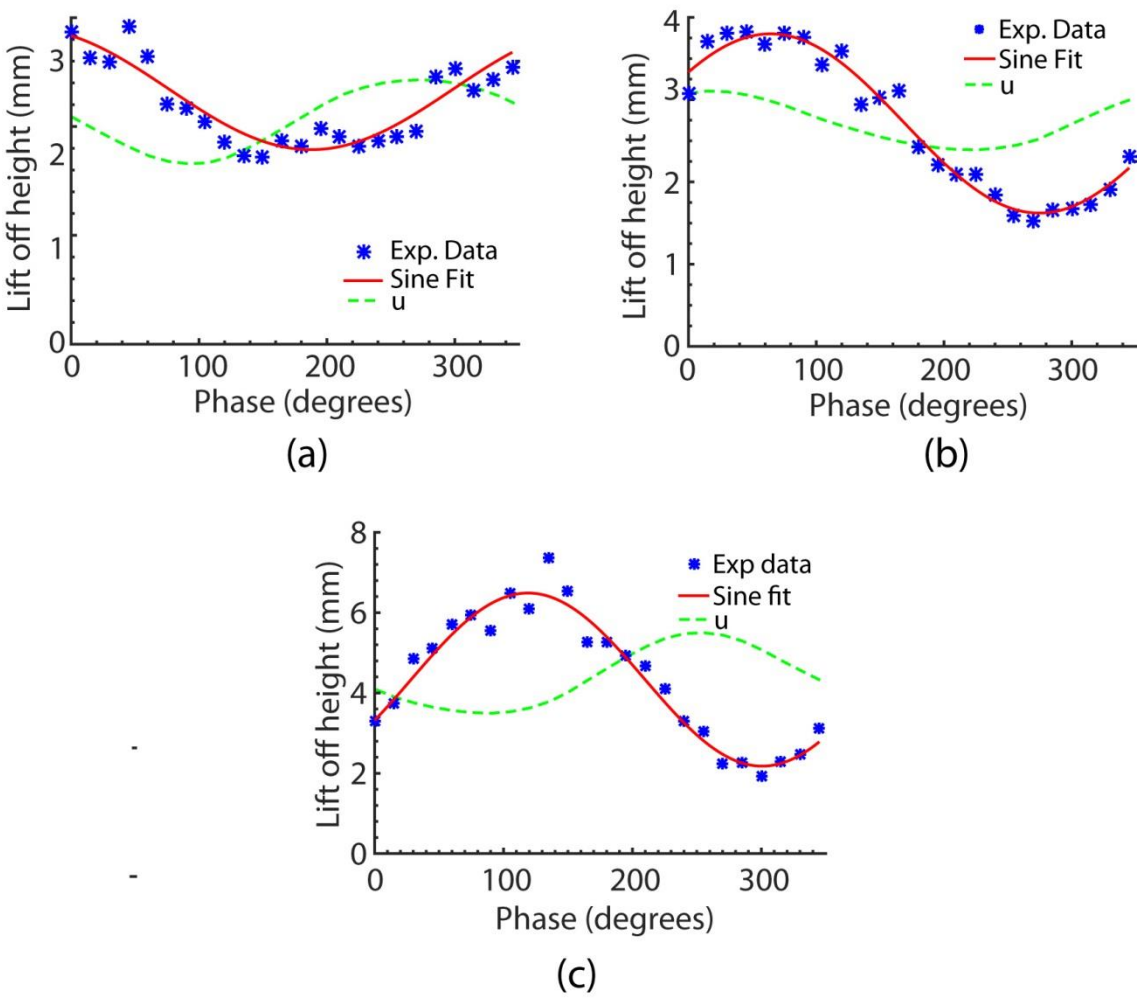

Figure 5-35: Lift-off height with respect to phase for (a) NPR-15-055-160-30, (b) NPR-10-055-160-30 and (c) NPR-10-055-160-50.

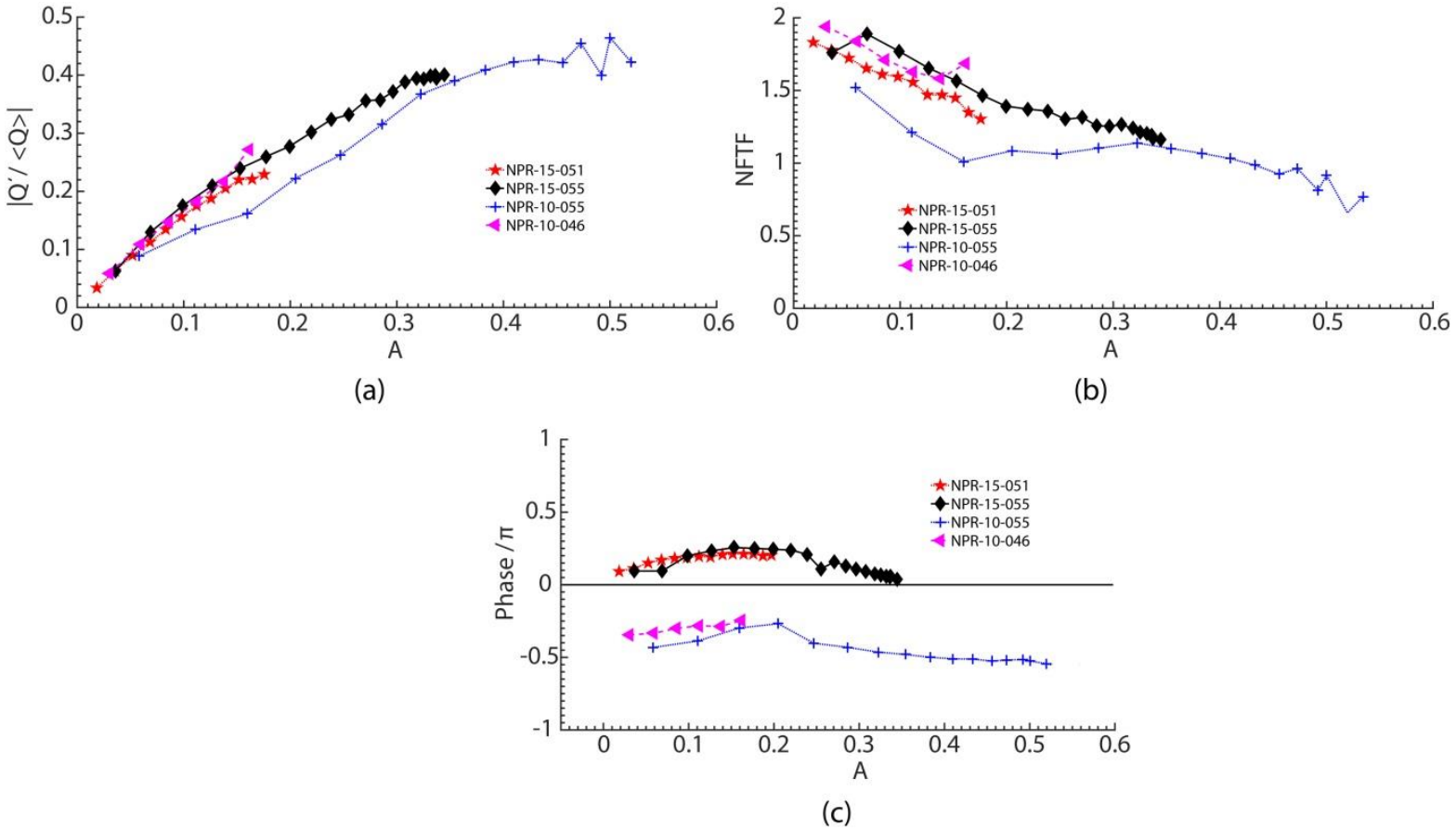

Figure 5-36: (a) Normalised global heat release fluctuations of NPR-15-055, NPR-15-051, NPR-10-055 and NPR-10-046 measured as a function of *A* using OH* chemiluminescence, (b) the corresponding transfer function and (c) its phase evaluated from the data of (a).

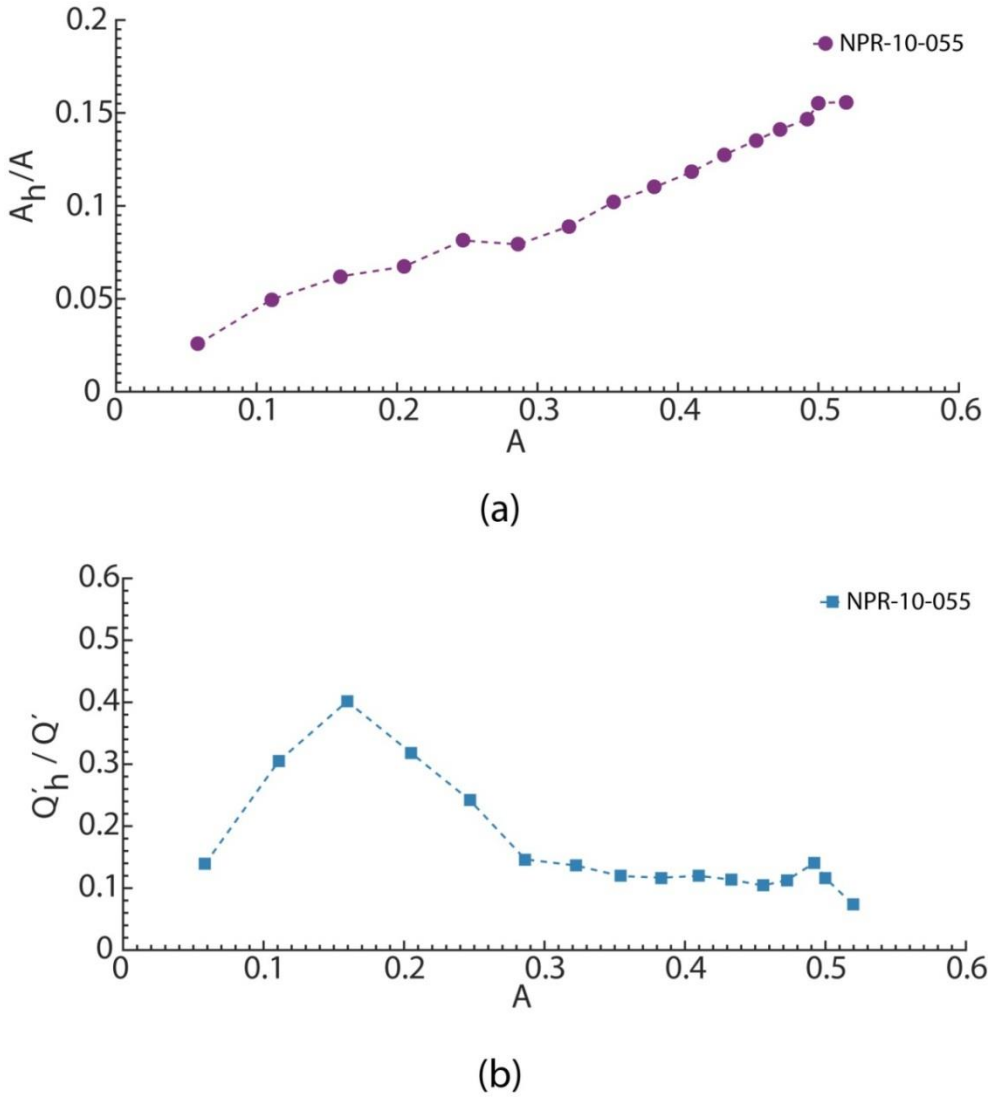

Figure 5-37: (a) Ratio of amplitude of inlet velocity fluctuation at first harmonic (320 Hz) A_h, to that at the forcing frequency (160 Hz), A, with respect to A, and (b) ratio of heat release fluctuation at the first harmonic (320 Hz) to that of the forcing frequency (160 Hz), (Q'_h/Q'), as a function of A. Flame: NPR-10-055.

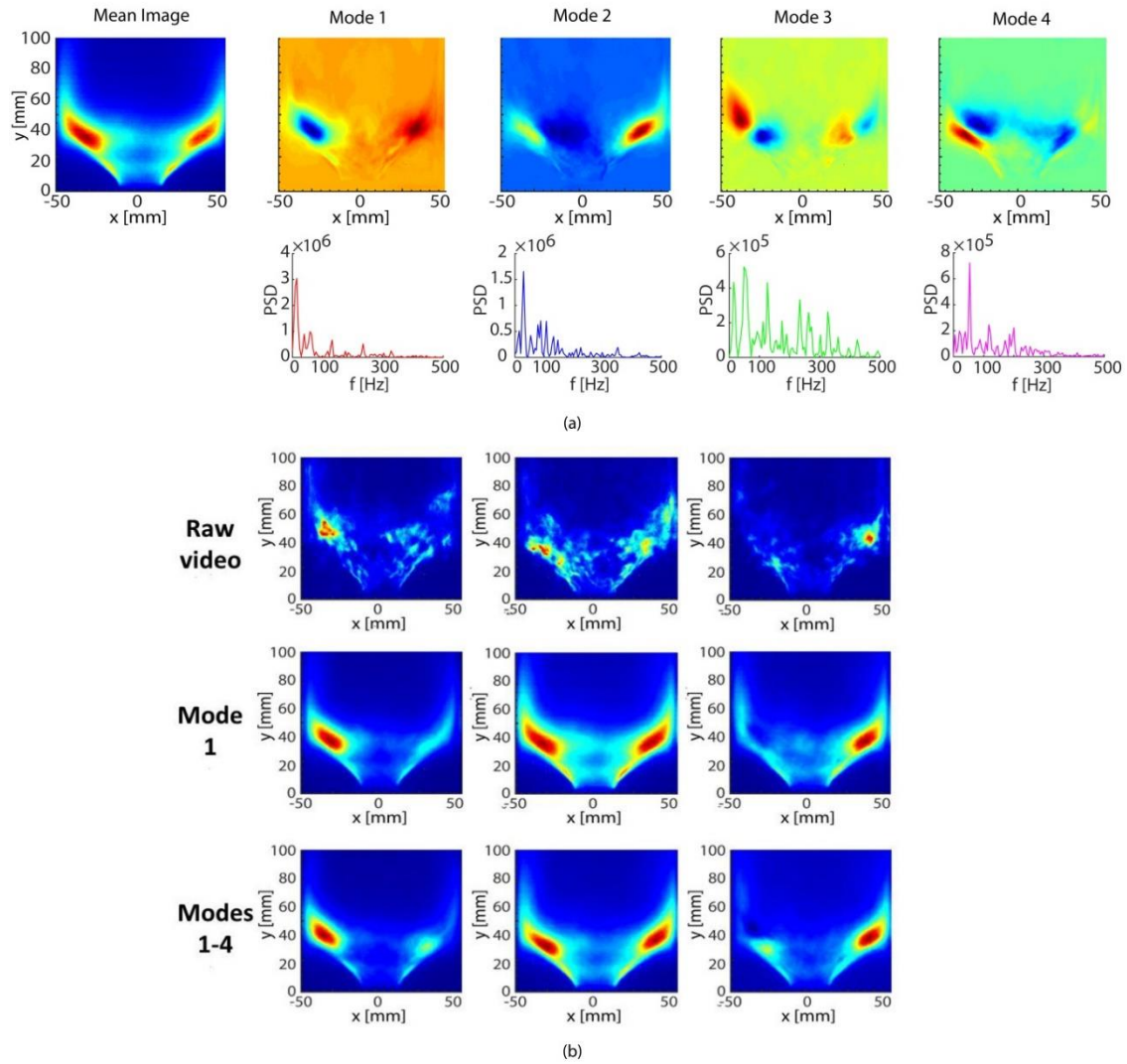

Figure 5-38: (a) Mean image and first four OH* chemiluminescence POD Modes and the respective PSD of POD time coefficients. (b) Instantaneous OH* chemiluminescence images (first row), and snapshots at the same times from reconstructed OH* movie using the mean and Mode 1 only (second row) and the mean and Modes 1-4 (third row). Flame: NPR-15-055

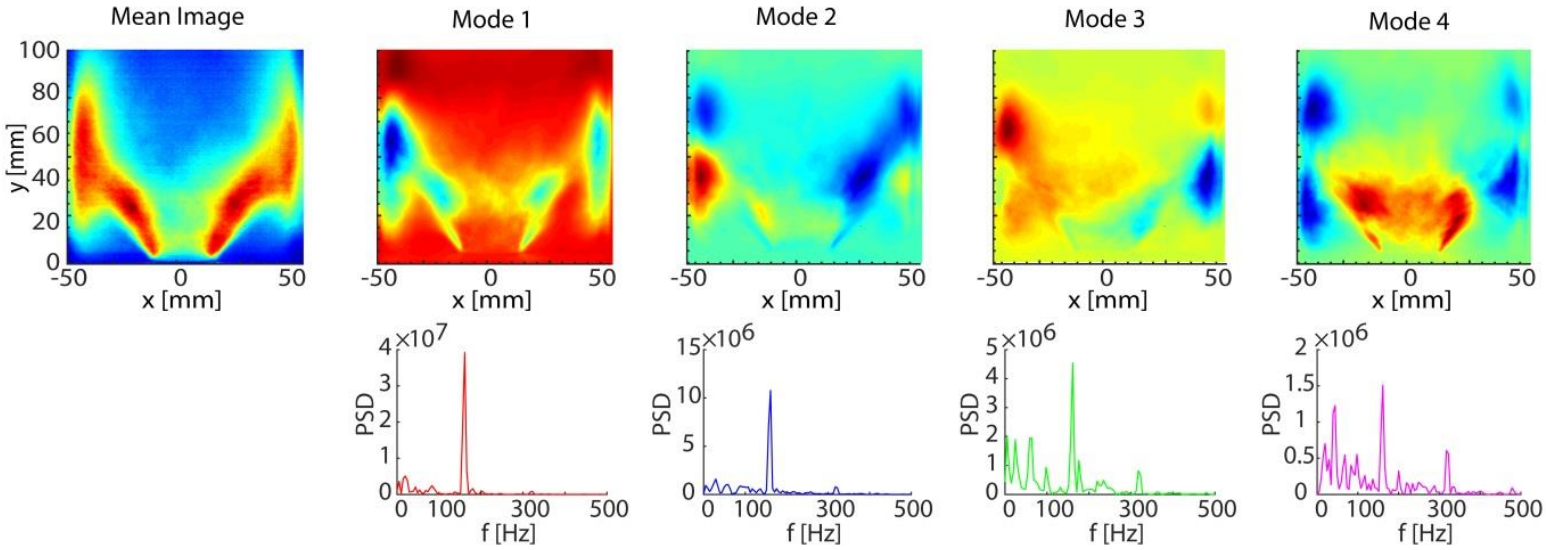

Figure 5-39: Mean Image and first four OH* chemiluminescence POD Modes and respective PSD of POD time coefficients for NPR-15-055-160-30.

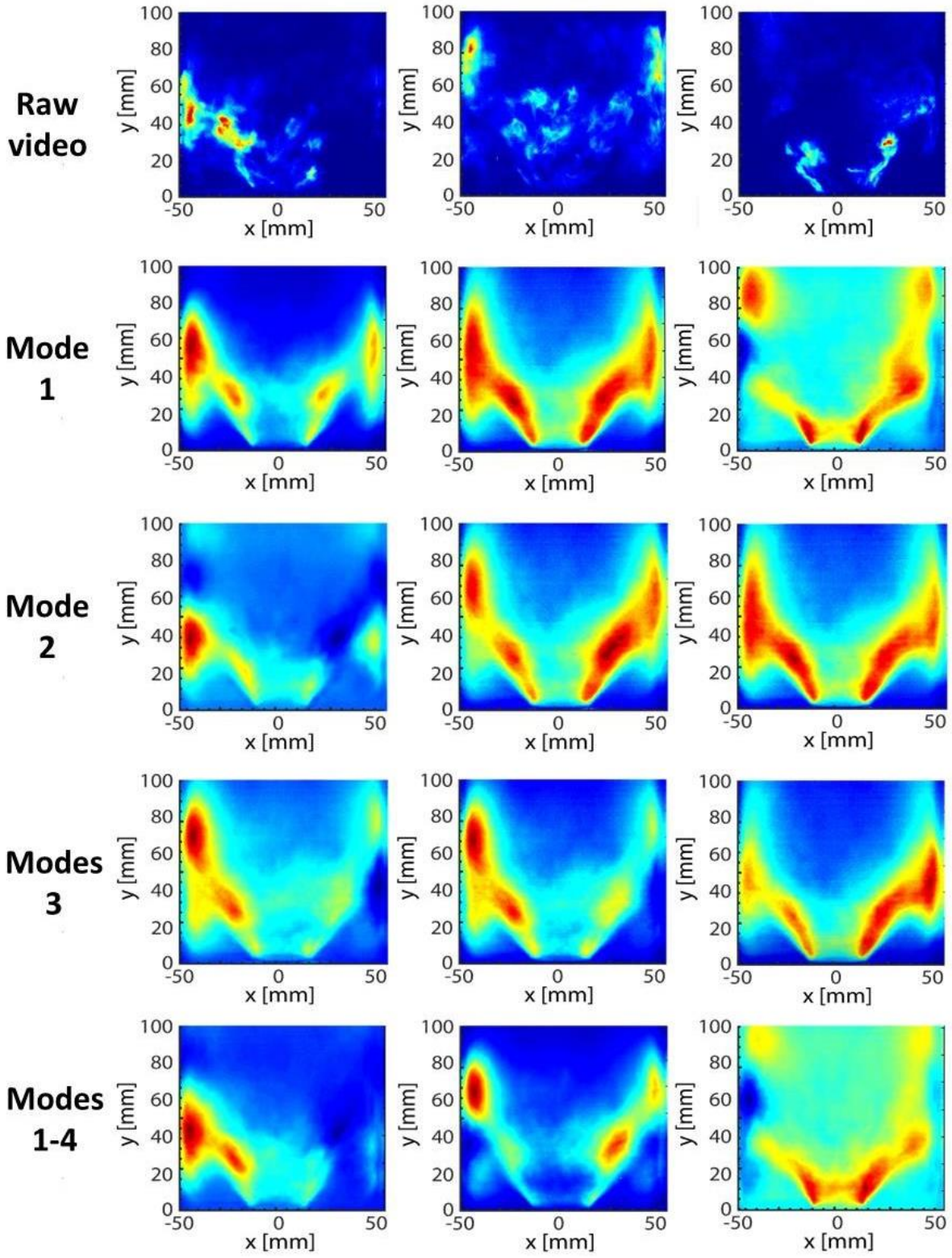

Figure 5-40: Instantaneous OH* chemiluminescence images (first row), and snapshots at the same times from reconstructed OH* movie using the mean and Mode 1 only (second row), the mean and Mode 2 only (third row), the mean and Mode 3 only (fourth row) and the mean and Modes 1-4 (fifth row) for NPR-15-055-160-30.

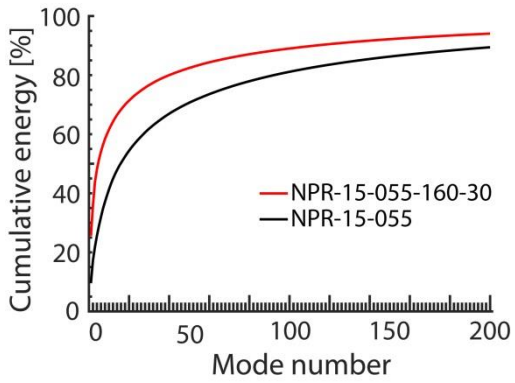

Figure 5-41: Cumulative energy of OH* chemiluminescence POD Modes of NPR-15-055 and NPR-15-055-160-30.

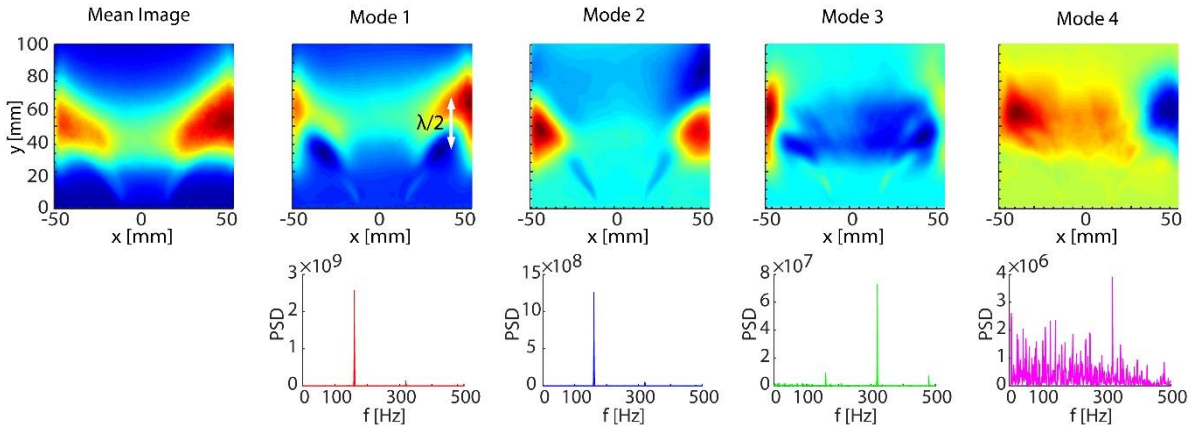

Figure 5-42: Mean Image and first four OH* chemiluminescence POD Modes and respective PSD of POD time coefficients for NPR-15-070-160-30.

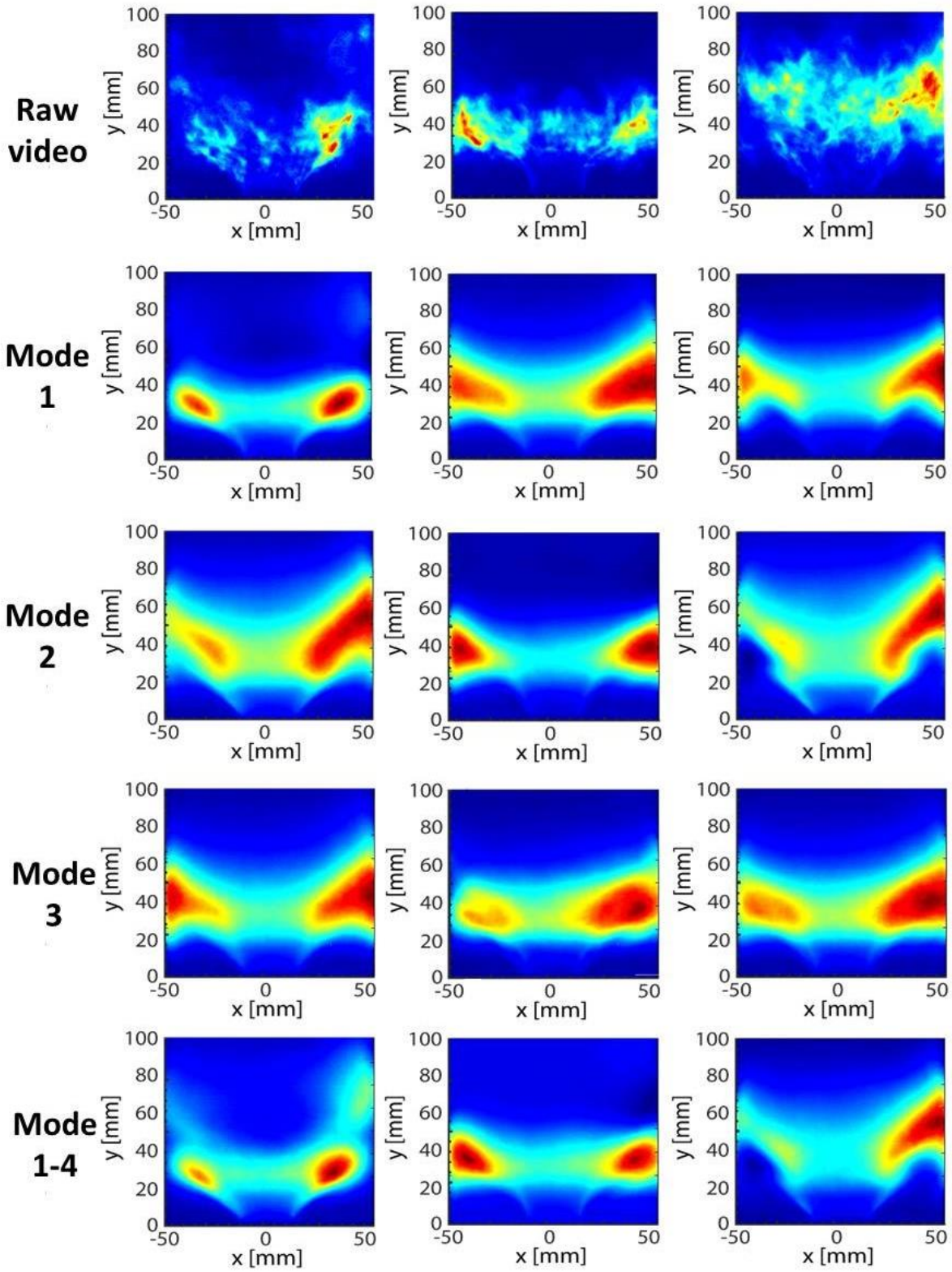

Figure 5-43: Instantaneous OH* chemiluminescence images (first row), and snapshots at the same times from reconstructed OH* movie using the mean and Mode 1 only (second row), the mean and Mode 2 only (third row), the mean and Mode 3 only (fourth row) and the mean and Modes 1-4 (fifth row) for NPR-15-070-160-30.

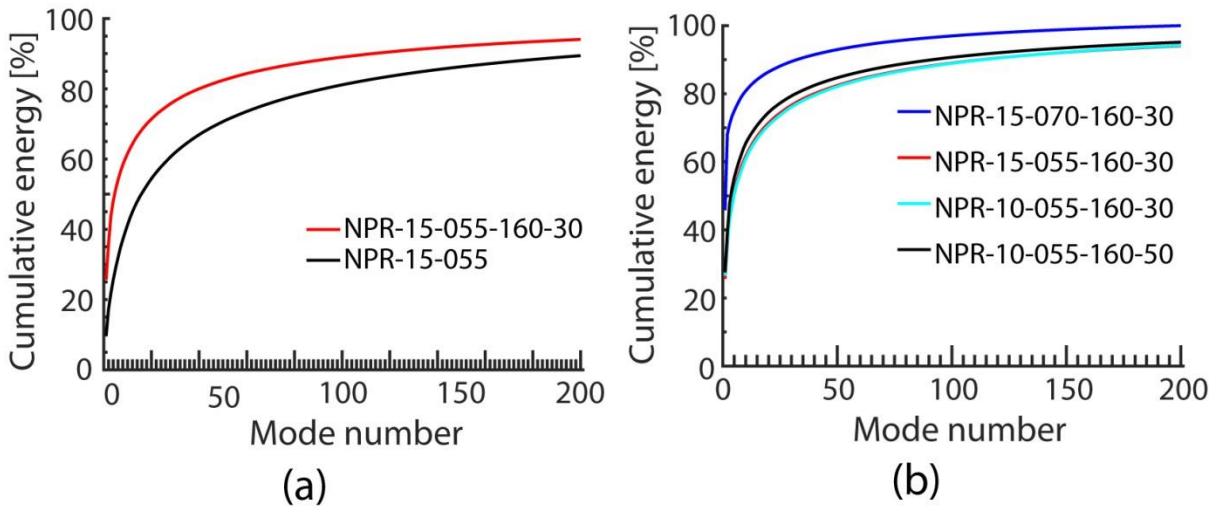

Figure 5-44: (a) Cumulative energy of OH* chemiluminescence POD Modes of NPR-15-070 and NPR-15-070-160-30 and (b) comparison of the cumulative energies of NPR-15-055-160-30, NPR-15-070-160-30, NPR-10-055-160-30 and NPR-10-055-160-50.

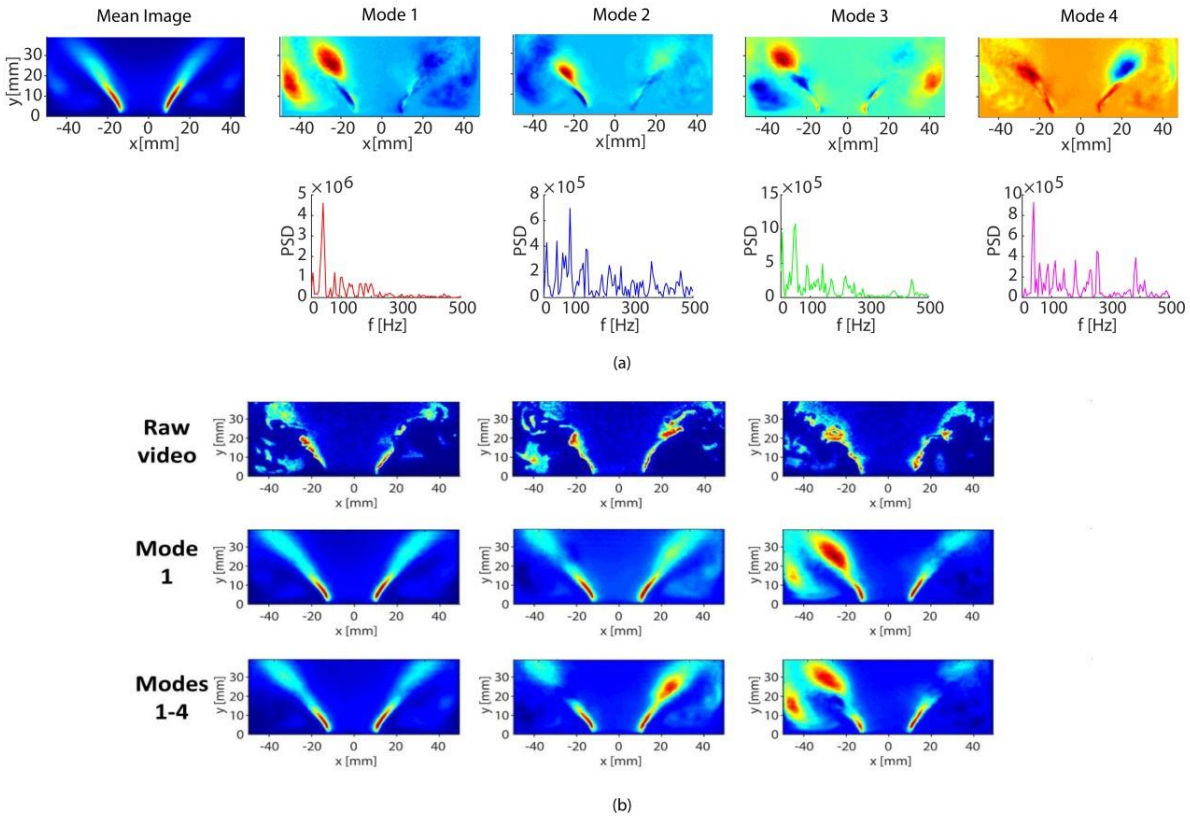

Figure 5-45: (a) Mean Image and first four OH PLIF POD Modes and respective PSD of POD time coefficients. (b) Instantaneous OH PLIF images (first row), and snapshots at the same times from reconstructed OH PLIF movie using the mean and Mode 1 only (second row) and the mean and Modes 1-4 (third row). Flame: NPR-15-055.

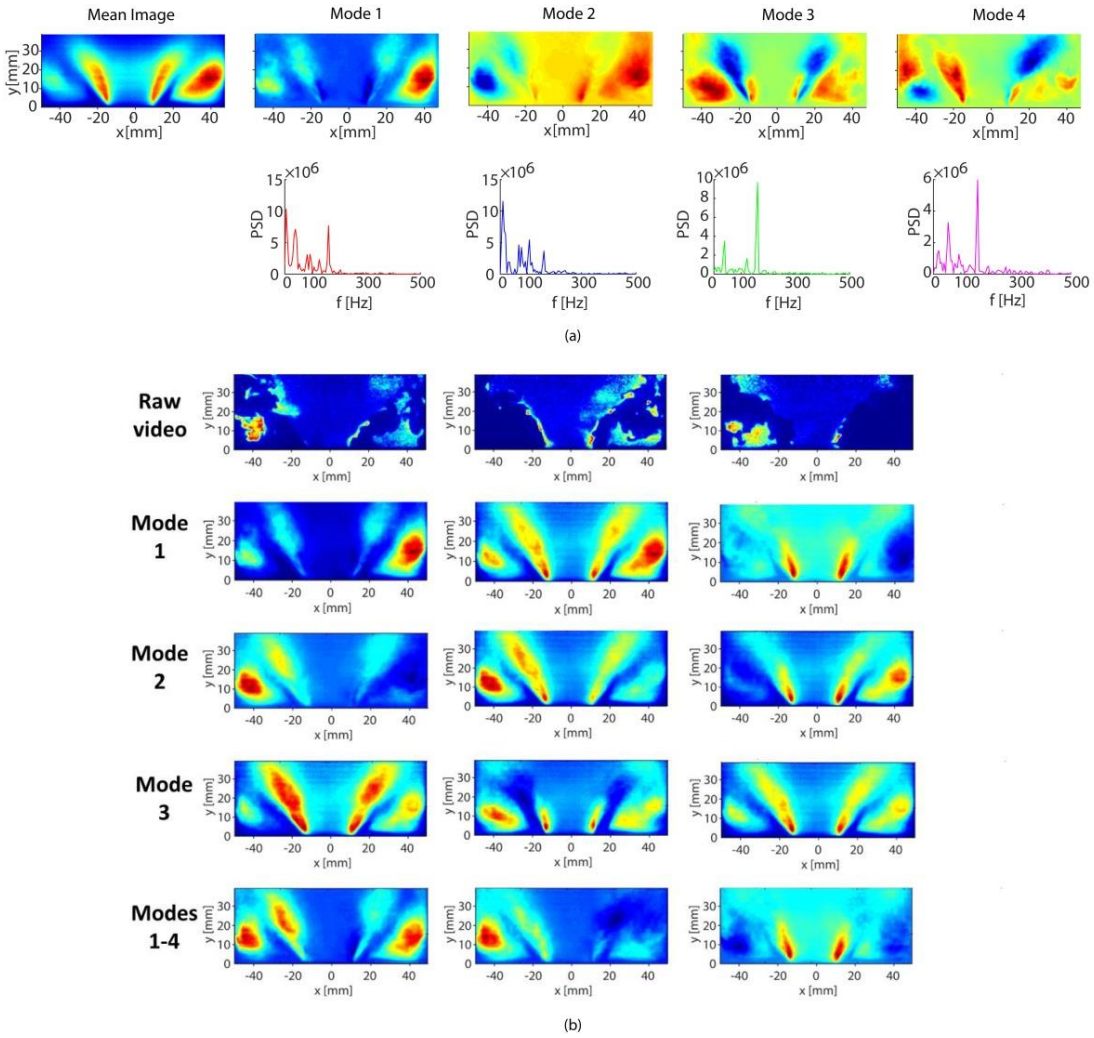

Figure 5-46: (a) Mean Image and first four OH PLIF POD Modes and respective PSD of POD time coefficients. (b) Instantaneous OH PLIF images (first row), and snapshots at the same times from reconstructed OH PLIF movie using the mean and Mode 1 only (second row), the mean and Mode 2 only (third row), the mean and Mode 3 only (fourth row) and the mean and Modes 1-4 (fifth row). Flame: NPR-15-055-160-30.

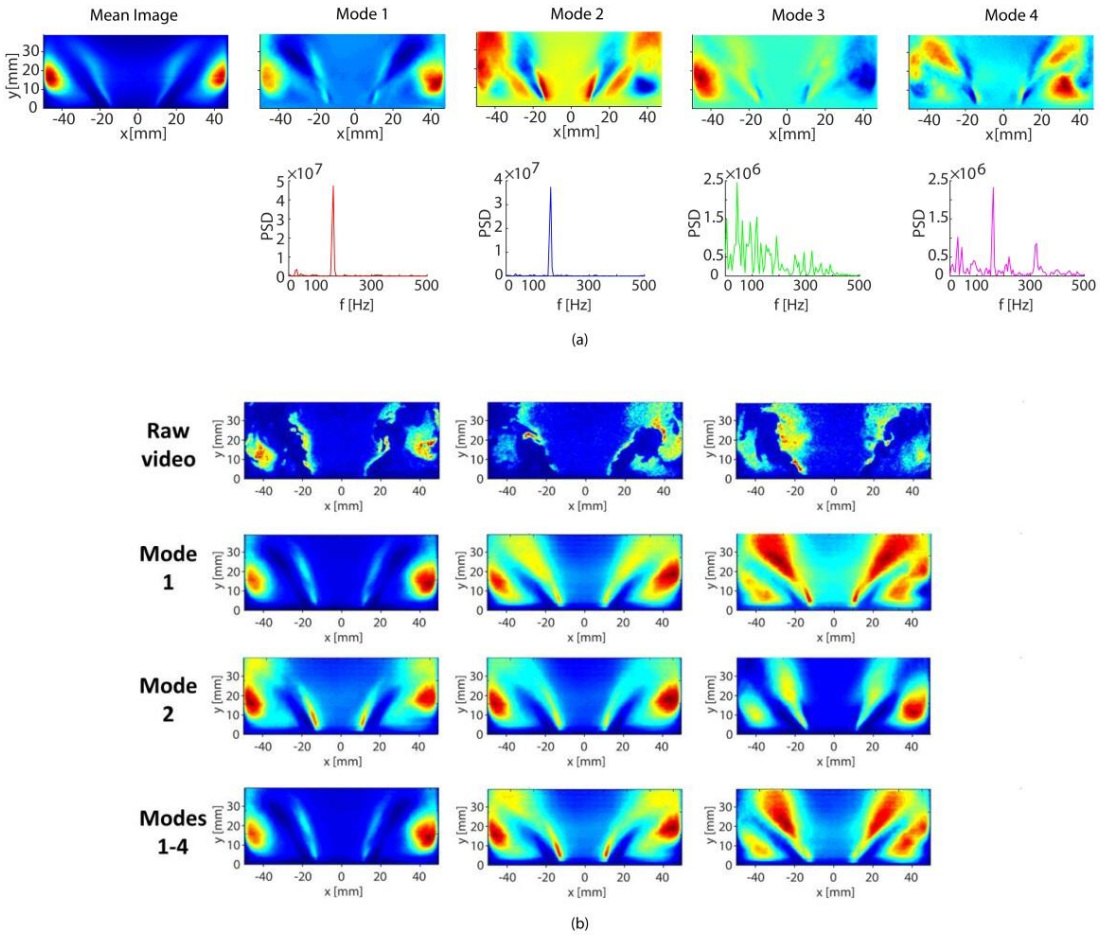

Figure 5-47: (a) Mean Image and first four OH PLIF POD Modes and respective PSD of POD time coefficients. (b) Instantaneous OH PLIF images (first row), and snapshots at the same times from reconstructed OH PLIF movie using the mean and Mode 1 only (second row), the mean and Mode 2 only (third row), and the mean and Modes 1-4 (fourth row). Flame: NPR-15-070-160-30.

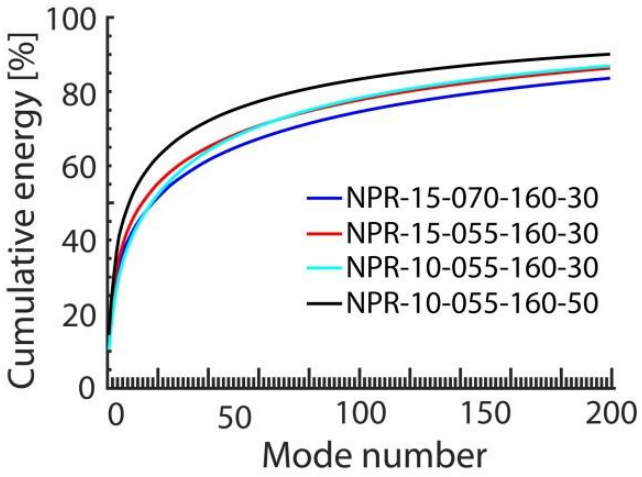

Figure 5-48: Cumulative energy of OH PLIF POD Modes of NPR-15-055-160-30, NPR-15-070-160-30, NPR-10-055-160-30 and NPR-10-055-160-50.

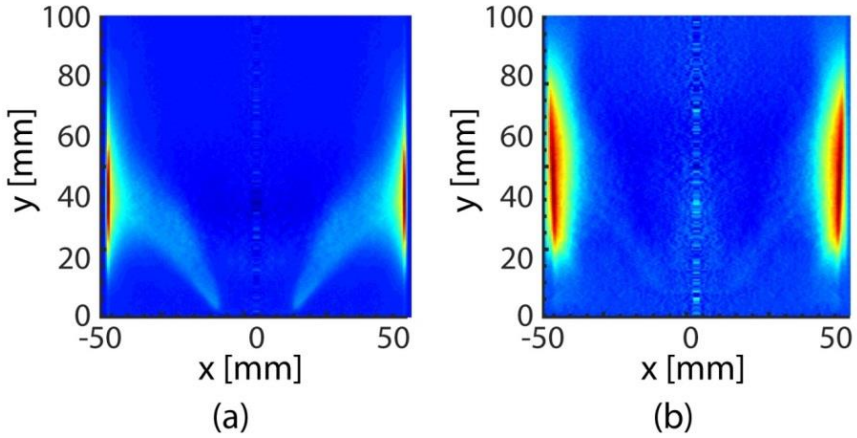

Figure 5-49: Inverse Abel transformed mean OH* chemiluminescence image of (a) NPR-15-070-160-30 and (b) P-15-070-160-30.

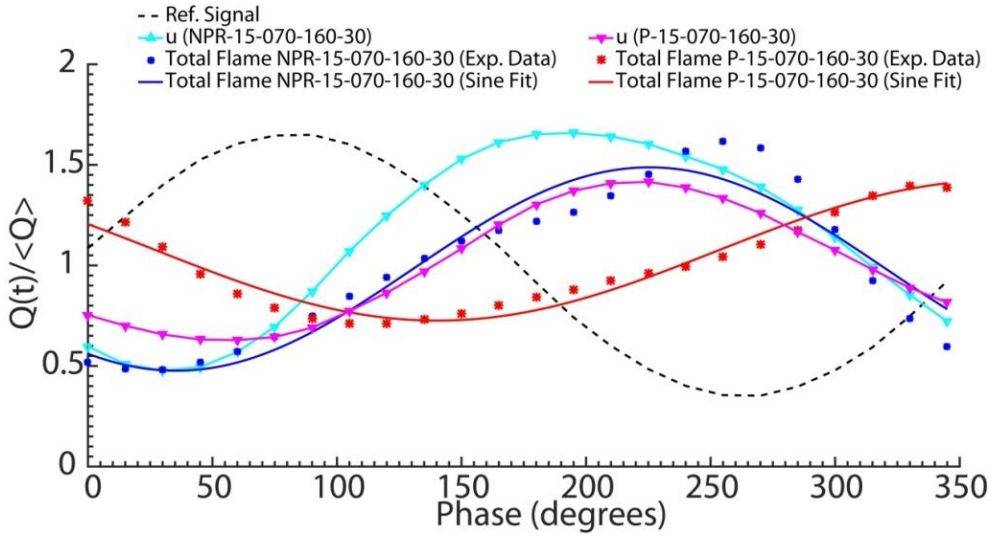

Figure 5-50: Comparison of OH* chemiluminescence variation over the forcing cycle for NPR-15-070-160-30 and P-15-070-160-30 (data presented in Figure 5-12 and Figure 4-6 respectively). The normalised acoustic velocity fluctuations are also presented.

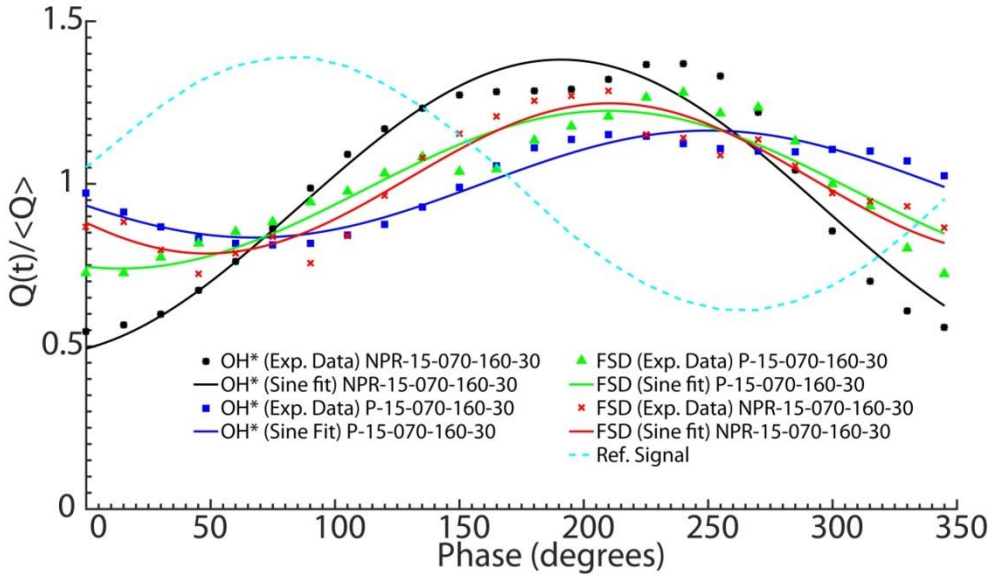

Figure 5-51: Comparison of the cyclic FSD variation, evaluated from the phase-averaged FSD images, presented in Figure 5-17 and Figure 4-9, revolved around the burner central axis, and the cyclic OH* chemiluminescence variation both based on a 40 mm window (40 mm is the height of the OH PLIF laser sheet) for NPR-15-070-160-30 and P-15-070-160-30.

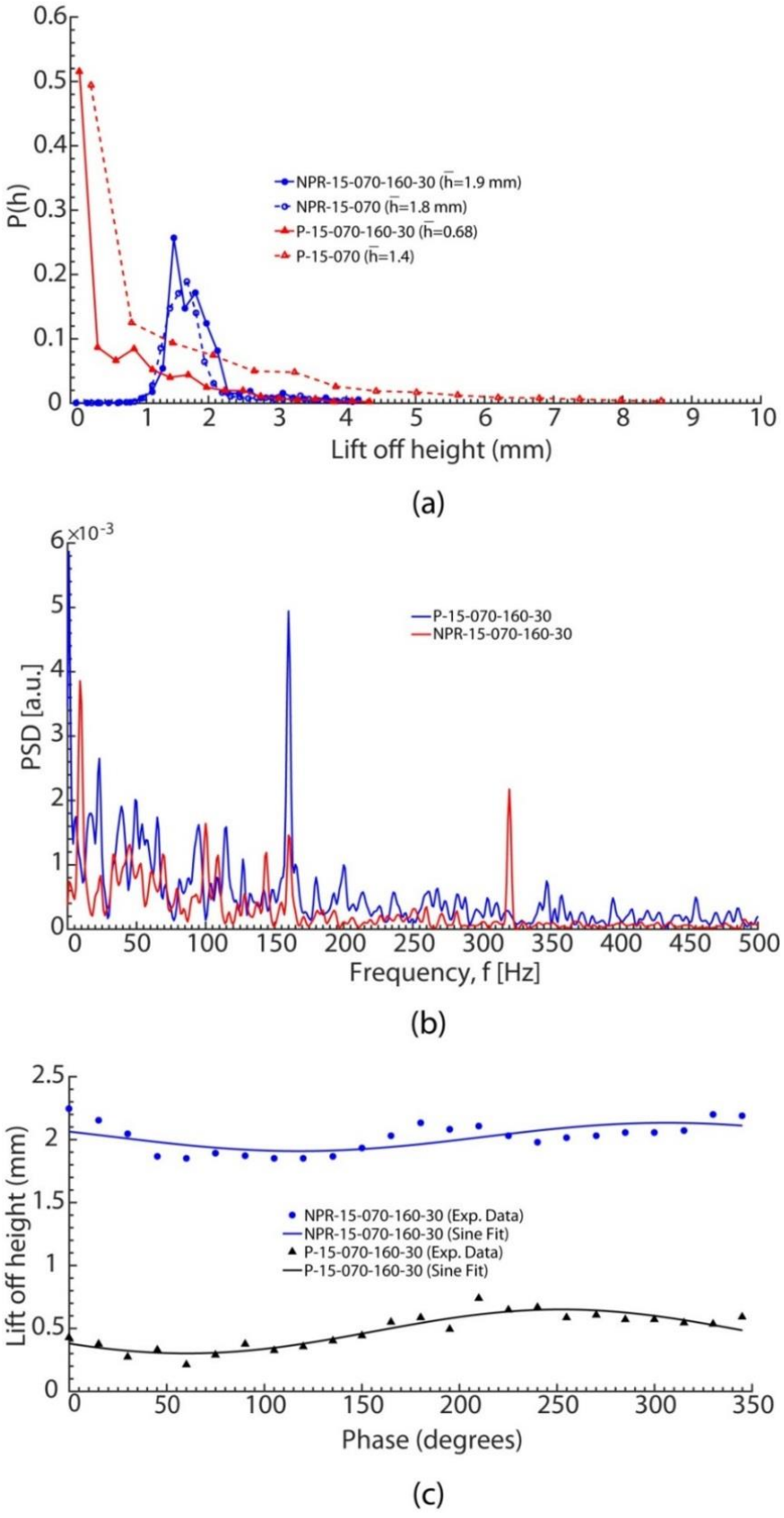

Figure 5-52: (a) Probability density function of the lift-off height, $P(h)$, with respect to h, (b) power spectra of lift-off height and (c) lift-off height with respect to phase for NPR-15-070-160-30 and P-15-070-160-30.

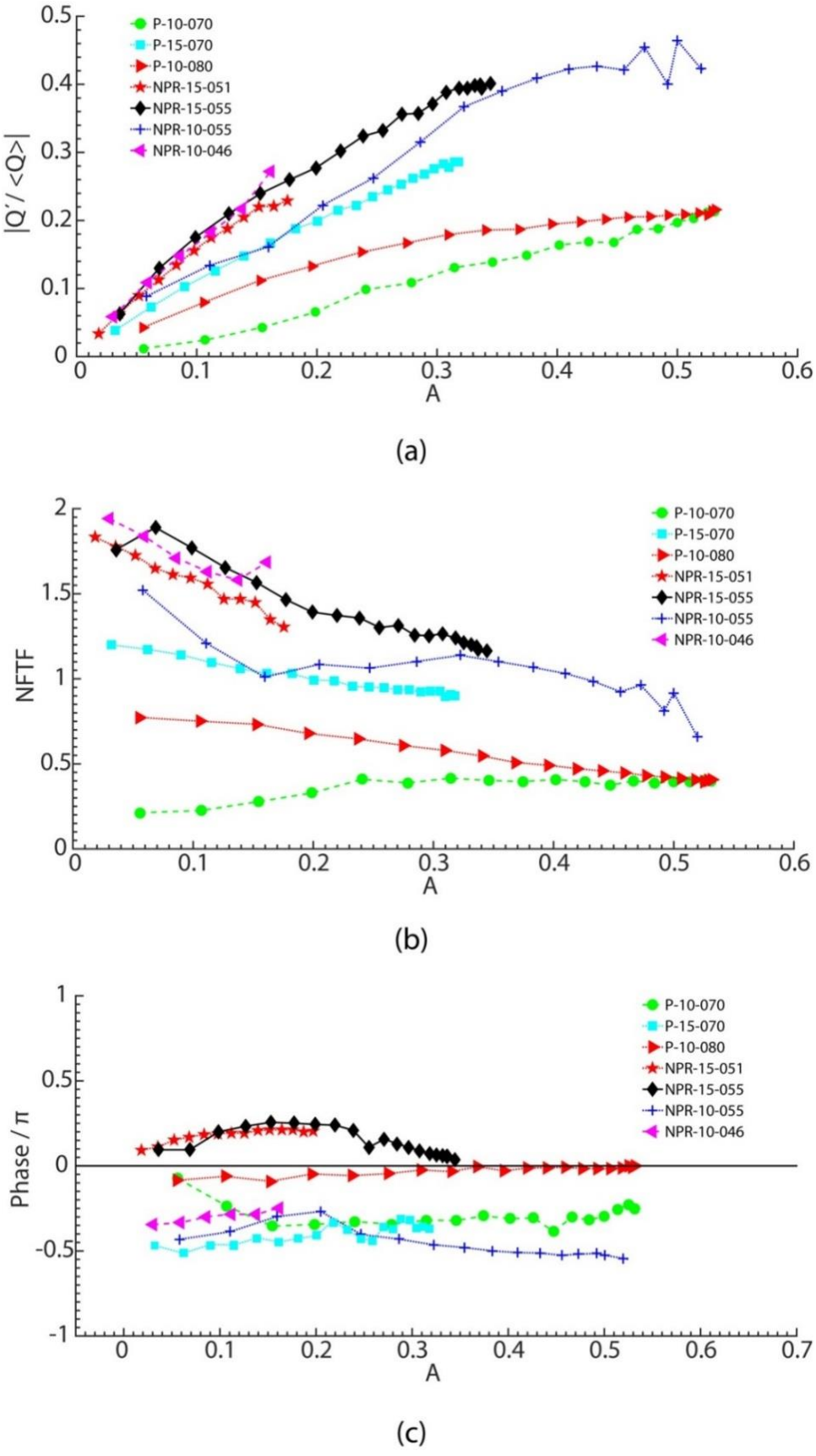

Figure 5-53: (a) Normalised global heat release fluctuations of NPR and Premixed flames measured as a function of *A* using OH* chemiluminescence, (b) the corresponding transfer function and (c) its phase evaluated from the data of (a).

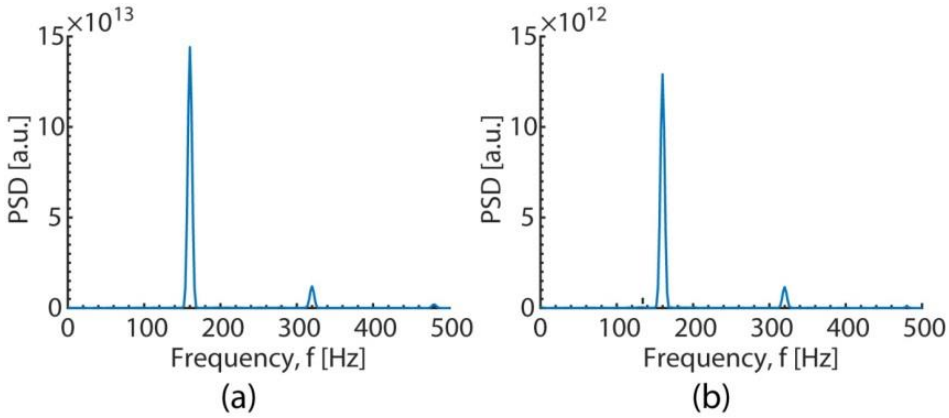

Figure 5-54: Power spectra of OH* chemiluminescence signal of (a) NPR-15-070-160-30 and (b) P-15-070-160-30.

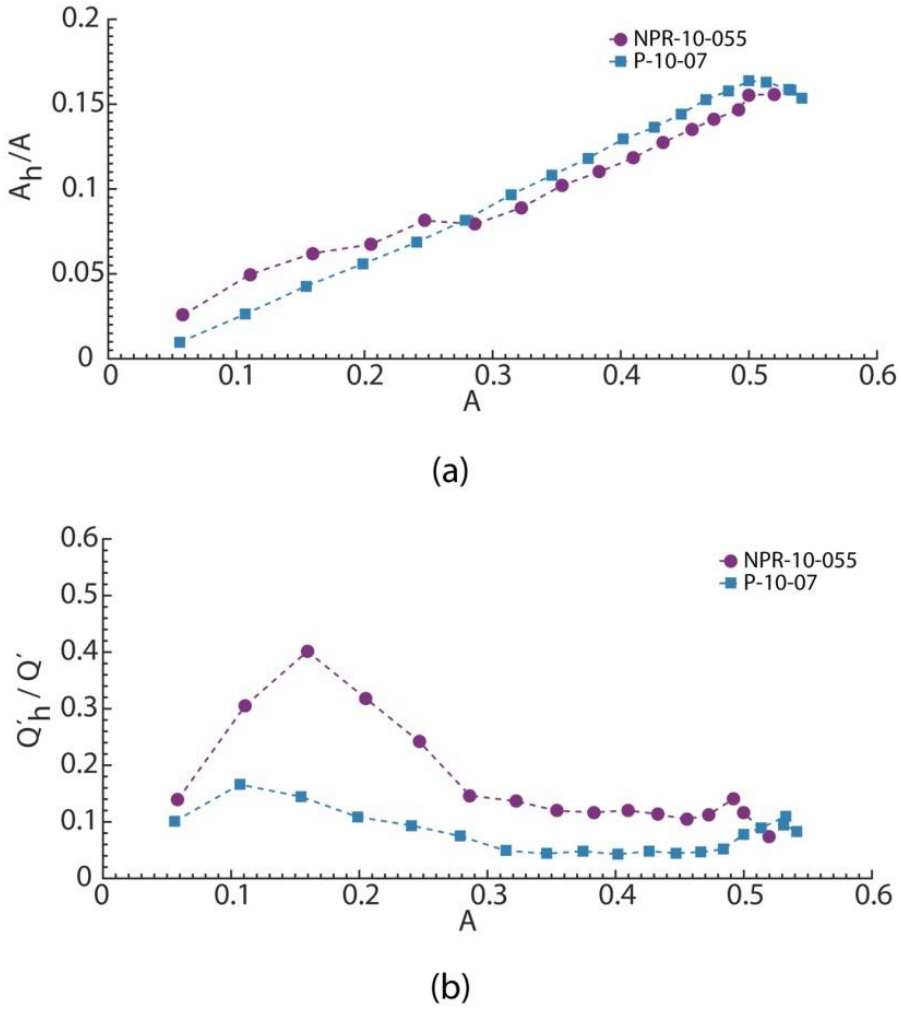

Figure 5-55: (a) Ratio of amplitude of inlet velocity fluctuation at first harmonic (320 Hz) A_h, to that at the forcing frequency (160 Hz), A, with respect to A, and (b) ratio of heat release fluctuation at the first harmonic (320 Hz) to that of the forcing frequency (160 Hz), (Q_h'/Q') , as a function of A. Flames: NPR-10-055 and P-10-070.

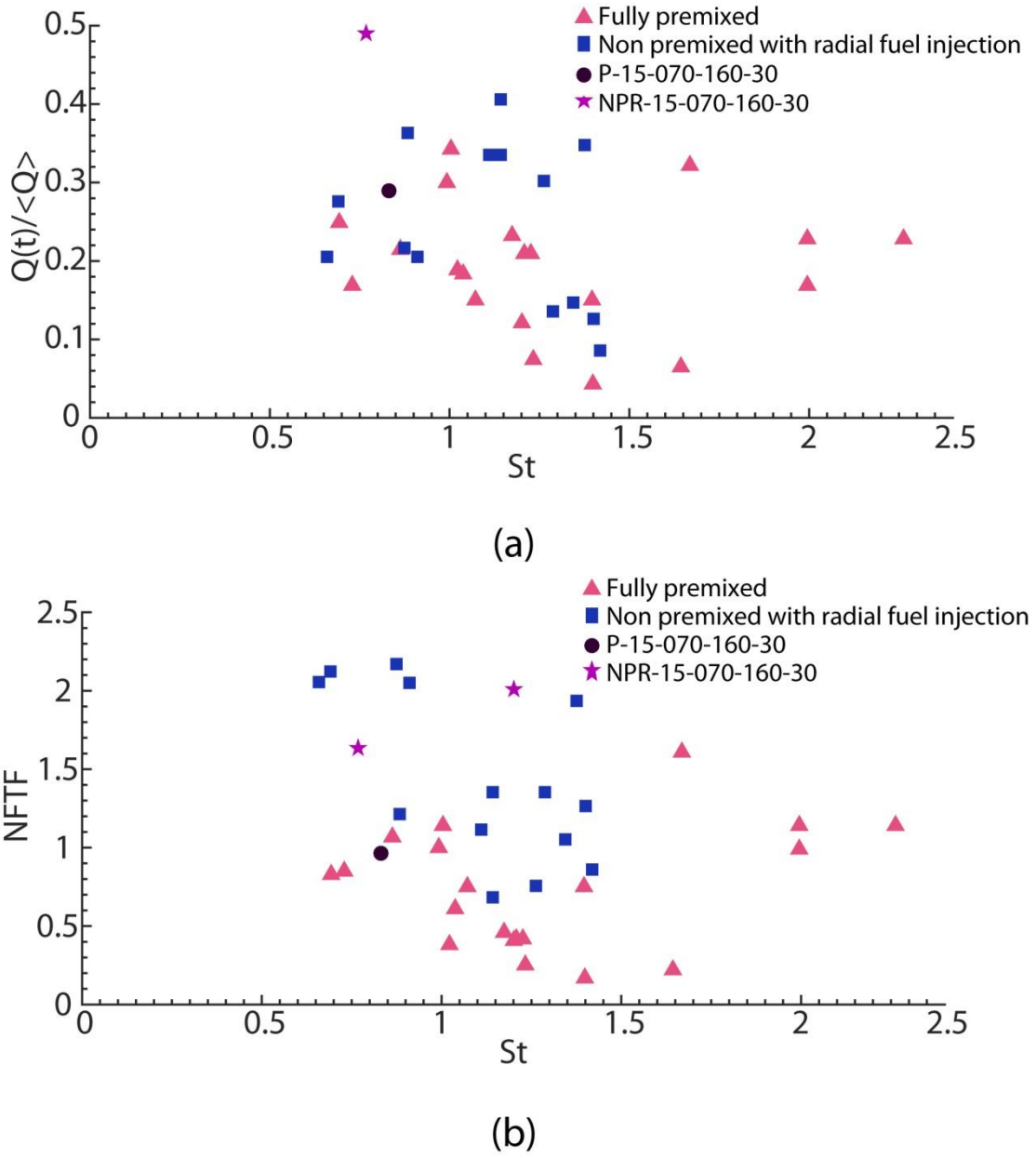

Figure 5-56: (a) Normalised heat release response and (b) transfer function plotted with respect to fL_{fl}/U for the fully premixed and NPR systems. The experimental conditions used have different bulk velocities, U (U=10-20 m/s), global equivalence ratios, φ (fully premixed: φ=0.6-0.8, NPR: φ=0.46-0.7), forcing frequencies, f (160 Hz or 280 Hz), and forcing amplitudes, A (A=0.1-0.5). P-15-070-160-30 and NPR-15-070-160-30 are also plotted.

5.6 Tables of Chapter 5

Condition	$U_{air}(m/s)$	$U_f(m/s)$	**Global φ**	**Air Flow Rate (lpm)**	**Methane Flow Rate (lpm)**
NPR-15-055 (Base case)	15 (93% of U_B when forced at 160 Hz and A=30%)	16.5	0.55	530	30
NPR-15-070	15 (74% of U_B when forced at 160 Hz and A=30%)	21.4	0.7	530	39
NPR-10-055	10 (91% of U_B when forced at 160 Hz and A=30%)	11	0.55	350	20

Table 5-1: Experimental conditions of the studied non-premixed with radial fuel injection (NPR) flames. The level of proximity of the forced flames to blow-off is indicated in brackets.

Condition	T_{conv}/T_{turb}	T_{chem}/T_{turb}	$T_{chem}/T_{f@160Hz}$	T_{diff}/T_{conv}	$T_{diff}/T_{f@160Hz}$
NPR-15-055 (Base case)	0.08	1.84	33.3	7.93	84.6
NPR-15-070	0.08	1.84	33.3	7.93	84.6
NPR-10-055	0.08	0.82	33.3	7.93	126.9

Table 5-2: Estimation of timescales of different processes.

Signals	φ (degrees)	$\Delta\varphi$ (degrees)
Total Flame	3	63
ISL	327	27
Top	37	97
ORZ	279	339
u	270	330
Impingement point	300	0

Table 5-3: Phase angle of $OH/<OH>$ peak values for ISL, Top, ORZ regions, velocity signal and impingement point. Flame: NPR-15-055-160-30.

Signals	φ (degrees)	$\Delta\varphi$ (degrees)
Total Flame	255	0
ISL	306	51
Top	33	138
ORZ	196	301
u	285	30
Impingement point	255	0

Table 5-4: Phase angle of $OH/<OH>$ peak values for ISL, Top, ORZ regions, velocity signal and impingement point. Flame: NPR-15-070-160-30.

Signals	φ (degrees)	$\Delta\varphi$ (degrees)
Total Flame	3	340
ISL	352	329
Top	35	12
ORZ	14	351
u	220	197
Impingement point	23	0

(a)

Signals	φ (degrees)	$\Delta\varphi$ (degrees)
Total Flame	5	315
ISL	5	315
Top	58	8
ORZ	23	333
u	255	205
Impingement point	50	0

(b)

Table 5-5: Phase angle of $OH/<OH>$ peak values for ISL, Top, ORZ regions, velocity signal and impingement point. Flames: (a) NPR-10-055-160-30 and (b) NPR-10-055-160-50.

OH* Chemiluminescence	NPR-15-055	NPR-15-055-160-30	NPR-15-070	NPR-15-070-160-30
Mode	**Energy (%)**	**Energy (%)**	**Energy (%)**	**Energy (%)**
1	9.6	25.6	7.4	45.8
2	7.6	10.1	6.5	22.4
3	4.6	8.0	5.4	3.0
4	3.8	4.4	5.3	2.3
1-4	25.6	48.1	24.6	73.5

Table 5-6: POD energy content of the first four OH* chemiluminescence POD Modes of NPR-15-055 and NPR-15-055-160-30.

OH PLIF	NPR-15-055	NPR-15-055-160-30	NPR -15-070	NPR-15-070-160-30
Mode	**Energy (%)**	**Energy (%)**	**Energy (%)**	**Energy (%)**
1	5.5	12.4	6.8	13.1
2	3.5	9.8	4.9	8.9
3	3.1	5.4	3.2	5.4
4	2.8	3.9	2.7	3.2
1-4	14.9	31.5	17.6	30.6

Table 5-7: POD energy content of the first four OH PLIF POD Modes of NPR-15-055 and NPR-15-055-160-30.

6 RESPONSE OF NON-PREMIXED FLAMES WITH AXIAL FUEL INJECTION

In this chapter, the results from the experiments studying the response of the non-premixed flames with axial fuel injection are presented briefly. The flow and acoustic conditions at which the experiments were conducted are described in Section 6.1. In Section 6.2, the results of the experiments are discussed. These include the qualitative description of the flame kinematics of one experimental condition, based on OH* chemiluminescence and OH PLIF measurements, as well as the estimation of the amplitude dependence of the transfer function. Finally, the results from the Proper Orthogonal Decomposition (POD) analysis are included to give an insight on the basic structures of the flame and their periodicity.

6.1 Experimental Condition

The results presented in this chapter were acquired by conducting experiments using the non-premixed with axial fuel injection configuration, described in detail in Section 2.1.4. The air stream was forced at 160 Hz and at forcing amplitudes, A, up to 33% of the velocity mean value. In this system, the acoustic oscillations imposed at the inlet, result in time-varying velocity field, and in time- and space-varying equivalence ratio oscillations. The span of mixture fraction fluctuations at the flame are expected to be larger than in the NPR system. The base case flame NPA-15-042-160-30, with air velocity U_{air}=15 m/s and global equivalence ratio φ=0.42 (Air Flow Rate=530lpm, Fuel Flow Rate=24 lpm). U_{air} was defined as the air flow rate divided by the open annular area between the bluff body and the outer duct at the exit of the burner inlet and U_f was calculated as the fuel flow rate divided by the area of the fuel nozzle exit.

6.2 Results

6.2.1 Effect of Forcing Amplitude on Lean Blow-off Limits

Figure 6-1 shows the lean blow-off limits of the forced NPA flames at 160 Hz. In order to determine the blow-off point, for a constant air flow rate and a given forcing amplitude, A, the fuel flow rate was decreased gradually in steps of 0.1 lpm every 40 seconds until blow-off occurred, recording the fuel blow-off flow rate. At each air flow rate, an average fuel blow-off flow rate of 10 individual measurements was calculated. The fuel velocity at blow-off constitutes the average value of ten blow-off events, while the standard deviation of these measurements normalised by the mean value was approximately 0.03. It should be noted that this low value was made possible because the step of fuel flow rate reduction was very small (0.1 lpm) and a large number of blow-off measurements were conducted. It can be deduced that forcing reduces the stability of the flame, which decreases with increasing forcing amplitude. In particular, for a constant U_{air} at blow-off, the greater the forcing amplitude A, the greater the U_f at blow-off, whereas for a constant U_f, the greater the forcing amplitude, the lower the U_{air} at blow-off. Also, for a given forcing amplitude A, as the U_f increases, the U_{air} increases. These findings are consistent with the blow-off measurements of NPR flames (Section 5.1).

However, a few differences are observed between the NPA and the NPR systems. The NPA system shows a greater sensitivity to changes in forcing amplitude compared to the NPR configuration, since for a given air flow rate and forcing amplitude it exhibits larger variations of the fuel flow rate (overall equivalence ratio) compared to the NPR. For example, considering a constant U_{air}=15.7 m/s, between A=0 and A=0.25, for the NPA system, U_f changes in the range of 15.5-26.9 m/s (the maximum variation from the U_f value at A=0 is approximately 70%). In the NPR system (Figure 5-1), for U_{air}=15.7 m/s, between A=0 and A=0.25, U_f changes in the range of 15.0-16.1 m/s (the maximum variation from the U_f value at A=0 is approximately 7%). This implies that the operating range of the NPA system is significantly reduced in the presence of forcing. However, considering the global equivalence ratio at blow-off, it should be noted that the NPA system can be operated much leaner compared to the NPR system for all the forcing amplitudes investigated in this work. Therefore, the higher sensitivity of the NPA system to changes in the amplitude of the fluctuations could be attributed to the higher sensitivity, typically associated to very lean conditions (small global equivalence ratio). The fluctuations of the air flow might have an important impact on the recirculation zone, changing significantly the mixing pattern and therefore affecting the lean blow-out. In contrast, in the NPR system the higher equivalence ratio at blow-off (for a given air velocity at the inlet), also

in the absence of forcing, indicates that this injection configuration is intrinsically less stable and this can be related to the injection location that causes the flame to be in a high strain region. The presence of air flow oscillations only slightly changes the operating range (already smaller compared to the NPA system). This also suggests that in the NPR case, the fluctuations of the air flow have a lower effect on the mixing pattern than that in the NPA case.

6.2.2 Flame Kinematics

Instantaneous OH* chemiluminescence and OH PLIF images of NPA-15-042-160-30 (Figure 6-2) show that the flame has a conical shape and is anchored at the bluff body edge. The OH zone is occasionally fragmented in different regions, partial absence of half branch, and attachment and lift-off at the bluff body edge are also seen. Phase-averaged OH* chemiluminescence images (Figure 6-3) show a reduced modulation of the flame shape and a less pronounced flame impingement on the wall compared with the fully premixed and NPR flames. Figure 6-4 reveals that the change in the flame angle is less pronounced than that in the other systems. Unlike fully premixed and NPR flames, the flame angle variation of NPA-15-042-160-30 during the cycle does not follow a sinusoidal trend (Figure 6-5).

In Figure 6-6, the local response of the flame is quantified based on OH PLIF images. The total variance, determining the OH fluctuations in the frequency range of 0-500 Hz, is the greatest in the inner shear layer (ISL) region. However, in the fully premixed and NPR systems the highest values of the variance were depicted in the near wall region. The metric of local flame sensitivity to the forcing frequency, R_L, defined in Section 2.3.3.3, is greater in the ISL region than in the other regions. This is consistent with the results of NPR flames, whereas in the case of fully premixed flames greater R_L values were observed in large regions on the downstream side of the OH PLIF plane than those in the ISL region close to the bluff body. Additionally, NPA-15-042-160-30 shows that in the region downstream of the fuel injection point, R_L is almost zero.

To investigate the behaviour of the various parts of the flame to forcing, the $OH/< OH >$ phase-averaged variation of the main flame regions (Section 2.3.3.4) is presented in Figure 6-7. The phase difference of the $OH/< OH >$ peak between the ISL and Top region is 104 degrees, whereas the ORZ is delayed 151 degrees with respect to that in the Top region.

Figure 6-8a plots the probability density function of the lift-off height, $P(h)$, with respect to h for forced and unforced NPA flames. The lift-off heights of NPA flames are significantly more pronounced than those of NPR flames, while the PDFs of NPA system have a much longer positive tail than those of NPR system. Unlike NPR flames, the average lift-off

height of forced NPA flames is lower than that of the respective unforced conditions. Closer to blow-off, for stable flame NPA-15-038-160-30, the peak of the PDF demonstrates that 40% of the samples reveal a lift-off height below 1.47 mm. For NPA-15-038, the peak reveals that 22% of the samples reveal a lift-off height around 4.8 mm. The average lift-off height is 6.57 mm and 8.55 mm for the forced and unforced flame respectively. Farther from blow-off, the PDFs of flames NPA-15-042-160-30 and NPA-15-042 are similar, with the average lift-off height being 7.28 mm and 8.32 mm respectively. In the NPA flames, the lift-off height is not periodic at the forcing frequency, as concluded by the absence of the 160 Hz peak in the PSD (Figure 6-8b). The sensitivity to the forcing observed in the lift-off height of the NPA system was lower compared to that of the NPR system. It should be noted that in the NPR system the location of the flame is closer to the strong acoustic oscillations at the exit of the annular air passage than that of the NPA system. However, as previously discussed, the NPA system seems to show a greater sensitivity to the forcing amplitude in terms of blow-off behaviour, which might be related to the very low global equivalence ratio that this configuration can reach without the presence of forcing.

6.2.3 Amplitude Dependence of the Flame Response

Following the previous analysis on flame kinematics at a specific forcing amplitude (A=30%), the overall flame response as a function of forcing amplitude is presented below for NPA-15-042, NPA-15-038 and NPA-21-038.

The results (Figure 6-9a) suggest that the nonlinear response of the NPA system to acoustic forcing is significantly lower compared to the NPR and fully premixed systems. The three NPA flames have similar $<Q'/<Q>$, suggesting the little sensitivity of the NPA system to input air velocity and global equivalence ratio. The maximum value is approximately 7% for NPA-15-042, which has the highest global equivalence ratio, implying that the NPA system might be sensitive to fuel flow rate. Close to blow-off, condition NPA-21-038 exhibits the lowest response. This could probably be explained by the fact that the possibilities of local extinctions are increased as the flame approaches blow-off.

The transfer functions show a nonlinear amplitude dependence (Figure 6-9b). NPA-15-038 exhibits the greatest reduction in NFTF compared with the other cases, with the NFTF decreasing from 0.37 to 0.19. A possible explanation for this response could lie in the fact that the flame when forced at low amplitudes is far from blow-off, showing a relatively high amplitude, but as A increases the flame is getting closer to blow-off, resulting in a lower response probably due to local extinction events that are becoming more frequent as blow-off

is being approached. For NPA-15-038, at low amplitudes, as A increases, $<Q'/<Q>$ increases and after A=27%, $<Q'/<Q>$ starts decreasing. During the experiments, it was observed that the amplitude A at which the normalised heat release started decreasing coincided with the initiation of a chaotic radial flame motion, which became more and more frequent and violent as the forcing amplitude was further increased, indicating that the flame was gradually approaching blow-off. The transfer function phase reveals an increasing trend with forcing amplitude (Figure 6-9c).

6.2.4 Proper Orthogonal Decomposition Analysis (POD)

In this section, the POD results of OH* chemiluminescence and OH PLIF images are discussed. The OH* chemiluminescence POD results presented below consist of the first few modes, the PSDs of POD time coefficients, the instantaneous OH* chemiluminescence images and their reconstruction based only on a small number of modes, as well as the relative cumulative energy content of POD modes. The OH PLIF POD results are also presented in a similar way. The following discussion focuses on: a) the basic structure of the flame extracted from POD, b) its temporal evolution, and c) the difference between the forced and unforced flame.

6.2.4.1 OH* Chemiluminescence POD Analysis

Concerning the spatial structure of NPA-15-042, the first four Modes show an antisymmetric pair of heat release fluctuations (Figure 6-10a), which as seen in the reconstructed images corresponds to a left-right flame motion (Figure 6-10b). Concerning the periodicity, the PSD of POD time coefficients of Mode 1 exhibits two peaks at 10 Hz and at 39 Hz, while the PSDs of the other modes show dominant peaks mainly below 100 Hz.

For NPA-15-042-160-30, in terms of spatial features, Mode 1 depicts an antisymmetric pair of heat release fluctuations (Figure 6-11a), which is characteristic of the transverse oscillating motion of the flame (Figure 6-11b). The PSD of Mode 1 reveals a dominant peak at 20 Hz and a smaller at 83 Hz, while the absence of a peak at 160 Hz implies that forcing does not influence greatly the behaviour of NPA-15-042-160-30. The shape of Mode 2 shows a combination of an axial and radial heat release variation, which represents an axial and transverse oscillating motion. In the PSD of Mode 2, two pronounced peaks are revealed at 160 Hz and at 34 Hz. Modes 3 and 4 show an axial dependence of the flame shape, which suggests the axial motion of the flame, as seen in the respective reconstructed images (Figure 6-11). The respective PSDs reveal that 160 Hz is the dominant frequency associated with this motion.

Concerning the POD energy, the cumulative energy content of the forced flame is greater than that of the unforced condition, while their energy difference becomes smaller at higher modes (Figure 6-12). Also, both curves, reveal a much steeper slope at lower mode numbers than at higher modes. The energy content of the first four modes is slightly higher in the forced case (35.1%) than in the unforced (29.8%). Also, the distribution of energy in the individual modes is similar in both cases (Table 6-1). This suggests again that forcing does not affect significantly the flame behaviour. The energy content of the first four POD Modes was significantly greater in the case of NPR-15-070-160-30 (73.5%), P-15-070-160-30 (63.3%) and SP-10-077-510 (69.2%) than that of flame NPA-15-042-160-30 (35.1%). In addition, unlike flame NPA-15-042-160-30, the energy content of the first four modes of the aforementioned forced conditions was much greater than that of the respective unforced cases (NPR-15-070: 24.6%, P-15-070: 29.3%, NPA-15-042: 29.8%). This implies that forcing affects more greatly the behaviour of the premixed and NPR flames than that of NPA flames.

6.2.4.2 OH PLIF POD Analysis

The first four OH PLIF POD Modes of NPA-15-042 show an antisymmetric OH structure (Figure 6-13a), which corresponds to the left-right motion, as seen in the time evolution of the reconstructed images (Figure 6-13b). The PSD of the POD time coefficients of Mode 1 reveals three dominant peaks at 15 Hz, 39 Hz and 63 Hz, while the PSDs of the other modes exhibit many frequencies.

For NPA-15-042-160-30, POD Modes 1, 2 and 4 (Figure 6-14a) show an antisymmetric OH structure close to the wall and are associated with the forcing frequency (160 Hz) and a few low frequency peaks (Mode 1: 83 Hz, 29 Hz, 10 Hz, Mode 2: 15 Hz, Mode 3: 5 Hz, 54 Hz). These Modes structure is representative of the combination of the flame angle variation with the left-right motion as observed in the respective reconstructed images (Figure 6-14b). The structure of Mode 3 is almost purely associated with the forcing frequency and corresponds to the change in the flame angle.

Concerning the POD energy, the cumulative energy content of the forced and unforced flame is very similar (Figure 6-12). The energy contained in the first four modes (Table 6-2) is slightly greater in the forced flame (24.5%) than in the unforced (19.8%). For NPA-15-042-160-30, the energy contained in the first 50 OH* chemiluminescence POD Modes is greater (77%) than that (62%) in the respective OH PLIF modes. The relatively small difference in the energy values suggests that the structures captured by the planar measurement constitute a good representation of those revealed by the line-of-sight measurement.

6.3 Conclusions

In this chapter, the experimental investigation of the response of the non-premixed with axial fuel injection system (i.e. time-varying velocity field, and time- and space-varying equivalence ratio) is presented briefly. OH* chemiluminescence measurements, acquired with a photomultiplier tube (PMT) and an ICCD camera, were used to study qualitatively the heat release response of the flames, while OH PLIF measurements were used to understand the response of the flame structure and the behaviour of the various parts of the flame. Apart from the flame kinematics analysis, the amplitude dependence of the transfer function was estimated. The dominant structures of the flames and their periodicity were characterised using the Proper Orthogonal Decomposition (POD) method.

Concerning the amplitude dependence of the non-premixed with axial fuel injection flame response, a nonlinear response was observed, which was significantly lower (the maximum normalised global heat release fluctuation was 7%) compared with the response of the NPR and the fully premixed systems. Close to blow-off, the flame response was greatly reduced compared with that farther from blow-off. The NPA showed a low sensitivity towards a change in the operating conditions. It was found that flames that initially, at low A were far from blow-off, revealed a relatively high response, but if with the increase in A they were approaching their blow-off condition, they started exhibiting a lower response, which could possibly be due to increased local extinction events and the initiation of a chaotic radial flame motion. For instance, close to blow-off the OH PLIF snapshots demonstrated that the OH zone was more fragmented and absence of the branches of the flame was seen more often than in the flames farther from blow-off. Additionally, acoustic oscillations have a noticeable effect on the lean blow-off limits. It was shown that the acoustic forcing reduces the stability of the flame and the stability decreases with the increase in forcing amplitude. The NPA system showed a greater sensitivity to the forcing amplitude compared to the system with radial injection in terms of changes in the operability limits.

As far as the flame kinematics are concerned, the following conclusions were reached. It was demonstrated that the various parts of the flame responded differently to acoustic forcing. The values of R_L (OH fluctuation at 160 Hz to the total variance of OH) were greater in the ISL region than in the other regions. This is consistent with the results of NPR flames, whereas in the case of fully premixed flames greater R_L values were observed in large regions on the downstream side of the OH PLIF plane than those in the ISL region close to the bluff body. Additionally, the NPA flame showed that in the region downstream of the fuel injection point, R_L was almost zero. In the NPA system, the change in the flame angle was found to be less

pronounced than that of the fully premixed and the NPR systems. Unlike these systems, the NPA flame angle variation did not follow a sinusoidal trend during the cycle. The lift-off heights of NPA flames are significantly more pronounced than those of NPR flames. Unlike NPR flames, forced NPA flames had reduced average lift-off heights compared to the unforced conditions. Unlike the NPR system, the lift-off height of NPA flames was not periodic at the forcing frequency.

From the POD analysis, the first OH* chemiluminescence POD Mode revealed an antisymmetric pair of heat release fluctuations, which represented a left-right flame motion. The absence of a 160 Hz (forcing frequency) peak at the PSD of POD time coefficients of the first POD Mode implied that forcing did not affect greatly the flame structure. The second OH* POD Mode represented a combination of an axial and left-right motion. The 160 Hz peak was revealed in the PSD of Modes 2-4. The OH PLIF POD results, apart from the aforementioned features, revealed the angle variation of the flame.

6.4 Figures of Chapter 6

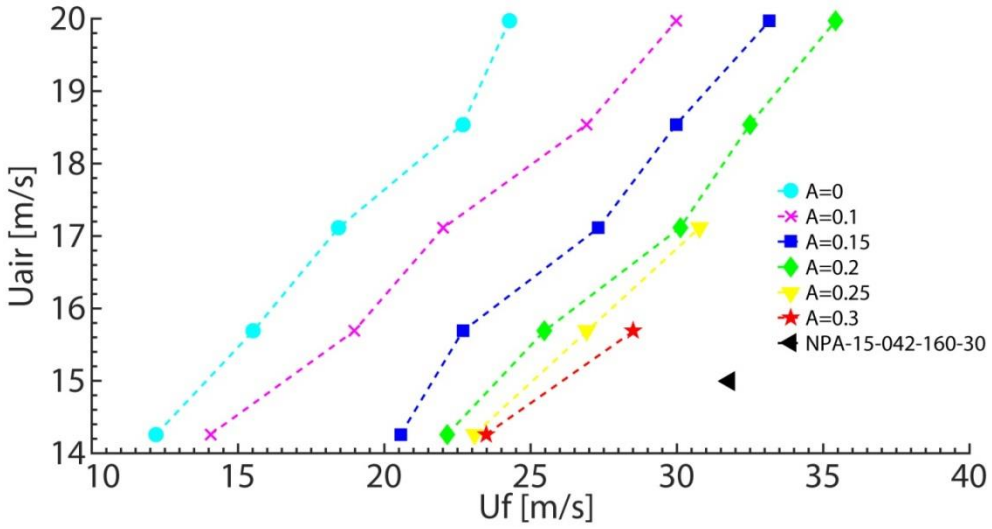

Figure 6-1: Air blow off velocity, U_{air}, as a function of fuel blow off velocity, U_f, (calculated at the exit of the fuel nozzle), for various forcing amplitudes A.

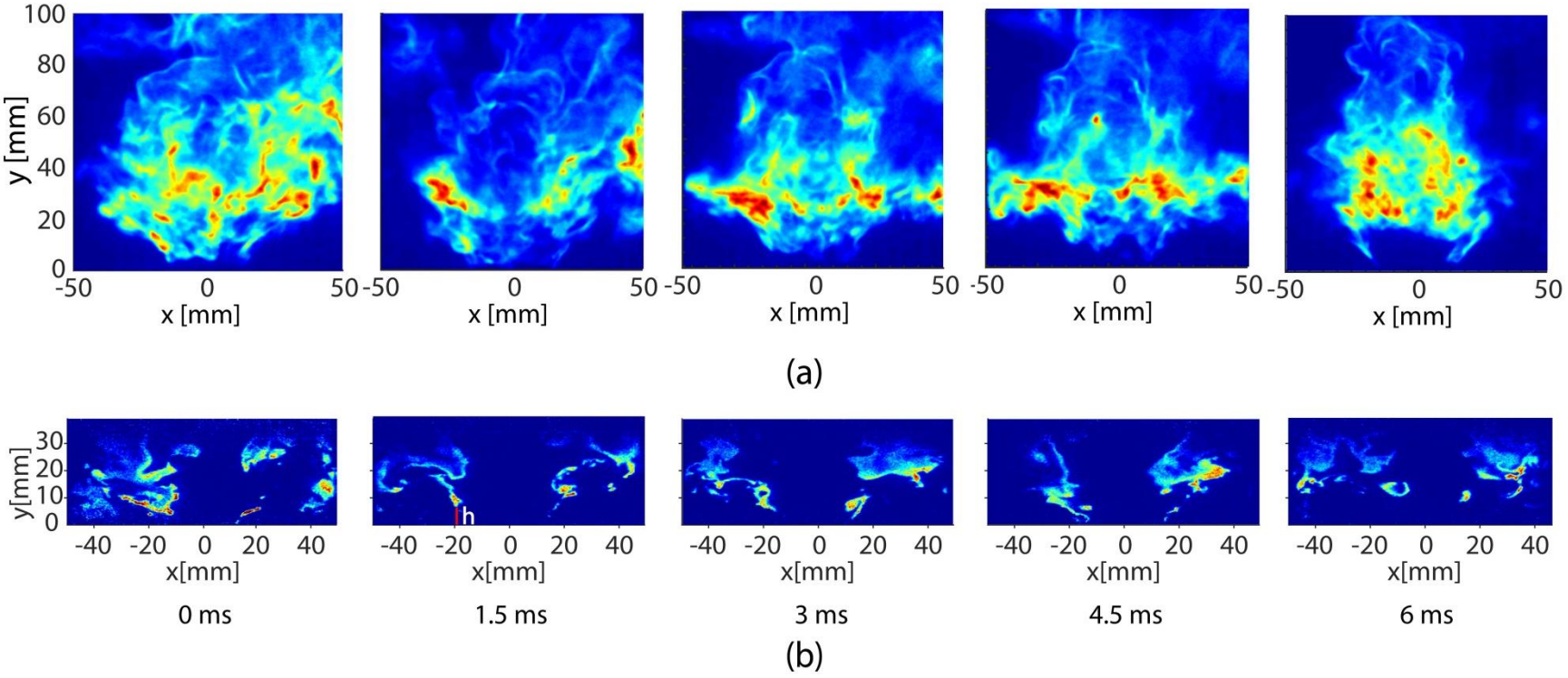

Figure 6-2: Instantaneous (a) OH* chemiluminescence and (b) OH PLIF images of NPA-15-042-160-30 (not recorded simultaneously during a cycle, *t*=0 ms corresponds to the beginning of the cycle). The same colormap for each image was used. Red line: lift-off height *h* at the bluff body edge.

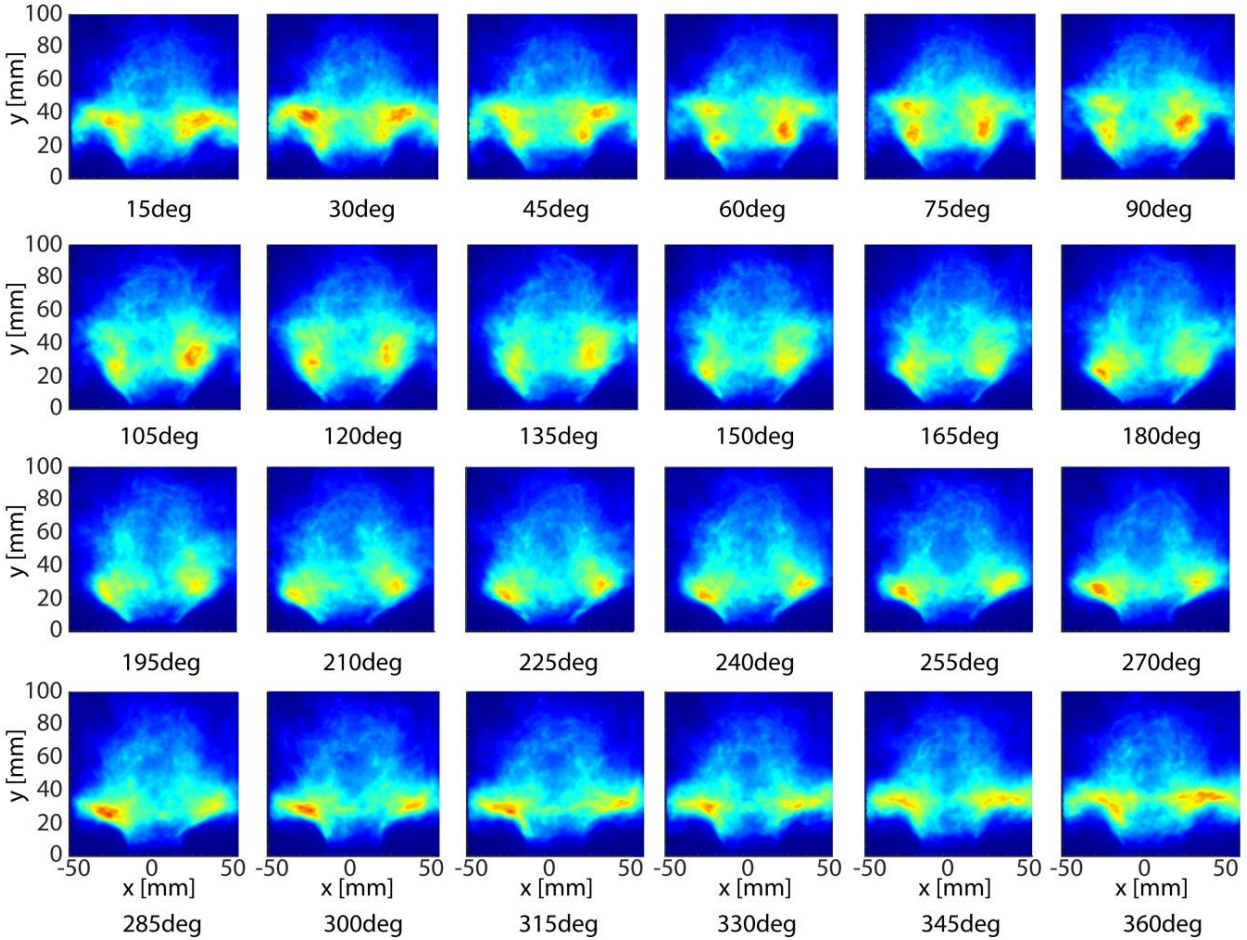

Figure 6-3: Phase-averaged OH* chemiluminescence images of NPA-15-042-160-30.

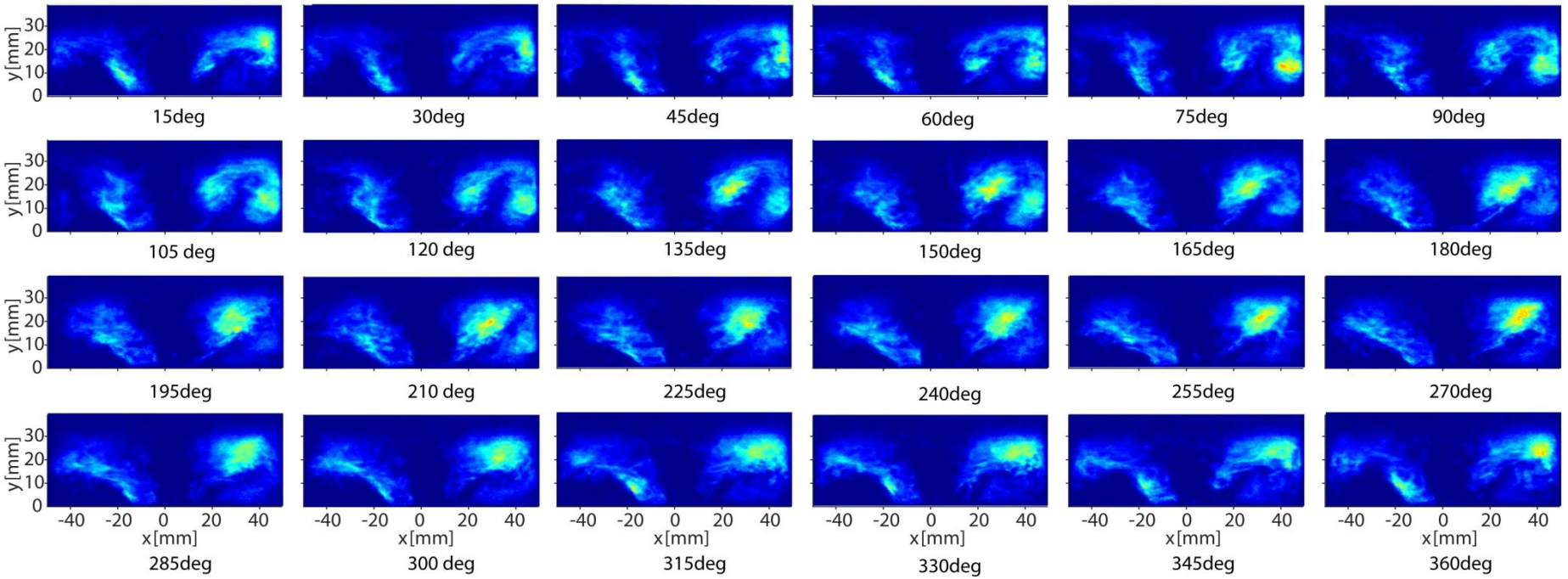

Figure 6-4: Phase-averaged OH PLIF images of NPA-15-042-160-30.

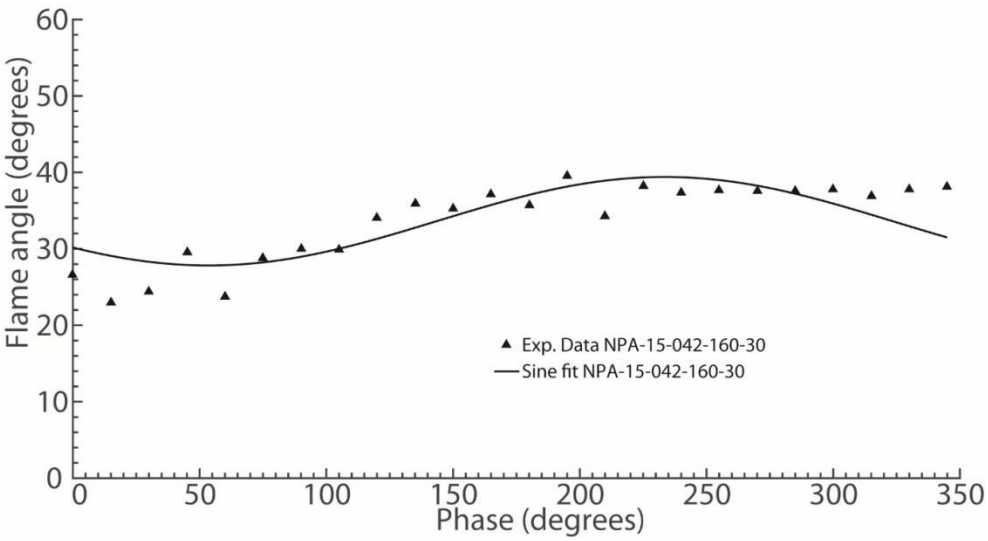

Figure 6-5: Flame angle variation with respect to phase of the acoustic cycle, based on phase-averaged OH PLIF images. Flame: NPA-15-042-160-30.

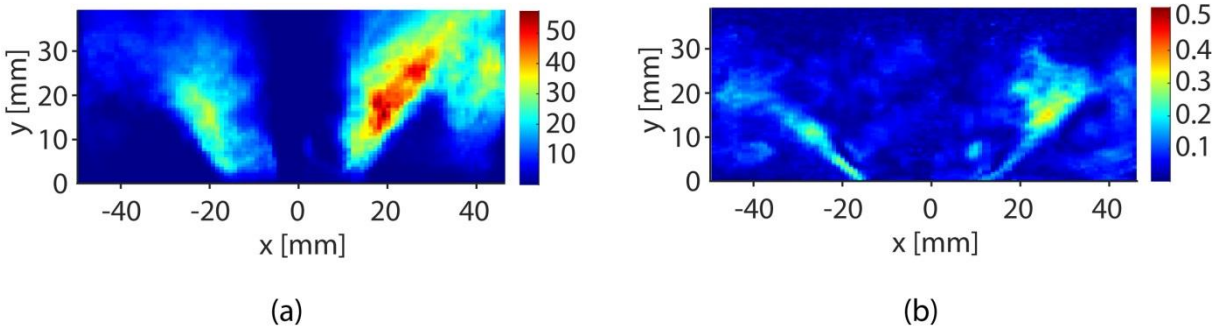

Figure 6-6: (a) Variance of OH (left) and (b) ratio R_L (OH fluctuation at 160 Hz to the total variance of OH) for NPA-15-042-160-30.

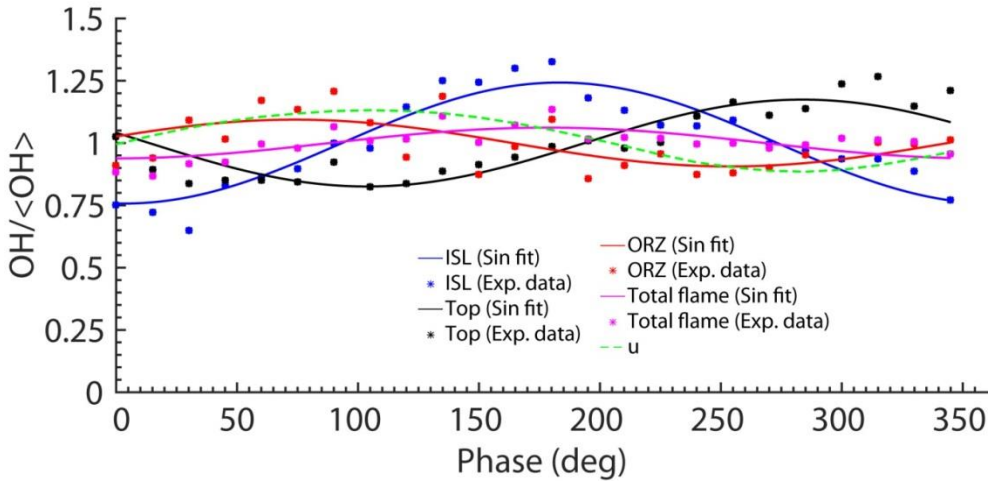

Figure 6-7: $OH/< OH >$ variation during the acoustic cycle, evaluated from phase-averaged OH PLIF images, calculated from the ISL, Top, ORZ and whole OH PLIF window. The green dashed line represents the normalised acoustic velocity fluctuations. Flame: NPA-15-042-160-30.

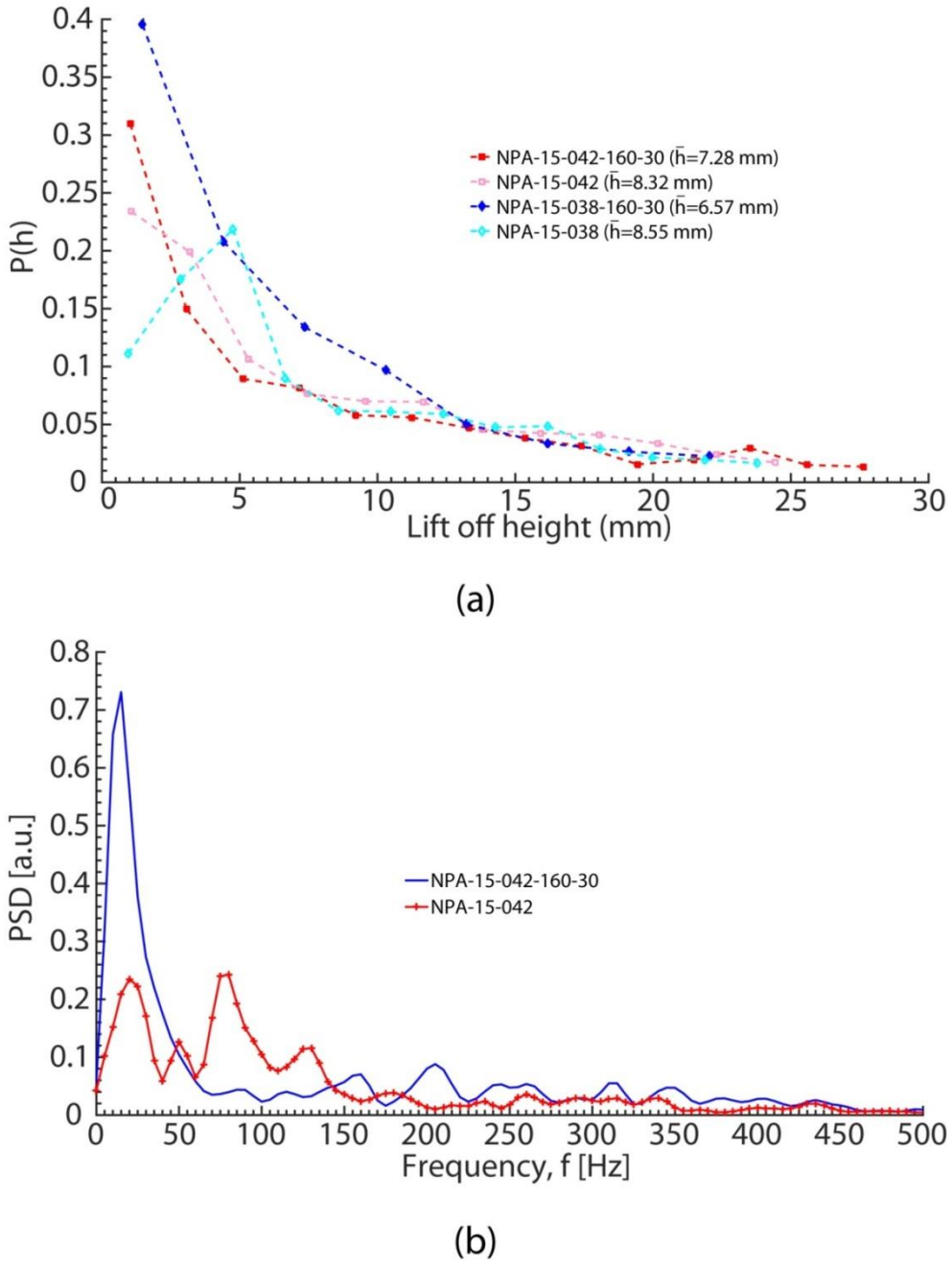

Figure 6-8: (a) Probability density function of the lift-off height, $P(h)$, with respect to h for forced and unforced flames. The average lift-off height $\bar{h}$ is indicated. (b) Power spectral densities of the lift-off height for NPA-15-042 and NPA-15-042-160-30.

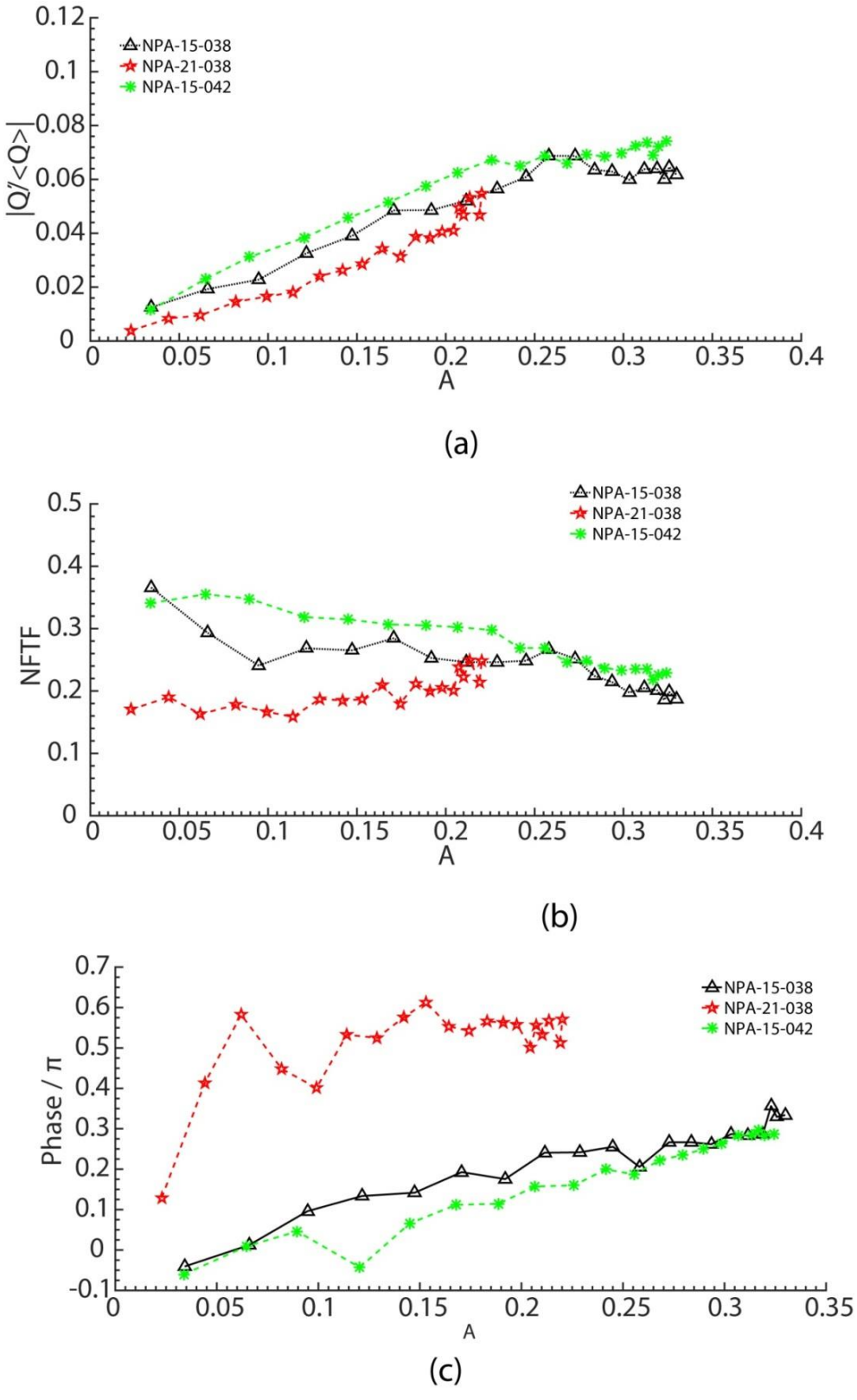

Figure 6-9: (a) Normalised global heat release fluctuation of NPA-15-042, NPA-15-038 and NPA-15-046 measured as a function of *A* using OH* chemiluminescence, (b) the corresponding transfer function and (c) its phase evaluated from the data of (a).

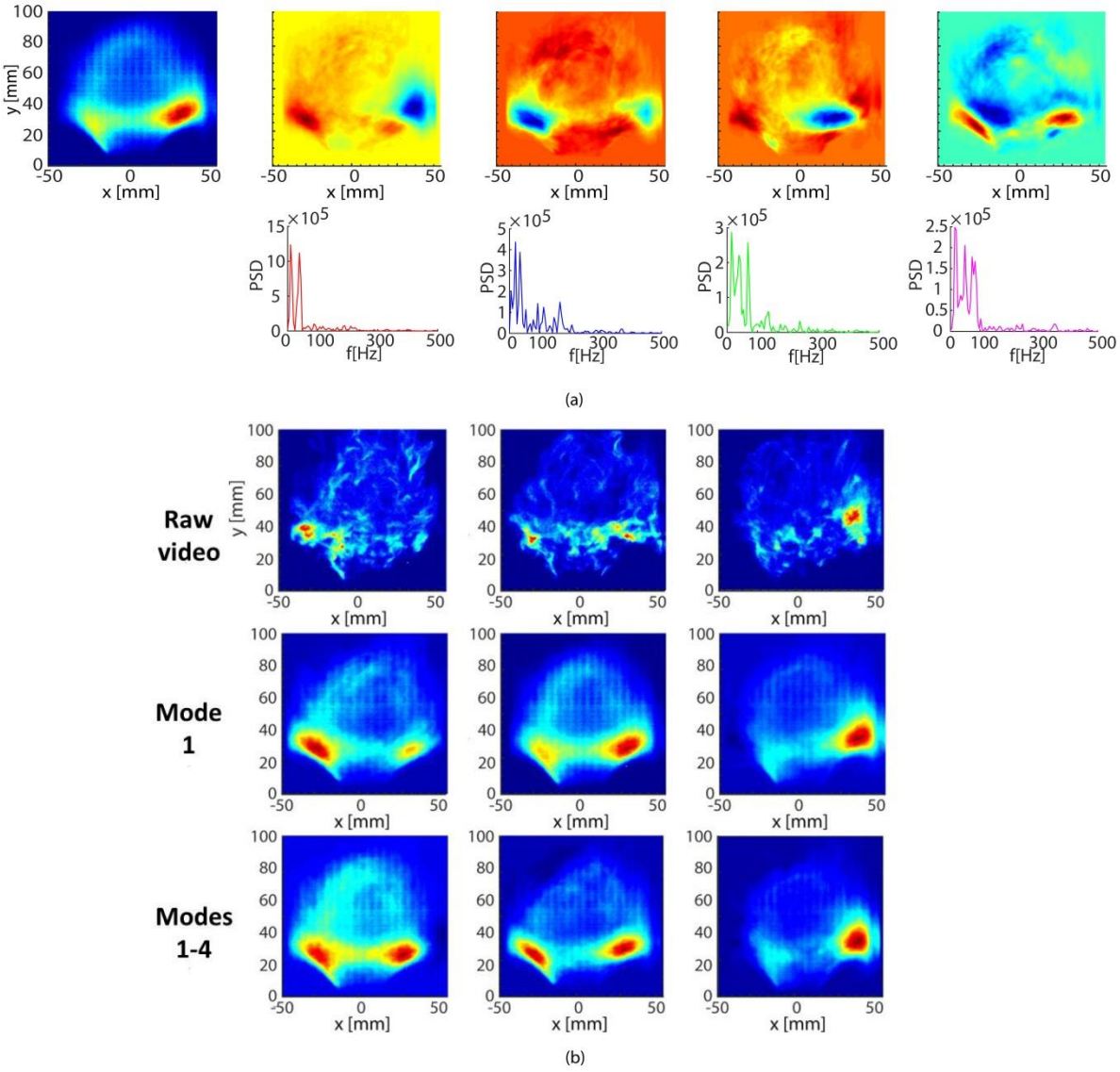

Figure 6-10: (a) Mean Image and first four OH* chemiluminescence POD Modes and the respective PSD of POD time coefficients. (b) Instantaneous chemiluminescence images (first row), snapshots at the same times from reconstructed OH* movie using the mean and Mode 1 only (second row) and the mean and Modes 1 to 4 (third row). Flame: NPA-15-042.

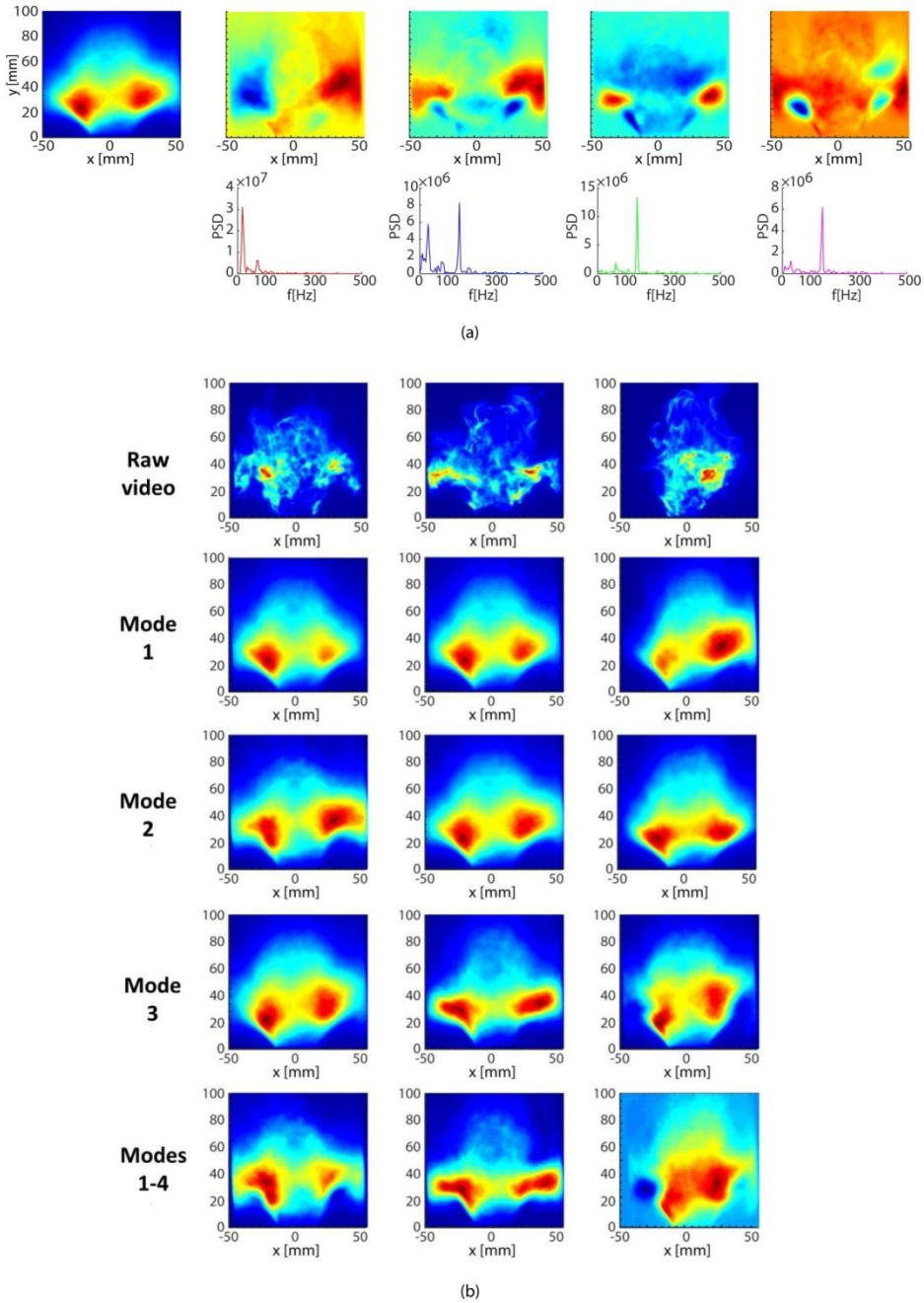

Figure 6-11: (a) Mean Image and first four OH* chemiluminescence POD Modes and the respective PSD of POD time coefficients. (b) Instantaneous OH* chemiluminescence images (first row), snapshots at the same times from reconstructed OH* movie using the mean and Mode 1 only (second row), the mean and Mode 2 only (third row), the mean and Mode 3 only (fourth row), and the mean and Modes 1 to 4 (fifth row). Flame: NPA-15-042-160-30.

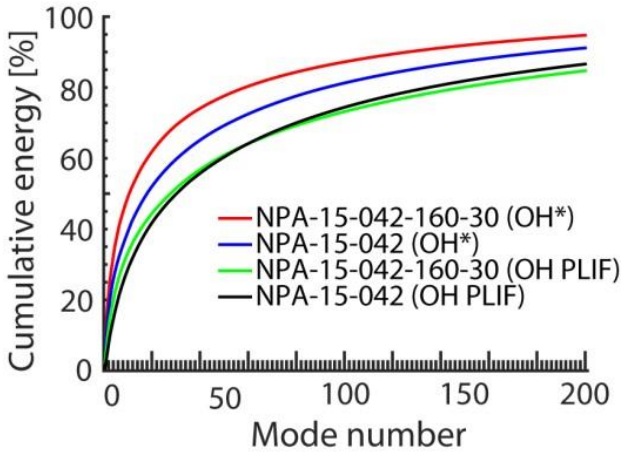

Figure 6-12: Cumulative energy of OH* chemiluminescence and OH PLIF POD Modes of NPA-15-042 and-15-042-160-30.

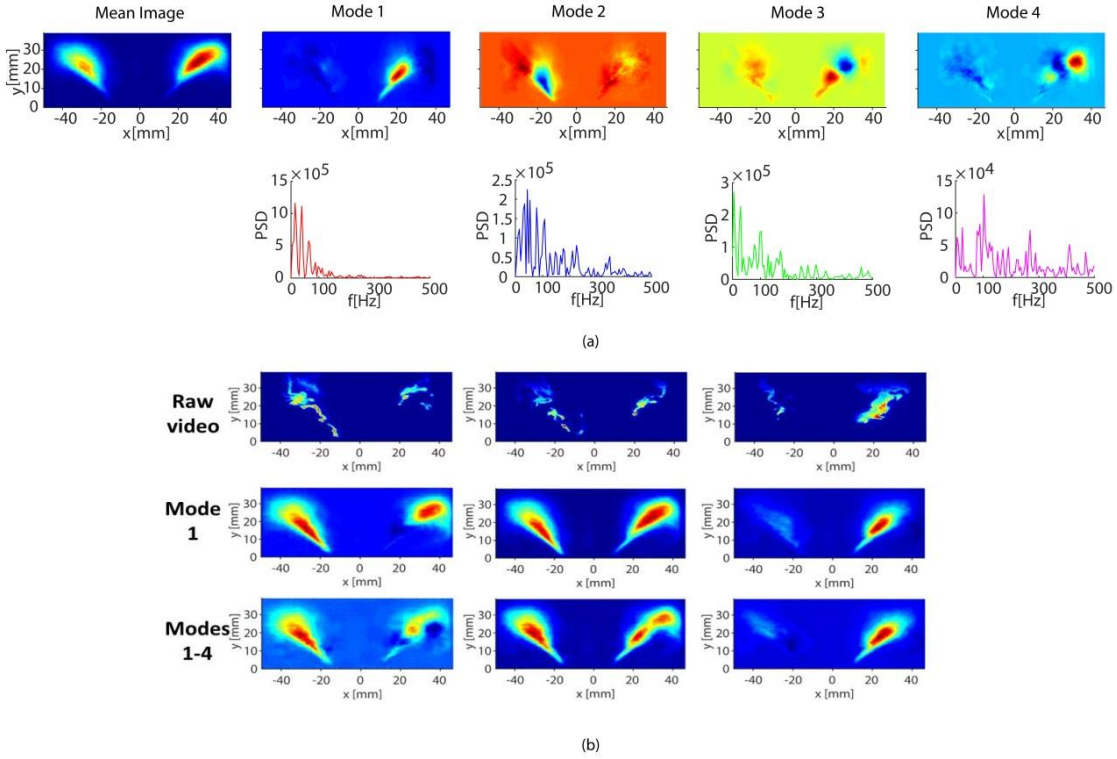

Figure 6-13: (a) Mean Image and first four OH PLIF POD Modes and the respective PSD of POD time coefficients. (b) Instantaneous OH PLIF images (first row), snapshots at the same times from reconstructed OH PLIF movie using the mean and Mode 1 only (second row) and the mean and Modes 1 to 4 (third row). Flame: NPA-15-042.

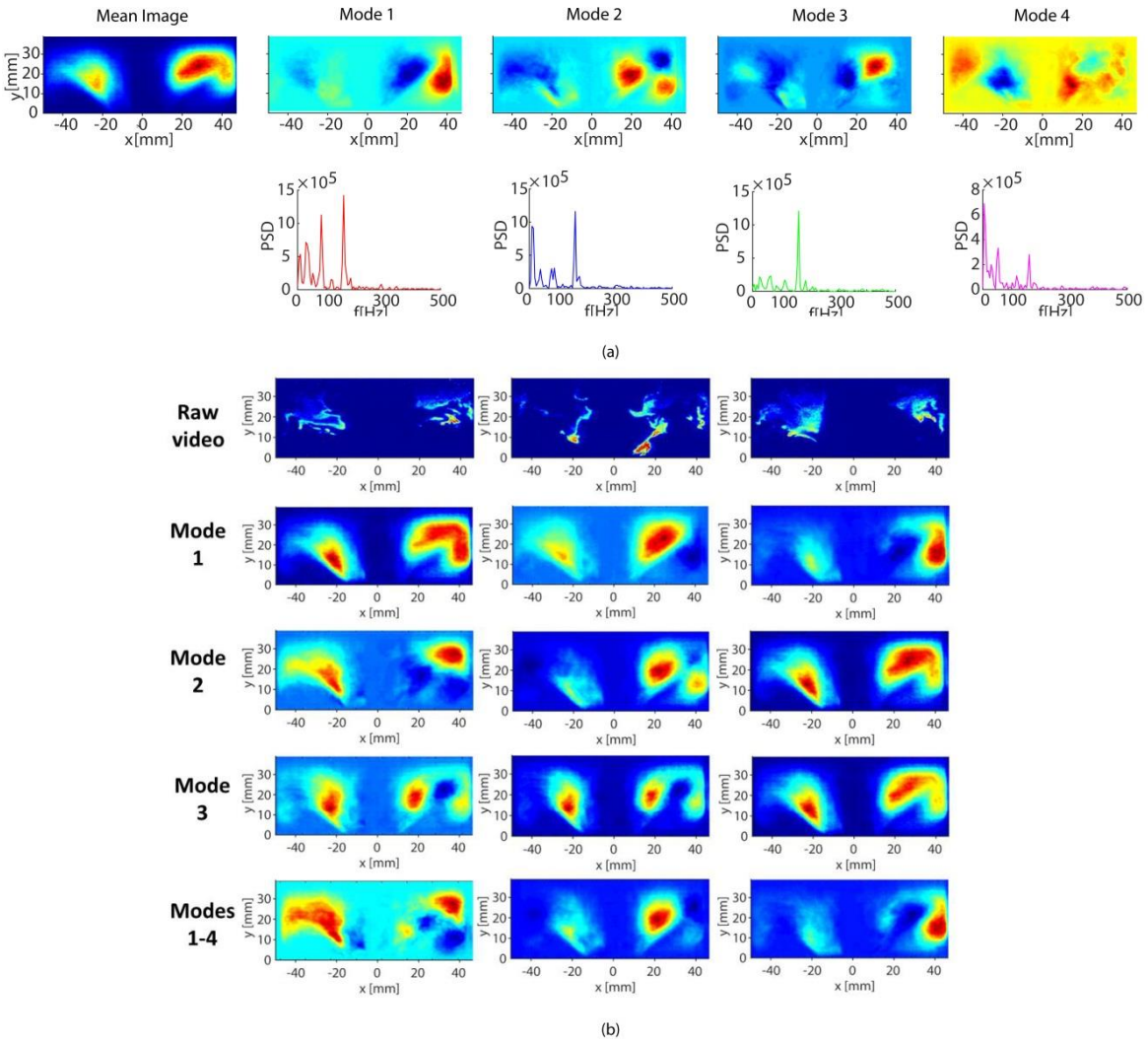

Figure 6-14: (a) Mean Image and first four OH PLIF POD Modes and the respective PSD of POD time coefficients. (b) Instantaneous OH* chemiluminescence images (first row), snapshots at the same times from reconstructed OH PLIF movie using the mean and Mode 1 only (second row), the mean and Mode 2 only (third row), the mean and Mode 3 only (fourth row), and the mean and Modes 1 to 4 (fifth row). Flame: NPA-15-042-160-30.

6.5 Tables of Chapter 6

OH* Chemiluminescence	NPA-15-042	NPA-15-042-160-30
Mode	**Energy (%)**	**Energy (%)**
1	13.4	13.7
2	7.0	10.3
3	5.4	6.8
4	4.0	4.3
1-4	29.8	35.1

Table 6-1: POD energy content of the first four OH* chemiluminescence POD Modes of NPA-15-042 and NPA-15-042-160-30.

OH PLIF	NPA-15-042	NPA-15-042-160-30
Mode	**Energy (%)**	**Energy (%)**
1	8.3	9.8
2	4.4	6.4
3	4.1	5.1
4	3.0	3.2
1-4	19.8	24.5

Table 6-2: POD energy content of the first four OH PLIF POD Modes of NPA-15-042 and NPA-15-042-160-30.

7 RESPONSE OF SPRAY FLAMES

In this chapter, the results from the experiments investigating the response of the ethanol spray flames to acoustic forcing are presented. The flow and acoustic conditions at which the experiments were conducted are described in Section 7.1. In Section 7.2, the results of the experiments are presented and discussed. These include a qualitative description of flame kinematics based on OH* chemiluminescence and OH PLIF measurements, as well as the effect of different parameters such as air velocity, global equivalence ratio and forcing amplitude. Also, the results from the Proper Orthogonal Decomposition (POD) analysis are included to give an insight on the basic structures of the flames and their periodicity. Finally, in Section 7.3 both spray and non-premixed with axial fuel injection systems are compared in terms of their kinematics and response.

7.1 Experimental Conditions

The results presented in this chapter were acquired by conducting experiments using the spray configuration (Section 2.1.5). The air stream was forced at 160 Hz and at velocity forcing amplitudes, A, up to 40% of the velocity mean value. The pressure oscillations caused by the external acoustic forcing are much smaller compared to the pressure drop at the atomiser (4-5 bar). Therefore, the pressure oscillations are insignificant and do not cause a modulation of the fuel flow rate, suggesting that the acoustic velocity rather than the acoustic pressure primarily affects the spray.

The flames studied in this chapter are presented in Table 7-1. The base experimental condition is S-15-033 with air velocity U_{air} =15 m/s and global equivalence ratio φ=0.33. The effect of global equivalence ratio and air velocity (S-15-024 and S-12-033 respectively) on the flame response were also investigated and analysed. As seen in Table 7-1, S-15-024 when forced at 160 Hz and A=30% (S-15-024-160-30) is closer to blow-off (the air velocity is 92% of that at the blow-off condition) than the base case when forced at 160 Hz and A=30%, whereas S-12-033-160-30 is farther from blow-off (U_{air} =70% U_B) compared with the base case.

7.2 Results

7.2.1 Kinematics of a Forced Spray Flame

Unforced flame S-15-033 is presented in Figure 7-1 to gain insight into its structure and into the difference with the forced flame. The unforced flame consists of two conical structures: the outer cone, the branches of which are anchored at the bluff body edge, and the inner cone which is not attached to the bluff body. From the comparison between S-15-033 and S-15-033-160-30, small changes are observed in the flame shape. The forced flame is 4 mm shorter than the unforced, while the inner and outer branches are thicker and more curved compared to S-15-033 (Figure 7-1).

Instantaneous OH* chemiluminescence and OH PLIF images of S-15-033-160-30 (Figure 7-2) show that the cone-shaped heat release zone is moving downstream, while a highly variable behaviour of the OH region is observed with the OH signal intensity varying significantly among the snapshots. The OH zone is occasionally fragmented in different regions, complete or partial absence of half branch, and attachment and lift-off at the bluff body edge are also seen. The average lift-off height is approximately 2 mm, and the lift-off height of S-15-033-160-30 does not show any periodicity at 160 Hz.

Phase-averaged OH* chemiluminescence images of S-15-033-160-30 (Figure 7-3) show a small modulation of the flame shape, and specifically a downstream movement of the heat release zone during the acoustic cycle. No impingement of the flame on the wall is observed. OH* chemiluminescence is a line-of-sight measurement and thus, no individual regions of the flame can be isolated. However, the edges of the images capture mainly the behaviour of the edge of the outer cone flame region, as they constitute a line-of-sight integration of OH* chemiluminescence emitted only from that part of the flame. This part of the images shows a change in the flame angle during the cycle, which is also revealed more clearly in the phase-averaged OH PLIF images (Figure 7-4). Unlike the variation in the angle of the outer branches of the flame during the cycle, the inner cone branches do not exhibit any significant modulation. During the cycle, the angle of the flame varies between approximately 31 and 50 degrees (Figure 7-5). The maximum value is revealed at 60 degrees and the minimum at 210 degrees of the acoustic cycle.

In Figure 7-6, the local response of the flame at the forcing frequency is quantified based on OH PLIF images. The variance and thus, the level of OH fluctuations associated with the whole frequency range (0-500 Hz), is high in the outer cone region, while relatively low values are observed in the inner cone. The metric of local flame sensitivity to the forcing

frequency, R_L, defined in Section 2.3.3.3, is greater in the branches of the flame in the outer cone region, downstream the annular air passage, than in other parts of the flame. R_L is low in the inner cone region downstream of the bluff body.

To investigate the behaviour of the various parts of the flame to forcing, the $OH/< OH >$ phase-averaged variation (see Section 2.3.3.4) of the main spray flame regions (i.e. inner cone and outer cone branches, as indicated in Figure 7-6) is presented in Figure 7-7. The velocity fluctuations are increasing from 30 to 210 degrees, where the maximum value is reached and then, they start decreasing. The $OH/< OH >$ in the outer cone region and the angle variation are approximately in phase during the acoustic cycle and both are almost in antiphase with the velocity (Figure 7-5, Figure 7-7). As the velocity fluctuations are increasing the flame angle is decreasing, thus the outer cone flame branches are steeper, and the OH intensity in the respective region is decreasing. This suggests that the greater variation observed in the $OH/< OH >$ of the outer cone compared to that of the inner part (Figure 7-7) is attributed mainly to the change in the angle of the flame during the acoustic cycle. For instance, as described below for some phases during the cycle the flame angle is such that the flame falls inside the studied window (i.e. outer cone), but as the angle decreases and the flame branch becomes steeper a smaller part of the flame falls inside the window of interest. The bigger the angle change, the greater the change in the $OH/< OH >$ observed in the window of interest. In this case, the magnitude of $OH/< OH >$ variation is dependent on the amount of flame that falls inside the studied window.

In addition, Figure 7-7 shows that even though relatively high OH fluctuations are revealed in the individual regions, a low $OH/< OH >$ variation is observed in the total OH PLIF window. This can be explained by the 150-degree phase difference, observed between the $OH/< OH >$ in the outer cone and that in the inner cone region, which has an evening out-like effect. In order to understand better the aforementioned behaviour of the flame in the inner and outer cone windows, the phase-averaged OH PLIF images that correspond to low and high values of the $OH/< OH >$ are also presented in Figure 7-7. At 45 degrees, the peak value observed in $OH/< OH >$ of the outer cone region is mainly attributed to the fact that the increased flame angle results in a big part of the flame falling inside the respective window. However, at the same phase angle the OH observed in the inner cone flame area is relatively low. At 210 degrees, the flame angle is much lower than before and only a small part of the flame is observed inside the outer cone window, which explains the minimum value of $OH/< OH >$. The inner cone window exhibits a high $OH/< OH >$ value (Figure 7-7) mainly due to the slight increase in the amount of flame falling inside it.

7.2.2 Effect of Air Velocity and Global Equivalence ratio

After the description of the kinematics of the base case S-15-033-160-30, it is important to investigate the influence of air velocity and global equivalence ratio on the flame response. For this purpose, S-15-024-160-30 and S-12-033-160-30 -closer and farther from blow-off, compared to the base case, respectively- were selected (Table 7-1) to discuss the most striking differences.

Concerning air velocity, the comparison between the time-averaged OH PLIF images of S-15-033-160-30 and S-12-033-160-30 (Figure 7-1d and Figure 7-8b respectively) reveals that their overall mean shape is similar. As far as fuel loading is concerned, its influence on flame response is important, since it affects the location of the main heat release zones. The time-averaged OH* chemiluminescence image of S-15-024-30-160-30 (not presented here) shows that the flame is approximately 10 mm shorter than S-15-033-160-30, which is expected as the former flame is closer to blow-off than the other cases. Also, it is observed that at the higher injection velocity the distance of the joint part of the inner flame branches from the nozzle exit is 2 mm greater than that of the lower velocity (Figure 7-1d, Figure 7-8b).

A sequence of instantaneous OH* chemiluminescence and OH PLIF images of S-15-024-30-160-30 and S-12-033-160-30 (Figure 7-9) highlight the main features of their behaviour. Comparing Figure 7-9 and Figure 7-2, it is shown that S-15-024-30-160-30, which is closer to blow-off (U=92% of U_B), apart from the decreased length, occasionally exhibits an asymmetric wedge-like shape. The OH PLIF snapshots of this case reveal that the OH zone is more fragmented than that of the other flames, while absence of the branches of the OH region is seen more often (Figure 7-9a). On the contrary, for S-12-033-160-30, which is farther from blow-off (U=70% of U_B), the characteristics observed in the other conditions (lift-off, missing parts of the OH regions) are less pronounced, and the OH regions are thicker than those close to blow-off (Figure 7-9b).

The phase-averaged OH* chemiluminescence (Figure 7-10) and OH PLIF images (Figure 7-11) of S-15-024-30-160-30 demonstrate that the flame does not exceed the height of 35 mm, unlike S-15-033-160-30 (Figure 7-3), where the maximum height during the cycle is approximately 45 mm, thus the main heat release zone is located closer to the bluff body plane. During the cycle, there is a variation in the flame angle (Figure 7-11), which was also the case in Figure 7-4, however here the outer cone region is significantly smaller especially downstream. A steeper flame angle is observed for S-15-024-160-30 (Figure 7-12a), which varies in the range of 26-45 degrees, unlike S-15-033-160-30 (Figure 7-5) and S-12-033-160-

30 (Figure 7-12b) whose angle modulation is in the range of 31-50 and 31-48 degrees respectively.

Comparing Figure 7-6, Figure 7-13b and Figure 7-13d, it is clear that for all the studied experimental conditions the outer cone region downstream of the annular air passage constitutes the location of the highest R_L values. In the inner cone region, downstream of the bluff body, R_L is very low in all three flames, however it is slightly greater for S-15-033-160-30. For S-15-024-160-30, the outer cone region is shorter and less thick than the other two cases, whereas S-12-033-160-30 reveals slightly thicker outer branches that extend closer to the wall. For all the above flames, the highest values of the variance of OH are observed in the outer cone region, while low values are seen in the inner cone.

As far as the individual parts of the flame are concerned, S-15-024-160-30 (Figure 7-14a), shows similar trends with S-15-033-160-30 (Figure 7-7) and particularly, $OH/< OH >$ in the outer cone region and angle variation (Figure 7-12) are almost in phase during the cycle, while having a phase difference of approximately 135 degrees with the $OH/< OH >$ in the inner cone region, thus resulting in a low $OH/< OH >$ variation of the total flame. On the contrary, for S-12-033-160-30, which is further from blow-off than the other flames, the $OH/< OH >$ variation in the outer cone region 'acts' exactly in anti-phase with that in the inner region (Figure 7-14b). This behaviour may suggest that as blow-off is approached the phase difference of OH fluctuations between the inner and outer region is being shifted farther from 180 degrees.

The probability density function of the lift-off heights (Figure 7-15) show that close to blow-off, S-15-024-160-30 and S-15-024 are mainly attached to the bluff body (for S-15-024-160-30, 92% of the samples exhibit a lift-off height below 1 mm). The lift-off exhibited by the forced flame shows a slight periodicity at 160 Hz, as concluded by the fact that in the lift-off height spectrum (Figure 7-15b), apart from a peak at 160 Hz, many noisy peaks can also be seen. Far from blow-off, S-12-033-160-30 and S-12-033 reveal a slightly more pronounced lift-off (average lift-off height $\bar{h}$ = 1.3 mm) than that observed close to blow-off. In this case, the lift-off periodicity at the forcing frequency is very pronounced, as the lift-off spectrum (Figure 7-15b) shows two peaks, one dominant peak at 160 Hz and a smaller peak at 320 Hz. S-15-033-160-30 and S-15-033 are lifted more than the other flames, with the average lift-off height being around 2 mm. The lift-off is not periodic at the forcing frequency, as concluded by the absence of the 160 Hz peak in the very noisy spectrum. In all cases the PDFs have a long positive tail. From the above analysis, it is suggested that the forced flames tend to have slightly reduced average lift-off heights compared to the unforced conditions. The phase-averaged lift-off height

of S-12-033-160-30 (Figure 7-15b) has a sinusoidal shape, which is almost in phase with the velocity signal (Figure 7-14b). The fact that the lift-off height of the flame that is farther from its blow-off condition shows a significantly greater periodicity at the forcing frequency than that revealed in the other conditions could possibly be explained by the reduced chaotic radial flame motion and the less fragmented flame sheet, as opposed to the increasingly fragmented sheet as blow-off condition is approached.

7.2.3 Amplitude Dependence of the Flame Response

Following the previous analysis on the flame kinematics at a particular forcing amplitude (A=30%), the overall flame response as a function of forcing amplitude is presented below for S-15-033, S-15-024 and S-12-033.

The results suggest that the heat release response to the inlet forcing amplitude for all three cases is very low, with the maximum value being approximately 11% for S-12-033 (Figure 7-16). For S-15-033, $<Q'/<Q>$ increases linearly with A up to A~20%, then it decreases up to A~25%, and after a small rise, it drops again from A~29% to A~34%. For S-15-024 $<Q'/<Q>$ increases almost linearly up to A~29% after which it remains almost constant, meeting the aforementioned curve. S-12-033 increases almost linearly up to A~33% and subsequently it continues increasing, but with a reduced slope. The NFTF of S-15-033 decreases from ~0.46 to ~0.18, exhibiting a much greater reduction rate than S-15-024, which reveals a gradual decrease from ~0.33 to ~0.19, meeting the former curve at A=32%. The NFTF of S-12-033 is almost constant in the range of 0.26-0.29. The NFTF phase behaviour of the three flames is different. The NFTF phase of S-15-033 shows little sensitivity on the forcing amplitude, that of S-15-024 reveals an almost linear increase with A, and the NFTF phase of S-12-033 increases and then decreases almost to the initial value.

The low heat release response of all three flames seems to be in agreement with the analysis in Sections 7.2.1 and 7.2.2, where it was conjectured that even though the individual windows showed relatively high OH fluctuations, the magnitude of OH fluctuations of the total OH PLIF image was lower than that of the individual regions, due the phase difference between the $OH/<OH>$ variation of the outer and inner cone region varying between 135 to 180 degrees. Also, the three flames have similar $<Q'/<Q>$ (6-8%) at forcing amplitude A=30%, suggesting the little sensitivity of the spray system response to input air velocity and global equivalence ratio.

Despite the low response, differences can be observed. Comparing the heat release response of S-15-033 and S-15-024 (same U_{air}, different ethanol flowrate), at low A the

response of the former flame is greater than that of the latter. As A increases further than A=20% the response of S-15-033 decreases and thus, the difference in response between the two flames decreases until the two curves meet at A=31%. A possible explanation for this behaviour could be that initially at lower amplitudes S-15-033 is far from blow-off and shows a relatively high response, but as A increases the flame gets closer to its blow-off condition, resulting in a lower response, possibly due to the local extinction events that could become more and more frequent as blow-off is approached. The greater response of S-15-033 at low A might be associated with the greater value of fuel flow rate, suggesting that at low A, the system's response is sensitive to the fuel flow rate. Comparing S-12-033 and S-15-024 (U_{air} different but same ethanol flowrate), the greater response of the former flame, observed at A greater than 25%, might be because it is not yet close to blow-off and thus, it does not experience possibilities of extinction. Up to A=25% the two flames show a very similar response, despite the difference in air velocity, suggesting that the air velocity has a smaller effect on the response than the fuel flow rate.

As described in previous sections, the NFTF results acquired from OH* chemiluminescence measurements need to be interpreted very carefully. The OH* chemiluminescence signal is investigated for different ethanol mass flow rates for a constant global equivalence ratio. As described by Figure 7-17, the OH* signal increases linearly with the fuel mass flow rate in the range of interest. This is consistent with previous studies on diffusion flames using gaseous fuels at globally lean conditions [182] and on spray flames [183]. The proportionality of the OH* chemiluminescence intensity with the flame thermal power suggests that OH* signal can be used qualitatively to infer relative changes of the heat release rate.

From the above analysis, the low response exhibited by ethanol spray flames is in good agreement with the response of the non-premixed system with axial fuel injection presented in Section 6.2.3. A direct comparison between these non-premixed systems is presented in Section 7.3.

7.2.4 Proper Orthogonal Decomposition (POD) Analysis

In this section, the POD results of OH* chemiluminescence and OH PLIF images are discussed. The OH* chemiluminescence POD results presented below consist of the first few modes, the PSDs of the POD time coefficients, the instantaneous OH* chemiluminescence images and their reconstruction based only on a small number of modes, as well as the relative cumulative energy content of POD modes. The OH PLIF POD results are also presented in a similar way. The following discussion focuses on: a) the basic structure of the flame extracted

from POD, b) its temporal evolution and c) the difference between the forced and unforced flame.

7.2.4.1 OH* Chemiluminescence POD Analysis

Figure 7-18a shows the first four POD modes and their respective PSD of POD time coefficients, while Figure 7-18b demonstrates raw OH* chemiluminescence snapshots and snapshots at the same times from the reconstructed OH* chemiluminescence movie based only on a small number of modes with the mean image for the unforced flame S-15-033.

Concerning the spatial structure of S-15-033, Mode 1 exhibits a banded shape (Figure 7-18a), which is characteristic of heat release fluctuations in the axial direction. The banded shape is more pronounced on the left side of the flame. The time evolution of the reconstructed image of Mode 1 with its modal time coefficients suggests an axial motion of the flame (Figure 7-18b). Mode 2 reveals a roughly antisymmetric pair of heat release fluctuations, which represents the transverse oscillating motion of the flame. These antisymmetric heat release fluctuations cannot be seen easily in the raw OH* chemiluminescence snapshots because of the underlying small-scale fluctuations. Modes 3 and 4 show a combination of the aforementioned spatial features. As the mode number increases more details of the flame structure are revealed. The PSD of POD time coefficients of a mode reveals the periodicity associated with the respective motion of the flame. In Figure 7-18a, the PSDs of the first three POD modes exhibit peaks mainly below 50 Hz, while the PSD of the fourth mode reveals, apart from the low frequencies, smaller peaks at frequencies greater than 50 Hz.

For S-15-033-160-30, in terms of spatial features, Mode 1 shows an antisymmetric pair of heat release fluctuations (Figure 7-19), which as seen in the respective reconstructed flame corresponds to a left-right flame motion (Figure 7-20). Concerning the periodicity, the PSD of Mode 1 exhibits peaks mainly below 50 Hz, whereas a very small peak is seen at 160 Hz (Figure 7-19). The fact that this low frequency dominant feature also constitutes a dominant characteristic of the unforced flame, suggests that forcing does not change drastically the behaviour of the spray flame. The axial dependence of the flame shape in Mode 2 suggests the axial motion of the flame, as demonstrated in the reconstructed flame of Mode 2. The respective PSD reveals that 160 Hz is the only frequency content associated with this motion, which thus constitutes the main dominant difference between the forced and unforced flames. The shapes of Modes 3 and 4 show a combination of axial and radial heat release variation, which represents an axial and transverse oscillating flame motion. In the PSD of Mode 3 the dominant peak is

revealed at 160 Hz, followed by two other smaller peaks at 13 and 23 Hz and the PSD of Mode 4 exhibits a high peak at 160 Hz and many smaller peaks below 50 Hz.

Concerning the POD energy, the energy content of the first four Modes is the same (48%) in both the forced and the unforced condition. Also, the distribution of energy in the individual Modes is similar in both cases (Table 7-2). This suggests again that forcing does not affect significantly the flame behaviour.

The OH* chemiluminescence POD data of S-15-024-160-30 and S-12-033-160-30 (not presented here) are similar with that of S-15-033-160-30. In case of S-15-033-160-30, Mode 1 (POD energy 22.3%) is mainly linked with frequencies lower than 50 Hz, whereas in S-15-024-160-30 (POD energy 20%) the periodicity of Mode 1 contains apart from the dominant low frequency peaks, a smaller peak at 160 Hz. Only Mode 1 of S-12-033-160-30 (POD energy 16%) is purely associated with a dominant peak at 160 Hz, which suggests that the acoustic forcing has a greater influence on this flame. In all three flames, Mode 2 exhibits a periodicity of only 160 Hz. From Figure 7-21, it is evident that the cumulative energy content of the three flames is very similar, with the values being slightly greater for S-15-033-160-30, followed by S-15-024-160-30 and S-12-033-160-30.

7.2.4.2 OH PLIF POD Analysis

The first OH PLIF POD Mode (Figure 7-22) of S-15-033 shows an asymmetric OH structure, of which the side of greater OH is significantly higher than the side of lower OH. This POD structure corresponds a combination of axial and left-right oscillating motions, described by the respective reconstructed OH PLIF images (Figure 7-22b) and is associated with frequencies below 50 Hz, as presented by the PSD of POD time coefficients (Figure 7-22a).

Modes 2 and 3 also represent a combination of axial and transverse motion, whereas Mode 4 reveals an almost purely transverse motion. The frequency content of Mode 2 is in the range of 0-50 Hz, whereas that of Modes 3 and 4 is extended to higher frequencies (up to 300 Hz), with the highest peaks being revealed in the low frequency range.

Concerning S-15-033-160-30, the structure of the first OH PLIF POD Mode consists of an antisymmetric pair of OH in the downstream region, whereas close to the bluff body edges there is a second, much smaller and of lower OH intensity, antisymmetric pair (Figure 7-23). The dominant feature corresponds to a 23 Hz axial and left-right oscillating motion, where the maximum OH region on the downstream side is revealed at the same time with a smaller region of high OH diagonally, close to the bluff body edge (Figure 7-23 and Figure 7-24).

Simultaneously, in the other diagonal two similar regions of minimum OH intensity are presented. The structure of Mode 4 has a variance in the axial direction. This axial motion of OH is associated purely with a 160 Hz frequency. The main features of the respective reconstructed OH PLIF POD image (Figure 7-24) are the angle variation of the outer cone branch and the fact that when maximum OH is observed in the outer cone regions, minimum OH is seen in the inner cone branches and vice versa. The above findings concerning the angle change and the out of phase variation of these regions are consistent with the analysis in Section 7.2.1. Thus, POD constitutes a useful method in the identification of dominant features and their periodicity that compose the complicated mechanisms of the flame response. The reconstructed OH PLIF images of both Modes 2 and 3 show a combination of axial and transversal motion, with the main difference being that in Mode 2 the left and right branches move downstream simultaneously, whereas in Mode 3 (not presented here) when one branch moves downstream the other one moves upstream. A similar pattern with Mode 3 was observed in Mode 1. In fact, Mode's 3 PSD (Figure 7-23b) reveals apart from the peaks at 160 Hz and at low frequencies, a high peak at 183 Hz (=160+23 Hz), where 23 Hz was the frequency component associated with the motion of Mode 1. The PSD of Mode 2 contains only peaks at 160 Hz and at lower frequencies.

The relative energy contained in the first four OH PLIF POD Modes and the energy distribution in the individual modes are similar in both the forced an unforced case (Table 7-3). In addition, for condition S-15-033-160-30, the cumulative energy contained in the first 50 OH* chemiluminescence POD modes (Figure 7-21) is slightly higher (85.7%) than that (79.3%) in the respective OH PLIF modes (Figure 7-25). The similar energy values suggest that the structures captured by the planar measurement constitute a good representation of those revealed by the line-of-sight measurement.

Figure 7-25 reveals that the cumulative energy content of S-15-024-160-30 and S-12-033-160-30 is similar (the first 50 POD Modes contain 73% and 71% respectively), while S-15-033-160-30 has a greater cumulative energy (the first 50 POD Modes contain 73% and 79% respectively). The features of OH PLIF POD data, described previously for S-15-033-160-30, are similar with those observed in S-15-024-160-30 and S-12-033-160-30 (not presented here).

7.3 Comparison Between Spray and Non-Premixed Flames with Axial Fuel Injection

In this Section, spray and non-premixed with axial fuel injection forced flames are compared in terms of their kinematics and NFTFs.

For the flame kinematics discussion, two experimental conditions, NPA-15-042 and S-15-033, are compared. To begin with, the observation of Figure 7-6 of S-15-033-160-30 and the respective figure of NPA-15-042-160-30 (Figure 6-6) suggests that in both systems R_L values are greater in the branches of the flame in the outer cone region, downstream of the annular air passage, than that in other parts of the flame. The main difference is that this region in the S-15-033-160-30 case forms a much wider angle than that in the NPA-15-042-160-30. The wider angle could be attributed to the fact that the hollow cone jet spray has a 60-degree angle, whereas the steeper branches in the NPA system could be due to vertical injection of the methane jet at the centre of the bluff body. In the region downstream of the bluff body, R_L values are almost zero for NPA-15-042-160-30, whereas they are relatively low for S-15-033-160-30.

As far as the individual parts of the flame are concerned, the two systems have different flame structures, thus the OH PLIF image was split into different regions. The $OH/<OH>$ variation of the outer cone region and the ISL for S-15-033-160-30 and NPA-15-042-160-30 respectively show similar trends (Figure 7-7, Figure 6-7). However, while for S-15-033-160-30 the angle variation and the $OH/<OH>$ in the outer cone region were almost in phase during the cycle, for NPA-15-042-160-30 a modulation in the flame angle was barely observed. These figures also reveal some similarities in the $OH/<OH>$ variation between the inner cone and ORZ regions for S-15-033-160-30 and NPA-15-042-160-30 respectively.

After having presented a general overview in terms of the flame kinematics of both systems, their NFTF behaviour is discussed below. It is evident that the curves of heat release response as a function of inlet forcing amplitude of both systems have similar trends and appear in the same region, while the majority of them saturates around A=30% (Figure 7-26). Also, in both systems conditions that are close to blow-off (i.e. NPA-21-038, S-15-024) exhibit low response. This could probably be explained by the fact that the possibilities of local extinctions are increased as the flame approaches blow-off. The NFTF curves reveal similar trends as well, and they appear in the same area especially for A greater than 25%.

However, the two systems present small differences in their response, for which careful interpretation is needed. The main exception is S-15-033, which below A=25% has a

greater response than the other flames. The high response might possibly be associated with the fact that this condition has a greater fuel flow rate than the other spray flames. It is also worth noting that in the NPA system, the flame that exhibits the highest response (NPA-15-042) has the highest global equivalence ratio. Therefore, it could be suggested that both the spray and NPA systems are sensitive to the fuel flow rate. Another striking feature is that S-12-033 has a higher response than all other curves for A greater than 27%, which could be attributed to the fact that it is far from blow-off and it does not experience possibilities of local extinction.

Below, the response of the experimental conditions NPA-15-038 and S-15-033, is compared. Both the normalised global heat release fluctuation and NFTF for S-15-033 are greater than those of NPA-15-038, but for A>25% the difference in their response becomes smaller and eventually, both curves meet at their saturation point. Both conditions exhibit a reduction in NFTF, with the NFTF for S-15-033 decreasing from 0.45 to 0.18, and for NPA-15-038 decreasing from 0.37 to 0.19. Both conditions when forced at low amplitudes are far from blow-off, showing a relatively high amplitude, but as A increases the flames are getting closer to blow-off, resulting in a lower response probably due to local extinction events that are becoming more frequent as blow-off is being approached. It is worth mentioning that in both flames at low amplitudes, as A increases, $<Q'/<Q>$ increases and after A=20% and A=27% for S-15-033 and for NPA-15-038 respectively, $<Q'/<Q>$ starts decreasing. During the experiments, it was observed that the amplitude A at which the normalised heat release started decreasing coincided with the initiation of a chaotic radial flame motion, which became more and more frequent and violent as the forcing amplitude was further increased, indicating that the flame was gradually approaching blow-off.

From the description of the flame kinematics and the comparison of their response, it is revealed that both the spray and NPA systems show many similarities, but also some differences which could not be neglected. In fact, spray constitutes a complex non-premixed system, where several phenomena are involved, such as fuel atomisation, droplet evaporation, droplet transport, which can cause modulation of fuel concentration and/or fuel distribution and therefore produce oscillations in the rate of heat release [159].

One of the main parameters that should be taken into consideration and could differentiate the response of the above systems is evaporation time. In this study, the evaporation time was estimated using a simplified one-dimensional model (developed by P. Sitte) of vaporization of a moving fuel droplet [184]. Figure 7-27 plots the evaporation time as a function of initial droplet diameter for a range of temperatures, assuming a mean relative velocity between the air and fuel droplet of 10 m/s. The Sauter mean diameter (SMD) of stable

ethanol spray flames at similar experimental conditions, measured using PDA (Phase Doppler Anemometry) on the same burner configuration, was found to vary in the range of 45-80 μm at locations between 10 and 40 mm downstream of the bluff body plane [151]. Both temperature T and droplet diameter (d_d) affect greatly the evaporation time (t_{evap}) of droplets. For a given T, the greater the d_d, the greater the t_{evap} is, while for a given d_d the evaporation time decreases with the increase in temperature. At T=300 K, for d_d varying between 50 and 100 μm, t_{evap} takes values between 206 to 678 ms respectively (Figure 7-27a). As temperature increases, t_{evap} reduces significantly. The temperature profile of the flame is assumed to take values in the range of 2000-2500 K in the reaction regions and around 1500-1700 K further upstream the reaction zone. Figure 7-27b estimates that in the range of d_d=50-100 μm and T=1500-2500 K, the evaporation time takes values between 2.6 and 19.4 ms.

The axial centre of heat release for S-15-033-160-30, estimated from the time-averaged OH* chemiluminescence image (Figure 7-1c), lies 21 mm downstream of the bluff body plane. Given that the bulk air velocity is 15 m/s, it is estimated that the fuel is transported to the major heat release zone after 1.4 ms. Comparing this time scale with t_{evap}, it can be conjectured that droplets may not have fully evaporated by the time they reach the major heat release zone. This is consistent with the fact that during the experiments a strong smell of ethanol was observed.

PDA measurements [151] on unforced stable spray flames far and close to blow-off (E1S1 and E1S2 respectively) showed that for all Z/D (Z axial distance, D bluff body diameter) only a few droplets existed at radial locations larger than $1.2D$. At small Z/D, the location of the peak SMD was aligned with the hollow-cone spray path, while at longer distances downstream, the SMD was more uniform, with a smaller value obtained at locations close to the flame zone. The SMD measured for the conditions close and far from blow-off were similar with the peak value close to spray jet around $70 - 80\ \mu m$, although a smaller SMD was obtained at outer flame zone at the lower velocity case (E1S1). The mean Mie images of the unforced ethanol flames at blow-off showed a less disperse spray compared to the stable flames far from blow-off. The instantaneous Mie images at blow-off revealed a non-axisymmetric profile of the spray. The spray angle was slightly narrower than 60 degrees [151].

7.4 Conclusions

Detailed experimental studies were performed to investigate the response of lean turbulent ethanol spray flames to acoustic forcing. OH* chemiluminescence measurements, acquired with a photomultiplier tube (PMT) and an ICCD camera, were used to study qualitatively the heat release response of the flames, while OH PLIF measurements were used also qualitatively to understand the response of the flame structure and the behaviour of the various parts of the flames. Apart from the flame kinematics analysis, the amplitude dependence of the transfer function was estimated. Special attention was given to the study of the effect of air velocity and global equivalence ratio on the flame response, as well as the behaviour of forced flames when blow-off condition is approached. The dominant structures of the flames and their periodicity were characterised using the Proper Orthogonal Decomposition (POD) method. Finally, a comparison between forced spray and non-premixed with axial fuel injection flames was performed in terms of their response.

Concerning the amplitude dependence of the spray flame response, a low, nonlinear response was observed in the flames studied (the maximum normalised global heat release fluctuation was approximately 11%). Additionally, it was suggested that the proximity of forced flames to the blow-off condition was crucial in their heat release response. In particular, for conditions that were far from blow-off in the entire range of forcing amplitudes tested, their response increased almost linearly with A, reaching greater values at high A compared to the conditions that were approaching blow-off. On the contrary, flames that were very close to blow-off, revealed a very low response. Flames that initially, at low A were far from blow-off, revealed a relatively high response, but if with the increase in A they were approaching their blow-off condition, they started exhibiting a lower response, which could possibly be due to increased local extinction events and the initiation of a chaotic radial flame motion. For instance, close to blow-off the OH PLIF snapshots demonstrated that the OH zone was more fragmented and absence of the branches of the flame was seen more often than in the flames farther from blow-off.

As far as the flame kinematics are concerned, the following conclusions were reached. It was revealed that the various parts of the flame responded differently to acoustic forcing. The outer cone region, downstream of the annular air passage constituted the location of the highest values of R_L (OH fluctuation at 160 Hz to the total variance of OH), whereas R_L was very low in the inner cone region, downstream of the bluff body. During the acoustic cycle a change in the angle of the outer flame branches was observed, whereas the angle of the inner cone flame branches did not show any significant modulation. In particular, for far from blow-off flames,

the angle variation and the $OH/<OH>$ in the outer cone region were in phase during the cycle and both were in antiphase with the $OH/<OH>$ in the inner cone region. However, as blow-off was approached the phase difference of OH fluctuations between the inner and outer region was shifted farther from 180 degrees. Even though relatively high OH fluctuations were revealed in the individual regions, a low $OH/<OH>$ variation was observed in the total OH PLIF window, due to the phase difference between the $OH/<OH>$ in the outer cone and that in the inner cone region, which had an evening out-like effect. During the cycle, a greater variation was observed in the $OH/<OH>$ of the outer cone compared to that of the inner part, which could be attributed mainly to the change in the angle of the flame during the acoustic cycle. Also, it was conjectured that forced flames had slightly reduced average lift-off heights compared to the unforced conditions and the lift-off height periodicity at the forcing frequency was significantly greater for flames far from blow-off than that revealed closer to blow-off.

The main findings of the POD analysis were the following. Two dominant flame structures were revealed in the first few Modes of the OH* chemiluminescence POD results: a) an antisymmetric pair of heat release fluctuations, which corresponded to a left-right flame motion and was associated with frequencies lower than 50 Hz. This low-frequency feature was characteristic of the unforced flame, which implied that acoustic forcing did not change drastically the behaviour of the spray flame. b) a banded shape, which represented the axial motion of the flame and was associated with the forcing frequency at 160 Hz. The fact that in both the forced and unforced flames the POD energy content of the first four Modes was the same and the distribution of energy in the individual Modes was similar, suggested that forcing did not alter significantly the flame structure. The greatest influence of the forcing was exhibited in the far from blow-off condition, in which the first Mode was purely associated with a frequency at 160 Hz. In the other flames Mode 1 was mainly dominated by the transverse flame motion, whereas Mode 2 in all flames revealed a periodicity only at 160 Hz. Higher modes showed a combination of the above spatial features. The OH PLIF POD results, apart from the aforementioned features, revealed the angle variation and the kinematics between the inner and outer cone regions (almost out of phase variation), which were described previously. Therefore, POD was found to be a useful method in the identification of dominant features and their periodicity in forced spray flames even at conditions that were close to blow-off.

Both spray and the non-premixed with axial fuel injection flames exhibited a low response and specifically, the curves of heat release response as a function of inlet forcing amplitude of both systems had similar trends and appeared in the same region, while most of them saturated at around A=30%. Also, in both systems the close to blow-off conditions

exhibited a low response. In the NPA system, the region downstream of the annular air passage showed grater R_L values than the other flame regions, but a modulation in the flame angle was barely observed.

7.5 Figures of Chapter 7

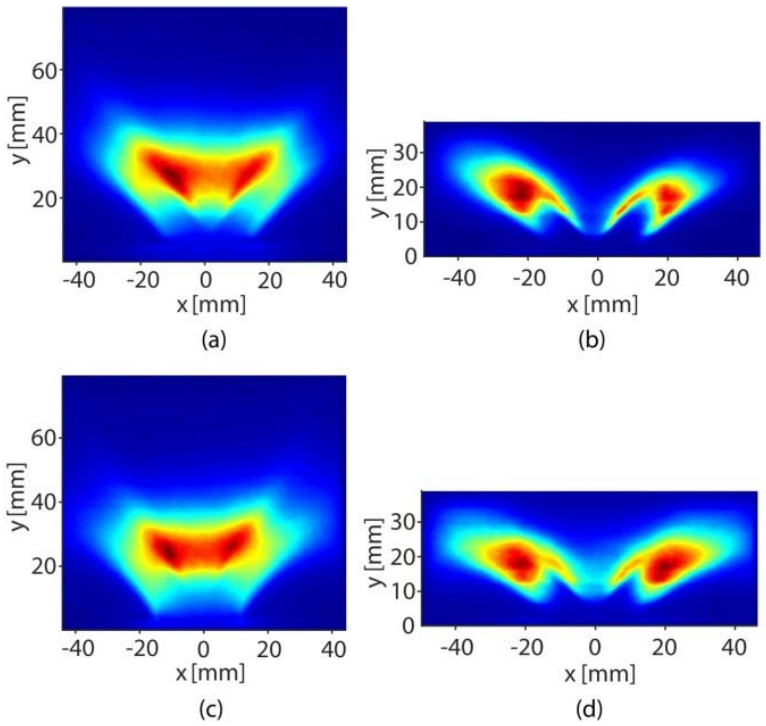

Figure 7-1: Time-averaged (a,c) OH* chemiluminescence and (b,d) OH PLIF image of S-15-033 and S-15-033-160-30.

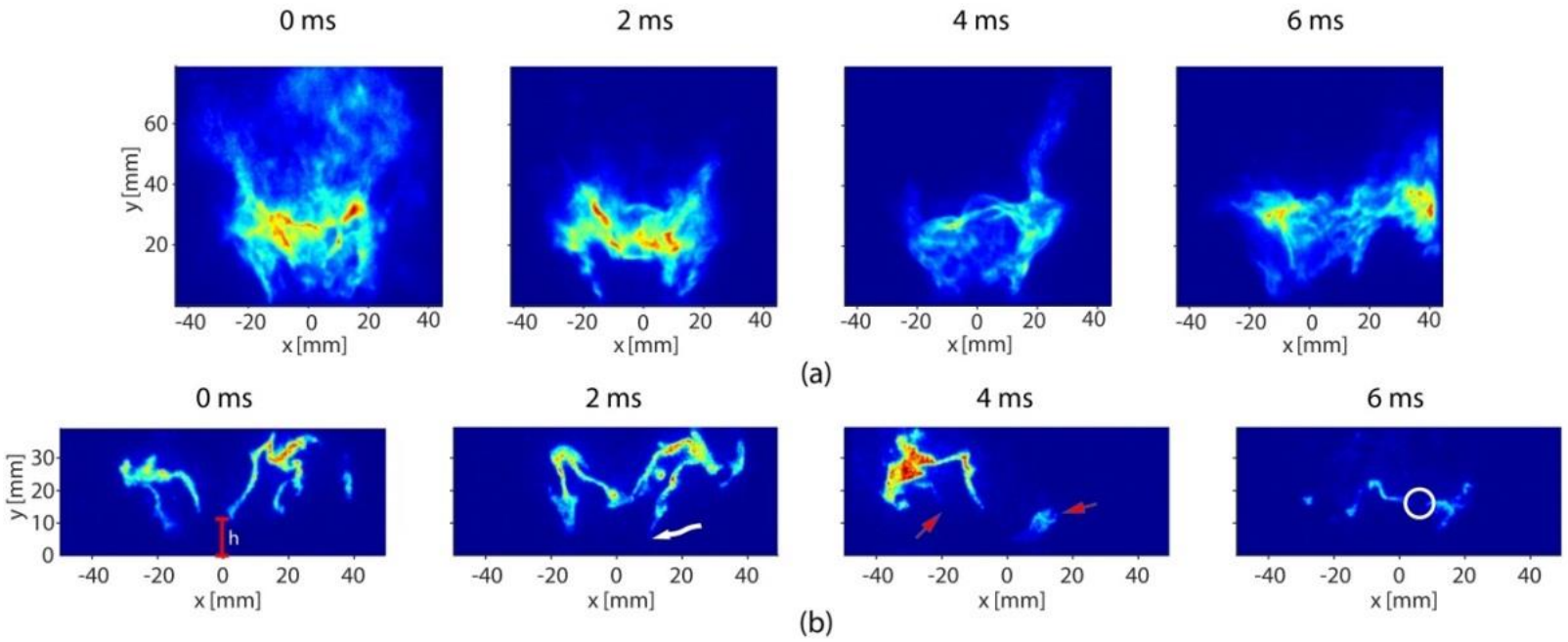

Figure 7-2: Instantaneous (a) OH* chemiluminescence and (b) OH PLIF images of S-15-033-160-30 (not recorded simultaneously) during the cycle (*t*=0 ms corresponds to the beginning of the cycle). The same colormap for each image was used. The main features of their behaviour are highlighted: red line: lift-off height *h* at the bluff body edge, white curved arrow: flame attached to the bluff body edge, red arrow: inner or/and outer branches missing, white circle: breaks of the OH zone.

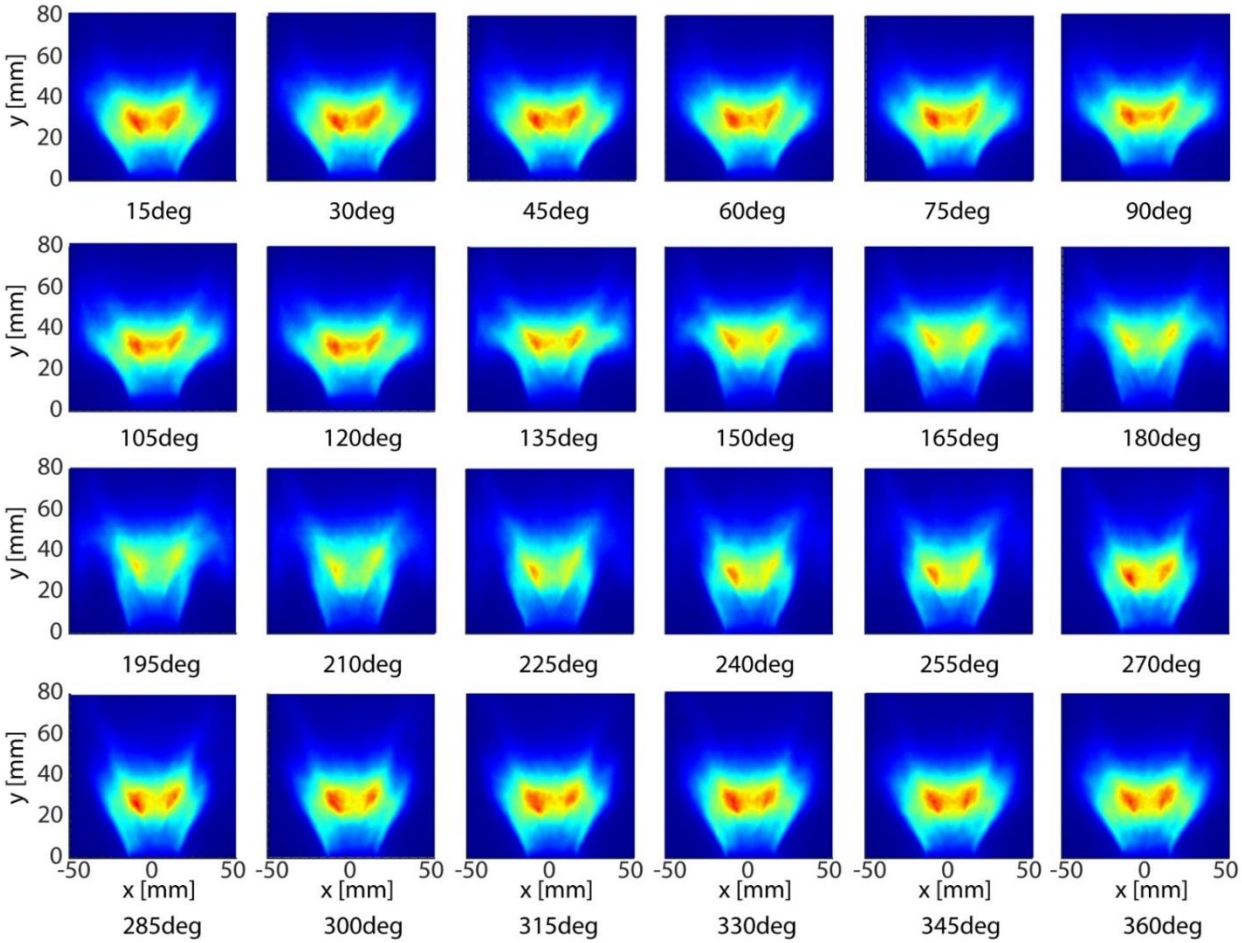

Figure 7-3: Phase-averaged OH* chemiluminescence images of S-15-033-160-30.

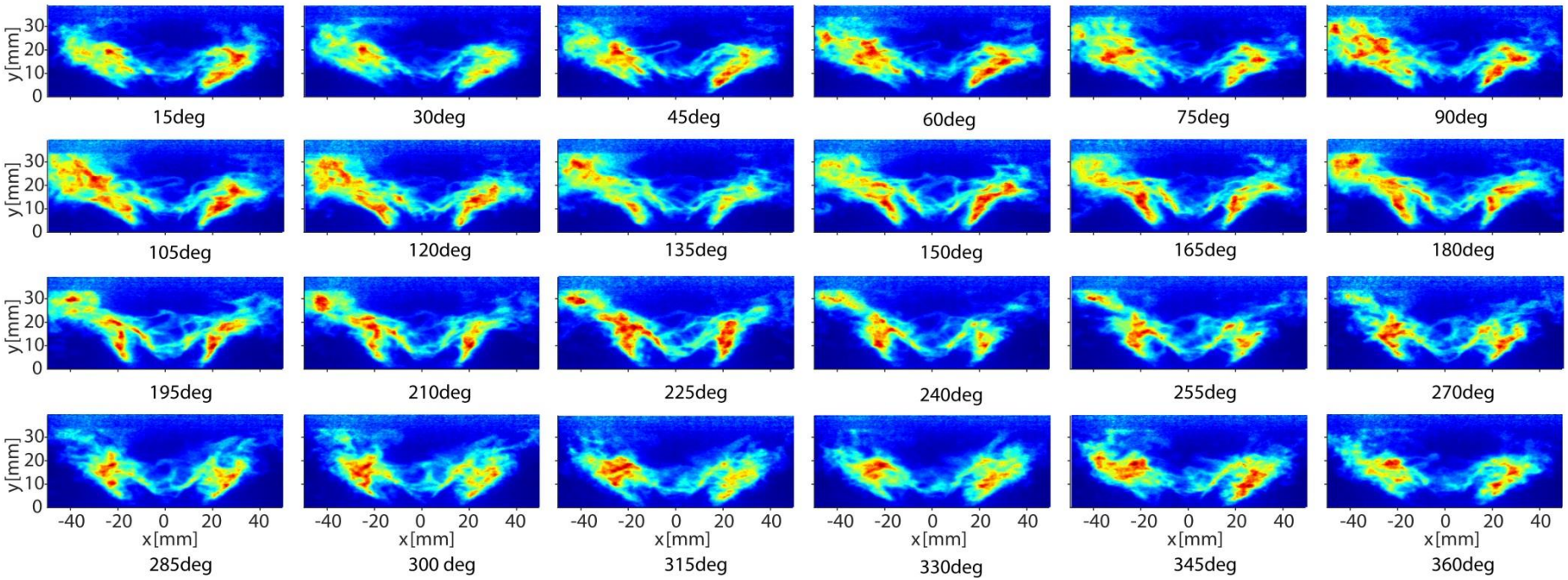

Figure 7-4: Phase-averaged OH PLIF images of S-15-033-160-30.

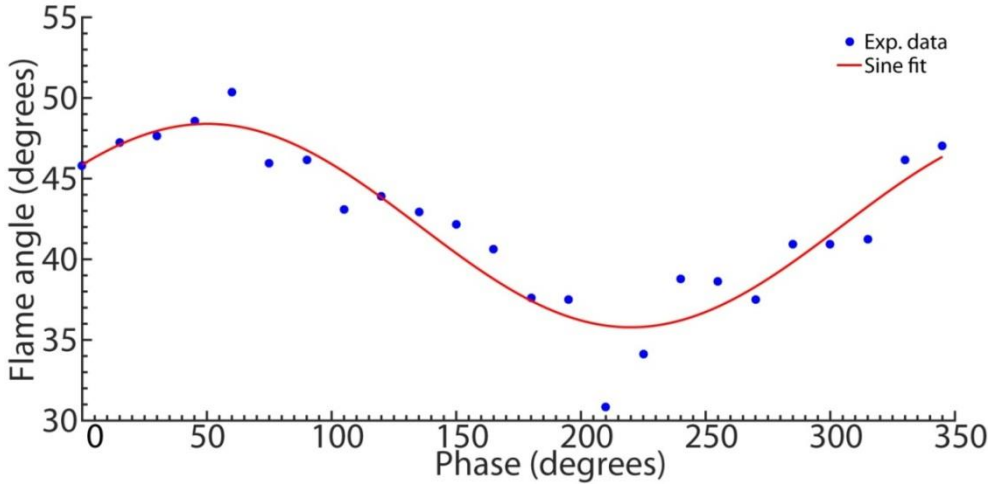

Figure 7-5: Flame angle variation with respect to phase of the acoustic cycle for S-15-033-160-30.

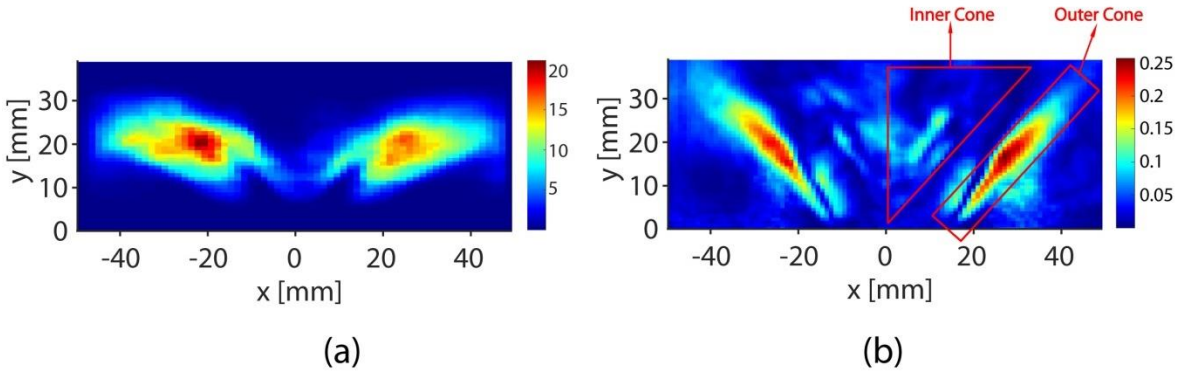

Figure 7-6: (a) Variance of OH and (b) ratio R_L (OH fluctuation at 160 Hz to the total variance of OH) for S-15-033-160-30.

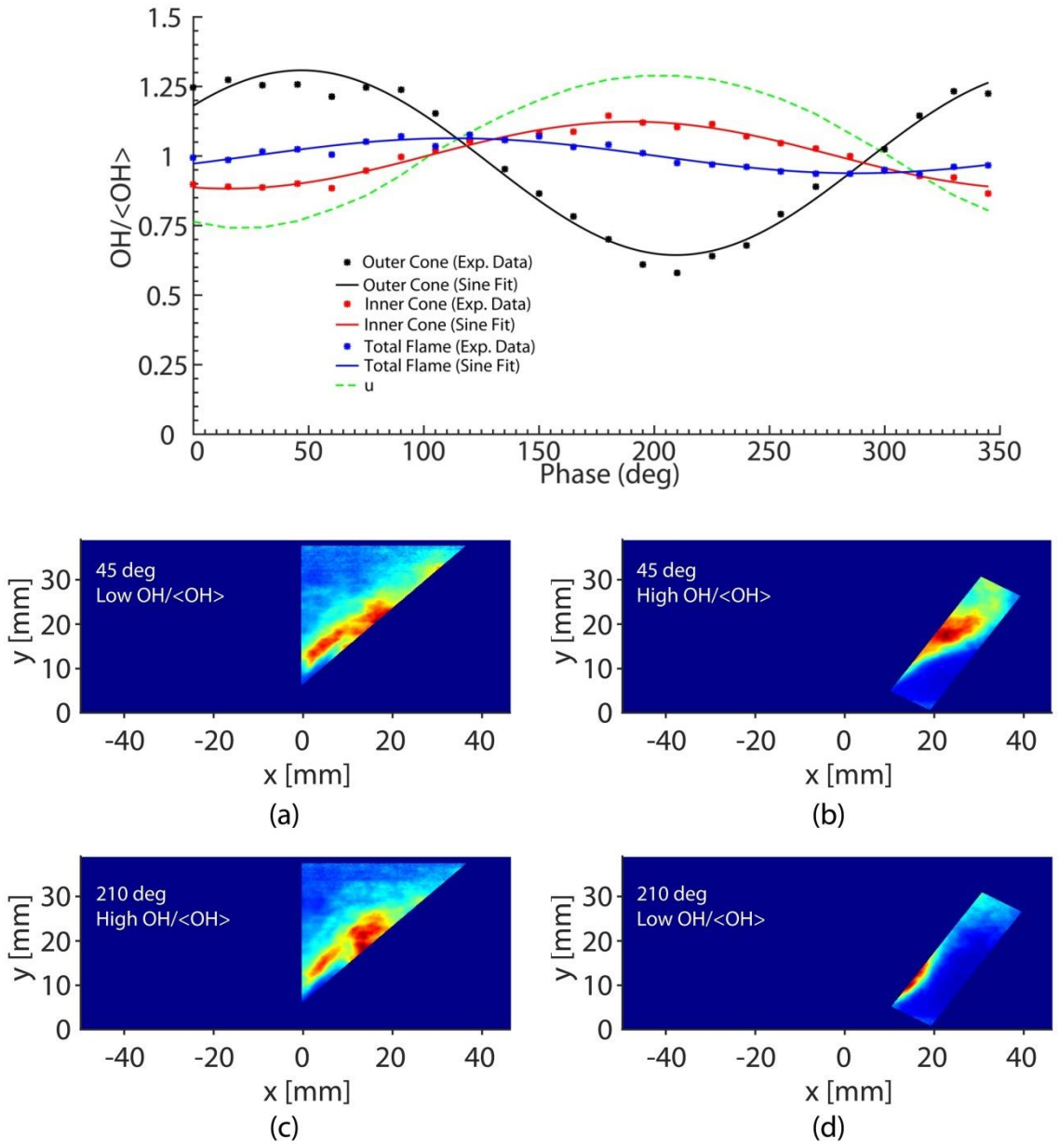

Figure 7-7: (top) $OH/< OH >$ variation during the acoustic cycle, evaluated from phase-averaged OH PLIF images (data presented in Figure 7-4), calculated from the outer, inner cone and whole OH PLIF window. The green dashed line represents the normalised acoustic velocity fluctuations. (bottom) Phase-averaged OH PLIF images of the inner (a and c) and outer cone (b and d) windows at phase angles 45 and 210 degrees, corresponding to low and high values of $OH/< OH >$. Flame: S-15-033-160-30.

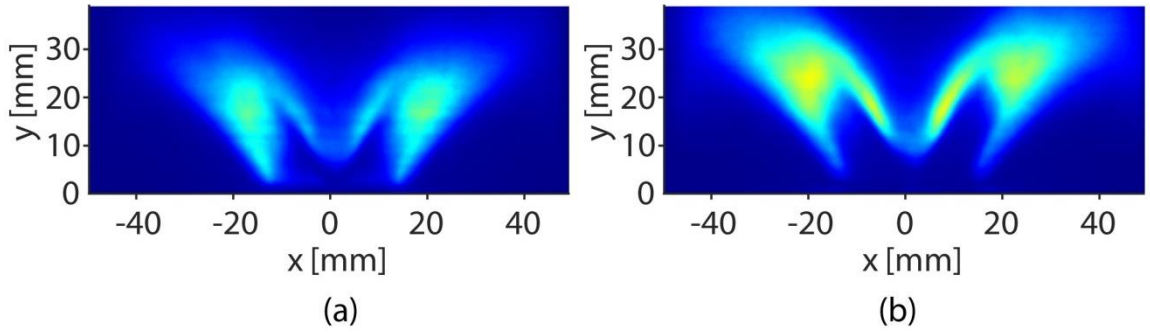

Figure 7-8: Time-averaged OH PLIF image of (a) S-15-024-160-30 and (b) S-12-033-160-30.

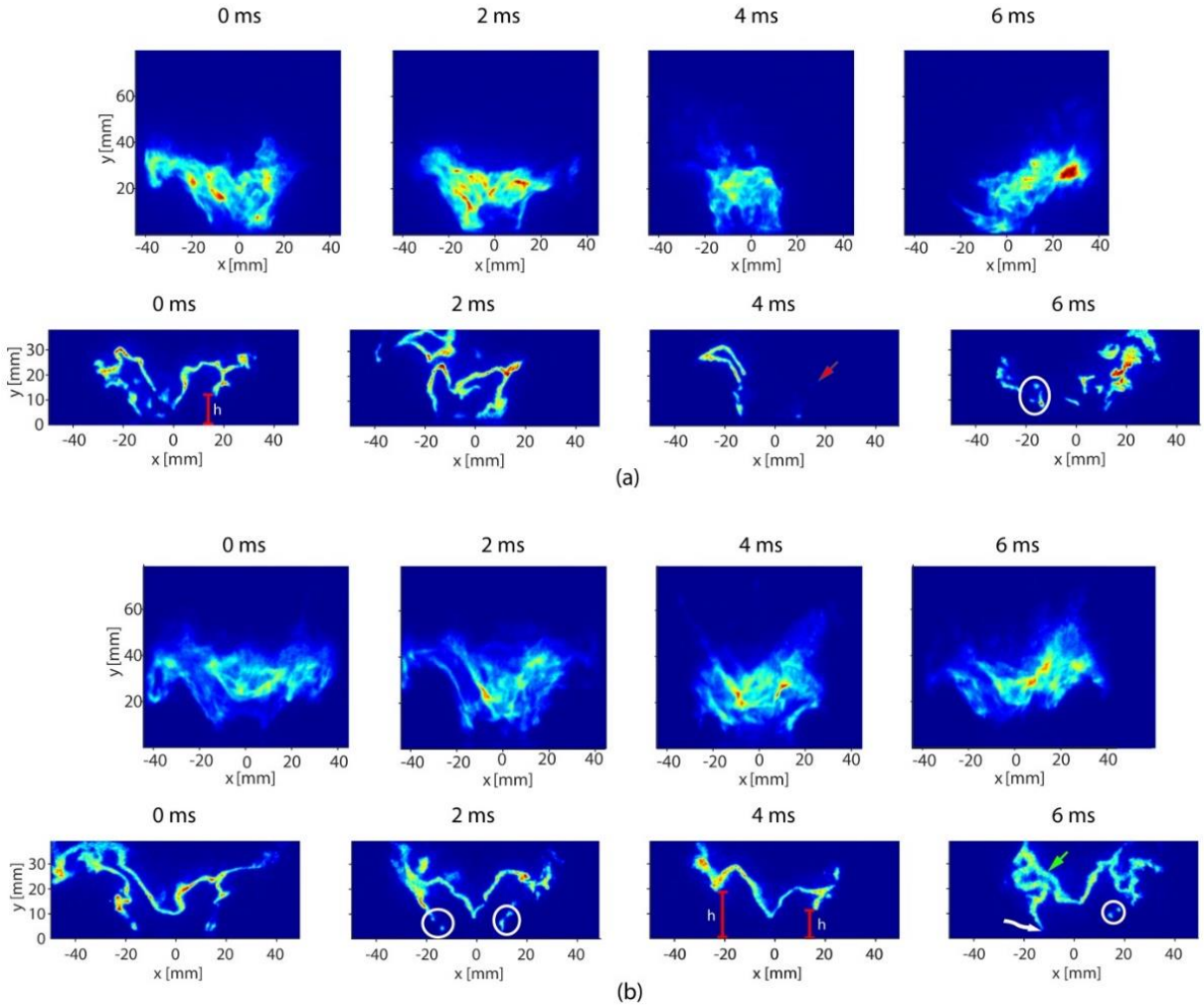

Figure 7-9: Instantaneous OH* chemiluminescence and OH PLIF images (not recorded simultaneously) of (a) S-15-024-160-30 and (b) S-12-033-160-30 during the cycle (*t*=0 ms corresponds to the beginning of the cycle). The same colormap for each image was used. The main features of their behaviour are highlighted: red line: lift-off height *h* at the bluff body edge, white curved arrow: flame attached to the bluff body edge, red arrow: inner or/and outer branches missing, circle: breaks of the OH zone, green arrow: thicker OH regions.

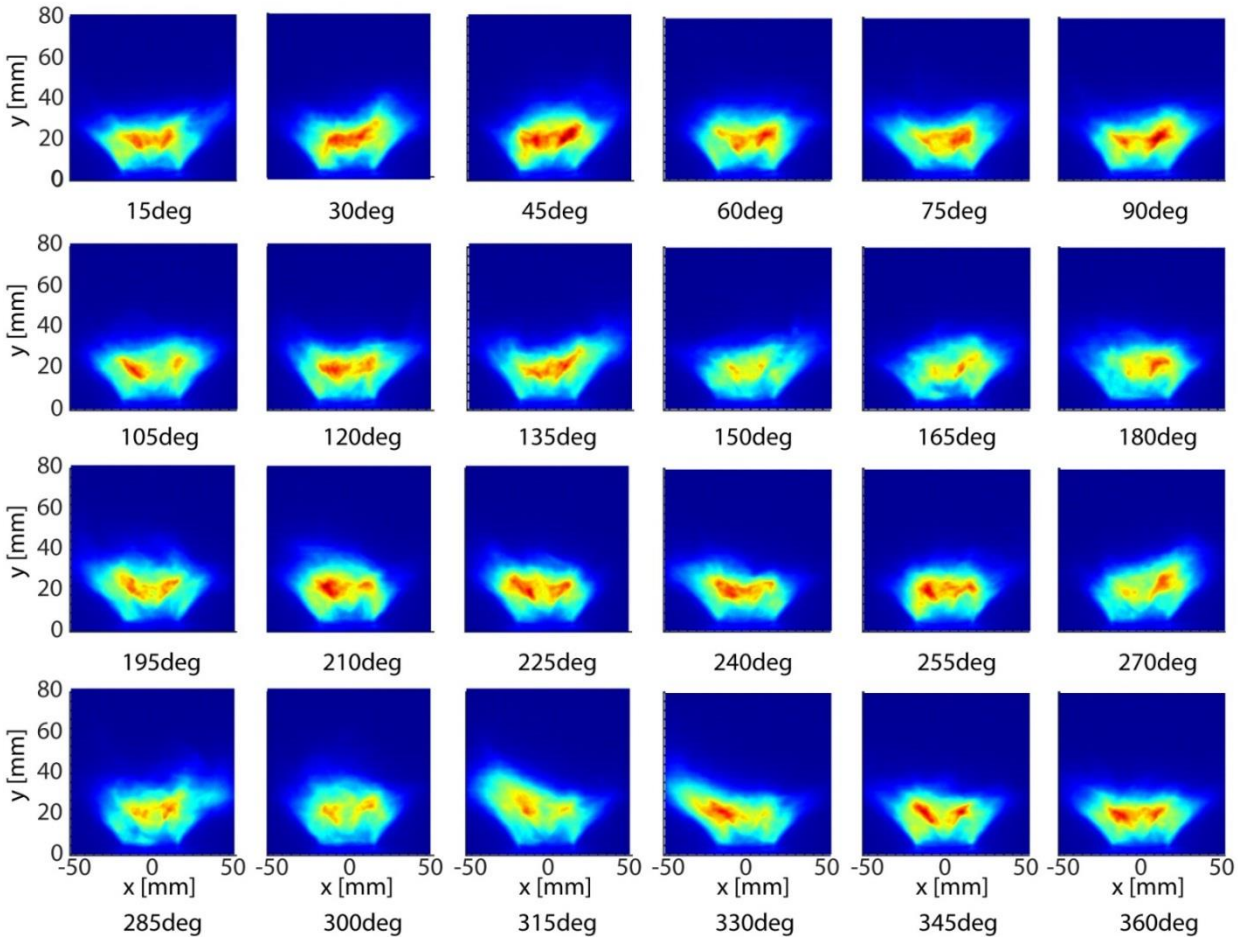

Figure 7-10: Phase-averaged OH* chemiluminescence images of S-15-024-160-30.

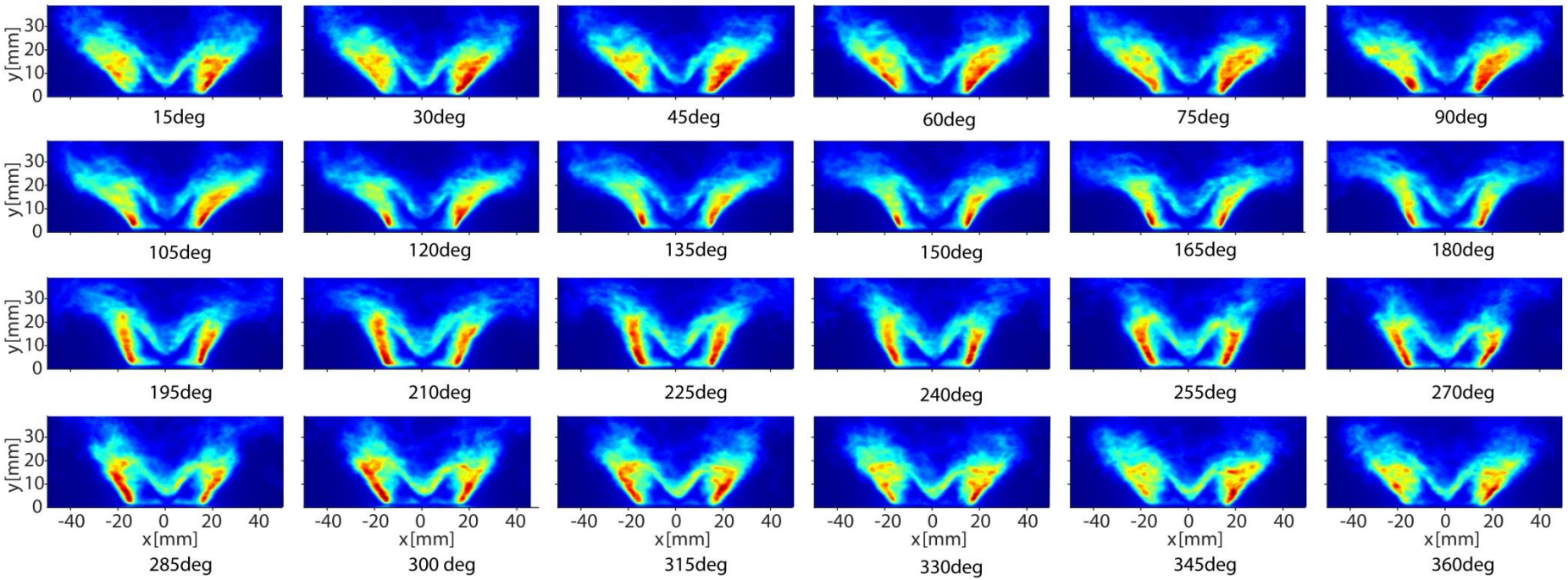

Figure 7-11: Phase-averaged OH PLIF images of S-15-024-160-30.

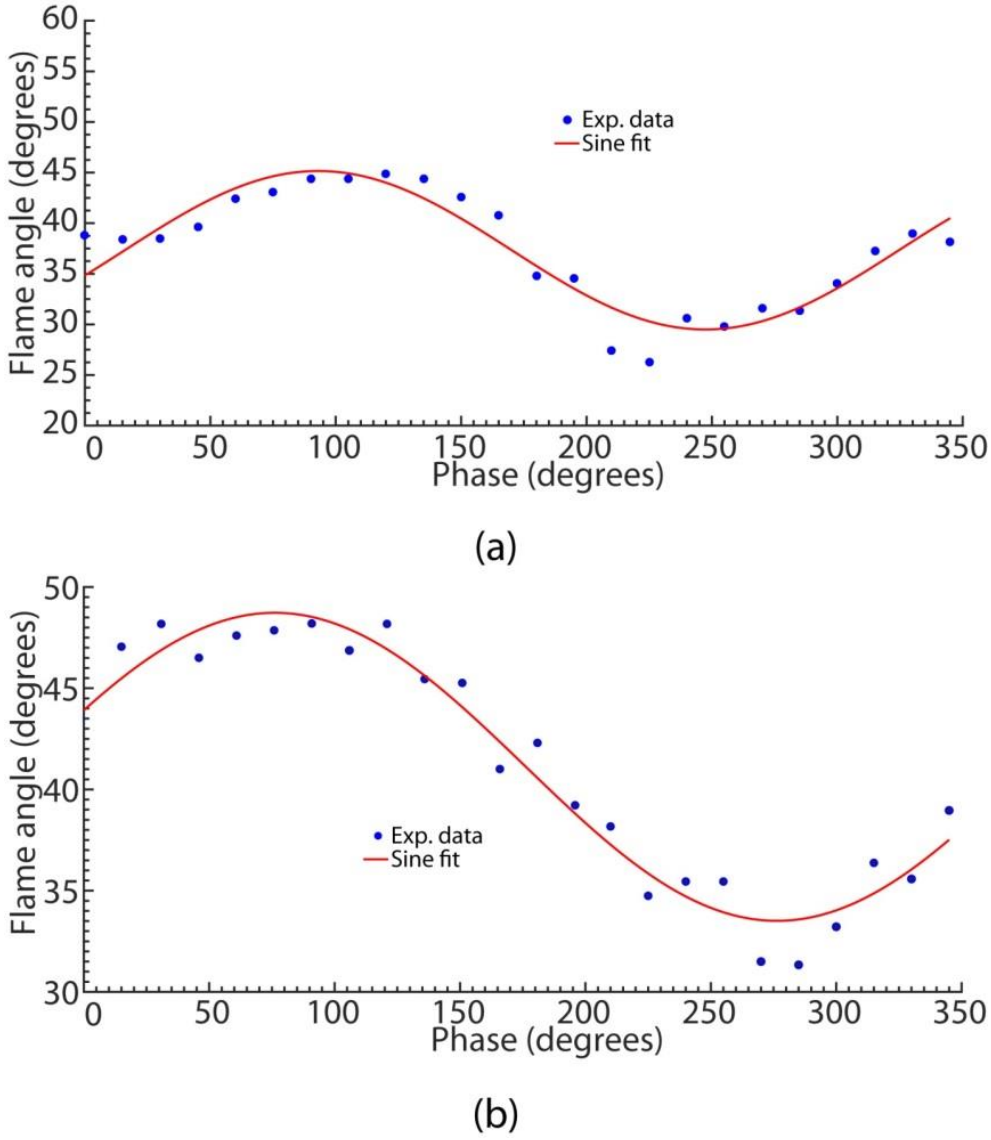

Figure 7-12: Flame angle variation with respect to phase of the acoustic cycle for (a) S-15-024-160-30 and (b) S-12-033-160-30.

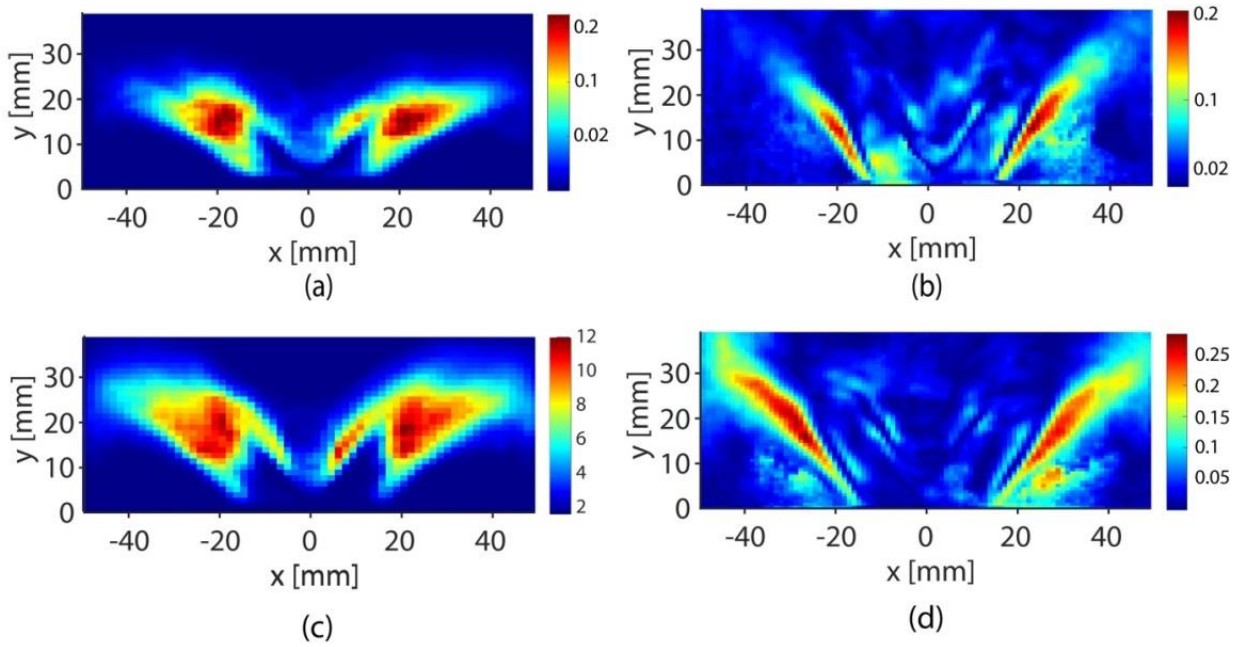

Figure 7-13: (left) Variance of OH and (right) ratio R_L (OH fluctuation at 160 Hz to the total variance of OH) for S-15-024-160-30 (a, b) and S-12-033-160-30 (c, d).

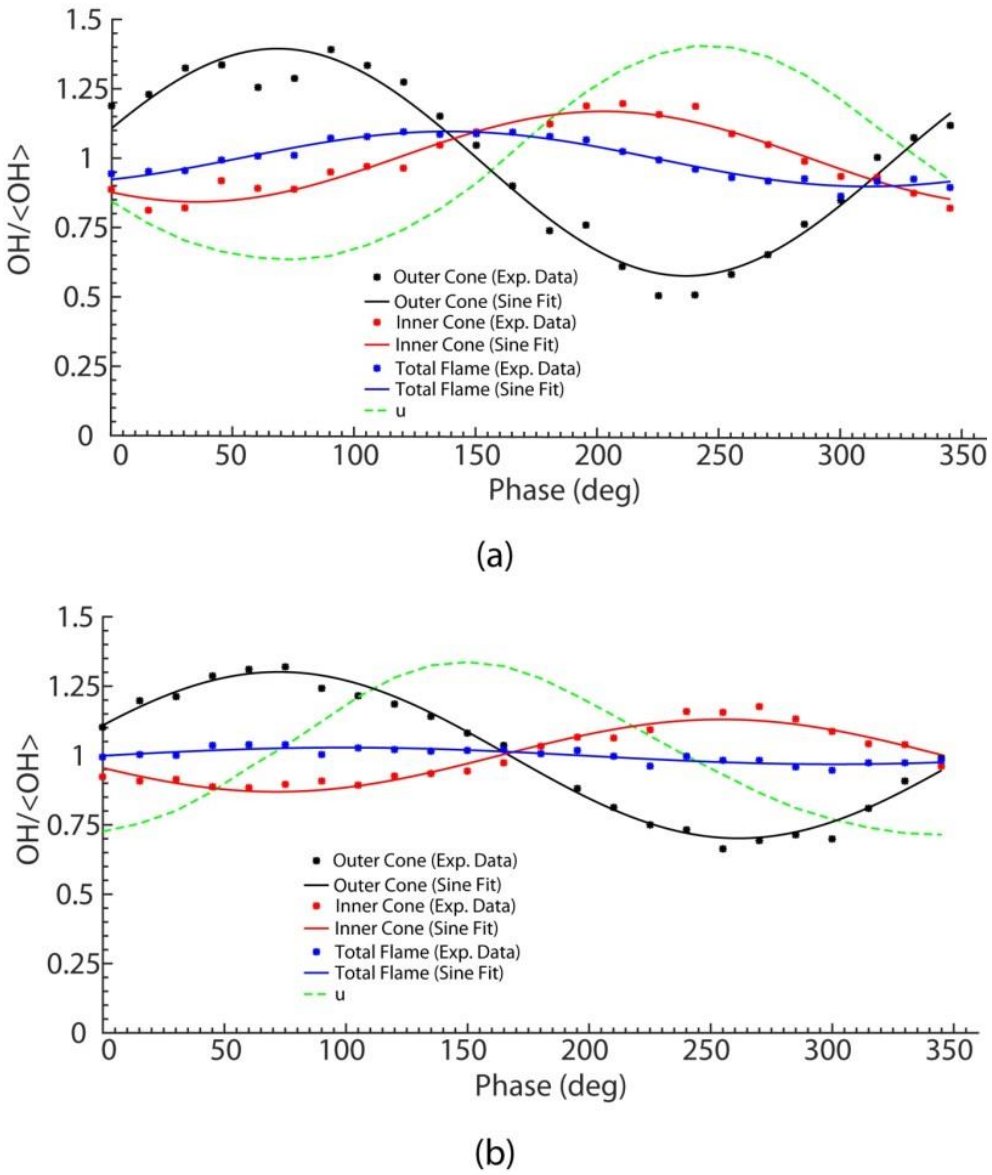

Figure 7-14: $OH/< OH >$ variation during the acoustic cycle, evaluated from phase-averaged OH PLIF images, calculated from the outer, inner cone and whole OH PLIF window. The green dashed line represents the normalised acoustic velocity fluctuations. Flames: (a) S-15-024-160-30 and (b) S-12-033-160-30.

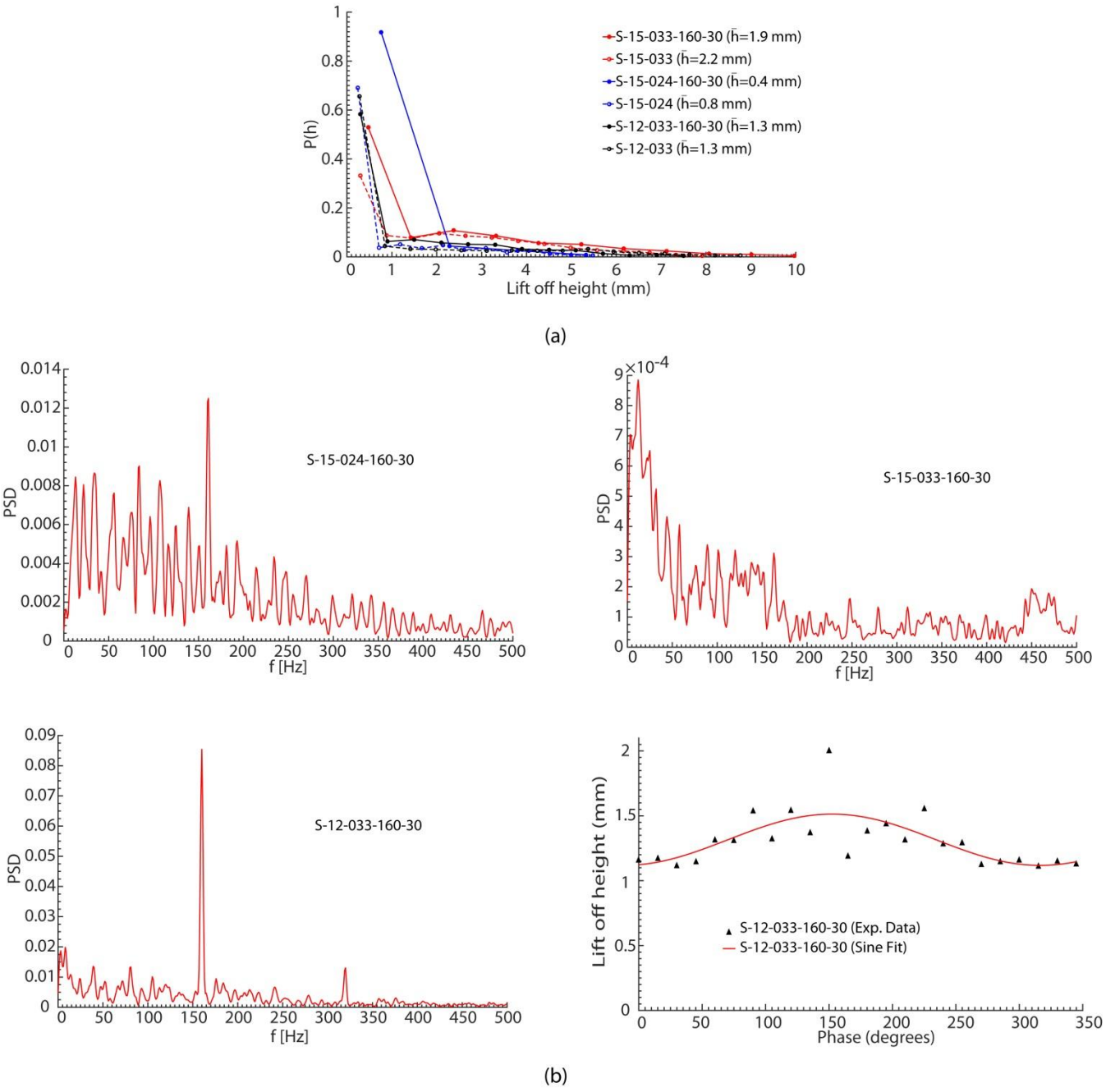

Figure 7-15: (a) Probability density function of the lift-off height, $P(h)$, with respect to h for both the forced and the unforced flames presented in Table 7-1. The average lift-off height $\bar{h}$ is indicated. (b) Power spectra of lift-off height and lift-off height with respect to phase for the different conditions.

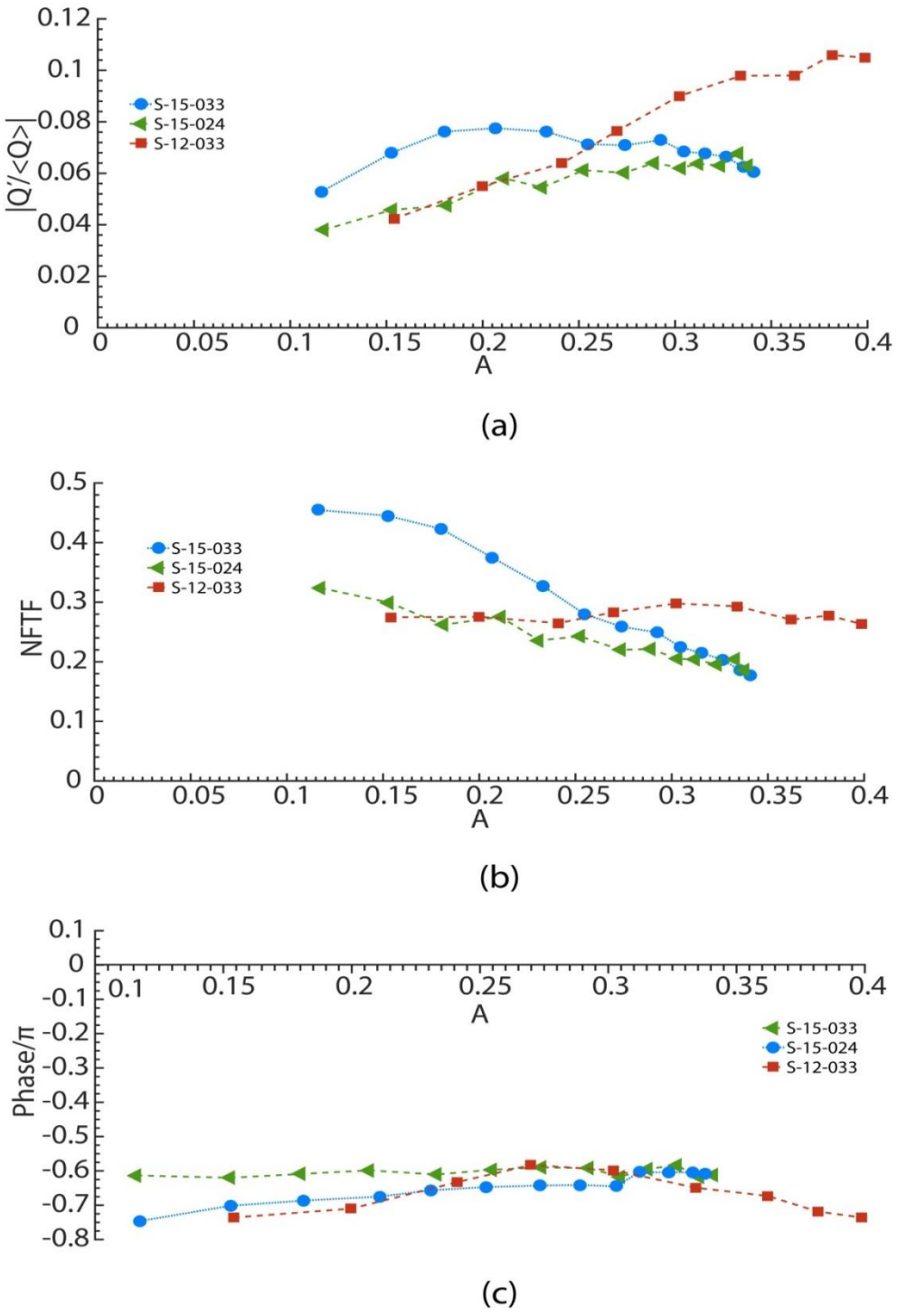

Figure 7-16: (a) Normalised global heat release fluctuation of S-15-033, S-15-024 and S-12-033 measured as a function of *A* using OH* chemiluminescence, (b) the corresponding transfer function and (c) its phase evaluated from the data of (a).

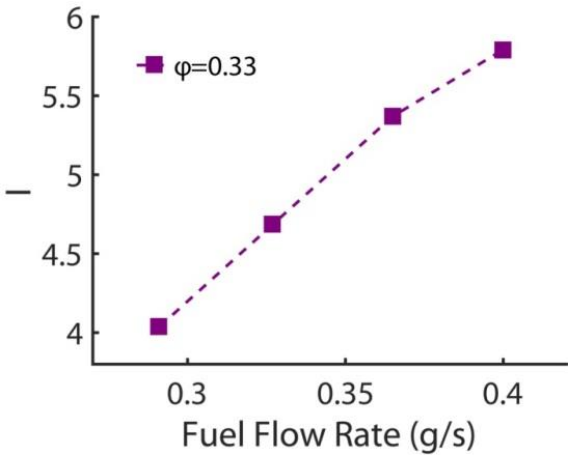

Figure 7-17: Mean intensity of the OH* chemiluminescence emission of the flame *I* with respect to the fuel mass flow rate when φ=0.33.

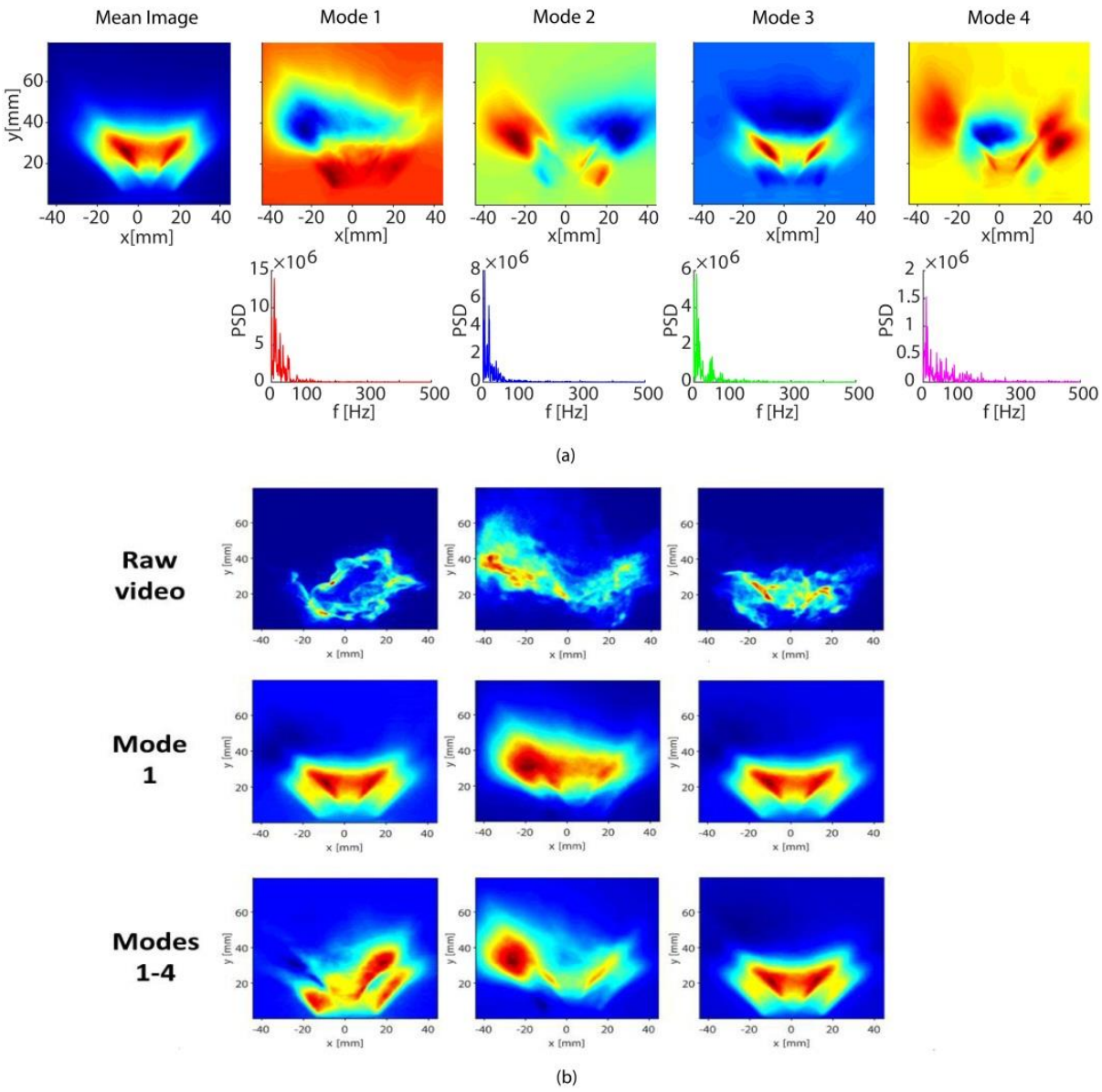

Figure 7-18: (a) Mean Image and first four OH* chemiluminescence POD Modes and the respective PSD of POD time coefficients. (b) Instantaneous OH* chemiluminescence images (first row), snapshots at the same times from reconstructed OH* movie using the mean and Mode 1 only (second row) and the mean and Modes 1 to 4 (fourth row). Flame: S-15-03.

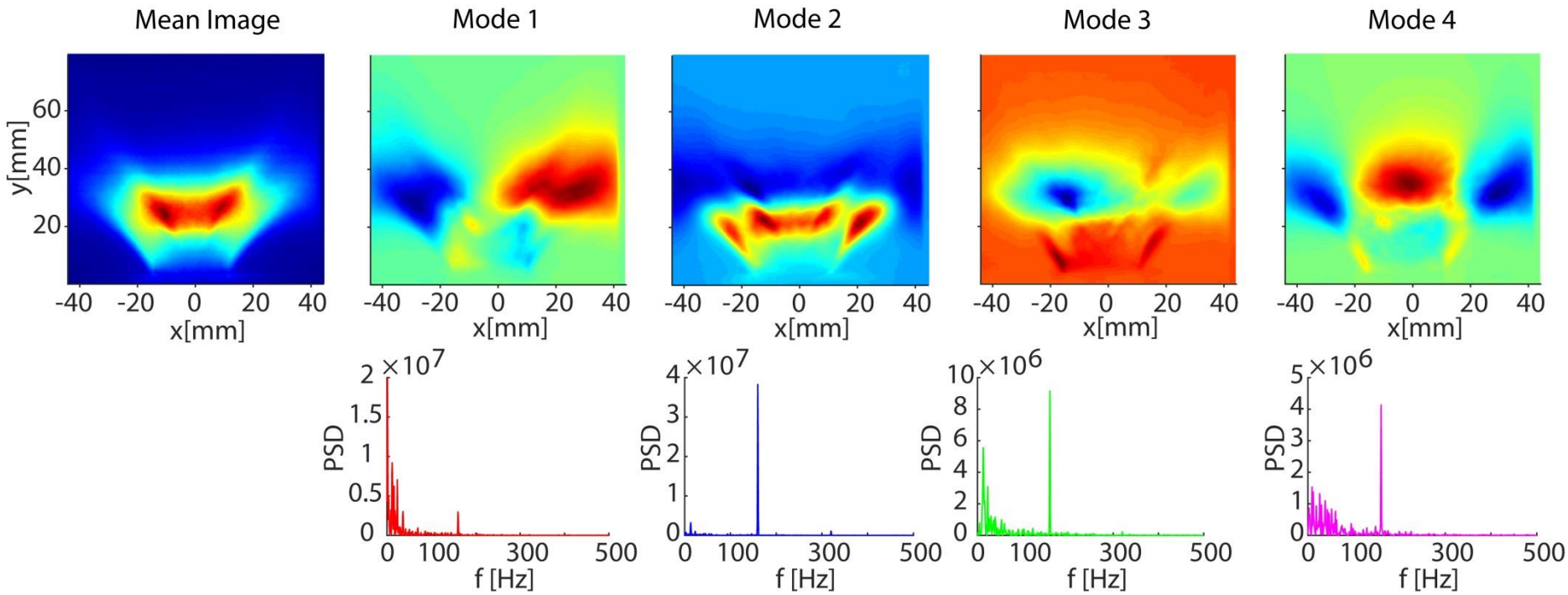

Figure 7-19: Mean Image and first four OH* chemiluminescence POD Modes and the respective PSD of POD time coefficients for S-15-033-160-30.

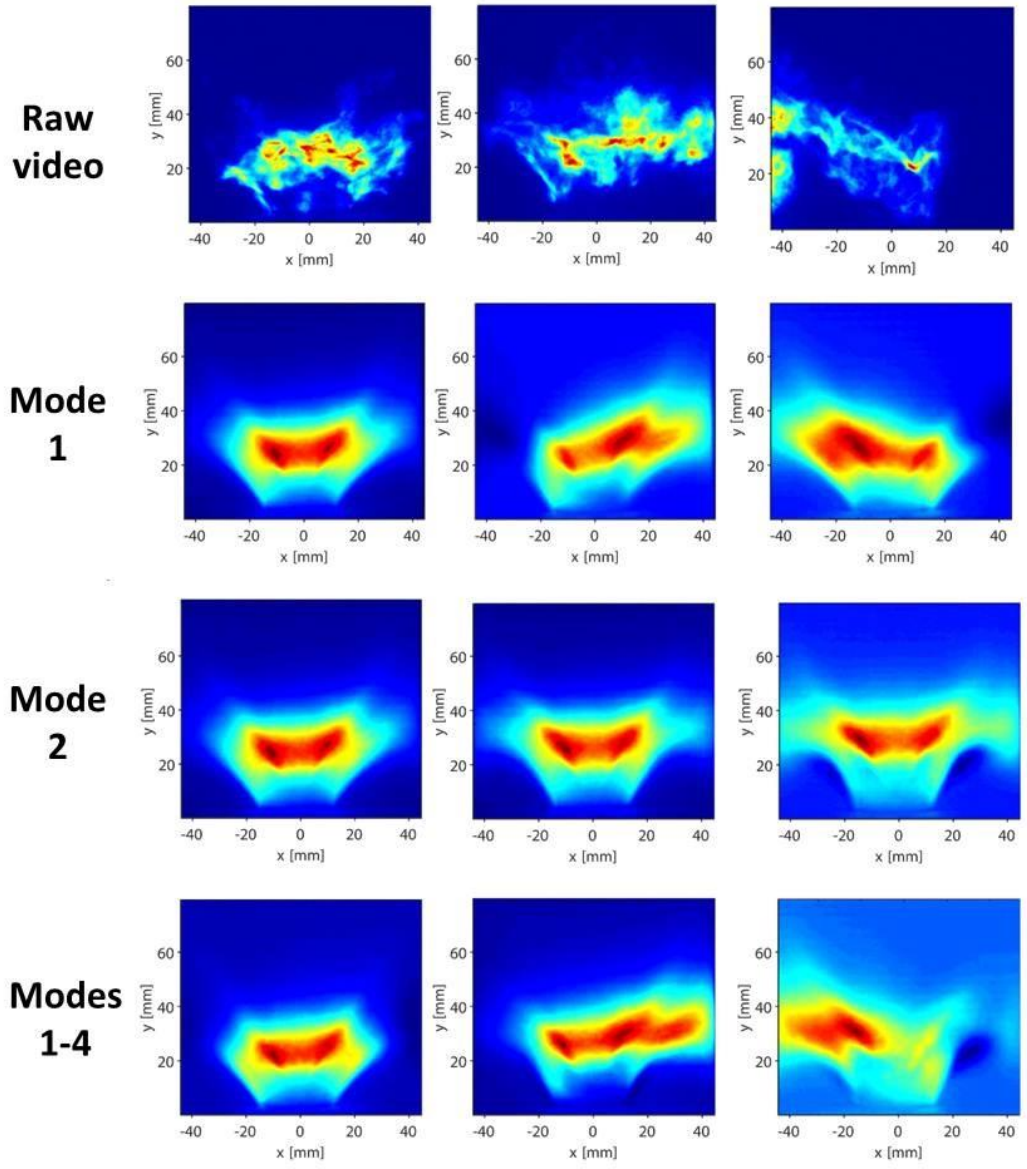

Figure 7-20: Instantaneous OH* chemiluminescence images (first row), snapshots at the same times from reconstructed OH* movie using the mean and Mode 1 only (second row), the mean and Mode 2 only (third row), and the mean and Modes 1 to 4 (fourth row) for S-15-033-160-30.

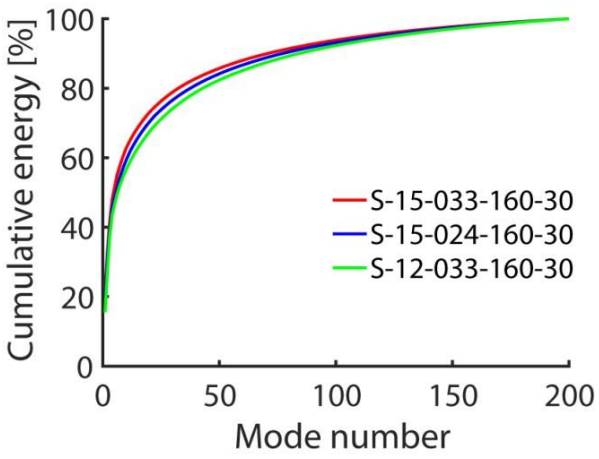

Figure 7-21: Cumulative energy of OH* chemiluminescence POD Modes of S-15-033-160-30, S-15-024-160-30 and S-12-033-160-30.

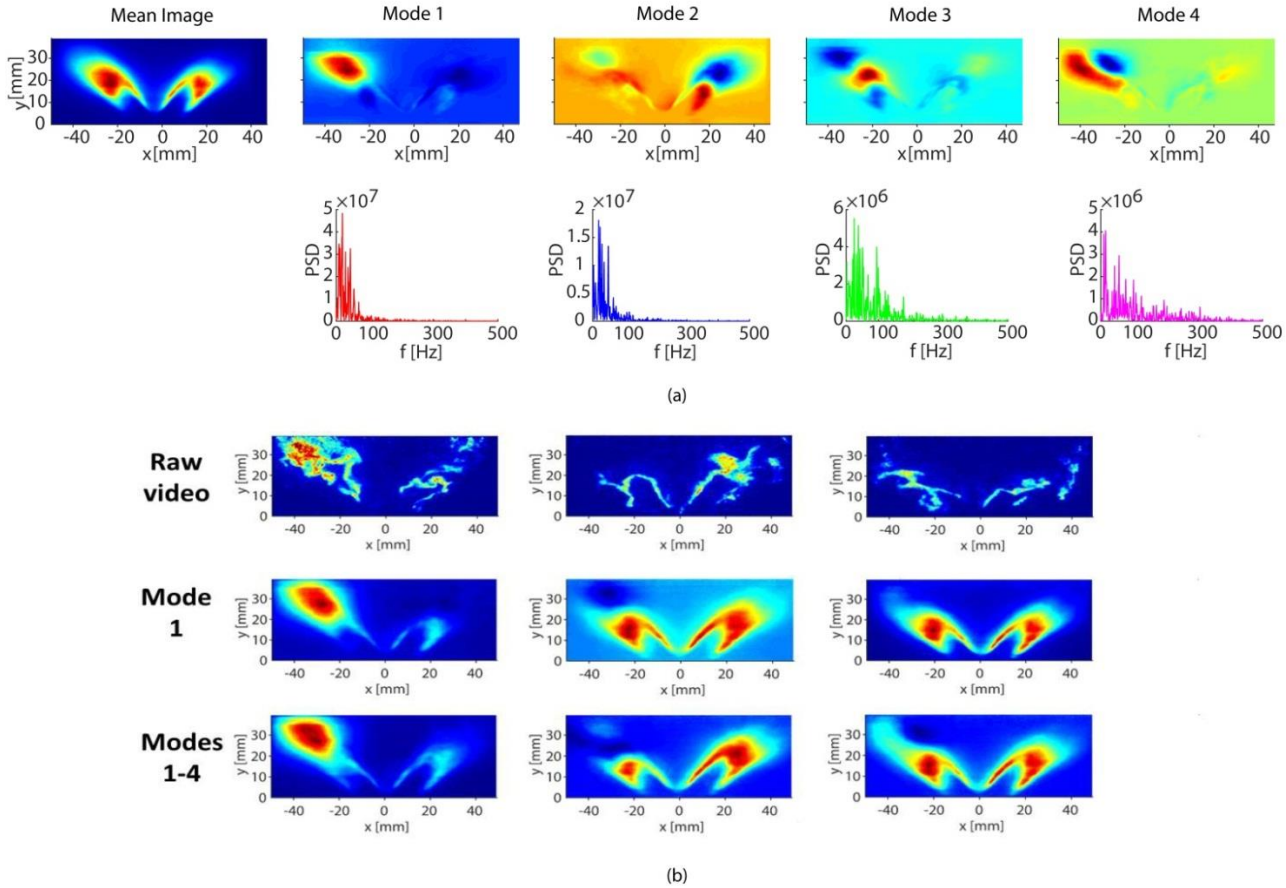

Figure 7-22: (a) Mean Image and first four OH PLIF POD modes and the respective PSD of POD time coefficients and (b) instantaneous OH PLIF images (first row), snapshots at the same times from reconstructed OH PLIF movie using the mean and Mode 1 only (second row), and the mean and Modes 1 to 4 (third row). Flame: S-15-033.

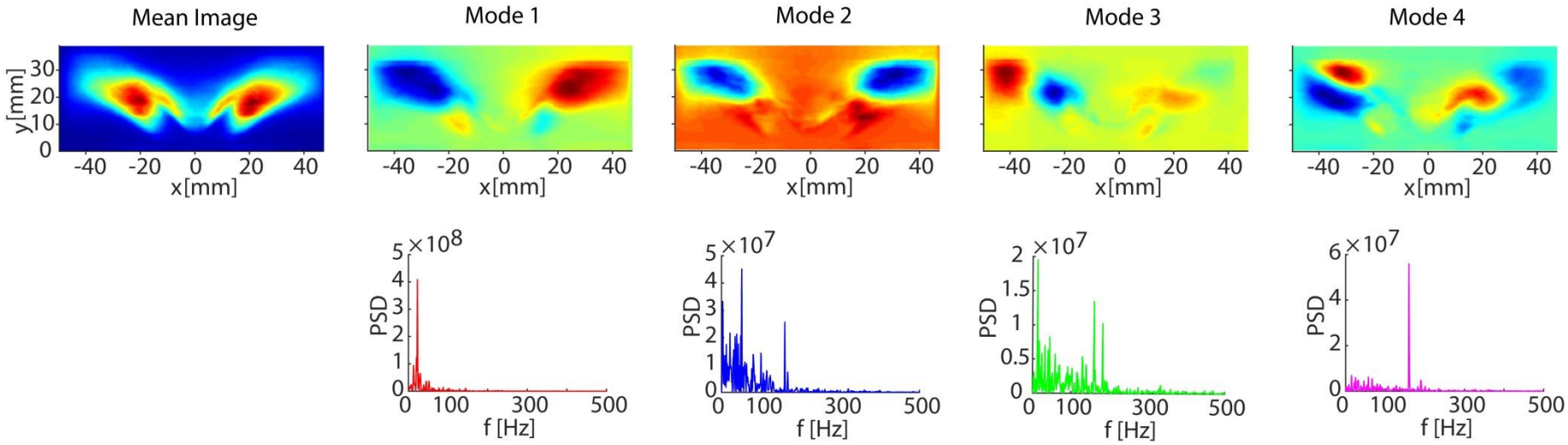

Figure 7-23: Mean Image and first four OH PLIF POD Modes and the respective PSD of POD time coefficients for S-15-033-160-30.

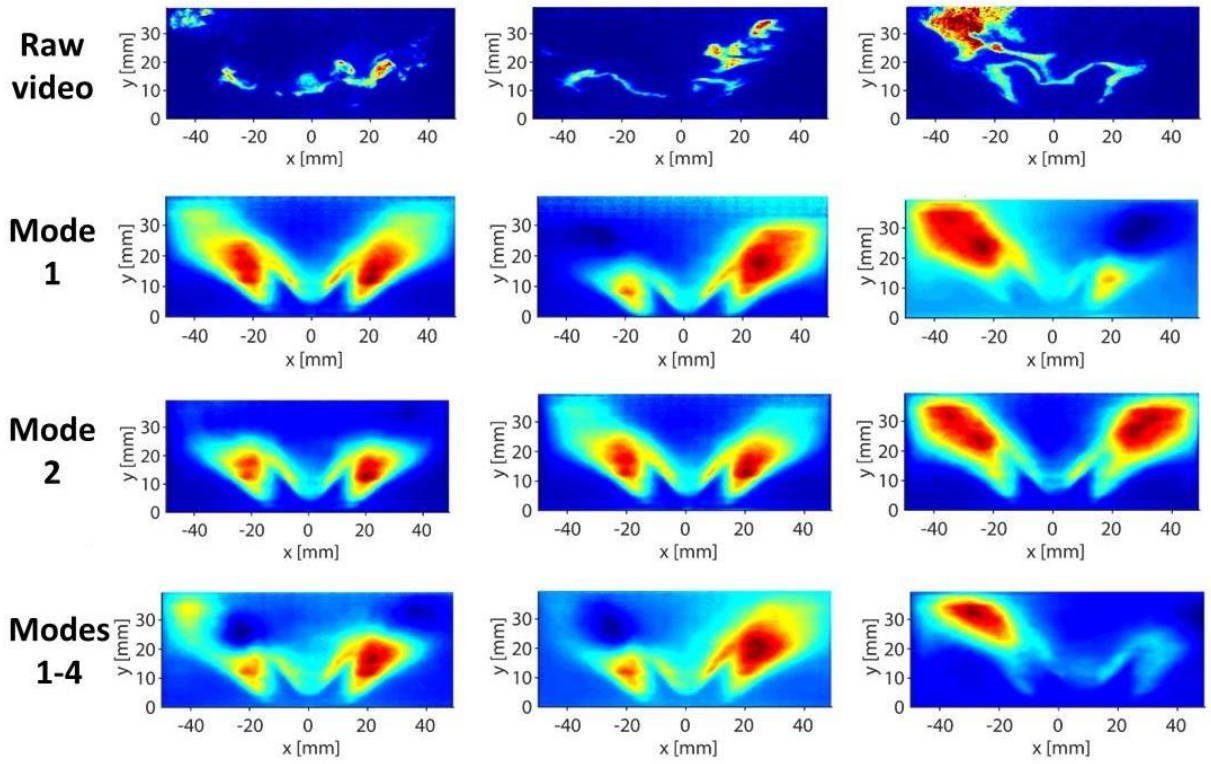

Figure 7-24: Instantaneous OH PLIF images (first row), snapshots at the same times from reconstructed OH PLIF movie using the mean and Mode 1 only (second row), the mean and Mode 2 only (third row), and the mean and Modes 1 to 4 (fourth row) for S-15-033-160-30.

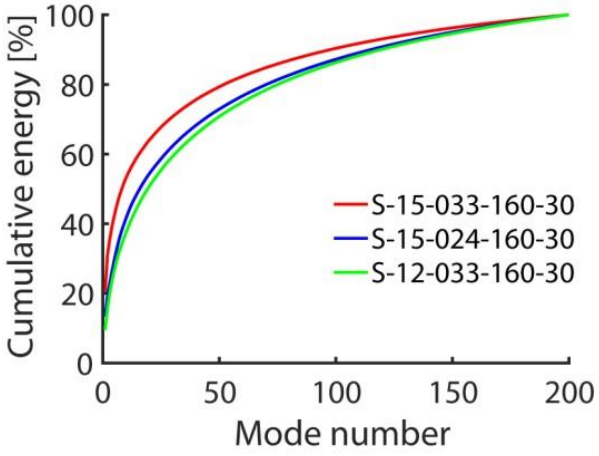

Figure 7-25: Cumulative energy of OH PLIF POD Modes of S-15-033-160-30, S-15-024-160-30 and S-12-033-160-30.

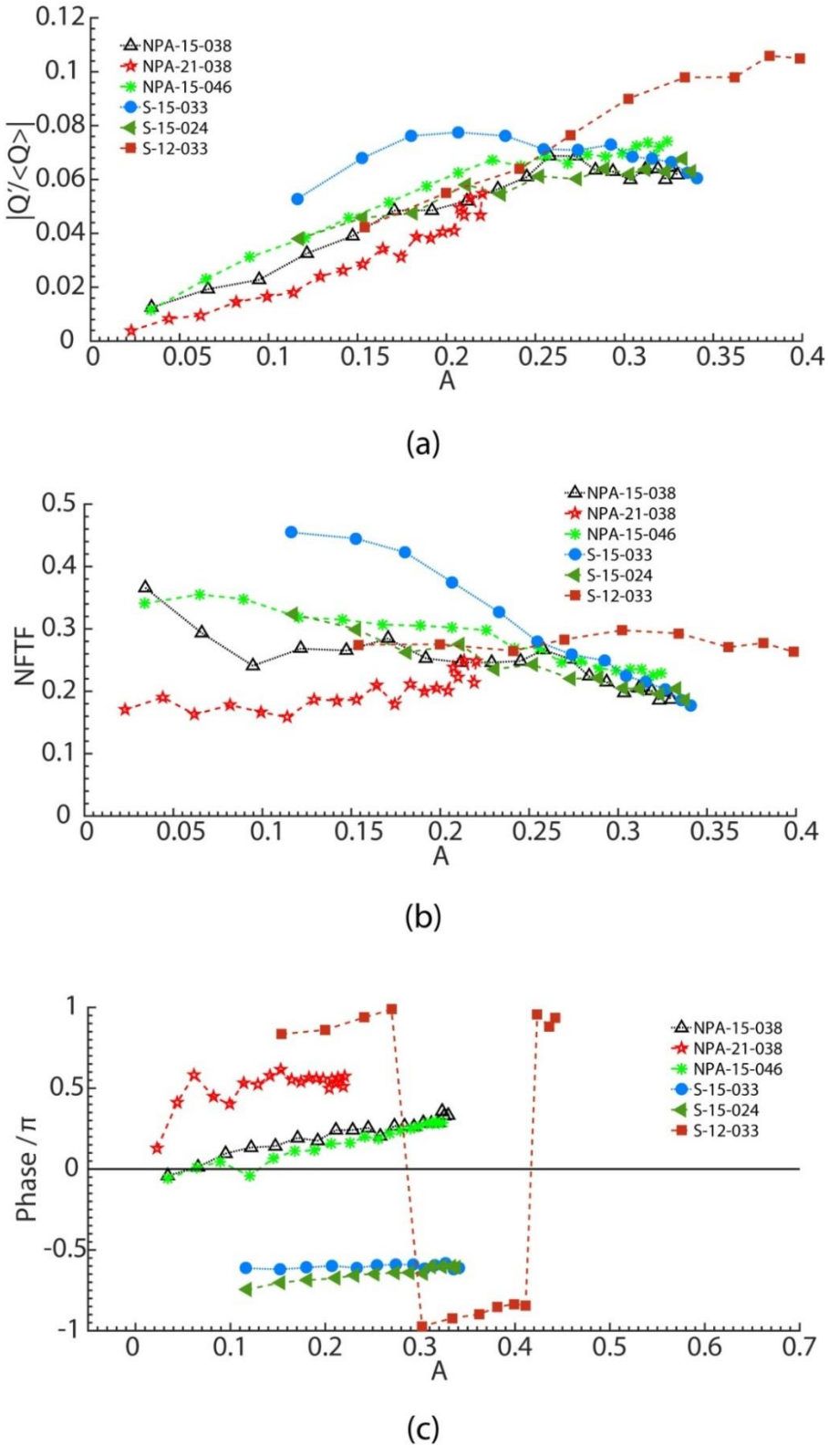

Figure 7-26: (a) Normalised global heat release fluctuation of NPA and spray flames measured as a function of *A* using OH* chemiluminescence and (b) the corresponding transfer function.

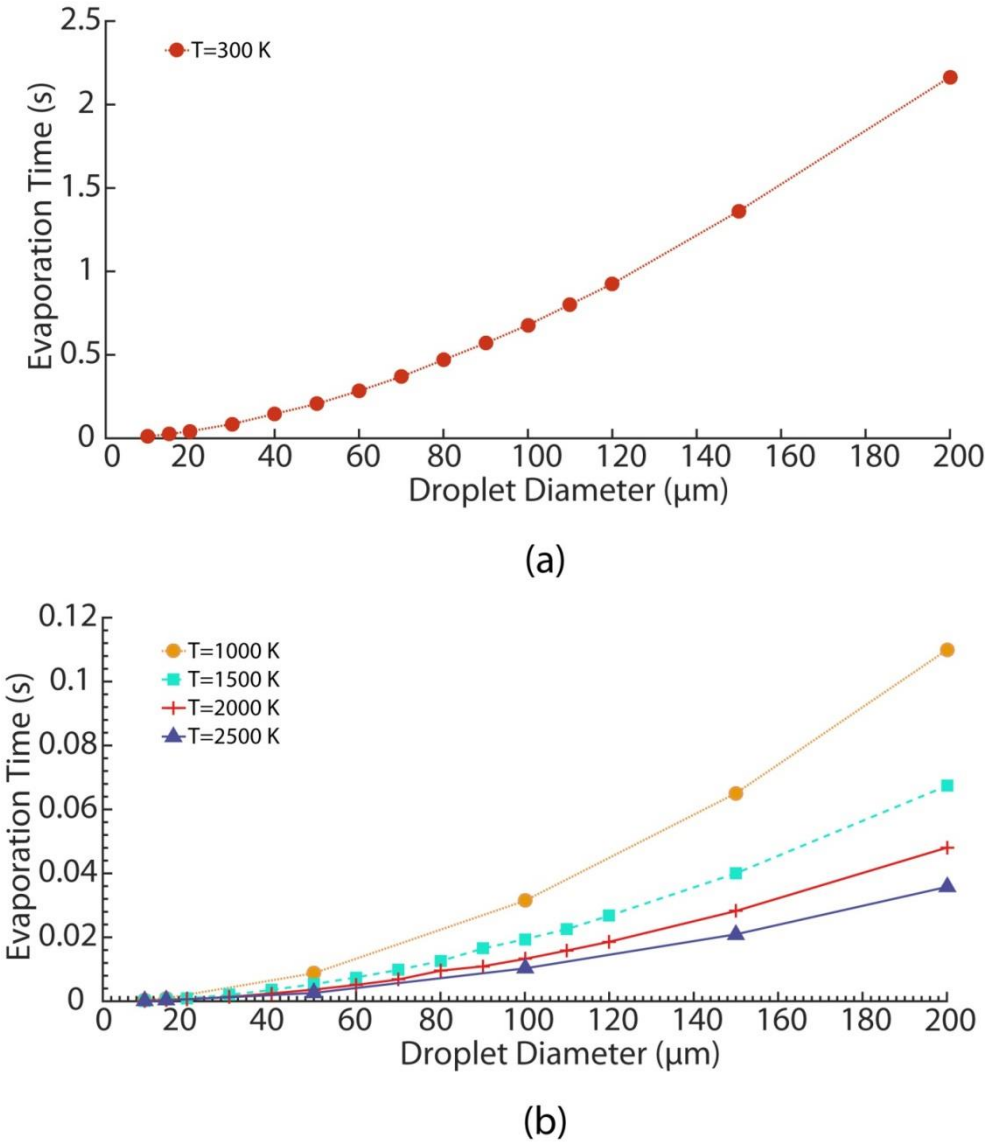

Figure 7-27: Evaporation time as a function of initial droplet diameter for (a) 300K and (b) 1000-2500 K, assuming a mean relative velocity between the air and fuel droplet of 10 m/s.

7.6 Tables of Chapter 7

Condition	$\boldsymbol{U_{air}(m/s)}$	**Global $\boldsymbol{\varphi}$**	**Air Flow Rate (lpm)**	**Ethanol Flow Rate (g/s)**
S-15-033 (Base case)	15 (For S-15-033-160-30, U_{air}=85%U_B)	0.33	550	0.4
S-15-024	15 (For S-15-024-160-30, U_{air}=92%U_B)	0.24	550	0.3
S-12-033	12 (For S-12-033-160-30, U_{air}=70%U_B)	0.33	420	0.3

Table 7-1: Experimental conditions of ethanol spray flames presented in this work. The level of proximity to blow-off when the flames are forced at 160 Hz and A=30% is indicated in brackets.

OH* Chemiluminescence	S-15-033	S-15-033-160-30
Mode	**Energy (%)**	**Energy (%)**
1	22.3	22.5
2	11.9	10.5
3	9.1	8.8
4	4.6	6.1
1-4	48	48

Table 7-2: POD energy content of the first four OH* chemiluminescence POD Modes of S-15-033 and S-15-033-160-30.

OH PLIF	S-15-033	S-15-033-160-30
Mode	**Energy (%)**	**Energy (%)**
1	20.8	20.6
2	7.3	10.5
3	4.3	4.6
4	3.3	3.9
1-4	35.7	39.6

Table 7-3: POD energy content of the first four OH PLIF POD Modes of S-15-033 and S-15-033-160-30.

8 CONCLUSIONS AND SUGGESTIONS FOR FURTHER RESEARCH

8.1 Conclusions

8.1.1 Self-Excited Fully Premixed System

Self-excited oscillations were induced by extending the length of the duct downstream of the bluff body. The important conclusions from the experimental investigation of self-excited turbulent premixed recirculating flames with swirl are summarized below:

1. The longer the duct length and the higher the equivalence ratio, the stronger the self-excited oscillations were, with the effect of duct length being much stronger.
2. The dominant frequencies of the system were found to increase with equivalence ratio and bulk velocity and decrease with duct length.
3. In most cases, at low φ, only one dominant frequency was exhibited, f_1, which was associated with the thermo-acoustic frequency, whereas at greater φ values, the system revealed up to three simultaneous periodic motions, which were suggested to correspond to the thermoacoustic frequency (f_1), PVC (f_2) and their interaction ($f_1 - f_2$).
4. The heat release fluctuations and flame transfer functions were estimated based on the most pronounced frequencies f_1 and f_2. The thermoacoustic frequency f_1 increased from 310 to 380 Hz with φ, while the PVC frequency f_2=263 Hz was not altered by φ. In both cases, the forcing amplitude A varied between 0.03 and 0.1 and the global heat release showed an increasing trend with φ. The transfer function values based on f_1 and f_2 oscillated around 1.3 and 1.7 respectively.
5. The Proper Orthogonal Decomposition analysis revealed that the POD energy was mainly concentrated in a dominant structure, which was shown in the case of an axially moving vortex-like structure.

6. A novel application of the POD method was proposed to estimate the convection velocity in self-excited flames from the most dominant reaction zone structures detected by OH* chemiluminescence imaging, which provides information on both the spatial modes and the frequency content of the POD coefficients. The convection velocity was found to be positively correlated to bulk velocity, however the effect of equivalence ratio was more complex. For a range of conditions, the convection velocity was found to be in the range of 1.4-1.7 bulk flow velocities at the inlet of the combustor. Given that the majority of the previous experimental studies were conducted using simple configurations, the investigation of the convection velocity based on a configuration relevant to industrial systems is of great scientific interest. The convection velocity is of importance in the modelling of self-excited flames and in the Nonlinear Flame Transfer Function (NFTF) analysis, because the convection velocity affects the flame response significantly.

8.1.2 Response of a Forced Fully Premixed System

The important conclusions from the experimental investigation of the response of lean fully premixed turbulent swirling flames to acoustic oscillations are summarised below:

1. The effect of the swirler on the flame response was found to be important, with the response of a non-swirling flame being greater than that of a swirling flame.
2. Concerning the amplitude dependence of the fully premixed flame response, a high, nonlinear response was observed, however the response was significantly reduced for conditions close to blow-off. This nonlinearity was associated with the formation of a vortex-like OH* chemiluminescence structure. A further nonlinearity occurred at high amplitudes and at some equivalence ratios, where part of the energy was transferred to the first harmonic, while the input velocity signal did not show any significant harmonic contents. Also, at low forcing amplitudes the system showed an increased sensitivity to equivalence ratio, while at greater A the system was not sensitive to changes in φ.
3. Concerning the flame kinematics, a method for quantifying the local response of the various parts of the flame at the forcing frequency was developed. This was achieved by using the ratio, R_L, of OH fluctuation contribution at 160±3 Hz to the total variance based on groups of pixels from the OH PLIF images. R_L was found to be much lower in the ISL region than in large regions on the downstream side of the flame.
4. The angle of the flame varied sinusoidally during the cycle. The angle variation was almost in phase with $OH/< OH >$ variation in the ISL region, while it was found to be in anti-phase

with the FSD variation during the cycle. Also, the point at which the flame branch in the ISL region impinges on the wall showed an axial movement, following also a sinusoidal trend.

5. At higher forcing amplitudes, greater lift-off heights were observed with more pronounced periodicity at the forcing frequency.
6. A relatively good agreement was reported between OH* chemiluminescence and FSD variation during the cycle, from which it could be deduced that the heat release modulation was mainly through flame surface modulation and that the FSD could capture the global heat release well.
7. The dominant mechanism of the system was captured mainly by the first two OH* chemiluminescence POD Modes, which revealed a banded shape, representative of the axial motion of the flame.
8. Based on this dominant reaction zone structure, the ratio of the convection velocity to the bulk velocity was estimated to be unity, which is lower than that of self-excited premixed flames.

8.1.3 Response of a Forced Non-Premixed System with Radial Fuel Injection

In this system, the degree of premixing was between the fully premixed and the non-premixed systems with very large mixture fraction fluctuations at the flame location. The important conclusions from the experimental investigation of the response of lean non-premixed flames with radial fuel injection to acoustic forcing are summarised below:

1. Concerning the amplitude dependence, a very high nonlinear response was observed, however the response was greatly reduced for conditions close to blow-off. The proximity of forced flames to the blow-off condition was found to be critical in their heat release response. Close to blow-off, the NPR system showed a low sensitivity towards a change in the operating conditions. A source of nonlinearity was associated with the fact that part of the energy was transferred to the first harmonic, while the velocity signal did not show any significant harmonic contents.
2. The quantification of the local response of the various parts of the flame at the forcing frequency showed that the ratio R_L (OH fluctuation at 160 Hz to the total variance of OH) in the ISL region close to the bluff body was significantly greater than that farther downstream.
3. During the acoustic cycle, the flame angle varied sinusoidally, while the point at which the flame branch in the ISL region impinges on the wall showed an axial movement, following also a sinusoidal trend.

4. Far from blow-off, lift-off was hardly affected by forcing. Closer to blow-off, the greater the destabilisation of the flame (as the flame was approaching blow-off) with an increase in forcing amplitude, the greater the lift-off heights. The lift-off height periodicity at the forcing frequency was very pronounced, especially at greater forcing amplitudes.
5. The cyclic OH* chemiluminescence variation showed a similar phase, but a greater amplitude than the cyclic FSD variation, implying that apart from the flame area, other mechanisms might also contribute to the heat release modulations. The area of the flame front was increasing as the flame angle was becoming steeper.
6. POD was found to be a useful tool in the identification of dominant features and their periodicity in forced NPR flames, even at conditions that were close to blow-off. The dominant mechanism of the system was captured mainly by the first two OH* chemiluminescence POD Modes, which revealed a banded shape, representative of the axial motion of the flame. Additionally, the flame angle variation was captured by the first two OH PLIF POD Modes. The influence of forcing on the flame response was greater for flames that were far from blow-off, leading to more pronounced features of the POD Modes and to stronger peaks at 160 Hz in the PSDs than those at closer proximity to blow-off. Closer to blow-off, the blow-off kinematics affected dramatically the flame structure and as a result, the influence of forcing on the flame structure was found to decrease.
7. Based on the first OH* Mode, the ratio of the convection velocity to the bulk velocity was estimated to be 0.54.

8.1.4 Comparison Between Fully Premixed and Non-Premixed with Radial Fuel Injection Systems

From the comparison between the NPR and the fully premixed flames, the main conclusions are the following:

1. The response of the NPR system was greater than that of the fully premixed system in the range of fL_{fl}/U studied, however, in both systems, close to blow-off the flame response was significantly reduced compared with that farther from blow-off. The curves of the heat release response as a function of forcing amplitude had a similar general trend. Unlike the NPR system, where a low sensitivity was observed towards a change in the operating conditions, the premixed showed an increased sensitivity to φ, particularly at low A.
2. In both systems, it was shown that for some flames, a source of nonlinearity in the heat release response was associated with the fact that part of the energy was transferred to the first

harmonic (320 Hz), while the velocity signal did not show any significant harmonic contents. The response of both flames at the first harmonic showed similar trends with the response of the NPR flame being greater than that of the premixed.

3. While for the NPR flame R_L was greater in the region downstream of the annular passage, close to the bluff body edge, than that in the other flame regions, in the premixed flame higher R_L values were seen in large regions on the downstream side of the OH PLIF plane.
4. In the fully premixed system, the good agreement between the OH* chemiluminescence and FSD variation implied that the heat release modulation was mainly through flame surface area modulation. Also, the agreement between the FSD variation of the premixed and NPR flames suggested that the flame area modulation mechanism, and how it was influenced by the flame angle, was common in both systems. Thus, in the NPR flame, the difference in the magnitude between the OH* chemiluminescence and FSD variation, previously mentioned, was mainly attributed to the equivalence ratio fluctuations constituting an important mechanism of the system. Therefore, in the NPR system, both the flame area and the equivalence ratio modulations were found to be important mechanisms of the heat release modulations.
5. Unlike NPR, in the premixed flame, forcing influenced the lift-off behaviour, however the average lift-off height of the premixed flames was lower than that of the respective NPR conditions.
6. Concerning the POD analysis, in both systems, the first two OH* chemiluminescence POD Modes revealed an axial motion of the flame, associated with the forcing frequency at 160 Hz, which was significantly more pronounced in the NPR system than that in the premixed, while the structure of the first two OH PLIF POD Modes revealed a change in the flame angle.
7. Based on the first OH* POD Mode, the ratio of the convection velocity to the bulk velocity was estimated to be 0.54 for the NPR flame, while it was found to be unity for the respective fully premixed flame.

8.1.5 Response of a Forced Non-Premixed System with Axial Fuel Injection

The important conclusions from the experimental investigation of the response of lean non-premixed flames with axial fuel injection to acoustic forcing are summarised below:

1. Concerning the amplitude dependence, a nonlinear response was observed, which was significantly lower compared with the response of the NPR and the fully premixed systems. Close to blow-off, the flame response was lower than that farther from blow-off. The acoustic forcing reduced the stability of the flame and the stability decreased with the increase in

forcing amplitude. The NPA system showed a greater sensitivity to the forcing amplitude compared to the system with radial injection in terms of changes in the operability limits.

2. The quantification of the local response of the various parts of the flame at the forcing frequency showed that the ratio R_L (OH fluctuation at 160 Hz to the total variance of OH) was greater in the ISL region than in the other regions. This is consistent with the results of NPR flames, whereas in the case of fully premixed flames greater R_L values were observed in large regions on the downstream side of the OH PLIF plane than those in the ISL region close to the bluff body. In the NPA flames, R_L was almost zero in the region downstream of the fuel injection point.
3. In the NPA system, the change in the flame angle was found to be less pronounced than that of the fully premixed and the NPR systems. Unlike these systems, the NPA flame angle variation did not follow a sinusoidal trend during the cycle.
4. The lift-off heights of NPA flames were significantly more pronounced than those of NPR flames. Unlike NPR flames, forced NPA flames had reduced average lift-off heights compared to the unforced conditions. The lift-off height of NPA flames was not periodic at the forcing frequency.
5. From the POD analysis, the first OH* chemiluminescence POD Mode represented a left-right flame motion. The absence of a 160 Hz (forcing frequency) peak at the PSD of POD time coefficients of the first POD Mode implied that forcing did not affect greatly the flame structure. The second OH* POD Mode represented a combination of an axial and left-right motion. The 160 Hz peak was revealed in the PSD of Modes 2-4. The OH PLIF POD results, apart from the aforementioned features, revealed the angle variation of the flame.

8.1.6 Response of a Forced Spray System

The important conclusions from the experimental investigation of the response of lean spray flames to acoustic forcing are summarised here:

1. Concerning the amplitude dependence, a low nonlinear response was observed, which was significantly reduced for conditions close to blow-off. The proximity of forced flames to the blow-off condition was found to be critical in their heat release response.
2. The quantification of the local response of the various parts of the flame at the forcing frequency showed that the ratio R_L (OH fluctuation at 160 Hz to the total variance of OH) was the highest in the outer cone region, downstream of the annular air passage, while R_L values were very low in the inner cone region, downstream of the bluff body.

3. During the acoustic cycle, a change in the angle of the outer flame branches was observed, whereas the angle of the inner cone branches did not show any significant modulation.
4. Forced flames had slightly reduced average lift-off heights compared to the unforced conditions and the lift-off height periodicity at the forcing frequency was significantly greater for flames far from blow-off than that revealed closer to blow-off.
5. The POD analysis, revealed that forcing did not alter significantly the flame structure. The greatest influence of forcing was exhibited for conditions far from blow-off. The dominant mechanism of the system was captured mainly by the first few OH* chemiluminescence Modes, which revealed a banded shape, representative of the axial flame motion and an anti-symmetric pair of heat release fluctuations, characteristic of a left-right motion. Additionally, the flame angle variation was captured by the first few OH PLIF POD Modes. The POD was found to be a useful method in the identification of dominant features and their periodicity in forced spray flames, even at conditions that were close to blow-off.

8.1.7 Comparison Between Non-Premixed with Axial Fuel Injection and Spray Systems

From the comparison between the NPA and the Spray flames, the main conclusions are the following:

1. Both spray and the non-premixed with axial fuel injection flames exhibited a low response and specifically, the curves of heat release response as a function of inlet forcing amplitude had similar trends and appeared in the same region, while most of them saturated at around A=30%. Also, in both systems the response was greatly reduced close to blow-off.
2. In the NPA system, the ISL region, downstream of the annular air passage, showed greater R_L values than the other flame regions, while R_L was almost zero in the region downstream of the fuel injection point. A similar response was exhibited by the Spray system, where the highest R_L values were observed in the outer cone region, downstream of the annular air passage, while R_L values were very low in the inner cone region, downstream of the bluff body.
3. In the Spray system, the angle of the outer flame branches varied sinusoidally during the cycle, while the angle of the inner cone branches did not show any significant modulation. In the NPA system, the change in the flame angle was less pronounced than that of the spray system and it did not follow a sinusoidal trend during the cycle.

4. In both the NPA and Spray systems, forced flames had reduced average lift-off heights compared to the unforced conditions. Unlike Spray flames, the lift-off height of NPA flames was not periodic at the forcing frequency. The Spray flame lift-off height periodicity at the forcing frequency was found to be significantly greater far from blow-off than that closer to blow-off.
5. Concerning the POD analysis, in both systems, the dominant mechanism of the system was captured mainly by the first few OH* chemiluminescence Modes, which were representative of a left-right flame motion and an axial motion. In both systems, the absence of a 160 Hz (forcing frequency) peak at the PSD of POD time coefficients of the first POD Mode implied that forcing did not affect greatly the flame structure. The same conclusion was drawn by the fact that in both systems, the POD energy content of the first four POD Modes and the distribution of energy in the individual modes was similar in the forced and unforced conditions. Finally, the flame angle variation was captured by the first few OH PLIF POD Modes.

8.2 Suggestions for further research

The extensive database produced from the present work on the response of fully premixed, non-premixed with radial, non-premixed with axial fuel injection flames and spray flames over a broad range of operating conditions can be useful for the validation of computational models and the development of reliable flame response models and lean-burn devices. Further detailed velocity measurements along with the present experimental data would improve the understanding of the existing results, and it would also contribute to the verification of input and other boundary conditions used by modelers.

In this work, special emphasis was placed on the amplitude dependence of the flame response. The response of flames to acoustic forcing for different forcing frequencies would improve the current prediction capabilities. Additionally, a comparison of the present results with those acquired from self-excited flames, using the configurations that were used in the present work, would result in more accurate modelling approaches.

Finally, in the case of spray, non-premixed with radial and non-premixed with axial fuel injection flames, the information on the premixedness and on the time-varying equivalence ratio distribution is very important for the further understanding of the nonlinear flame response. Time and space resolved experimental measurements could improve the understanding from the existing data on the nonlinear response.

9 REFERENCES

1. Lefebvre, A. and D. Ballal, *Gas turbine Combustion: Alternative Fuels and Emissions*. Third ed. 2010: CRC Press.

2. el_Hossaini, M.K., *Review of the New Combustion Technologies in Modern Gas Turbines*, in Progress in Gas Turbine Performance, E. Benini, Editor. 2013, InTech: Rijeka. p. Ch. 06.

3. Candel, S., *Combustion dynamics and control: Progress and challenges.* Proceedings of the Combustion Institute, 2002. **29**(1): p. 1-28.

4. Lieuwen, T. and K. McManus, *Introduction: combustion dynamics in lean-premixed prevaporized (LPP) gas turbines.* Journal of Propulsion and Power, 2003. **19**(5): p. 721-721.

5. Keller, J.J., *Thermoacoustic oscillations in combustion chambers of gas turbines*. AIAA journal, 1995. **33**(12): p. 2280-2287.

6. Ahmed, S.A., *Three component velocity measurements of an isothermal confined swirling flow*. Proceedings of the Institution of Mechanical Engineers, Part G: Journal of Aerospace Engineering, 1997. **211**(2): p. 113-122.

7. Beer, J.M. and N.A. Chigier, *Combustor Aerodynamics*. 1972, London: Applied Science Publishers.

8. Chterev, I., D. Foti, J. Seitzman, S. Menon, and T. Lieuwen. *Flow field characterization in a premixe*d, swirling annular flow. in 50th AIAA Aerospace Sciences Meeting including the New Horizons Forum and Aerospace Exposition. 2012.

9. Syred, N., W. Fick, T. O'Doherty, and A.J. Griffiths, *The effect of the precessing vortex core on combustion in a swirl burner.* Combustion Science and Technology, 1997. **125**(1-6): p. 139-157.

10. Syred, N., *A review of oscillation mechanisms and the role of the precessing vortex core (PVC) in swirl combustion systems*. Progress in Energy and Combustion Science, 2006. **32**(2): p. 93-161.

11. Stöhr, M., I. Boxx, C.D. Carter, and W. Meier, *Experimental study of vortex-flame interaction in a gas turbine model combustor.* Combustion and Flame, 2012. **159**(8): p. 2636-2649.

12. Ducruix, S., Schuller, T., Durox, D., Candel, S., *Combustion dynamics and instabilities: Elementary coupling and driving mechanisms.* Journal of propulsion and power, 2003. **19**(5): p. 722-734.

13. Zinn, B.T. and T.C. Lieuwen, Combustion Instabilities: *Basic Concepts, in Combustion Instabilities In Gas Turbine Engines*: *Operational Experience, Fundamental Mechanisms, and Modeling*, T.C. Lieuwen and V. Yang, Editors. 2006, American Institute of Aeronautics and Astronautics. p. 3-26.

14. Culick, F.E. and V. Yang, *Overview of combustion instabilities in liquid-propellant rocket engines.* Liquid Rocket Engine Combustion Instability, 1995. **169**: p. 3-37.

15. Rogers, D.E., *A mechanism for high-frequency oscillation in ramjet combustors and afterburners*. Journal of Jet Propulsion, 1956. **26**(6): p. 456-462.

16. Langhorne, P., *Reheat buzz: an acoustically coupled combustion instability. Part 1. Experiment*. Journal of Fluid Mechanics, 1988. **193**: p. 417-443.

17. Bloxsidge, G., A. Dowling, and P. Langhorne, *Reheat buzz: an acoustically coupled combustion instability. Part 2. Theory.* Journal of fluid mechanics, 1988. **193**: p. 445-473.

18. Lieuwen, T.C. and V. Yang, *Combustion Instabilities In Gas Turbine Engines: Operational Experience, Fundamental Mechanisms, and Modeling*. Progress in Astronautics and Aeronautics. 2006: American Institute of Aeronautics and Astronautics. -1.

19. Woodfield, P., J. Kent, and T. Dixon, *Computational modelling of combustion instability in bagasse-fired furnaces.* Experimental Thermal and Fluid Science, 2000. **21**(1): p. 17-25.

20. McManus, K., T. Poinsot, and S. Candel, *A review of active control of combustion instabilities.* Progress in energy and combustion science, 1993. **19**(1): p. 1-29.

21. Rayleigh, J.S.W., *The Theory of Sound*. Vol. 2. 1945, New York: Dover.

22. Balachandran, R., A. Dowling, and E. Mastorakos. *Dynamics of bluff-body stabilised flames subjected to equivalence ratio oscillations*. in Proceeding of the European Combustion Meeting. 2011.

23. Balachandran, R., *Experimental Investigation of the Response of Turbulent Premixed Flames to Acoustic Oscillations*, in Department of Engineering. 2005, University of Cambridge: Cambridge, UK.

24. Han, Z., S. Balusamy, and S. Hochgreb, *Spatial Analysis on Forced Heat Release Response of Turbulent Stratified Flames.* Journal of Engineering for Gas Turbines and Power, 2015. **137**(6): p. 061504-061504-8.

25. Kypraiou, A.-M., N. Worth, and E. Mastorakos, *Experimental Investigation of the Response of Premixed and Non-premixed Turbulent Flames to Acoustic Forcing*, in 54th AIAA Aerospace Sciences Meeting. 2016, American Institute of Aeronautics and Astronautics.

26. Arndt, C.M., M. Severin, C. Dem, M. Stöhr, A.M. Steinberg, and W. Meier, *Experimental analysis of thermo-acoustic instabilities in a generic gas turbine combustor by phase-correlated PIV, chemiluminescence, and laser Raman scattering measurements*. Experiments in Fluids, 2015. **56**(4): p. 69.

27. Kim, K., J. Lee, B. Quay, and D. Santavicca, *Response of partially premixed flames to acoustic velocity and equivalence ratio perturbations.* Combustion and Flame, 2010. **157**(9): p. 1731-1744.

28. Peluso, S., B.D. Quay, J.G. Lee, and D.A. Santavicca. *Comparison between self-excited and forced flame response of an industrial lean premixed gas turbine injector*. in Proceedings of the ASME Turbo Expo. 2011.

29. Crocco, L., *Transverse combustion instability in liquid propellant rocket motors*. ARS Journal, 1962. **32**(3): p. 366-373.

30. Lieuwen, T., H. Torres, C. Johnson, and B.T. Zinn, *A mechanism of combustion instability in lean premixed gas turbine combustors.* Transactions-American Society of Mechanical Engineers Journal of Engineering for Gas Turbines and Power, 2001. **123**(1): p. 182-189.

31. Schadow, K. and E. Gutmark, *Combustion instability related to vortex shedding in dump combustors and their passive control.* Progress in Energy and Combustion Science, 1992. **18**(2): p. 117-132.

32. Merk, H. *An analysis of unstable combustion of premixed gases*. in Symposium (International) on Combustion. 1957. Elsevier.

33. Yi, T. and D.A. Santavicca. *Flame transfer functions and their applications to combustion analysis and control*. in ASME Turbo Expo 2009: Power for Land, Sea, and Air. 2009. American Society of Mechanical Engineers.

34. Yi, T., E.J. Gutmark, and B.K. Walker, *Stability and Control of Lean Blowout in Chemical Kinetics-Controlled Combustion Systems.* Combustion Science and Technology, 2009. **181**(2): p. 226-244.

35. Muruganandam, T., S. Nair, D. Scarborough, Y. Neumeier, J. Jagoda, T. Lieuwen, J. Seitzman, and B. Zinn, *Active control of lean blowout for turbine engine combustors.* Journal of Propulsion and Power, 2005. **21**(5): p. 807-814.

36. Yi, T. and E.J. Gutmark, *Real-Time Prediction of Incipient Lean Blowout in Gas Turbine Combustors*. AIAA Journal, 2007. **45**(7): p. 1734-1739.

37. Fritsche, D., M. Füri, and K. Boulouchos, *An experimental investigation of thermoacoustic instabilities in a premixed swirl-stabilized flame*. Combustion and Flame, 2007. **151**(1): p. 29-36.

38. Carter, C.D., M. Aigner, W. Meier, I.G. Boxx, A.M. Steinberg, and C.M. Arndt, *Flow-Field and Flame Dynamics of a Gas Turbine Model Combustor During Transition Between Thermo-Acoustically Stable and Unstable States*. 2010(43970): p. 677-687.

39. Allison, P., J. Driscoll, and M. Ihme, *Acoustic Behavior of a Partially-Premixed Gas Turbine Model Combustor*, in 50th AIAA Aerospace Sciences Meeting including the New Horizons Forum and Aerospace Exposition. 2012, American Institute of Aeronautics and Astronautics.

40. Balachandran, R., B.O. Ayoola, C.F. Kaminski, A.P. Dowling, and E. Mastorakos, *Experimental investigation of the nonlinear response of turbulent premixed flames to imposed inlet velocity oscillations.* Combustion and Flame, 2005. **143**(1–2): p. 37-55.

41. Steinberg, A.M., I. Boxx, M. Stöhr, C.D. Carter, and W. Meier, *Flow-flame interactions causing acoustically coupled heat release fluctuations in a thermo-acoustically unstable gas turbine model combustor*. Combustion and Flame, 2010. **157**(12): p. 2250-2266.

42. Worth, N.A. and J.R. Dawson, *Cinematographic OH-PLIF measurements of two interacting turbulent premixed flames with and without acoustic forcing*. Combustion and Flame, 2012. **159**(3): p. 1109-1126.

43. Durox, D., J.P. Moeck, J.-F. Bourgouin, P. Morenton, M. Viallon, T. Schuller, and S. Candel, *Flame dynamics of a variable swirl number system and instability control.* Combustion and Flame, 2013. **160**(9): p. 1729-1742.

44. Caux-Brisebois, V., A.M. Steinberg, C.M. Arndt, and W. Meier, *Thermo-acoustic velocity coupling in a swirl stabilized gas turbine model combustor.* Combustion and Flame, 2014. **161**(12): p. 3166-3180.

45. Huang, Y. and V. Yang, *Dynamics and stability of lean-premixed swirl-stabilized combustion.* Progress in Energy and Combustion Science, 2009. **35**(4): p. 293-364.

46. Balachandran, R., S.R. Chakravarthy, and R.I. Sujith, *Characterization of an Acoustically Self-Excited Combustor for Spray Evaporation.* Journal of Propulsion and Power, 2008. **24**(6): p. 1382-1389.

47. Steinberg, A.M., I. Boxx, M. Stöhr, W. Meier, and C.D. Carter, *Effects of flow structure dynamics on thermoacoustic instabilities in swirl-stabilized combustion.* AIAA journal, 2012. **50**(4): p. 952-967.

48. Balusamy, S., L.K.B. Li, Z. Han, M.P. Juniper, and S. Hochgreb, *Nonlinear dynamics of a self-excited thermoacoustic system subjected to acoustic forcing.* Proceedings of the Combustion Institute, 2015. **35**(3): p. 3229-3236.

49. Allison, P.M., Y. Chen, M. Ihme, and J.F. Driscoll, *Coupling of flame geometry and combustion instabilities based on kilohertz formaldehyde PLIF measurements.* Proceedings of the Combustion Institute, 2015. **35**(3): p. 3255-3262.

50. Dowling, A.P., *The calculation of thermoacoustic oscillations.* Journal of Sound and Vibration, 1995. **180**(4): p. 557-581.

51. Noiray, N., D. Durox, T. Schuller, and S. Candel, *Self-induced instabilities of premixed flames in a multiple injection configuration.* Combustion and Flame, 2006. **145**(3): p. 435-446.

52. Kim, K. and D. Santavicca, *Linear stability analysis of acoustically driven pressure oscillations in a lean premixed gas turbine combustor.* Journal of Mechanical Science and Technology, 2009. **23**(12): p. 3436-3447.

53. Paschereit, C.O., E. Gutmark, and W. Weisenstein, *Coherent structures in swirling flows and their role in acoustic combustion control.* Physics of Fluids, 1999. **11**(9): p. 2667-2678.

54. Stöhr, M., C.M. Arndt, and W. Meier, *Effects of Damköhler number on vortex–flame interaction in a gas turbine model combustor*. Proceedings of the Combustion Institute, 2013. **34**(2): p. 3107-3115.

55. Roux, S., G. Lartigue, T. Poinsot, U. Meier, and C. Bérat, *Studies of mean and unsteady flow in a swirled combustor using experiments, acoustic analysis, and large eddy simulations*. Combustion and Flame, 2005. **141**(1–2): p. 40-54.

56. Santhosh, R., A. Miglani, and S. Basu, *Transition and acoustic response of recirculation structures in an unconfined co-axial isothermal swirling flow*. Physics of Fluids, 2013. **25**(8): p. 083603.

57. Steinberg, A.M., I. Boxx, M. Stöhr, C.D. Carter, and W. Meier, *Flow–flame interactions causing acoustically coupled heat release fluctuations in a thermo-acoustically unstable gas turbine model combustor*. Combustion and Flame, 2010. **157**(12): p. 2250-2266.

58. Moeck, J.P., J.F. Bourgouin, D. Durox, T. Schuller, and S. Candel, *Nonlinear interaction between a precessing vortex core and acoustic oscillations in a turbulent swirling flame.* Combustion and Flame, 2012. **159**(8): p. 2650-2668.

59. Peluso, S., *Flame Response Mmechanisms in a Lean-Premixed Gas Turbine Combustor*, in College of Engineering 2012, The Pennsylvania State University

60. Huang, Y., S. Wang, and V. Yang, *Systematic Analysis of Lean-Premixed Swirl-Stabilized Combustion.* AIAA Journal, 2006. **44**(4): p. 724-740.

61. Weigand, P., W. Meier, X.R. Duan, W. Stricker, and M. Aigner, *Investigations of swirl flames in a gas turbine model combustor: I. Flow field, structures, temperature, and species distributions*. Combustion and Flame, 2006. **144**(1-2): p. 205-224.

62. Gonzalez, E., J. Lee, and D. Santavicca, *A Study of Combustion Instabilities Driven by Flame-Vortex Interactions*, in 41st AIAA/ASME/SAE/ASEE Joint Propulsion Conference & Exhibit. 2005, American Institute of Aeronautics and Astronautics.

63. Lee, H.J., K.T. Kim, J.G. Lee, B.D. Quay, and D.A. Santavicca. *An experimental study on the coupling of combustion instability mechanisms in a lean premixed gas turbine combustor*. in Proceedings of the ASME Turbo Expo. 2009.

64. Dem, C., M. Stöhr, C.M. Arndt, A.M. Steinberg, and W. Meier, *Experimental study of turbulence-chemistry interactions in perfectly and partially premixed confined swirl flames.* Zeitschrift für Physikalische Chemie, 2015. **229**(4): p. 569-595.

65. Meier, W., P. Weigand, X.R. Duan, and R. Giezendanner-Thoben, *Detailed characterization of the dynamics of thermoacoustic pulsations in a lean premixed swirl flame.* Combustion and Flame, 2007. **150**(1): p. 2-26.

66. Weigand, P., W. Meier, X. Duan, R. Giezendanner-Thoben, and U. Meier, *Laser diagnostic study of the mechanism of a periodic combustion instability in a gas turbine model combustor.* Flow, Turbulence and combustion, 2005. **75**(1): p. 275-292.

67. Bellows, B.D., Y. Neumeier, and T. Lieuwen, *Forced Response of a Swirling, Premixed Flame to Flow Disturbances.* Journal of Propulsion and Power, 2006. **22**(5): p. 1075-1084.

68. Kim, D., J.G. Lee, B.D. Quay, D.A. Santavicca, K. Kim, and S. Srinivasan, *Effect of flame structure on the flame transfer function in a premixed gas turbine combustor.* Journal of Engineering for Gas Turbines and Power, 2010. **132**(2).

69. Kim, K.T., J.G. Lee, H.J. Lee, B.D. Quay, and D.A. Santavicca, *Characterization of forced flame response of swirl-stabilized turbulent lean-premixed flames in a gas turbine combustor.* Journal of Engineering for Gas Turbines and Power, 2010. **132**(4).

70. Külsheimer, C. and H. Büchner, *Combustion dynamics of turbulent swirling flames.* Combustion and Flame, 2002. **131**(1–2): p. 70-84.

71. Fleifil, M., A.M. Annaswamy, Z.A. Ghoneim, and A.F. Ghoniem, *Response of a laminar premixed flame to flow oscillations: A kinematic model and thermoacoustic instability results*. Combustion and Flame, 1996. **106**(4): p. 487-510.

72. Schuller, T., D. Durox, and S. Candel, *A unified model for the prediction of laminar flame transfer functions: comparisons between conical and V-flame dynamics*. Combustion and Flame, 2003. **134**(1–2): p. 21-34.

73. You, D., Y. Huang, and V. Yang, *A generalized model of acoustic response of turbulent premixed flame and its application to gas-turbine combustion instability analysis*. Combustion Science and Technology, 2005. **177**(5-6): p. 1109-1150.

74. Armitage, C., R. Balachandran, E. Mastorakos, and R. Cant, *Investigation of the nonlinear response of turbulent premixed flames to imposed inlet velocity oscillations.* Combustion and Flame, 2006. **146**(3): p. 419-436.

75. Schuller, T., S. Ducruix, D. Durox, and S. Candel, *Modeling tools for the prediction of premixed flame transfer functions.* Proceedings of the Combustion Institute, 2002. **29**(1): p. 107-113.

76. Bourehla, A. and F. Baillot, *Appearance and Stability of a Laminar Conical Premixed Flame Subjected to an Acoustic Perturbation*. Combustion and Flame, 1998. **114**(3–4): p. 303-318.

77. Ducruix, S., D. Durox, and S. Candel, *Theoretical and experimental determinations of the transfer function of a laminar premixed flame.* Proceedings of the combustion institute, 2000. **28**(1): p. 765-773.

78. Kartheekeyan, S. and S.R. Chakravarthy, *An experimental investigation of an acoustically excited laminar premixed flame.* Combustion and Flame, 2006. **146**(3): p. 513-529.

79. Preetham, H. Santosh, and T. Lieuwen, *Dynamics of laminar premixed flames forced by harmonic velocity disturbances.* Journal of Propulsion and Power, 2008. **24**(6): p. 1390-1402.

80. Birbaud, A.L., D. Durox, S. Ducruix, and S. Candel, *Dynamics of confined premixed flames submitted to upstream acoustic modulations.* Proceedings of the Combustion Institute, 2007. **31 I**: p. 1257-1265.

81. Karimi, N., M.J. Brear, S.H. Jin, and J.P. Monty, *Linear and non-linear forced response of a conical, ducted, laminar premixed flame.* Combustion and Flame, 2009. **156**(11): p. 2201-2212.

82. Kim, K.T., J.G. Lee, B.D. Quay, and D.A. Santavicca, *The dynamic response of turbulent dihedral V flames: An amplification mechanism of swirling flames.* Combustion Science and Technology, 2010. **183**(2): p. 163-179.

83. Borghesi, G., F. Biagioli, and B. Schuermans, *Dynamic response of turbulent swirling flames to acoustic perturbations.* Combustion Theory and Modelling, 2009. **13**(3): p. 487-512.

84. Straub, D.L. and G.A. Richards. *Effect of fuel nozzle configuration on premix combustion dynamics*. in ASME 1998 International Gas Turbine and Aeroengine Congress and Exhibition. 1998. American Society of Mechanical Engineers.

85. Lieuwen, T.C., *Experimental investigation of limit-cycle oscillations in an unstable gas turbine combustor*. Journal of Propulsion and Power, 2002. **18**(1): p. 61-67.

86. Dowling, A.P., *Nonlinear self-excited oscillations of a ducted flame.* Journal of fluid mechanics, 1997. **346**: p. 271-290.

87. Lieuwen, T. and Y. Neumeier, *Nonlinear pressure-heat release transfer function measurements in a premixed combustor.* Proceedings of the Combustion Institute, 2002. **29**(1): p. 99-105.

88. Thumuluru, S.K. and T. Lieuwen, *Characterization of acoustically forced swirl flame dynamics.* Proceedings of the Combustion Institute, 2009. **32 II**: p. 2893-2900.

89. Bellows, B.D., M.K. Bobba, A. Forte, J.M. Seitzman, and T. Lieuwen, *Flame transfer function saturation mechanisms in a swirl-stabilized combustor.* Proceedings of the Combustion Institute, 2007. **31 II**: p. 3181-3188.

90. Bellows, B.D., M.K. Bobba, J.M. Seitzman, and T. Lieuwen, *Nonlinear Flame Transfer Function Characteristics in a Swirl-Stabilized Combustor.* Journal of Engineering for Gas Turbines and Power, 2006. **129**(4): p. 954-961.

91. Terhaar, S., B. Ćosić, C.O. Paschereit, and K. Oberleithner, *Impact of shear flow instabilities on the magnitude and saturation of the flame response.* Journal of Engineering for Gas Turbines and Power, 2014. **136**(7).

92. Palies, P., D. Durox, T. Schuller, and S. Candel, *The combined dynamics of swirler and turbulent premixed swirling flames.* Combustion and Flame, 2010. **157**(9): p. 1698-1717.

93. Schimek, S., J.P. Moeck, and C.O. Paschereit, *An experimental investigation of the nonlinear response of an atmospheric swirl-stabilized premixed flame.* Journal of Engineering for Gas Turbines and Power, 2011. **133**(10).

94. Baillot, F., D. Durox, and R. Prud'homme, *Experimental and theoretical study of a premixed vibrating flame*. Combustion and Flame, 1992. **88**(2): p. 149-152,IN1,153-168.

95. Dowling, A.P. and S.R. Stow, *Acoustic analysis of gas turbine combustors.* Journal of propulsion and power, 2003. **19**(5): p. 751-764.

96. Lieuwen, T., *Modeling Premixed Combustion-Acoustic Wave Interactions: A Review.* Journal of propulsion and power, 2003. **19**(5): p. 765-781.

97. Orchini, A. and M.P. Juniper. *Heat release response to forced flow oscillations of a low-order modelled laboratory scale dump combustor*. in Proceedings of the ASME Turbo Expo. 2015.

98. Brookes, S.J., R.S. Cant, I.D.J. Dupere, and A.P. Dowling, *Computational modelling of self-excited combustion instabilities.* Journal of Engineering for Gas Turbines and Power, 2001. **123**(2): p. 322-326.

99. Tay Wo Chong, L., R. Kaess, T. Komarek, S. Föller, and W. Polifke, *Identification of flame transfer functions using LES of turbulent reacting flows.* High Performance Computing in Science and Engineering, Garching/Munich 2009, 2010: p. 255-266.

100. Han, X. and A.S. Morgans, *Simulation of the flame describing function of a turbulent premixed flame using an open-source LES solver*. Combustion and Flame, 2015. **162**(5): p. 1778-1792.

101. Ruan, S., T.D. Dunstan, N. Swaminathan, and R. Balachandran, *Computation of Forced Premixed Flames Dynamics.* Combustion Science and Technology, 2016. **188**(7): p. 1115-1135.

102. Hurle, I., R. Price, T. Sugden, and A. Thomas. *Sound emission from open turbulent premixed flames*. in Proceedings of the Royal Society of London A: Mathematical, Physical and Engineering Sciences. 1968. The Royal Society.

103. Higgins, B., M.Q. McQuay, F. Lacas, J.C. Rolon, N. Darabiha, and S. Candel, *Systematic measurements of OH chemiluminescence for fuel-lean, high-pressure, premixed, laminar flames.* Fuel, 2001. **80**(1): p. 67-74.

104. Schuermans, B., F. Guethe, D. Pennell, D. Guyot, and C.O. Paschereit, *Thermoacoustic Modeling of a Gas Turbine Using Transfer Functions Measured Under Full Engine Pressure.* Journal of Engineering for Gas Turbines and Power, 2010. **132**(11): p. 111503-111503-9.

105. Ćosić, B., S. Terhaar, J.P. Moeck, and C.O. Paschereit, *Response of a swirl-stabilized flame to simultaneous perturbations in equivalence ratio and velocity at high oscillation amplitudes*. Combustion and Flame, 2015. **162**(4): p. 1046-1062.

106. Balusamy, S., L.K.B. Li, Z. Han, and S. Hochgreb, *Extracting flame describing functions in the presence of self-excited thermoacoustic oscillations.* Proceedings of the Combustion Institute, 2017. **36**(3): p. 3851-3861.

107. Lieuwen, T., *Nonlinear kinematic response of premixed flames to harmonic velocity disturbances.* Proceedings of the Combustion Institute, 2005. **30**(2): p. 1725-1732.

108. Marble, F.E. and S.M. Candel, *An analytical study of the non-steady behavior of large combustors.* Symposium (International) on Combustion, 1979. **17**(1): p. 761-769.

109. Shanbhogue, S., D.-H. Shin, S. Hemchandra, D. Plaks, and T. Lieuwen, *Flame-sheet dynamics of bluff-body stabilized flames during longitudinal acoustic forcing.* Proceedings of the Combustion Institute, 2009. **32**(2): p. 1787-1794.

110. Bobusch, B.C., B. Ćosić, J.P. Moeck, and C. Oliver Paschereit, *Optical Measurement of Local and Global Transfer Functions for Equivalence Ratio Fluctuations in a Turbulent Swirl Flame.* Journal of Engineering for Gas Turbines and Power, 2013. **136**(2): p. 021506-021506-8.

111. Hermeth, S., *Mechanisms affecting the dynamic response of swirled flames in gas turbines*, in Mécanique, Energétique, Génie civil et Procédés 2012, INP Toulouse.

112. Chaudhuri, S. and B.M. Cetegen, *Response dynamics of bluff-body stabilized conical premixed turbulent flames with spatial mixture gradients*. Combustion and Flame, 2009. **156**(3): p. 706-720.

113. Kim, K.T. and S. Hochgreb, *The nonlinear heat release response of stratified lean-premixed flames to acoustic velocity oscillations*. Combustion and Flame, 2011. **158**(12): p. 2482-2499.

114. Bade, S., M. Wagner, C. Hirsch, T. Sattelmayer, and B. Schuermans. *Influence of fuel-air mixing on flame dynamics of premixed swirl burners*. in ASME Turbo Expo 2014: Turbine Technical Conference and Exposition. 2014. American Society of Mechanical Engineers.

115. Peterleithner, J., N.V. Stadlmair, J. Woisetschläger, and T. Sattelmayer, *Analysis of Measured Flame Transfer Functions With Locally Resolved Density Fluctuation and OH-Chemiluminescence Data.* Journal of Engineering for Gas Turbines and Power, 2015. **138**(3): p. 031504-031504-9.

116. Yi, T. and D.A. Santavicca, *Flame Spectra of a Turbulent Liquid-Fueled Swirl-Stabilized Lean-Direct Injection Combustor.* Journal of Propulsion and Power, 2009. **25**(5): p. 1058-1067.

117. Lee, J. and D. Santavicca, *Experimental diagnostics for the study of combustion instabilities in lean premixed combustors*. Journal of propulsion and power, 2003. **19**(5): p. 735-750.

118. Ayoola, B., R. Balachandran, J. Frank, E. Mastorakos, and C. Kaminski, *Spatially resolved heat release rate measurements in turbulent premixed flames.* Combustion and flame, 2006. **144**(1): p. 1-16.

119. Panoutsos, C.S., Y. Hardalupas, and A. Taylor, *Numerical evaluation of equivalence ratio measurement using OH and CH chemiluminescence in premixed and non-premixed methane-air flames*. Combustion and flame, 2009. **156**: p. 273-291.

120. Chaparro, A.A. and B.M. Cetegen, *Blowoff characteristics of bluff-body stabilized conical premixed flames under upstream velocity modulation*. Combustion and Flame, 2006. **144**(1-2): p. 318-335.

121. Chaudhuri, S., *Blowoff mechanism of harmonically forced bluff body stabilized turbulent premixed flames*. Combustion and flame. **159**(2): p. 638-640.

122. Biswas, S., K. Kopp-Vaughn, M.W. Renfro, and B.M. Cetegen, *Phase resolved characterization of conical premixed flames near and far from blowoff.* Combustion and Flame, 2013. **160**(12): p. 2843-2855.

123. Chaudhuri, S. and B.M. Cetegen, *Blowoff characteristics of bluff-body stabilized conical premixed flames in a duct with upstream spatial mixture gradients and velocity oscillations*. Combustion Science and Technology, 2009. **181**(4): p. 555-569.

124. Mirat, C., D. Durox, and T. Schuller, *Analysis of the Spray and Transfer Function of Swirling Spray Flames From a Multi-Jet Steam Assisted Liquid Fuel Injector*. 2014(45684): p. V04AT04A008.

125. Gajan, P., A. Strzelecki, B. Platet, R. Lecourt, and F. Giuliani, *Investigation of Spray Behavior Downstream of an Aeroengine Injector with Acoustic Excitation.* Journal of Propulsion and Power, 2007. **23**(2): p. 390-397.

126. Luo, K., H. Pitsch, M. Pai, and O. Desjardins, *Direct numerical simulations and analysis of three-dimensional n-heptane spray flames in a model swirl combustor.* Proceedings of the Combustion Institute, 2011. **33**(2): p. 2143-2152.

127. Eckstein, J., E. Freitag, C. Hirsch, and T. Sattelmayer, *Experimental Study on the Role of Entropy Waves in Low-Frequency Oscillations for a Diffusion Burner*. 2004(41669): p. 743-751.

128. Yu, K.H. and K.J. Wilson, *Scale-up experiments on liquid-fueled active combustion control.* Journal of propulsion and power, 2002. **18**(1): p. 53-60.

129. Duvvur, A., C. Chiang, and W. Sirignano, *Oscillatory fuel droplet vaporization-driving mechanism for combustion instability.* Journal of propulsion and Power, 1996. **12**(2): p. 358-365.

130. Hsiao, G.C., H. Meng, and V. Yang, *Pressure-coupled vaporization response of n-pentane fuel droplet at subcritical and supercritical conditions*. Proceedings of the Combustion Institute, 2011. **33**(2): p. 1997-2003.

131. Zhu, M., A. Dowling, and K. Bray. *Combustion Oscillations in Burners with Fuel Spray Atomisers*. in ASME 1999 International Gas Turbine and Aeroengine Congress and Exhibition. 1999. American Society of Mechanical Engineers.

132. Zhang, C., P. Zou, B. Wang, X. Xue, Y. Lin, and C.-J. Sung, *Comparison of Flame Dynamics at Stable and Near-LBO Conditions for Swirl-Stabilized Kerosene Spray Combustion*. 2015(56680): p. V04AT04A044.

133. Berkooz, G., P. Holmes, and J.L. Lumley, *The proper orthogonal decomposition in the analysis of turbulent flows.* Annual Review of Fluid Mechanics, 1993. **25**(1): p. 539-575.

134. Bizon, K., G. Continillo, K.C. Leistner, E. Mancaruso, and B.M. Vaglieco, *POD-based analysis of cycle-to-cycle variations in an optically accessible diesel engine.* Proceedings of the Combustion Institute, 2009. **32**(2): p. 2809-2816.

135. Duwig, C. and C. Fureby, *Large eddy simulation of unsteady lean stratified premixed combustion.* Combustion and Flame, 2007. **151**(1): p. 85-103.

136. Ayache, S. and E. Mastorakos, *Investigation of the "TECFLAM" non-premixed flame using large eddy simulation and proper orthogonal decomposition*. Flow, Turbulence and Combustion, 2013. **90**(2): p. 219-241.

137. Danby, S.J. and T. Echekki, *Proper orthogonal decomposition analysis of autoignition simulation data of nonhomogeneous hydrogen–air mixtures.* Combustion and Flame, 2006. **144**(1): p. 126-138.

138. Frouzakis, C., Y. Kevrekidis, J. Lee, K. Boulouchos, and A. Alonso, *Proper orthogonal decomposition of direct numerical simulation data: Data reduction and observer construction.* Proceedings of the Combustion Institute, 2000. **28**(1): p. 75-81.

139. Kopp-Vaughan, K.M., T.R. Jensen, B.M. Cetegen, and M.W. Renfro, *Analysis of blowoff dynamics from flames with stratified fueling.* Proceedings of the Combustion Institute, 2013. **34**(1): p. 1491-1498.

140. Kostka, S., S. Roy, B. Huelskamp, A. Lynch, B. Kiel, and J. Gord. *Characterization of bluff-body-flame vortex shedding using proper orthogonal decomposition*. in 49th AIAA Aerospace Sciences Meeting including the New Horizons Forum and Aerospace Exposition. 2011.

141. Zhang, J. and A. Ratner. *Analysis of the Thermoacoustic Flame Instability With Proper Orthogonal Decomposition*. in ASME 2015 International Mechanical Engineering Congress and Exposition. 2015. American Society of Mechanical Engineers.

142. Duwig, C., S. Ducruix, and D. Veynante, *Studying the Stabilization Dynamics of Swirling Partially Premixed Flames by Proper Orthogonal Decomposition.* Journal of Engineering for Gas Turbines and Power, 2012. **134**(10): p. 101501-101501-10.

143. Denisov, A. and A. Ravi, *Premixed Swirling Flame Response to Acoustic Forcing Studied With High-Speed PIV and OH* Chemiluminescence*. 2015(56697): p. V04BT04A030.

144. Boxx, I., C.M. Arndt, C.D. Carter, and W. Meier, *High-speed laser diagnostics for the study of flame dynamics in a lean premixed gas turbine model combustor*. Experiments in Fluids, 2012. **52**(3): p. 555-567.

145. Kamal, M.M., C. Duwig, S. Balusamy, R. Zhou, and S. Hochgreb, *Proper Orthogonal Decomposition Analysis of Non-Swirling Turbulent Stratified and Premixed Methane/Air Flames*. 2014(45691): p. V04BT04A023.

146. Sieber, M., C.O. Paschereit, and K. Oberleithner. *Advanced identification of coherent structures in swirl-stabilized combustors*. in Proceedings of the ASME Turbo Expo. 2016.

147. Kashinath, K., S. Hemchandra, and M.P. Juniper, *Nonlinear thermoacoustics of ducted premixed flames: The influence of perturbation convection speed.* Combustion and Flame, 2013. **160**(12): p. 2856-2865.

148. Birbaud, A.L., D. Durox, and S. Candel, *Upstream flow dynamics of a laminar premixed conical flame submitted to acoustic modulations.* Combustion and Flame, 2006. **146**(3): p. 541-552.

149. Zinn, B.T. and T.C. Lieuwen, *Combustion instabilities: Basic concepts.* Combustion Instabilities in Gas Turbine Engines: Operational Experience, Fundamental Mechanisms, and Modeling, 2005. **210**: p. 3-26.

150. Lechler, *Hollow cone nozzles Axial-low flow Series 212*, in *http://www.lechler.de/is-bin/intershop.static/WFS/LechlerUS-Shop-Site/LechlerUS-Shop/en_US/PDF/02_produkte/industrie/02_Hollow_Cone_Nozzles/Series_212_HollowCones.pdf*. 2017.

151. Yuan, R., *Measurements in Swirl-stabilised Spray Flames at Blow-off*, in Department of Engineering. 2015, University of Cambridge: Cambridge. p. 78.

152. Alicat, Technical Data for Alicat MC and MCR Mass Flow Controllers., in *http://www.alicat.com/documents/specifications/Alicat_Mass_Controller_Specs.pdf*. 2014.

153. Bronkhorst, LIQUI-FLOW TM: Series L30 Digital Mass Flow Meters / Controllers for Liquids, in *http://www.bronkhorst.com/files/downloads/brochures/liqui-flow_l30.pdf*. 2017.

154. Seybert, A.F. and D.F. Ross, *Experimental determination of acoustic properties using a two-microphone random-excitation technique.* the Journal of the Acoustical Society of America, 1977. **61**(5): p. 1362-1370.

155. Samaniego, J.M., B. Yip, T. Poinsot, and S. Candel, *Low-frequency combustion instability mechanisms in a side-dump combustor.* Combustion and Flame, 1993. **94**(4): p. 363-370,IN1-IN2,371-380.

156. Shih, W.P., J.G. Lee, and D.A. Santavicca, *Stability and emissions characteristics of a lean premixed gas turbine combustor.* Symposium (International) on Combustion, 1996. **26**(2): p. 2771-2778.

157. Haber, L.C., U. Vandsburger, W.R. Saunders, and V.K. Khanna. *An examination of the relationship between chemiluminescent light emissions and heat release rate under non-adiabatic conditions*. in Proceedings of the ASME Turbo Expo. 2000.

158. Bellows, B.D., Q. Zhang, Y. Neumeier, T. Lieuwen, and Z. B.T. *Forced Response Studies of a Premixed Flame to Flow Disturbances in a Gas Turbine Combustor* in 41st AIAA Aerospace Sciences Meeting and Exhibit 2003. Reno, NV.

159. Lee, J.G. and D.A. Santavicca, *Experimental Diagnostics Of Combustion Instabilities, in Combustion Instabilities In Gas Turbine Engines: Operational Experience, Fundamental Mechanisms, and Modeling*, T. Lieuwen and V. Yang, Editors. 2006, American Institute of Aeronautics and Astronautics. p. 481-529.

160. Nguyen, Q.-V. and P.H. Paul. *The time evolution of a vortex-flame interaction observed via planar imaging of CH and OH*. in Symposium (International) on Combustion. 1996. Elsevier.

161. Truffin, K. and T. Poinsot, *Comparison and extension of methods for acoustic identification of burners.* Combustion and Flame, 2005. **142**(4): p. 388-400.

162. Veynante, D., J.M. Duclos, and J. Piana. *Experimental analysis of flamelet models for premixed turbulent combustion*. in Symposium (International) on Combustion. 1994. Elsevier.

163. Balachandran, R., A.P. Dowling, and E. Mastorakos, *Non-linear Response of Turbulent Premixed Flames to Imposed Inlet Velocity Oscillations of Two Frequencies.* Flow, Turbulence and Combustion, 2008. **80**(4): p. 455-487.

164. Renard, P.H., J.C. Rolon, D. Thévenin, and S. Candel, *Investigations of heat release, extinction, and time evolution of the flame surface, for a nonpremixed flame interacting with a vortex*. Combustion and Flame, 1999. **117**(1-2): p. 189-205.

165. Candel, S., D. Durox, T. Schuller, P. Palies, J.F. Bourgouin, and J.P. Moeck, *Progress and challenges in swirling flame dynamics.* Comptes Rendus - Mecanique, 2012. **340**(11-12): p. 758-768.

166. Paschereit, C.O., E. Gutmark, and W. Weisenstein, *Excitation of thermoacoustic instabilities by interaction of acoustics and unstable swirling flow*. AIAA journal, 2000. **38**(6): p. 1025-1034.

167. Bizon, K., G. Continillo, L. Russo, and J. Smuła, *On POD reduced models of tubular reactor with periodic regimes.* Computers & Chemical Engineering, 2008. **32**(6): p. 1305-1315.

168. Ilak, M. and C.W. Rowley, *Modeling of transitional channel flow using balanced proper orthogonal decomposition*. Physics of Fluids, 2008. **20**(3).

169. Rehimi, F., F. Aloui, S.B. Nasrallah, L. Doubliez, and J. Legrand, *Experimental investigation of a confined flow downstream of a circular cylinder centred between two parallel walls.* Journal of Fluids and Structures, 2008. **24**(6): p. 855-882.

170. Armitage, C.A., R. Balachandran, E. Mastorakos, and R.S. Cant, *Investigation of the nonlinear response of turbulent premixed flames to imposed inlet velocity oscillations.* Combustion and Flame, 2006. **146**(3): p. 419-436.

171. Semlitsch, B., O. Orchini Alessandro, D. Dowling Ann P, and M. Juniper Matthew P, *G-equation modelling of thermo-acoustic oscillations of partially-premixed flames.* International Journal of Spray and Combustion Dynamics, 2016.

172. Lee, S.Y., S. Seo, J.C. Broda, S. Pal, and R.J. Santoro, *An experimental estimation of mean reaction rate and flame structure during combustion instability in a lean premixed gas turbine combustor*. Proceedings of the Combustion Institute, 2000. **28**(1): p. 775-782.

173. Lee, J.G. and D.A. Santavicca, *Experimental Diagnostics for the Study of Combustion Instabilities in Lean Premixed Combustors*. Journal of Propulsion and Power, 2003. **19**(5): p. 735-750.

174. Bellows, B. and T. Lieuwen, *Nonlinear Response of a Premixed Combustor to Forced Acoustic Oscillations*, in 42nd AIAA Aerospace Sciences Meeting and Exhibit. 2004, American Institute of Aeronautics and Astronautics.

175. Chaparro, A., E. Landry, and B.M. Cetegen, *Transfer function characteristics of bluff-body stabilized, conical V-shaped premixed turbulent propane–air flames*. Combustion and Flame, 2006. **145**(1–2): p. 290-299.

176. Sung, C.J. and C.K. Law, *Structural sensitivity, response, and extinction of diffusion and premixed flames in oscillating counterflow*. Combustion and Flame, 2000. **123**(3): p. 375-388.

177. Brown, T.M., R.W. Pitz, and C.J. Sung, *Oscillatory stretch effects on the structure and extinction of counterflow diffusion flames.* Symposium (International) on Combustion, 1998. **27**(1): p. 703-710.

178. Kistler, J.S., C.J. Sung, T.G. Kreut, C.K. Law, and M. Nishioka, *Extinction of counterflow diffusion flames under velocity oscillations.* Symposium (International) on Combustion, 1996. **26**(1): p. 113-120.

179. Cant, R.S. and E. Mastorakos, *An Introduction to Turbulent Reacting Flows*. 2008, London: Imperial College Press.

180. Nair, S. and T. Lieuwen, *Acoustic Detection of Blowout in Premixed Flames.* Journal of Propulsion and Power, 2005. **21**(1): p. 32-39.

181. Lieuwen, T.C., *Unsteady combustor physics*. 2012: Cambridge University Press.

182. Price, R.B., I.R. Hurle, and T.M. Sugden, *Optical studies of the generation of noise in turbulent flames.* Symposium (International) on Combustion, 1969. **12**(1): p. 1093-1102.

183. Mirat, C., D. Durox, and T. Schuller. *Analysis of the Spray and Transfer Function of Swirling Spray Flames From a Multi-Jet Steam Assisted Liquid Fuel Injector*. in ASME Turbo Expo 2014: Turbine Technical Conference and Exposition. 2014. Düsseldorf, Germany.

184. Abramzon, B. and W.A. Sirignano, *Droplet vaporization model for spray combustion calculations.* International Journal of Heat and Mass Transfer, 1989. **32**(9): p. 1605-1618.

185. Stow, S.R. and A.P. Dowling, *Thermoacoustic Oscillations in an Annular Combustor*. 2001(78514): p. V002T02A004.

10 APPENDICES

10.1 Appendix A

This appendix contains one figure on the next page.

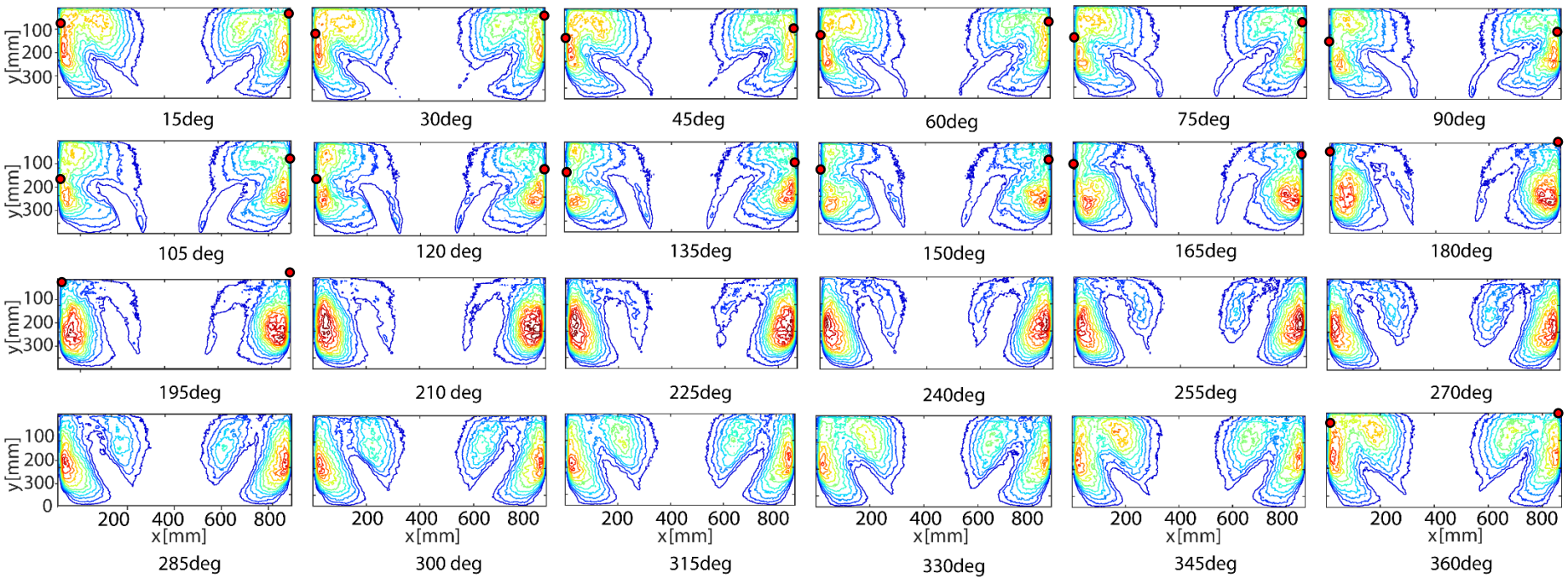

Figure 10-1: Phase-averaged iso-contour plots of OH PLIF of P-15-070-160-30. The impingement points are indicated with the red markers.

10.2 Appendix B

10.2.1 Two-Microphone Technique

The two-microphone technique was used by [185] to determine the velocity fluctuation downstream at different positions in a combustor using two microphones within the inlet section. This method allows the determination of velocity fluctuations at positions that are very difficult to contain instrumentation.

The model assumes that the burner inlet section is circular and composed of narrow straight ducts connected by short sections of area change. We will assume a perfect gas, $\rho = p/RT$ where ρ is density, p is pressure, R is the ideal gas constant and T is the temperature. Since a narrow circular geometry is used, we will assume that the variation in the radial direction is negligible. The flow is taken to be composed of a steady axial mean flow (denoted by bars e.g. $\bar{u}$) and a small perturbation (denoted by dashes e.g. u'),

For straight sections, straight ducts are assumed to be narrow, with length L, and cross-sectional area A . The perturbations can be expressed as the sum of two acoustic waves: an incident and reflected acoustic wave.

$$p'(x) = A_+ e^{i(-k_+ x)} + A_- e^{i(k_- x)}$$

$$u'(x) = \frac{A_+ e^{i(-k_+ x_1)} - A_- e^{i(k_- x_1)}}{\rho c}$$

$$\rho'(x) = \frac{p'(x)}{c^2}$$

For the position of each microphone at position, x_1 and x_2, the perturbation of pressure at each position can be represented as:

$$p'(x_1) = A_+ e^{i(-k_+ x_1)} + A_- e^{i(k_- x_1)}$$

$$p'(x_2) = A_+ e^{i(-k_+ x_2)} + A_- e^{i(k_- x_2)}$$

$$k_+ = \frac{2\pi f}{c + u}$$

$$k_- = \frac{2\pi f}{c - u}$$

To determine the complex amplitude of the two acoustic waves, the following set of linear equations (shown here in matrix form) must be solved:

$$[A_+ \quad A_-] = \begin{bmatrix} e^{i(-k_+ x_1)} & e^{i(k_- x_1)} \\ e^{i(-k_+ x_2)} & e^{i(k_- x_2)} \end{bmatrix}^{-1} \begin{bmatrix} p'(x_1) \\ p'(x_2) \end{bmatrix}$$

Once the complex amplitudes of the acoustic waves have been determined, the pressure, velocity and pressure perturbations at the end of straight tube (at position L) can be solved using:

$$[p'(L) \quad u'(L)] = \begin{bmatrix} e^{i(-k_+ L)} & e^{i(k_- L)} \\ \frac{e^{i(-k_+ L)}}{\rho c} & \frac{-e^{i(k_- L)}}{\rho c} \end{bmatrix} \begin{bmatrix} A_+ \\ A_- \end{bmatrix}$$

$$\rho'(L) = \frac{p'(L)}{c^2}$$

For regions of area decrease we assume the flow is isentropic. We can therefore find the mean flow. We also assume that the length of the area change section is short compared to axial and circumferential wavelengths. By considering conservation of mass, energy, entropy and angular momentum in a thin section along the area change, it can be shown that the perturbations in mass flux, enthalpy flux, and entropy flux are all conserved across the area change [185].

Using the following equations for mass flow, enthalpy and entropy, all mean quantities at each position (denoted by bars) can be determined.

Mass flow equation:

$$\dot{m} = \rho u A$$

Mass flux perturbation:

$$\dot{m}' = \bar{\rho} u' A + \rho' \bar{u} A$$

Enthalpy equation:

$$h = C_p T + \frac{u^2}{2}$$

Enthalpy flux perturbation:

$$h' = \frac{c_p p'}{R\bar{\rho}} - \frac{c_p \bar{p} \rho'}{R(\bar{\rho})^2} + \bar{u} u'$$

Entropy equation:

$$s = C_p \ln T - R \ln p$$

Enthalpy flux perturbation:

$$s' = \frac{c_v p'}{\bar{p}} - \frac{c_p \rho'}{\bar{\rho}}$$

The perturbation fluxes can then be calculated using the mean quantities by the following set of equations, shown in matrix form:

$$[\dot{m}' \quad h' \quad s'] = \begin{bmatrix} 0 & \bar{\rho}A & \bar{u}A \\ \frac{c_p}{R\bar{\rho}} & \bar{u} & -\frac{c_p \bar{p}}{R(\bar{\rho})^2} \\ \frac{c_v}{\bar{p}} & 0 & -\frac{c_p}{\bar{\rho}} \end{bmatrix} \begin{bmatrix} p' \\ u' \\ \rho' \end{bmatrix}$$

Once the perturbation vector is computed, using the equations for the conservation of mass flow, enthalpy and entropy, the mean quantities at position of the decrease area can be calculated. The pressure, velocity and pressure perturbations at this location is calculated using the following set of equations, shown in matrix form.

$$[p' \quad u' \quad \rho'] = \begin{bmatrix} 0 & \bar{\rho}A & \bar{u}A \\ \frac{c_p}{R\bar{\rho}} & \bar{u} & -\frac{c_p \bar{p}}{R(\bar{\rho})^2} \\ \frac{c_v}{\bar{p}} & 0 & -\frac{c_p}{\bar{\rho}} \end{bmatrix}^{-1} \begin{bmatrix} \dot{m}' \\ h' \\ s' \end{bmatrix}$$

Swirlers are treated as an area decrease, as the swirler has narrow passages which is also much shorter axially than the acoustic wavelength.

10.3 Appendix C

10.3.1 Publications

Kypraiou AM, Allison PM, Giusti A, Mastorakos E, "*Experimenatl investigation of the forced response of a non-premixed flame with radial fuel injection*" (In preparation).

Giusti A, Zhang H, Kypraiou AM, Allison P, Mastorakos E, "*Numerical investigation of the forced response of a non-premixed flame with radial fuel injection*" (In preparation).

Kypraiou AM, Karimi N, Dowling AP, Mastorakos E, "*Proper orthogonal decomposition analysis of a turbulent swirling self-excited premixed flame*". (Submitted for publication).

10.3.2 Conference Presentations

Kypraiou AM, Allison PM, Giusti A, Mastorakos E, "*Response of flames with different degrees of premixedness to acoustic oscillations*". Accepted at: Tenth Mediterranean Combustion Symposium, September 17-21 2017, Naples, Italy.

Kypraiou AM, Giusti A, Allison PM, Mastorakos E, "*Dynamics of forced non-premixed flames close to blow-off*". Accepted at: Tenth Mediterranean Combustion Symposium, September 17-21 2017, Naples, Italy.

Kypraiou AM, Worth NA, Mastorakos E, "*Experimental investigation of the response of premixed and non-premixed turbulent flames to acoustic forcing*". AIAA Science and Technology Forum 2016, 4 – 8 January 2016, San Diego, CA, USA.

Kypraiou AM, Worth NA, Mastorakos E, "*Experimental investigation of the response of turbulent non-premixed flames to acoustic forcing*". Ninth Mediterranean Combustion Symposium 7 – 11 June 2015, Rhodes, Greece.

Kypraiou AM, Karimi N, Dowling AP, Mastorakos E, "*Proper orthogonal decomposition analysis of a turbulent swirling self-excited premixed flame*". AIAA Science and Technology Forum 2015, 5 – 9 January 2015, Kissimmee, FL, USA.

Kypraiou AM, Karimi N, Dowling AP, Mastorakos E, "*Thermoacoustic analysis of turbulent swirling self-excited premixed flames*". Autumn Meeting and Annual General Meeting of The Combustion Institute (British Section), 24 September 2014, London, UK.

Kypraiou AM, Karimi N, Dowling AP, Mastorakos E, "*Proper orthogonal decomposition analysis of a turbulent swirling self-excited premixed flame*". Joint British and Scandinavian-Nordic Section Combustion Meeting, 27-28 March 2014, Cambridge, UK.

Kypraiou AM, Mastorakos E, "*Ethylene reforming from steady and transient operation of a non-catalytic porous media burner*". Joint British and Scandinavian-Nordic Section Combustion Meeting, 27-28 March 2014, Cambridge, UK.

Kypraiou AM, Dowling AP, Mastorakos E, "*Experimental investigation of entropy waves in liquid fuelled combustor*". IMPACT-AE Technical Review Meeting, 3-4 December 2013, Paris, France.